

Asymmetries in mixed beauty decays

JACCO ANDREAS DE VRIES

Copyright © 2017 Jacco de Vries, all rights reserved.
Asymmetries in mixed beauty decays
“Asymmetrieën in gemengde schoonheidsvervalen”
Thesis, Vrije Universiteit, Amsterdam

Cover design by Arvid van Dam
Printed by Gildeprint
ISBN 978-94-6233-869-2



This work is part of the research programme of the Foundation for Fundamental Research on Matter (FOM), which is part of the Netherlands Organisation for Scientific Research (NWO). The work is carried out at the National Institute for Subatomic Physics (Nikhef) in Amsterdam, The Netherlands.

VRIJE UNIVERSITEIT

Asymmetries in mixed beauty decays

ACADEMISCH PROEFSCHRIFT

ter verkrijging van de graad Doctor aan
de Vrije Universiteit Amsterdam,
op gezag van de rector magnificus
prof.dr. V. Subramaniam,
in het openbaar te verdedigen
ten overstaan van de promotiecommissie
van de Faculteit der Bètawetenschappen
op woensdag 14 maart 2018 om 13.45 uur
in de aula van de universiteit,
De Boelelaan 1105

door

Jacco Andreas de Vries

geboren te Groningen

promotor: prof.dr. M.H.M. Merk

copromotor: dr. J.A.N. van Tilburg

Voor Karin

Contents

1	Introduction	1
1.1	The Standard Model	4
1.1.1	Fundamentals	4
1.1.2	The quark sector	8
1.2	<i>CP</i> violation	11
1.2.1	Sakharov conditions	11
1.2.2	Direct <i>CP</i> violation	13
1.2.3	Neutral-meson mixing	15
1.2.4	Time evolution	17
1.2.5	<i>CP</i> violation in interference	20
1.2.6	Standard Model expectations and beyond	20
1.2.7	History of <i>CP</i> violation in mixing	22
1.2.8	Measuring a_{sl}^d and a_{sl}^s	25
2	The LHCb experiment	31
2.1	The LHC and conditions at point 8	33
2.2	Tracking of charged particles	35
2.2.1	Magnet	36
2.2.2	Vertex Locator	37
2.2.3	Tracker Turicensis	38
2.2.4	Inner Tracker	39
2.2.5	Outer Tracker	39
2.2.6	Material	40
2.2.7	Track reconstruction	41
2.3	Particle identification	43
2.3.1	Ring-imaging Cherenkov detectors	44
2.3.2	Calorimeters	44
2.3.3	Muon stations	45
2.3.4	Particle ID	47
2.4	Trigger	47
2.5	Simulation	49

3	Detection asymmetries	51
3.1	The asymmetry of $\mu^+\pi^-$ pairs	52
3.1.1	The J/ψ tag-and-probe method	54
3.1.2	The D^* partial-and-full method	58
3.1.3	Comparing the methods	61
3.2	The asymmetry of $K^+\pi^-$ pairs	62
3.2.1	The asymmetry of K^+K^- pairs	66
3.3	Hadron identification asymmetry	66
3.4	Trigger and muon PID asymmetry	70
3.4.1	Asymmetry of two trigger lines	73
4	CP violation in mixing of B^0 mesons	77
4.1	Method	77
4.2	Selection	78
4.2.1	Removal of identifiable backgrounds	79
4.2.2	Mass fit and signal yields	82
4.3	Simulation and background studies	83
4.3.1	Signal simulation	83
4.3.2	Contributions from peaking backgrounds	84
4.3.3	Determination of the B^+ fraction	85
4.4	Decay-time model	86
4.4.1	Determination of the k -factors	87
4.4.2	Decay-time resolution	88
4.4.3	Signal model	91
4.4.4	Simulation studies	92
4.4.5	Background models	93
4.4.6	Full model	95
4.5	Detection asymmetries	96
4.5.1	The $\mu^+\pi^-$ asymmetry	97
4.5.2	The $K^+\pi^-$ asymmetry	97
4.5.3	The muon trigger and PID asymmetry	99
4.5.4	Summary	100
4.6	Results	101
4.7	Systematic uncertainties	102
4.7.1	B^+ background	103
4.7.2	Other backgrounds	104
4.7.3	Uncertainties on the k -factor	105
4.7.4	Other fit-related systematic uncertainties	105
4.7.5	Further consistency checks	108

5	<i>CP</i> violation in mixing of B_s^0 mesons	111
5.1	Method	111
5.2	Selection	112
5.2.1	Removal of identifiable backgrounds	113
5.2.2	Peaking backgrounds	117
5.2.3	Fit strategy and measured asymmetry	118
5.3	Simulation and peaking backgrounds	121
5.3.1	Signal simulation	121
5.3.2	Contributions from peaking backgrounds	121
5.3.3	Asymmetries in the background modes	122
5.3.4	Effect on a_{sl}^s	123
5.4	Detection asymmetries	124
5.4.1	The $\mu^+\pi^-$ asymmetry	124
5.4.2	The K^+K^- asymmetry	124
5.4.3	PID asymmetry	126
5.4.4	The trigger and muon PID asymmetry	128
5.4.5	Total detection asymmetry	129
5.5	Results	129
6	Discussion	133
6.1	The picture after LHCb run 1	133
6.2	Thoughts about the dimuon anomaly	134
6.3	Future prospects	136
6.3.1	Additional charm decay channels	136
6.3.2	Additional beauty decay channels	137
6.3.3	Reducing errors due to calibration samples	137
6.3.4	Reducing errors due to backgrounds	138
6.3.5	Beyond run 1	138
6.4	Closing remarks	139
A	Time integration of the a_{sl}^s analysis	143
B	Additional material in the a_{sl}^d analysis	145
C	Additional material in the a_{sl}^s analysis	153
D	Using hadronic decays	155
	References	157
	Summary	167
	Samenvatting	169
	Acknowledgements	173

Contents

1

Introduction

The study of fundamental physics is about understanding what everything is made of, and how this interacts with each other. It is driven by curiosity, whereas applications of this new knowledge are possibly being developed later. Currently, we have a precise understanding of fundamental processes of matter directly around us. It is shaped by quarks that are bound together in baryons by the strong force and form nuclei. Electromagnetism combines nuclei with electrons to form atoms, and the weak force allows for radioactive decay. However, when we use our knowledge of the “small” to explain observations of the “very big” — at the scale of nebulae, galaxies and beyond — it quickly turns out that our knowledge is insufficient. In fact, we only understand about 5% of the total energy content of the observable universe. In order to answer more fundamental questions such as “Why is the universe the way it is today?” or “How is it possible that we exist at all?”, understanding the phenomena at these larger scales is important. Modern fundamental physics research is about shedding light on these questions. In particular, high-energy physicists try to understand large scale cosmological observations by making high-precision, systematic measurements of the interactions of fundamental particles.

The last century has seen large progress in understanding the fundamental building blocks of nature, starting from the discovery of the electron by Thompson in 1897. Further experimental progress has been made with the discovery of quarks in 1968 in deep-inelastic-scattering experiments at the Stanford Linear Accelerator Center (SLAC), and theoretical progress with the complete formulation of the Standard Model (SM) of particle physics shortly after. The most recently discovered particles that the SM predicted are the top quark in 1995 at the Large Electron Positron collider (LEP), the tau neutrino in 2000 at the Tevatron collider and the Higgs boson in 2012 at the Large Hadron Collider (LHC) completing the last piece of the SM.¹ The SM describes the known particle interactions — electromagnetic, weak- and strong nuclear forces — except gravity, which is too weak to have any effect at the level of individual particle interactions, when probed at energies far below the Planck scale $M_{pl} \approx 10^{19}$ GeV. Its predictions for physical processes have been experimentally tested to high precision in various ways during the past decades, and

¹In the late 19th century physicists generally believed that fundamental physics was almost fully understood. Obviously, this turned out not to be the case.

the measurements have been in agreement with the SM.² For an impressive overview, see Ref. [2, 3].

Nevertheless, open issues remain for which the SM has no answer. For instance, observations of galaxy rotation speeds, gravitational lensing and the power spectrum of the cosmic microwave background indicate the existence of matter that couples gravitationally, so-called dark matter [4]. It appears to be about a factor 5 more abundant in the universe than the normal baryonic matter, although we have never managed to observe it directly. Ongoing efforts include searches for its production in collider experiments, through scattering of cosmic dark matter particles in experiments such as LUX and XENON1T, and in searches for gamma rays from dark matter pair annihilation in the universe [5]. Another fundamental open question is why there is any matter in today’s universe at all. Known physics processes that convert energy to matter, create an equal amount of antimatter. The same is believed to have happened during the big bang. In the present day, however, all objects we see are made of matter. How this came about is not clear, since matter and antimatter would annihilate already in the early universe, resulting in only a sea of radiation and leave no matter to form any stars or planets. What is the reason for the matter dominance? Could it be that antimatter populates different regions of the universe? In that case, we would expect to observe gamma rays from annihilation processes at the boundaries of these “antimatter pockets”, since even the vacuum of space is not completely empty. In addition, similar to high-energetic cosmic rays consisting of matter particles, we would expect to find cosmic radiation of antiparticles originating from these regions, which have not been observed [6]. Finally, could it be that gravity has an opposite effect on antimatter, and is thus “pushed out” of the universe? This idea is being tested at CERN [7], but so far there are no indications to believe that this is the case. The most likely explanation for a matter-dominated universe is the existence of a process that is different for matter and antimatter, which eventually results in an excess of matter in the early universe (see Sec. 1.2.1). Such processes exist within the SM and are called C - and CP violating. Can the SM perhaps explain the matter dominance that we observe in the universe?

The amount of matter excess can be described by the difference of baryon-antibaryon densities, divided by the amount of radiation in the cosmic microwave background (CMB),

$$\eta \equiv \frac{n_B - n_{\bar{B}}}{n_\gamma} \approx (6.1 \pm 0.3) \times 10^{-10}, \quad (1.0.1)$$

where the amount of radiation in the CMB depends on matter-antimatter annihilation processes which occurred when the universe was still in thermal equilibrium. The baryon asymmetry [2] is inferred from the abundance of light elements like ^3He and ^7Li in big-bang nucleosynthesis. More recent determinations are obtained from the CMB, by measuring the effect that the baryon density has had on the acoustic peaks of the CMB spectrum, when the universe was still in thermal equilibrium [8]. Both methods are in agreement.

²This ignores the measurements of an anomalous magnetic moment of the muon and lepton universality tests (in ratios of τ^- to μ^- and μ^- to e^- processes) which are currently at 3-4 standard deviations away from their predictions [1], as well as the proton radius puzzle in muonic atoms.

In 1987 Cecilia Jarlskog proposed an invariant parameter to quantify the amount of CP violation in the SM [9]. It is written as

$$\begin{aligned}
J &= \det[M_{ij}^{\text{up } 2}, M_{ij}^{\text{down } 2}] \\
&= (m_t^2 - m_c^2)(m_t^2 - m_u^2)(m_c^2 - m_u^2)(m_b^2 - m_s^2)(m_b^2 - m_c^2)(m_s^2 - m_d^2) \\
&\quad \times \Im(V_{\alpha i} V_{\beta j} V_{\alpha j}^* V_{\beta i}^*) \quad (\alpha, \beta, i, j \in 1, 2, 3, i \neq j, \alpha \neq \beta),
\end{aligned} \tag{1.0.2}$$

where M_{ij}^{up} and M_{ij}^{down} are the up- and down quark mass matrices, m_x are the individual physical quark masses and $V_{\alpha i}$ are CKM elements that will be introduced in Sect. 1.1.2. This Jarlskog invariant is independent of any phase convention, and is zero if there is no CP violation. In order to construct a dimensionless measure of the amount of CP violation in the SM, the energy density (or equivalently, temperature) of the universe at the time that quark masses became non-zero (due to the Higgs mechanism), $T \gtrsim 100 \text{ GeV}$ is used (see Sect. 1.2.1), to find an asymmetry parameter:

$$\frac{J}{(100 \text{ GeV})^{12}} \approx 10^{-20}, \tag{1.0.3}$$

which appears to be at least 10 orders of magnitude smaller than the asymmetry in Eq. 1.0.1. This implies that there is not enough CP violation in the SM to explain the matter-antimatter asymmetry in the universe.

Beyond the Standard Model

Extending the SM with additional particles and/or forces allows to introduce additional sources of CP violation, as well as candidates for dark matter. Searching for these new particles at colliders can be done in two ways. Firstly, direct production of new particles can occur when the collision energy is larger than the mass of the new particle. This process is limited by the centre-of-mass energy of the collider, which is 13 TeV for the proton-proton collisions at the LHC. For pair production, the centre-of-mass energy must be at least twice the mass. For associated production with e.g. a top quark it can be less. However, for proton colliders such as the LHC one has to take into account the fraction of energy of the actual colliding parton inside the proton. This suppresses the direct production rate of high-mass particles.

Secondly, indirect detection can be done by precisely measuring a known SM process. New particles and forces can contribute to such a process and cause a deviation with respect to the SM predictions. This is how the existence of the charm quark was inferred from kaon decays in 1970, and how the process of B -mixing indicated in 1987 that the top quark must be heavy, before its discovery. Processes that are particularly sensitive to new contributions are particle transitions that occur through quantum loop diagrams in the SM. New particles that couple to the on-shell states may contribute in the virtual loop, without having to be created directly. This can affect the total probability, angular distributions or phase of the process. The size of their effect on a process is determined by their coupling to the SM particles, and is suppressed by the difference between their mass and the energy

transfer in the system. The sensitivity of indirectly measuring effects from new particles is thus still limited by their mass, but a sensitivity to masses of $\mathcal{O}(10 - 1000 \text{ TeV})$ can be reached using such measurements, depending on the process and the physics model. Any hint of physics beyond the SM at $\mathcal{O}(10 \text{ TeV})$ is likely to be accessible for direct detection in a future collider such as the future circular collider (FCC).

This work

The goal of this research is to make precision measurements of processes that are predicted in the SM with high accuracy. The studied process is CP violation in mixing in the B^0 and B_s^0 systems, which involves the sensitive quantum loops described above. The SM predictions of the relevant parameters, a_{sl}^d and a_{sl}^s , are practically equal to zero. Any measured deviation from zero hints at new contributions, which may affect the amount of CP violation in the early universe.

The large amounts of B^0 and B_s^0 mesons required for these measurements are produced by the LHC, a 27-km-circumference proton synchrotron at CERN, in the years 2011 and 2012. The data are collected by the LHCb detector, where the b stands for the b quark. The main challenge in measuring a_{sl}^d and a_{sl}^s is to understand the detection efficiency differences between matter and antimatter particles with high precision. Before discussing the analysis details, however, a short review of the SM and the concept of CP violation is presented.

1.1 The Standard Model

In the following section, the basic concepts and nomenclature of the SM and CP violation in the quark sector are introduced. These concepts underlie certain decisions that are made in the following chapters, and allow for easy reference. Throughout this thesis, natural units where $c = \hbar = 1$ are used.

1.1.1 Fundamentals

In the SM particles are represented by excitations of associated fields in 4-dimensional space-time. The fundamental matter particles in the SM are fermions; spin-1/2 fields that are further subdivided into quarks and leptons. Quarks come in six flavours, up (u), down (d), strange (s), charm (c), beauty (b) and top (t), increasing in mass. Leptons also come in six flavours, electron (e), muon (μ), tau (τ^-), and three corresponding neutrinos, ν_e , ν_μ and ν_τ .

Symmetries play a fundamental role in the SM. They are linked to conservation laws by Noether's theorem. Continuous external and internal symmetries are discussed here, while discrete symmetries are discussed in Sec. 1.1.2. The observation that any physical process on a field, e.g. an electromagnetic interaction on an electron, must be invariant under a time translation leads to energy conservation. The invariance of these processes under

spatial translations results in conservation of momentum. Free relativistic spin-1/2 fields that obey energy and momentum conservation are described by the Dirac Lagrangian density

$$\mathcal{L} = \bar{\psi}(i\gamma^\mu\partial_\mu - m)\psi, \quad (1.1.1)$$

where the fermion fields are represented by so-called spinors, ψ , the γ^μ are the gamma matrices, ∂_μ is the partial derivative, and μ runs over space and time indices. The equations of motion of the fields are obtained from the Euler-Lagrange equations using the Dirac Lagrangian density. These equations allows particle solutions for both positive or negative energy (or travelling forwards and backwards in time), introducing the concept of a particle with negative energy being equal to an antiparticle with positive energy. For every fermion described above an antiparticle is introduced, indicated by an overhead bar.

Interactions are introduced by requiring that the Lagrangian density is locally invariant under a continuous internal symmetry called a gauge symmetry. Electromagnetism is obtained by enforcing a local $U(1)$ symmetry on the fields. This means that the Lagrangian density has to be invariant under local phase shifts of the fermion fields. To maintain invariance the partial derivative is replaced by the covariant derivative in the Dirac Lagrangian density:

$$\partial_\mu \rightarrow D_\mu \equiv (\partial_\mu + ie a_\mu). \quad (1.1.2)$$

This introduces a spin-1 gauge field a_μ with a coupling to the fermion fields, and a dimensionless coupling constant e describing the strength of the interaction. The infinitesimal generator of this $U(1)$ group is called weak hypercharge or Y_W , and its eigenvalues are conserved quantum numbers of the fermion. The a_μ field itself, also called a vector boson field (or force carrier), is described by the Proca Lagrangian density for spin-1 fields,

$$\mathcal{L} = -\frac{1}{16\pi}(\partial^\mu a^\nu - \partial^\nu a^\mu)(\partial_\mu a_\nu - \partial_\nu a_\mu) + \frac{1}{8\pi}m^2 a^\rho a_\rho, \quad (1.1.3)$$

where $m = 0$ for the photon.

In 1957, observations using decays of ^{60}Co atoms demonstrated that the weak interaction only acts on particles with negative, or left-handed, chirality [10].³ In analogy to spin, the weak isospin T is introduced. For right-handed particles, $T = 0$ by construction and each fermion is considered to be a weak isospin singlet. For left-handed particles, $T = 1/2$, and up- and down-type fermions within one generation are considered to be the same particle under the weak interaction, with only a different value for the third component of the weak isospin, T_3 . For antiparticles the right-handed fields form weak isospin doublets, and the left-handed fields form weak isospin singlets. In other words, the left-handed fermions (right-handed antifermions) are grouped into weak isospin doublets, e.g. $\psi_L = (u_L, d_L)^T$, and the weak interaction originates from the $SU(2)$ rotational symmetry in these isospin doublets. The Lie group $SU(2)$ has three infinitesimal generators — represented by the three Pauli matrices, $\tau^{1,2,3}$ — and requiring local gauge invariance introduces three fields,

³In terms of the field theory operators, this means that the operator coupling between the SM fermions and the (charged) weak force carriers is of the form $\gamma^\mu(1 - \gamma^5)$ or $(V - A)$ (“vector minus axial vector”).

$b_\mu^{1,2,3}$. The covariant derivative for the weak interaction is of the form

$$\partial_\mu \rightarrow D_\mu \equiv \partial_\mu + ig\vec{\tau} \cdot \vec{b}_\mu, \quad (1.1.4)$$

where g is the dimensionless coupling constant of the weak interaction. The off-diagonal Pauli matrices cause a transformation between up- and down-type fermions, resulting in flavour-changing processes. In fact, linear combinations of τ_1 and τ_2 form τ_+ and τ_- , which purely transform up-type to down-type, and vice-versa. The fields associated with τ_\pm are the W^\pm boson fields or charged currents. τ_3 is diagonal and thus flavour-preserving.

The weak interaction is similar to the electromagnetic force, only its range is found to be very short, indicating that the corresponding force carriers are heavy. This poses a problem, since the mass term (i.e. a term with the field squared) for a gauge boson in the Lagrangian density (Eq. 1.1.3) breaks gauge invariance. The solution [11, 12] is to introduce a complex scalar field which is a weak isospin doublet,

$$\phi = \frac{1}{\sqrt{2}} \begin{pmatrix} \phi_1 + i\phi_2 \\ \phi_3 + i\phi_4 \end{pmatrix}. \quad (1.1.5)$$

The Lagrangian density of the scalar field is described by the Klein-Gordon equation with a potential,

$$\mathcal{L} = (D_\mu\phi)^\dagger(D^\mu\phi) - V(\phi), \quad (1.1.6)$$

and couples to the gauge fields ($a_\mu, b_\mu^{1,2,3}$) through the covariant derivative. The potential takes the shape $V(\phi) = \mu^2\phi^\dagger\phi + \lambda(\phi^\dagger\phi)^2$, which is similar to a 'Mexican hat' (see Fig. 1.1) for $\mu^2 < 0$. At high energies — in the early universe — any value for ϕ where the potential is significantly smaller than the temperature is equally likely, and averages out to zero due to the symmetry in $V(\phi)$. However, at lower energies the potential forces the ϕ fields to go into the lowest energy configuration in the 'rim of the hat', also called the vacuum expectation value (VEV). This means that one of the fields must be non-zero; and $\phi_1 = \phi_2 = \phi_4 = 0$ and $\phi_3 = v + h$ are chosen, where v is a constant (describing the 'horizontal' distance from the central peak to the lower rim of the hat) and h describes the fluctuations of the field around the VEV. The degrees of freedom that are lost in the ϕ field, $\phi_{1,2,4}$, re-appear as mass terms for the vector bosons (W^\pm, Z^0) in the Lagrangian density due to the covariant derivative [13–15]. In other words, at high energies the electroweak Lagrangian is gauge symmetric, and is "spontaneously" broken at lower energies to form massive gauge fields. In addition, an additional scalar field h is introduced to the theory, with a mass term of its own, 3- and 4-point self-couplings, and couplings to the vector bosons proportional to the newly created mass terms. This is called the Brout-Englert-Higgs mechanism of spontaneous symmetry breaking, and was applied to electroweak (EW) theory by Weinberg and Salam. Together with Glashow they were awarded the 1979 Nobel prize in physics for their work on the EW interaction. The scalar field h is called the Higgs field, and the discovery of the Higgs boson at the LHC in 2012 [16, 17] completed the SM and resulted in the Nobel prize in physics for Englert and Higgs in 2013. One of the four vector bosons is the massless photon field. In order to ensure that

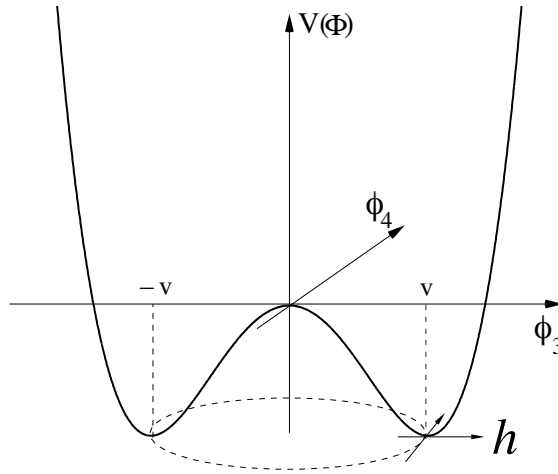


Figure 1.1: Potential $V(\phi)$ of the scalar Higgs field in Eq. 1.1.6, visualized in the ϕ_3, ϕ_4 plane. In the broken phase, the field theory is described from the minimum of the potential at the VEV, $|\phi_3| = v$. Perturbations around this minimum are described by the Higgs field h .

one of the four vector bosons remains massless after spontaneous symmetry breaking, the weak hypercharge of the Higgs field has to be $Y = +1$. In addition, a linear combination of the a_μ and b_μ^3 fields is made, parametrized by the weak mixing angle θ_W ,

$$\begin{aligned} A_\mu &= a_\mu \cos(\theta_W) + b_\mu^3 \sin(\theta_W) \\ Z_\mu &= -a_\mu \sin(\theta_W) + b_\mu^3 \cos(\theta_W) \end{aligned} \quad (1.1.7)$$

The coupling of a fermion to A_μ , the massless photon field, is $Q = T_3 + Y_W/2$ and also known as the classical charge. The A_μ and Z_μ fields, together with the W_μ^\pm fields, are the force carriers of the EW interaction.

The strong force is responsible for binding the quarks together in hadrons: baryons (three quarks or three antiquarks) such as the proton (uud), neutron (udd) or Λ_b^0 ($u\bar{d}b$), and mesons (one quark and one antiquark) such as the b mesons B^0 ($\bar{b}d$), B^+ ($\bar{b}u$) and B_s^0 ($\bar{b}s$), the d mesons D^- ($\bar{c}d$) and D_s^- ($\bar{c}s$), kaons K^+ ($\bar{s}u$) and pions π^+ ($u\bar{d}$). The strong force is described by introducing a colour-charge quantum number, which comes in three variants, “red”, “green” and “blue”, and by requiring that the Lagrangian density is invariant under a local rotation in this colour space corresponding to elements of the group $SU(3)$. Only quarks have a non-zero colour charge and couple to the strong force. There are eight infinitesimal generators of $SU(3)$, represented by the eight Gell-mann matrices, and thus eight fields called gluons. These gluons are all massless and differ only from each other by the colour charges they carry. The SM content is summarized in Fig. 1.2.

The probability of a quantum process to occur is calculated with perturbation theory. The calculations are represented by Feynman diagrams, and adding more vertices to the

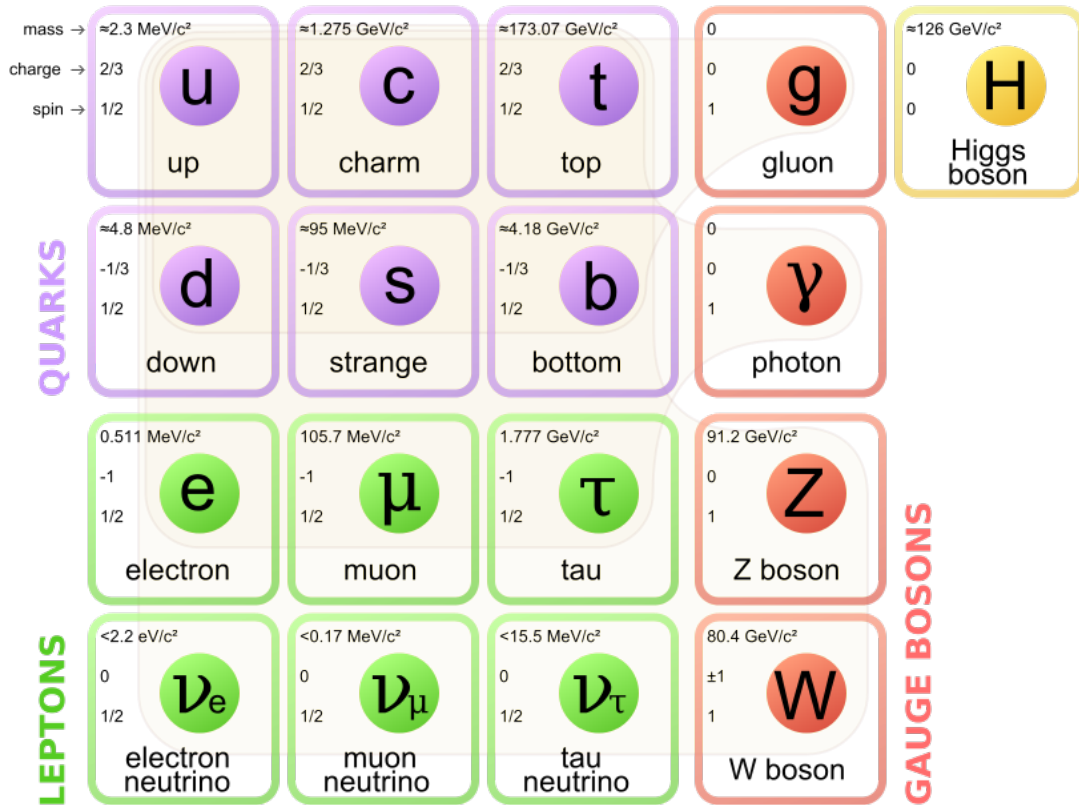


Figure 1.2: Overview of the fermions, force carrying bosons and Higgs boson in the SM. Values shown are the PDG best known values of 2008 [2]. Credit: Wikipedia.

diagram corresponds to calculating higher order perturbations of the process. Unlike in the electroweak interaction, the strong coupling strength, α_s , is larger than one in the case of low-energy processes. Therefore, perturbation theory can only be applied in QCD for the calculation of high-energy parts of a diagram. Alternatively, certain approximations and models allow to make numerical statements about the soft, bound QCD part (see Sec.1.2.6), although this is usually the limiting factor on the precision of SM calculations. In calculations involving B mesons, an approximation can be made using the fact that one quark constituent is much heavier than the other. This is called heavy quark effective theory (HQET), and allows for more precise theoretical calculations. Inputs from measurements allow to constrain the validity of these approximations and models, while direct numerical calculations are attempted using e.g. lattice QCD.

1.1.2 The quark sector

Not only mass terms of vector bosons break gauge symmetry: also the $m\bar{\psi}\psi$ term in the Dirac Lagrangian density (Eq. 1.1.1) is not gauge invariant under the weak interaction. In order to insert mass terms for the fermions, the same Higgs field is used that gives mass to the weak vector bosons by introducing couplings of fermions to the Higgs field by hand.

These are called the Yukawa couplings,

$$- \mathcal{L}_{\text{Yukawa}} = Y_{ij} \bar{\psi}_{L,i} \phi \psi_{R,j} + \text{hermitian conjugates (h.c.)}, \quad (1.1.8)$$

where $\psi_{L,i}$ is a vector of the left weak-isospin doublets, with one component for each flavour generation i ,⁴

$$\psi_{L,i} = \begin{pmatrix} q_{L,i}^{\text{up}} \\ q_{L,i}^{\text{down}} \end{pmatrix} = \begin{pmatrix} u_L \\ d_L \end{pmatrix}, \begin{pmatrix} c_L \\ s_L \end{pmatrix}, \begin{pmatrix} t_L \\ b_L \end{pmatrix}. \quad (1.1.9)$$

The ϕ is the complex scalar Higgs field (Eq. 1.1.5) that demotes the left-handed isospin doublets to singlet terms. The right-handed fields $\psi_{R,j}$ are the weak-isospin singlets and Y_{ij} is a complex 3-by-3 matrix in flavour space. After spontaneous symmetry breaking, $\phi = \begin{pmatrix} 0 \\ v \end{pmatrix}$ and the Lagrangian becomes

$$- \mathcal{L}_{\text{Yukawa}} = M_{ij}^{\text{up-up}} \bar{q}_{L,i}^{\text{up}} q_{R,j}^{\text{up}} + M_{ij}^{\text{down-down}} \bar{q}_{L,i}^{\text{down}} q_{R,j}^{\text{down}} + h.c., \quad (1.1.10)$$

where the $M_{ij} = \frac{v}{\sqrt{2}} Y_{ij}$ matrices represent the mass terms for the quarks. For leptons, similar Yukawa couplings are introduced. The matrices M_{ij} are allowed to have off-diagonal components that mix flavour generations. This would mean that the current fields are not in a Hamiltonian eigenstate, and thus the quarks in this basis do not have a well-defined mass and lifetime. Diagonalization of M_{ij} occurs in general through a transformation with two unitary matrices $M_{ij}^{\text{diag}} = V_L M_{ij} V_R^\dagger$. Inserting $V_L^\dagger V_L = V_R^\dagger V_R = \mathbb{1}$ on both sides of M_{ij} in Eq. 1.1.10, the corresponding rotation of the quark fields in the Hamiltonian eigenstate basis is

$$\bar{q}_{L/R,i}^{\mathbf{H},\text{up/down}} = (V_{L/R}^{\text{up/down}})_{ij} \bar{q}_{L/R,j}^{\text{up/down}}. \quad (1.1.11)$$

The Yukawa Lagrangian now contains well-defined mass terms, but the quark fields have to be expressed in the same basis throughout the whole Lagrangian. This is relevant for the coupling of the left-handed quarks with the W^\pm bosons through the covariant derivative in the Dirac Lagrangian, which contains terms like

$$\begin{aligned} & \bar{q}_{L,i}^{\text{up}} \gamma^\mu W_\mu^- q_{L,j}^{\text{down}} + \bar{q}_{L,i}^{\text{down}} \gamma^\mu W_\mu^+ q_{L,j}^{\text{up}} \\ & = \bar{q}_{L,i}^{\mathbf{H},\text{up}} (V_{CKM})_{ij} \gamma^\mu W_\mu^- q_{L,j}^{\mathbf{H},\text{down}} + \bar{q}_{L,i}^{\mathbf{H},\text{down}} (V_{CKM})_{ij}^\dagger \gamma^\mu W_\mu^+ q_{L,j}^{\mathbf{H},\text{up}}, \end{aligned} \quad (1.1.12)$$

where $V_{CKM} = V_L^{\text{up}} V_L^{\text{down}\dagger}$ is called the Cabibbo-Kobayashi-Maskawa matrix, and describes the relative coupling of the W^\pm bosons to a specific up-type quark and a specific down-type quark⁵.

The CKM matrix is a complex 3-by-3 matrix, constrained by unitarity. In general such a matrix can be described by $n^2 = 9$ degrees of freedom, of which $\frac{1}{2}n(n-1) = 3$ Euler angles and $9 - 3 = 6$ phases. Since V_{CKM} only appears in combinations with quarks like

⁴For convenience the colour index is omitted here.

⁵By convention the up-type flavour and Hamiltonian eigenstates are chosen to be equal, and the down-type quarks are rotated

Eq. 1.1.12, choices of the relative quark phases can compensate for $2n - 1 = 5$ phases in V_{CKM} . This leaves one free phase in V_{CKM} , usually called δ_{CP} . Note that for less than three flavour generations, there is no complex phase (which means that there would be no CP violation in the SM). The CKM description and the prediction of CP violation was attributed the Nobel prize in physics in 2008. The CKM matrix is often given in the Wolfenstein parametrization,

$$V_{\text{CKM}} = \begin{pmatrix} V_{ud} & V_{us} & V_{ub} \\ V_{cd} & V_{cs} & V_{cb} \\ V_{td} & V_{ts} & V_{tb} \end{pmatrix} \approx \begin{pmatrix} 1 - \frac{1}{2}\lambda^2 & \lambda & A\lambda^3(\rho - i\eta) \\ -\lambda & 1 - \frac{1}{2}\lambda^2 & A\lambda^2 \\ A\lambda^3(1 - \rho - i\eta) & -A\lambda^2 & 1 \end{pmatrix}, \quad (1.1.13)$$

which is written here up to $O(\lambda^3)$, where $\lambda \approx 0.23$. The flavour structure is remarkable: diagonal elements representing transition probabilities within one flavour generation are close to one, while off-diagonal elements are suppressed. A proper explanation for this structure is lacking, but inspires models beyond the SM with additional (broken) symmetries. The unitarity condition ($V_{\text{CKM}}^\dagger V_{\text{CKM}} = \mathbb{1}$) is tested by measuring processes involving these CKM elements and combinations of them, and has been a major goal of flavour physics for many years. Any deviation from unitarity would indicate contributions from a new generation, or from non-SM processes that are not flavour invariant.

In analogy, the lepton sector has a similar matrix originating from the Yukawa couplings, called U_{PMNS} . By convention the down-type leptons (e^- , μ^- , τ^-) have identical mass- and flavour eigenstates, while the up-types (ν_e , ν_μ , ν_τ) are rotated into their mass eigenstates (ν_1 , ν_2 , ν_3). Besides a completely different matrix structure, the phenomenology is also different in the lepton sector. A quark is defined, and mostly identified, as a Hamiltonian eigenstate in which it will partake in strong interactions. Only when the weak interaction is involved, a down-type quark is regarded as a superposition of all down-type quark flavour eigenstates. In contrast, a neutrino only partakes in the weak interaction and is identified by its flavour eigenstate. In addition, neutrinos are not bound by QCD and can travel large distances coherently in their superposition of Hamiltonian eigenstates due to their small mass differences. The resulting neutrino flavour oscillations prove the existence of neutrino mass differences, and its discovery was awarded the Nobel prize in Physics in 2015. Such phenomenology will not be observable in the quark sector, but it is mentioned because it may originate from the same principle of Yukawa couplings, although the couplings are very small.

Apart from its success in predicting processes in nature, the SM requires inputs for many fundamental parameters. All in all, the degrees of freedom in the SM are the 12 fermion masses, the coupling strengths to the 3 gauge groups, 2×4 parameters for V_{CKM} and U_{PMNS} and the Higgs mass and VEV. Including θ_{QCD} , which describes the size of CP violation in strong interactions,⁶ there are 26 free parameters in the SM that require experimental determination.⁷

⁶ θ_{QCD} has been constrained to be $< 10^{-10}$ using neutron electric dipole moment measurements [2, 18], indicating a fine-tuning problem in the contributing diagrams known as the *strong CP problem*.

⁷This is assuming that neutrinos only have a Dirac mass. If they are Majorana (i.e. neutrinos are their

1.2 *CP* violation

This section is focused on the discrete symmetry transformations that are probed when measuring *CP* violation. The parity operator P flips spatial directions: on a scalar field it implies $P\phi(x, t) = \phi(-x, t)$. For Dirac spinors the transformed fields are required to obey the Dirac equation, resulting in $P\psi(x, t) = e^{i\phi}\gamma^0\psi(-x, t)$ (and $P\bar{\psi}(x, t) = e^{-i\phi}\bar{\psi}(-x, t)\gamma^0$). The phase ϕ is arbitrary. As this transformation flips the spatial direction of a particle, also its helicity is inverted, which in the massless limit equals the chirality or handedness. The weak interaction only couples to the left-handed particles (right-handed antiparticles), and thus maximally violates parity.

The charge operator C transforms a particle to its antiparticle wave function, which has opposite electrical charge, while leaving the helicity unchanged. On a scalar field the operation is defined as $C\phi(x, t) = \phi^\dagger(x, t)$, which is also defined for neutral particles. Requiring that fermions also obey the Dirac equation after C transformation results in $C\psi(x, t) = i\gamma^2\gamma^0\bar{\psi}^T(x, t)$ (and $C\bar{\psi}(x, t) = i\psi^T(x, t)\gamma^2\gamma^0$). Again, the weak interaction maximally violates charge operation symmetry, since the helicity does not flip sign under C .

The combined *CP* operation on a fermion takes the form $CP\psi(x, t) = ie^{i\phi}\gamma^2\gamma^0\psi^*(-x, t)$, which takes a fermion state to the antifermion state with opposite helicity, and intuitively seems to leave the weak interaction invariant. The transformation of a Yukawa-like term in the Lagrangian transforms into $CP(\bar{\psi}_1\phi\psi_2) = \bar{\psi}_2\phi^\dagger\psi_1$. Applying this to Eq. 1.1.8, the result is that the Yukawa Lagrangian is invariant under the *CP* operation if $Y_{ij} = Y_{ij}^*$, or in other words, if the complex phase δ_{CP} in V_{CKM} is zero. If this phase is non-zero, violation of *CP* symmetry in the weak sector may occur.

1.2.1 Sakharov conditions

In the introduction we discussed that there was not enough *CP* violation in the universe to explain the size of the observed baryon asymmetry. In fact, more than just the occurrence of *CP* violation is needed. In 1967 Sakharov noted three conditions required to produce a net baryon asymmetry in the universe, later to be known as the Sakharov conditions: [20]

- baryon number violation
- thermal non-equilibrium
- C and *CP* violation

Consider the following toy model [21]. In order to create a net baryon number from a state with no net baryons, a process must exist that violates baryon number,

$$X \rightarrow Y + B, \tag{1.2.1}$$

own antiparticle) there are additional degrees of freedom. Extensions to the SM that try to understand the unnatural small size of neutrino masses, such as a “seesaw mechanism” [19], require a Majorana mass. Whether this is the case is actively being researched in e.g. neutrino-less double beta decay experiments such as GERDA.

where X and Y are particles without baryon number, while B is a particle with non-zero baryon number. If there is enough energy in the system and the particles are continuously in contact with each other, one can assume that the reverse process ($Y + B \rightarrow X$) happens at the same rate. Thermal non-equilibrium ensures this not to be the case, and suppresses the reverse process by a Boltzmann factor $\sim e^{-M_X/T}$, where M_X is the mass of X . The violation of C implies that a process creating a net amount of baryons has a different probability than the charge-conjugate process, which creates antibaryons,

$$P(X \rightarrow Y + B) \neq P(\bar{X} \rightarrow \bar{Y} + \bar{B}). \quad (1.2.2)$$

The violation of CP then ensures that a left-handed process creating a net amount of baryons is not balanced by the right-handed equivalent creating antibaryons, which would still leave the total (left- plus right-handed) baryon number invariant:

$$P(X_L \rightarrow Y_L + B_L) \neq P(\bar{X}_R \rightarrow \bar{Y}_R + \bar{B}_R). \quad (1.2.3)$$

Finally, CPT symmetry makes sure that the total probability of all processes equals the sum of probabilities of all antiparticle equivalent processes. Therefore, a second competing process to which X (\bar{X}) can decay, say $X \rightarrow Y + Z$ (and $\bar{X} \rightarrow \bar{Y} + \bar{Z}$) must exist, where Z has a different baryon number than B , in order to end up with a non-zero net baryon number.⁸ One source of C and CP violation is provided by the EW interaction as discussed in the previous section. The CP violation in the quark sector, in particular in neutral B mixing, is the main subject of this dissertation.

Baryon number violation is allowed by the SM as well, as is seen in quantum processes known as triangle anomalies [21]. These anomalies violate (left-handed) baryon number B and lepton number L individually but conserve $(B - L)$. These processes are associated with transitions between an infinite number of vacua at finite temperature that have different baryon numbers, and are called sphalerons. In the early universe, at temperatures larger than the EW symmetry breaking scale ($T \gtrsim 100$ GeV) they are thought to have been abundant. In various models beyond the SM, other processes such as leptoquark interactions can occur that would also violate baryon (and lepton) number.

Thermal non-equilibrium can occur if the expansion of the universe occurs faster than the typical interaction rate of the processes described above. As such, a period of inflation would be a good candidate. However, there are various reasons to believe that a net baryon excess has to be created after inflation [22], one of which is that the universe should be basically empty after a period of exponential expansion. Two of the most popular alternative explanations exist in the literature: leptogenesis and electroweak baryogenesis. In leptogenesis models, a lepton asymmetry is created in the very early universe due to the decay of heavy right-handed neutrinos. This eventually turns into a baryon asymmetry at lower energies due to sphaleron processes. In contrast, EW baryogenesis can potentially occur within the SM. In EW baryogenesis, the baryon asymmetry is created around the

⁸Compare this to the equal lifetimes of B^+ and B^- mesons, even though some CP -conjugate partial widths differ, e.g. $\Gamma(B^+ \rightarrow \pi^0 K^+) \neq \Gamma(B^- \rightarrow \pi^0 K^-)$.

EW scale, through the EW-symmetry-breaking bubble wall. If the EW phase transition is of first-order, bubbles with the broken phase inside will appear and expand in a sea of the unbroken phase as the universe cools down. It is at the border of these quickly expanding bubbles that thermal non-equilibrium may occur. The process is roughly described as follows [21, 23]. Scattering of quarks on the domain wall leads to $M_{ij}\psi_L\bar{\psi}_R$ Yukawa interactions and therefore have a non-zero reflection coefficient, while $\bar{\psi}_L$ and ψ_R penetrate the wall unimpeded. This creates an excess of $\psi_L + \bar{\psi}_R$ over $\bar{\psi}_L + \psi_R$, just outside the bubble. In addition, CP violation would ensure a dominance of ψ_L over $\bar{\psi}_R$ outside the wall. This is illustrated by Fig. 1.3. Weak sphaleron processes turn this CP asymmetry into a net baryon asymmetry just outside the bubble. The expansion of the bubble wall then causes baryons to quickly diffuse through the wall. Inside, the sphaleron processes are suppressed due to the larger VEV, and the baryon asymmetry is “frozen”. The validity of this mechanism strongly depends on the existence of expanding bubbles, which occurs only in a first-order phase transition. Whether the EW phase transition is indeed of first order has to be determined by measuring the Higgs self-coupling parameters in the future. If this is the case, the process of electroweak baryogenesis can be embedded within the SM, assuming a modified Higgs potential, and given that there are additional sources of CP violation.

In order to measure the amount of CP violation, three types can be distinguished: direct CP violation, CP violation in mixing, and CP violation in the interference between mixing and decay.

1.2.2 Direct CP violation

Measuring CP violation effectively means performing a measurement that is sensitive to the complex phases of amplitudes of a process. Consider as an example a process consisting

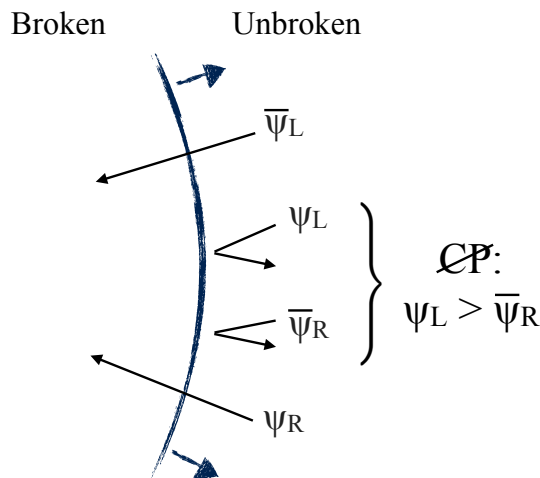


Figure 1.3: Illustration of the scattering of fermions on the expanding bubble wall, adapted from [21].

of a single Feynman diagram, such as $B^+ \rightarrow \pi^0 \mu^+ \bar{\nu}_\mu$. There is a weak phase associated to the CKM element V_{ub} (Eq. 1.1.13), but since the probability of the process is proportional to the absolute square of V_{ub} , this phase does not affect the decay rate. In order to be sensitive to the CP -violating phase, one requires two diagrams of the same process $P \rightarrow f$ that will interfere, with a relative phase difference between the two,

$$\begin{aligned} \mathcal{A}_1 &= |\mathcal{A}_1| e^{i\varphi_1}, \\ \mathcal{A}_2 &= |\mathcal{A}_2| e^{i\varphi_2}, \\ |\mathcal{A}|^2 &= |\mathcal{A}_1 + \mathcal{A}_2|^2 = |\mathcal{A}_1|^2 + |\mathcal{A}_2|^2 + 2|\mathcal{A}_1||\mathcal{A}_2|(e^{i(\varphi_1-\varphi_2)} + e^{i(\varphi_2-\varphi_1)}) \\ &= |\mathcal{A}_1|^2 + |\mathcal{A}_2|^2 + 2|\mathcal{A}_1||\mathcal{A}_2| \cos(\Delta\varphi), \end{aligned} \quad (1.2.4)$$

where \mathcal{A} is an amplitude and $\Delta\varphi = (\varphi_1 - \varphi_2)$. The phase φ_i consists of the CP -conserving, or strong phase δ_i and the CP -violating, or weak phase ϕ_i : $\varphi_i = (\phi_i + \delta_i)$. Now consider the CP -conjugate process (i.e. $\phi \rightarrow -\phi$ and $\delta \rightarrow \delta$),

$$\begin{aligned} |\mathcal{A}|^2 &= |\mathcal{A}_1 + \mathcal{A}_2|^2 = |\mathcal{A}_1|^2 + |\mathcal{A}_2|^2 + 2|\mathcal{A}_1||\mathcal{A}_2| \cos(\Delta\delta + \Delta\phi) \\ |\bar{\mathcal{A}}|^2 &= |\bar{\mathcal{A}}_1 + \bar{\mathcal{A}}_2|^2 = |\mathcal{A}_1|^2 + |\mathcal{A}_2|^2 + 2|\mathcal{A}_1||\mathcal{A}_2| \cos(\Delta\delta - \Delta\phi). \end{aligned} \quad (1.2.5)$$

Notice that without a different CP -conserving phase, i.e., $\Delta\delta = 0$, we would not be able to observe a difference in decay rates between CP -conjugate processes due to the symmetric nature of the cosine. This CP -conserving phase is due to the strong interaction.

The amount of CP violation in a process can be expressed as the asymmetry in the decay rates,

$$A = \frac{\Gamma(P \rightarrow f) - \Gamma(\bar{P} \rightarrow \bar{f})}{\Gamma(P \rightarrow f) + \Gamma(\bar{P} \rightarrow \bar{f})} \quad (1.2.6)$$

where $\Gamma(\bar{P} \rightarrow \bar{f})$ is the CP -conjugate process of $\Gamma(P \rightarrow f)$.

An intuitive process where two diagrams with a relative weak phase difference contribute, is a decay into a final state containing a same-flavour quark-antiquark pair. This indicates a contribution from a loop diagram called a ‘‘penguin diagram’’, as is the case in the decay $B^+ \rightarrow \pi^0 K^+$, see Fig. 1.4. This type of CP violation is called direct CP violation or A_{CP}^{dir} ,

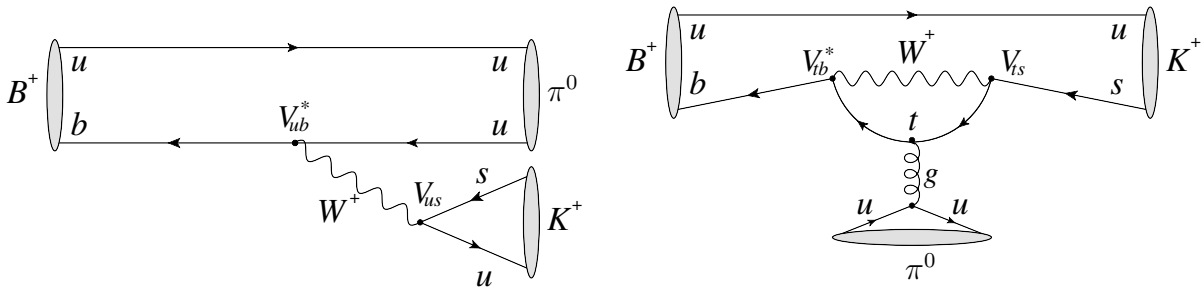


Figure 1.4: The main (left) tree and (right) penguin diagrams of the decay $B^+ \rightarrow K^+ \pi^0$. The interference between the two diagrams results in an observable amount of direct CP violation.

and has been measured to be 0.040 ± 0.021 for this specific decay [3]. In terms of the decay amplitudes and phases (Eq. 1.2.4), this quantity is equal to

$$A_{CP}^{\text{dir}} = \frac{-2|\mathcal{A}_1||\mathcal{A}_2| \sin(\Delta\delta) \sin(\Delta\phi)}{|\mathcal{A}_1|^2 + |\mathcal{A}_2|^2 + 2|\mathcal{A}_1||\mathcal{A}_2| \cos(\Delta\delta) \cos(\Delta\phi)}. \quad (1.2.7)$$

In this example, the weak phases involved originate from $\arg(V_{ub}^*V_{us})$ in the tree diagram, and $\arg(V_{tb}^*V_{ts})$ in the penguin diagram, and a non-trivial strong phase difference can be expected.

1.2.3 Neutral-meson mixing

Neutral mesons such as the B^0 can change into their CP conjugate, \bar{B}^0 , a phenomenon known as mixing. The mixing process provides a mean to observe CP violation. It can be described in a model-independent way with a few parameters, which will be related to SM predictions later on. In this subsection the B^0 will be used for simplicity, but everything applies equally to the B_s^0 system.

There are various bases in which to express the B^0 - \bar{B}^0 system. The first is the production or flavour eigenstate basis, ($|B^0\rangle, |\bar{B}^0\rangle$). Production via the strong interaction creates the mesons in a well-defined quark flavour content. For generality, consider the arbitrary superposition $\psi(t) = a(t)|B^0\rangle + b(t)|\bar{B}^0\rangle$. In the space spanned by ($|B^0\rangle, |\bar{B}^0\rangle$), the state vector is $\psi(t) = \begin{pmatrix} a(t) \\ b(t) \end{pmatrix}$. The time evolution of this state is governed by the Hamiltonian operator \hat{H} according to the Schrödinger equation,

$$i \frac{d}{dt} \psi = \hat{H} \psi \quad \rightarrow \quad \psi(t) = e^{-iEt} \psi(0). \quad (1.2.8)$$

The effective Hamiltonian that will be used consists of two parts. The first is the self-energy of the system, which is Hermitian in order to have real eigenvalues, while the second part is non-Hermitian and is responsible for the weak decay. Without mixing this looks like

$$\hat{H} = \hat{M} - \frac{i}{2} \hat{\Gamma} = \begin{pmatrix} M_{B^0} & 0 \\ 0 & M_{\bar{B}^0} \end{pmatrix} - \frac{i}{2} \begin{pmatrix} \Gamma_{B^0} & 0 \\ 0 & \Gamma_{\bar{B}^0} \end{pmatrix}. \quad (1.2.9)$$

Consider the time evolution of the B^0 - \bar{B}^0 system while allowing for mixing. In general, this means introducing off-diagonal terms to the Hamiltonian, as

$$\hat{H} = \begin{pmatrix} M_{11} & M_{12} \\ M_{21} & M_{22} \end{pmatrix} - \frac{i}{2} \begin{pmatrix} \Gamma_{11} & \Gamma_{12} \\ \Gamma_{21} & \Gamma_{22} \end{pmatrix}, \quad (1.2.10)$$

where $M_{11} = M_{22}$ and $\Gamma_{11} = \Gamma_{22}$ due to CPT invariance, and $M_{21} = M_{12}^*$, $\Gamma_{21} = \Gamma_{12}^*$ and $M_{11}, \Gamma_{11} \in \mathbb{R}$. In order to describe the complete B^0 - \bar{B}^0 time evolution, the Hamiltonian matrix should actually be expressed in the basis of B^0, \bar{B}^0 plus all the contributing final states to which both can decay. This can be approximated to Eq. 1.2.10 with Hermitian \hat{M} and $\hat{\Gamma}$ by assuming that the overall time dependence of the B^0 and \bar{B}^0 states is exponential. This is known as the Wigner-Weisskopf approximation [24].

The $B^0-\bar{B}^0$ oscillations are, to first order, due to the off-shell weak box diagram shown in Fig. 1.5, and contribute to $M_{12}^{(*)}$. The contribution of $\Gamma_{12}^{(*)}$ is attributed to decays to which both B^0 and \bar{B}^0 can decay, e.g. CP eigenstates like $J/\psi\phi$ and D^+D^- . This is most easily visualized if the state is expressed in CP eigenstate basis,⁹

$$\begin{pmatrix} |B^{\text{even}}\rangle \\ |B^{\text{odd}}\rangle \end{pmatrix} = \frac{1}{\sqrt{2}} \begin{pmatrix} |B^0\rangle + |\bar{B}^0\rangle \\ |B^0\rangle - |\bar{B}^0\rangle \end{pmatrix} \quad (1.2.11)$$

Decays to CP -even final states are only accessible from the $|B^{\text{even}}\rangle$ state, and are more abundant due to the large branching ratio of the CP -even $B \rightarrow D^+D^-$ decays. Hence, the CP -even component has a larger decay width. After some time evolution of the system, re-expressing the state in the flavour basis results effectively in some net fraction of \bar{B}^0 created when initially starting with a B^0 state.

In order to properly define a mass and lifetime, ψ is expressed in terms of the Hamiltonian eigenstates. These are the states in which the system propagates freely. The eigenvalues of the Hamiltonian (Eq. 1.2.10) correspond to

$$\lambda_{\pm} = M_{11} - \frac{i}{2}\Gamma_{11} \pm F \quad ; \quad F = \sqrt{(M_{12} - \frac{i}{2}\Gamma_{12})(M_{12}^* - \frac{i}{2}\Gamma_{12}^*)}, \quad (1.2.12)$$

Interpreting these eigenvalues in terms of a mass and decay width,

$$\begin{aligned} m_H - \frac{i}{2}\Gamma_H &= (M_{11} - \Re F) - \frac{i}{2}(\Gamma_{11} - 2\Im F), \\ m_L - \frac{i}{2}\Gamma_L &= (M_{11} + \Re F) - \frac{i}{2}(\Gamma_{11} + 2\Im F), \end{aligned} \quad (1.2.13)$$

where the subscripts H and L stand for the two Hamiltonian eigenstates, the so-called “ B -heavy” and “ B -light”. Two observables that will be used are the mass and decay width

⁹We choose the convention $CP|B^0\rangle = +|\bar{B}^0\rangle$.

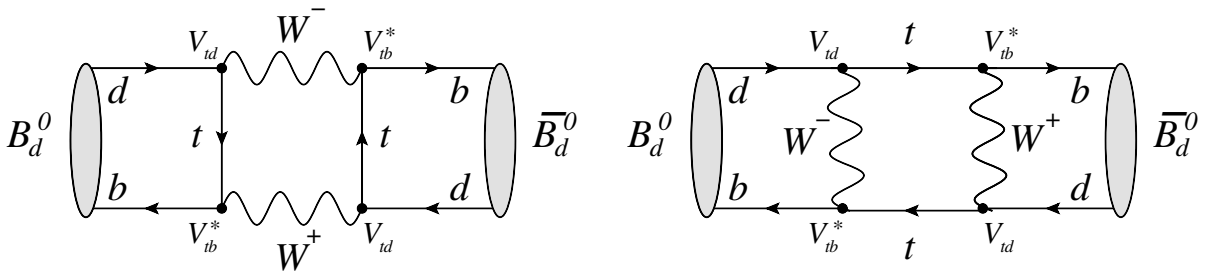


Figure 1.5: The dominant Feynman diagrams of $B^0 - \bar{B}^0$ oscillations. The corresponding amplitude is parametrized by Eq. 1.2.26.

difference of the two Hamiltonian eigenstates: [25, 26]

$$\begin{aligned}\Delta m &\equiv (m_H - m_L) = 2\Re(F) \approx 2|M_{12}|\left(1 - \frac{|\Gamma_{12}|^2 \sin^2 \phi_{12}}{8|M_{12}|^2}\right) \approx 2|M_{12}| \\ \Delta\Gamma &\equiv (\Gamma_L - \Gamma_H) = 4\Im(F) \approx 2|\Gamma_{12}|\cos \phi_{12}\left(1 + \frac{|\Gamma_{12}|^2 \sin^2 \phi_{12}}{8|M_{12}|^2}\right) \approx 2|\Gamma_{12}|\cos \phi_{12},\end{aligned}\tag{1.2.14}$$

where a first-order Taylor expansion for $\frac{|\Gamma_{12}|}{|M_{12}|} \ll 1$ is done, which holds for both B systems, and where the following notations are used,

$$\begin{aligned}M_{12} &= |M_{12}|e^{i\phi_M} \\ \Gamma_{12} &= |\Gamma_{12}|e^{i\phi_\Gamma} \\ \phi_{12} &= \arg\left(-\frac{M_{12}}{\Gamma_{12}}\right) = \pi + \phi_M - \phi_\Gamma.\end{aligned}\tag{1.2.15}$$

The mass difference Δm is also known as the mixing frequency, and is in the order of inverse picoseconds. The decay width difference $\Delta\Gamma$ is mostly driven by the branching ratio of the CP -even $B^0 \rightarrow D^+D^-$ and $B_s^0 \rightarrow D_s^+D_s^-$ decays, and is much smaller than Δm in both B systems. Due to Cabibbo suppression of the $B^0 \rightarrow D^+D^-$ decay, $\Delta\Gamma_d$ is small and terms linear in $\Delta\Gamma_d$ can be safely ignored. The experimental and SM values for m_{12} (Δm) and Γ_{12} ($\Delta\Gamma$) are discussed in Sec.1.2.6.

The Hamiltonian eigenstates are expressed in terms of the original flavour eigenstates as follows¹⁰.

$$\begin{pmatrix} |B_H\rangle \\ |B_L\rangle \end{pmatrix} = \begin{pmatrix} p|B^0\rangle - q|\bar{B}^0\rangle \\ p|B^0\rangle + q|\bar{B}^0\rangle \end{pmatrix} \quad \rightarrow \quad \begin{pmatrix} |B^0\rangle \\ |\bar{B}^0\rangle \end{pmatrix} = \begin{pmatrix} \frac{1}{2p}(|B_H\rangle + |B_L\rangle) \\ \frac{1}{2q}(|B_L\rangle - |B_H\rangle) \end{pmatrix}\tag{1.2.16}$$

Comparing Eq. 1.2.16 to Eq. 1.2.11 it is clear that the Hamiltonian eigenstates are equal to the CP eigenstates if $\left|\frac{q}{p}\right| = 1$. The ratio of q/p can be expressed in terms of the mass and decay widths by finding the eigenvectors,

$$\hat{H} \begin{pmatrix} p \\ q \end{pmatrix} = \lambda_\pm \begin{pmatrix} p \\ q \end{pmatrix} \quad \rightarrow \quad \frac{q}{p} = \pm \sqrt{\frac{M_{12}^* - \frac{i}{2}\Gamma_{12}^*}{M_{12} - \frac{i}{2}\Gamma_{12}}},\tag{1.2.17}$$

where the positive value is chosen such that $m_H > m_L$.

1.2.4 Time evolution

The amount of CP violation in the mixing process is expressed as the asymmetry in the probabilities of the B^0 and \bar{B}^0 flavour eigenstates to turn into each other. For the time evolution of a flavour eigenstate, the eigenstates (Eq. 1.2.16) are substituted twice into the solution of the Schrödinger equation (Eq. 1.2.8),

¹⁰It is known from experiment that the heavy eigenstate is mostly CP -odd (fully if $|q/p| = 1$).

$$\begin{aligned}
 |B^0(t)\rangle &= \frac{1}{2p} \left[e^{-i(m_H - \frac{i}{2}\Gamma_H)t} |B_H(0)\rangle + e^{-i(m_L - \frac{i}{2}\Gamma_L)t} |B_L(0)\rangle \right] \\
 &= \frac{1}{2p} \left[e^{-i(m_H - \frac{i}{2}\Gamma_H)t} (p|B^0\rangle - q|\bar{B}^0\rangle) + e^{-i(m_L - \frac{i}{2}\Gamma_L)t} (p|B^0\rangle + q|\bar{B}^0\rangle) \right] \\
 |\bar{B}^0(t)\rangle &= \frac{1}{2q} \left[e^{-i(m_L - \frac{i}{2}\Gamma_L)t} |B_L(0)\rangle - e^{-i(m_H - \frac{i}{2}\Gamma_H)t} |B_H(0)\rangle \right] \\
 &= \frac{1}{2q} \left[e^{-i(m_L - \frac{i}{2}\Gamma_L)t} (p|B^0\rangle + q|\bar{B}^0\rangle) - e^{-i(m_H - \frac{i}{2}\Gamma_H)t} (p|B^0\rangle - q|\bar{B}^0\rangle) \right]. \quad (1.2.18)
 \end{aligned}$$

Using the following definitions,

$$\begin{aligned}
 g_+(t) &\equiv \frac{1}{2} \left(e^{-i(m_H - \frac{i}{2}\Gamma_H)t} + e^{-i(m_L - \frac{i}{2}\Gamma_L)t} \right) = \frac{1}{2} e^{-iMt} e^{-\frac{1}{2}\Gamma t} \left(e^{-i\frac{1}{2}\Delta mt} e^{+\frac{1}{4}\Delta\Gamma t} + e^{+i\frac{1}{2}\Delta mt} e^{-\frac{1}{4}\Delta\Gamma t} \right), \\
 g_-(t) &\equiv \frac{1}{2} \left(e^{-i(m_H - \frac{i}{2}\Gamma_H)t} - e^{-i(m_L - \frac{i}{2}\Gamma_L)t} \right) = \frac{1}{2} e^{-iMt} e^{-\frac{1}{2}\Gamma t} \left(e^{-i\frac{1}{2}\Delta mt} e^{+\frac{1}{4}\Delta\Gamma t} - e^{+i\frac{1}{2}\Delta mt} e^{-\frac{1}{4}\Delta\Gamma t} \right), \quad (1.2.19)
 \end{aligned}$$

where the average mass and decay width of the mass eigenstates are defined as

$$M = \frac{M_H + M_L}{2} \quad ; \quad \Gamma = \frac{\Gamma_L + \Gamma_H}{2}, \quad (1.2.20)$$

the time evolution of either state can be compactly written as

$$\begin{aligned}
 |B^0(t)\rangle &= g_+(t)|B^0\rangle - \left(\frac{q}{p}\right)g_-(t)|\bar{B}^0\rangle, \\
 |\bar{B}^0(t)\rangle &= -\left(\frac{p}{q}\right)g_-(t)|B^0\rangle + g_+(t)|\bar{B}^0\rangle. \quad (1.2.21)
 \end{aligned}$$

The probability of observing a B^0 (\bar{B}^0) state at a certain time, when starting from a \bar{B}^0 (B^0) state, is then

$$\begin{aligned}
 |\langle B^0|B^0(t)\rangle|^2 &= |g_+(t)|^2 = \frac{e^{-\Gamma t}}{2} \left(\cosh\left(\frac{1}{2}\Delta\Gamma t\right) + \cos(\Delta mt) \right) \\
 |\langle \bar{B}^0|\bar{B}^0(t)\rangle|^2 &= |g_+(t)|^2 = \frac{e^{-\Gamma t}}{2} \left(\cosh\left(\frac{1}{2}\Delta\Gamma t\right) + \cos(\Delta mt) \right) \\
 |\langle \bar{B}^0|B^0(t)\rangle|^2 &= \left|\frac{q}{p}\right|^2 |g_-(t)|^2 = \left|\frac{q}{p}\right|^2 \frac{e^{-\Gamma t}}{2} \left(\cosh\left(\frac{1}{2}\Delta\Gamma t\right) - \cos(\Delta mt) \right) \\
 |\langle B^0|\bar{B}^0(t)\rangle|^2 &= \left|\frac{p}{q}\right|^2 |g_-(t)|^2 = \left|\frac{p}{q}\right|^2 \frac{e^{-\Gamma t}}{2} \left(\cosh\left(\frac{1}{2}\Delta\Gamma t\right) - \cos(\Delta mt) \right) \quad (1.2.22)
 \end{aligned}$$

These probabilities oscillate with a frequency Δm , which is due to the weak box diagrams (Eq. 1.2.14). They decay according to the average B^0 lifetime $\frac{1}{\Gamma}$. The “turn-on” effect of

the cosh term is small due to a small value of $\Delta\Gamma$, and the cosh term can be ignored in the B^0 system, and is small in the B_s^0 system.

In fact, the phenomenology in the other neutral meson systems, K^0 and D^0 , is quite different due to different values of Δm and $\Delta\Gamma$. The survival probabilities of Eq. 1.2.22 for all four neutral meson systems are shown in Fig. 1.6. From Eq. 1.2.22 it can be seen that the transition probability $P(B^0 \rightarrow \bar{B}^0)$ does not equal the CP conjugate probability $P(\bar{B}^0 \rightarrow B^0)$ when $|\frac{p}{q}| \neq 1$, or in other words, when the Hamiltonian eigenstates do not equal the CP eigenstates. This is called CP violation in mixing, and is quantified as

$$a_{sl} \equiv A_{CP}^{\text{mix}} = \frac{P(\bar{B}^0 \rightarrow B^0)(t) - P(B^0 \rightarrow \bar{B}^0)(t)}{P(\bar{B}^0 \rightarrow B^0)(t) + P(B^0 \rightarrow \bar{B}^0)(t)} = \frac{|\frac{p}{q}|^2 - |\frac{q}{p}|^2}{|\frac{p}{q}|^2 + |\frac{q}{p}|^2} \approx 2 \left(1 - \left|\frac{q}{p}\right|\right), \quad (1.2.23)$$

where in the last step the approximation $|\frac{q}{p}| \approx 1$ or small CP violation is used, which is expected in both B^0 systems. Observe that there is no time dependence in the amount of CP violation in mixing itself, just as was the case for CP violation in decay (Eq. 1.2.6).

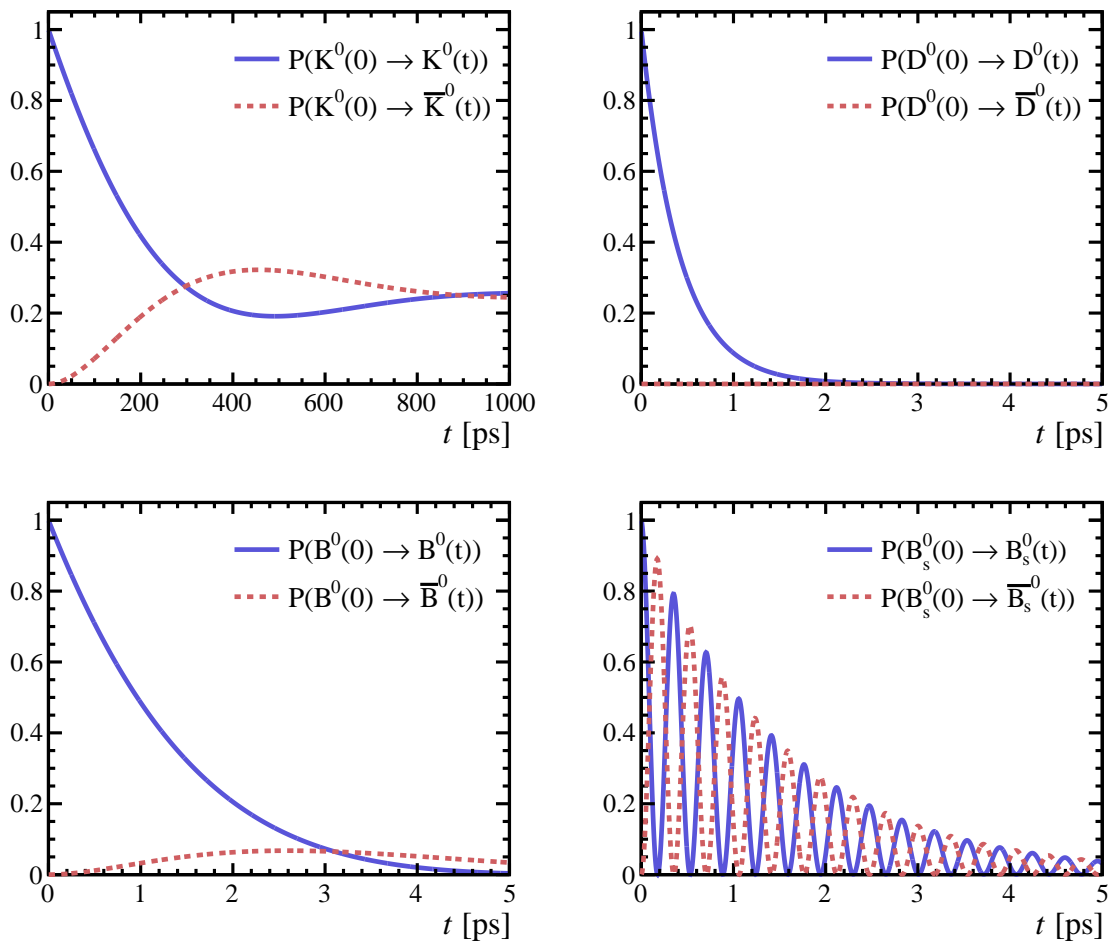


Figure 1.6: Survival probabilities of the four neutral meson systems, using Eq. 1.2.22 and the values of Γ , Δm and $\Delta\Gamma$ of the respective systems.

Going one step further by filling in Eq. 1.2.17 and 1.2.15,

$$a_{\text{sl}} \approx \frac{|\Gamma_{12}|}{|M_{12}|} \sin(\phi_{12}) \approx \frac{\Delta\Gamma}{\Delta m} \tan(\phi_{12}), \quad (1.2.24)$$

where a first-order Taylor expansion with $\frac{|\Gamma_{12}|}{|M_{12}|} \ll 1$ is made, and Eq. 1.2.14 is used. To disentangle a decay to a B^0 from a decay to a \bar{B}^0 , a flavour-specific (fs) final state is chosen in order to measure CP violation in mixing. In other words, a decay is chosen for which $f \neq \bar{f}$ and $B^0 \not\rightarrow \bar{f}$, $\bar{B}^0 \not\rightarrow f$ cannot occur without mixing. This is the case for the semileptonic (sl) decays used in this thesis.

The observable in Eq. 1.2.24 is in principle sensitive to effects from direct CP violation, but in semileptonic decays there is no penguin diagram to interfere with the tree diagram. Therefore, a_{sl} is purely sensitive to CP violation in mixing.

1.2.5 CP violation in interference

There is a third type of CP violation to briefly touch upon, since it will be relevant in Chapter 6. This is called CP violation in the interference between mixing and decay. The two diagrams involved are decays of the type $B^0 \rightarrow f$ and $B^0 \rightarrow \bar{B}^0 \rightarrow f$, i.e. interference between either mixing or not, before decaying to a final state which is accessible to both B^0 and \bar{B}^0 . One can construct a CP asymmetry that is sensitive to the CP violation in interference as e.g.

$$A_{CP}^{\text{int}}(t) = \frac{P(B^0_{(\rightarrow\bar{B}^0)} \rightarrow f)(t) - P(\bar{B}^0_{(\rightarrow B^0)} \rightarrow f)(t)}{P(B^0_{(\rightarrow\bar{B}^0)} \rightarrow f)(t) + P(\bar{B}^0_{(\rightarrow B^0)} \rightarrow \bar{f})(t)}. \quad (1.2.25)$$

A candidate decay mode is $B_s^0 \rightarrow D_s^- K^+$. A special case is a decay to a CP eigenstate, where $f = \bar{f}$, such as e.g. the decay $B_s^0 \rightarrow J/\psi \phi$. In the B^0 system the amount of CP violation in interference is found to be sizeable [27], although for the B_s^0 system it is found to be compatible with zero [28]. There is a rich and decay-time dependent phenomenology in this type of CP violation, which is beyond the scope of this thesis.

1.2.6 Standard Model expectations and beyond

A connection between the effective model-independent mixing formalism and the standard model can be made. The amplitude M_{12} — also called the dispersive part of the mixing process — is computed from the box diagram (Fig. 1.5), and results in the following expression [29].

$$M_{12} = \frac{G_F^2 M_{B^0}}{12\pi^2} M_W^2 (V_{tb} V_{t(d,s)}^*)^2 \hat{\eta}_B S_0(m_t^2/M_W^2) f_{B^0}^2 B, \quad (1.2.26)$$

where G_F is the Fermi constant, M_W , M_{B^0} and m_t are the masses of the W^\pm boson, B^0 meson and top quark, and V_{ij} are the CKM elements at the vertices. The Inami-Lim function S_0 represents the contribution of the propagators in the box and is a function of

the ratio of the propagator quark masses over the W^\pm mass [30], while $\hat{\eta}_B$ represents the short-distance QCD leading-order (LO) and next-to-leading-order (NLO) corrections [31]. The dominant contribution to M_{12} is the box diagram with a top quark in the loop, due to the combination of CKM factors and the Inami-Lim function. The long-distance QCD effects are parametrized by the B^0 decay constant f_{B^0} and the bag parameter B . These hadronic parameters are constrained from experimental input or calculated using lattice QCD, and have a relatively large uncertainty. The absolute size of $|M_{12}|$ can be experimentally determined by measuring the mixing frequency Δm using decays like $B^0 \rightarrow D^- \pi^+$. To summarize the current theoretical and experimental status [2, 26],

$$\begin{aligned} \Delta m_s^{\text{theo}} &= (18.3 \pm 2.7) \text{ ps}^{-1}, & \Delta m_d^{\text{theo}} &= (0.528 \pm 0.078) \text{ ps}^{-1}, \\ \Delta m_s^{\text{exp}} &= (17.757 \pm 0.021) \text{ ps}^{-1}, & \Delta m_d^{\text{exp}} &= (0.5064 \pm 0.0019) \text{ ps}^{-1}. \end{aligned} \quad (1.2.27)$$

The current experimental precision is much higher than the theoretical prediction. This makes it hard to interpret whether $|M_{12}|$ contains contributions from new physics, if the effect does not significantly exceed the uncertainty on the hadronic parameters.

The calculation of the amplitude Γ_{12} — also called the absorptive part of the mixing process — is much more involved than the calculation of M_{12} since all on-shell CP eigenstates have to be considered. In the B_s^0 system it is dominated by the Cabibbo-favoured $b \rightarrow c\bar{c}s$ tree diagram but subleading contributions are non-negligible. In the B^0 system there is no clear leading contribution due to CKM suppression of V_{cd} . The calculation involves a technique called heavy-quark expansion (HQE) which makes use of the fact that the b quark is much heavier than the other quarks in the system. On the other hand, $|\Gamma_{12}|$ can be reasonably well predicted from the largest experimentally known branching ratios to CP final states such as $B_s^0 \rightarrow D_s^+ D_s^-$. In addition, measurements of CP violation in interference like $B_s^0 \rightarrow J/\psi \phi$ are sensitive to $\Delta\Gamma_s$. To summarize [2, 26, 32],

$$\begin{aligned} \left. \frac{\Delta\Gamma_s}{\Gamma_s} \right|_{\text{theo}} &= (0.133 \pm 0.032), & \left. \frac{|\Delta\Gamma_d|}{\Gamma_d} \right|_{\text{theo}} &= (0.0040 \pm 0.0009), \\ \left. \frac{\Delta\Gamma_s}{\Gamma_s} \right|_{\text{exp}} &= (0.124 \pm 0.011), & \left. \frac{|\Delta\Gamma_d|}{\Gamma_d} \right|_{\text{exp}} &= (0.003 \pm 0.015), \end{aligned} \quad (1.2.28)$$

The total decay widths of B^0 and B_s^0 are roughly the same, $1/\Gamma_s^{\text{exp}} = (1.510 \pm 0.005) \text{ ps}$ and $1/\Gamma_d^{\text{exp}} = (1.520 \pm 0.004) \text{ ps}$ [2]. One can see that in both systems, the ratio $\Delta\Gamma/\Delta m$ is about $\mathcal{O}(0.01)$, justifying the earlier approximations assuming $\frac{|\Gamma_{12}|}{|M_{12}|} \ll 1$. New physics in Γ_{12}^s would originate from effects in not-yet detected decays to CP final states as e.g. $B_s^0 \rightarrow \tau^+ \tau^-$, for which the branching ratios are expected to be small. In addition, there is not much room for new physics in $\Delta\Gamma_s$ when comparing the theoretical and experimental errors. Hence possible new physics in the B_s^0 mixing process are mainly expected to originate from M_{12}^s . In the B^0 system, new physics contributions may originate from both Γ_{12}^d and M_{12}^d .

In the prediction of the ratio M_{12}/Γ_{12} , as is the case for the a_{sl} observables (Eq. 1.2.24) one expects cancellations in the hadronic parameters, resulting in a more precise SM

prediction. Recent efforts of calculating the a_{sl} parameters for both neutral B systems in the SM result in [26, 29]

$$\begin{aligned} a_{\text{sl}}^d &= (-4.7 \pm 0.6) \times 10^{-4}, \\ a_{\text{sl}}^s &= (2.2 \pm 0.3) \times 10^{-5}. \end{aligned} \tag{1.2.29}$$

Note that the central values of these asymmetries are at the subpermille level, with an $\mathcal{O}(10\%)$ relative uncertainty.

Theoretically the B -mixing transitions are interesting because they are neutral and flavour changing, $|\Delta B| = 2$. Such processes do not occur at tree-level in the SM since the weak current is charged. However, many extensions of the SM include flavour-changing neutral currents (FCNC) at tree level, which could drastically affect the amplitude and phase of the mixing process. Popular examples are models that include Z' and W' particles, as e.g. models with dynamical EW symmetry breaking like topcolour or top-seesaw models, little Higgs models where the Higgs boson itself results from a higher broken symmetry, and even models that aim to unify gravity with the SM like Kaluza-Klein models or Stueckelberg extensions in string theory. For a comprehensive overview see Ref. [33]. Other examples are theories that involve leptoquarks. In addition, potential contributions from new particles in the quantum loops will affect the total amplitude and phase, and will be particularly visible due to the absence of a dominant tree diagram for this process. A typical example comes from supersymmetry (SUSY), where the W^\pm bosons are replaced by charginos ($\tilde{\chi}_{1,2}^\pm$) and the top quark by a stop quark (\tilde{t}). These new processes might affect a_{sl}^d and a_{sl}^s through a modification of $|\Delta m|$, $|\Delta\Gamma|$ (mostly in the B^0 system) and ϕ_{12} .

1.2.7 History of CP violation in mixing

CP violation was first observed in the neutral kaon system, with the Cronin-Fitch experiment in 1964 [34]. Under CP symmetry the Hamiltonian eigenstate K_L^0 (K -long) is fully CP odd and has to decay to three pions, while the K_S^0 (K -short) is CP even and can thus decay to two pions. The large difference in available phase space is responsible for a large difference in lifetime of the Hamiltonian eigenstates. In the B systems, $\Delta\Gamma$ is small with respect to Δm and the Hamiltonian eigenstates are labelled by their mass instead. The Cronin-Fitch experiment was set up in such a way that kaons produced from a target travelled $\sim 300 K_S^0$ lifetimes before a decay would be detected. Hence, all observed decays were expected to originate from K_L^0 . Decays of $K_L^0 \rightarrow \pi^+\pi^-$ were indeed observed, owing to CP asymmetry in mixing of the neutral kaon system. This has later been confirmed with high accuracy by subsequent experiments like KLOE (INFN-LNF) and NA48 (CERN) to be $\epsilon_K = (2.22 \pm 0.01) \times 10^{-3}$, or $\left| \frac{q}{p} \right|_{K^0} = \frac{1-\epsilon_K}{1+\epsilon_K} = 0.99557 \pm 0.00002$. Precision studies of CP violation in rare kaon decays are currently done by experiments like KLOE-2 and NA62.

The amount of CP violation in D mesons is expected to be extremely small in the SM, due to CKM suppression in combination with small Inami-Lim factors [30], leading to a highly suppressed mixing rate. The relatively large effect that contributions from new physics could have, makes the charm sector well suited to search for new physics. However, no significant CP violation in the charm sector has yet been observed [3]. Measurements in charm physics were made by CLEO (Cornell University) starting from 1979, as well as the fixed-target experiments E791 and FOCUS (Fermilab). The first evidence of mixing in the charm sector was found relatively recently in 2007 by the BaBar [35] (SLAC), Belle [36] (KEK) and CDF [37] (Fermilab) collaborations. The experiments BES-III (IHEP Beijing) and the LHCb experiment, which was the first single experiment to measure charm mixing with 5 standard deviations (σ) significance, continue to measure the precision of these results to a level of below 10^{-3} with data sets containing hundreds of millions of charm mesons. Furthermore, a dedicated charm experiment called PANDA at the FAIR facility in Darmstadt is currently under construction.

Mixing in the B^0 system was first observed by the ARGUS collaboration (DESY) in 1987 by searching for same-sign dimuons [38], and soon after confirmed by CLEO [39]. A same-sign dimuon final state may occur when one of the two B mesons produced in the $\Upsilon(4S)$ resonance changes flavour, and both undergo a semileptonic decay. The somewhat heavier B_s^0 meson was first produced in large amounts at the Tevatron, colliding protons and antiprotons with a centre-of-mass energy up to 1.8 TeV at Fermilab. The first observation of mixing in the B_s^0 system was made by the CDF collaboration in 2006 [40].

Mixing turned out to be most prominent in the B systems (see also Fig. 1.6). Combined with the option to use HQET for precise theoretical predictions (Sec. 1.2.6), measuring CP violation in mixing of the B^0 and B_s^0 systems is a promising path towards finding new physics. Before LHCb, measurements of a_{sl}^d had been performed at the B -factories, Belle [41] and BaBar [42], as well as D0 at the Tevatron [43]. Measurements of a_{sl}^s had only been done by D0 [44]. The averaged experimental values in August 2013 — before the first LHCb publication on a_{sl} — were

$$\begin{aligned} a_{\text{sl}}^d &= (-0.30 \pm 0.30)\% \\ a_{\text{sl}}^s &= (-0.12 \pm 0.76)\%. \end{aligned} \tag{1.2.30}$$

All measurements of a_{sl}^d and a_{sl}^s made at that time are summarized in Fig. 1.7, and all results are seen to be consistent with the SM expectations, within errors. In addition to measuring a_{sl}^d and a_{sl}^s individually, the D0 collaboration measured the difference in the rate of same-sign dimuons in 2011 [45],

$$A_{\mu\mu} = \frac{N(\mu^+\mu^+) - N(\mu^-\mu^-)}{N(\mu^+\mu^+) + N(\mu^-\mu^-)} = X a_{\text{sl}}^d + Y a_{\text{sl}}^s, \tag{1.2.31}$$

similar to the method used by the ARGUS collaboration. Here, X and Y are the respective contributions to $A_{\mu\mu}$ due to CP violation in mixing of B^0 and B_s^0 mesons. A deviation from the SM prediction of 3.9σ was observed, leading to debates in the particle physics community. In this measurement, same-sign muons can originate from mixed B^0 mesons

and B_s^0 mesons, as well as from other decays. In order to disentangle these contributions, the distance of closest approach of the muon to the primary collision vertex is used, also called impact parameter (IP). Due to the fast mixing frequency Δm_s , 50% of B_s^0 mesons are expected to have changed flavour when demanding any appreciable muon IP, while the fraction of mixed B^0 mesons still increases with the muon IP requirement. The sample was split up into bins of muon IP, and the relative amount of mixed B_s^0 over B^0 in each bin was determined from simulation. A correlated value for a_{sl}^d and a_{sl}^s was obtained in this way, highlighted by the yellow ellipse in Fig. 1.7.

It was later realized that other CP -violating effects can also contribute to a same-sign dimuon asymmetry [46]. These were not taken into account in the 2011 result. In an update from the D0 collaboration in 2013 using the full data set, a value for the contribution from CP violation in interference of B^0 mesons is taken into account, using the theoretical prediction of $\Delta\Gamma_d/\Gamma_d = (0.42 \pm 0.08) \times 10^{-2}$. This resulted in $a_{\text{sl}}^d = (-0.62 \pm 0.42)\%$ and $a_{\text{sl}}^s = (-0.86 \pm 0.74)\%$ with a correlation of $\rho = -0.79$. The deviation from the SM prediction reduced to 3.4σ [47]. When allowing for new physics in a_{sl}^d , a_{sl}^s and $\Delta\Gamma_d/\Gamma_d$ by floating all three parameters in the fit independently, a deviation of 3σ with the SM prediction remains.

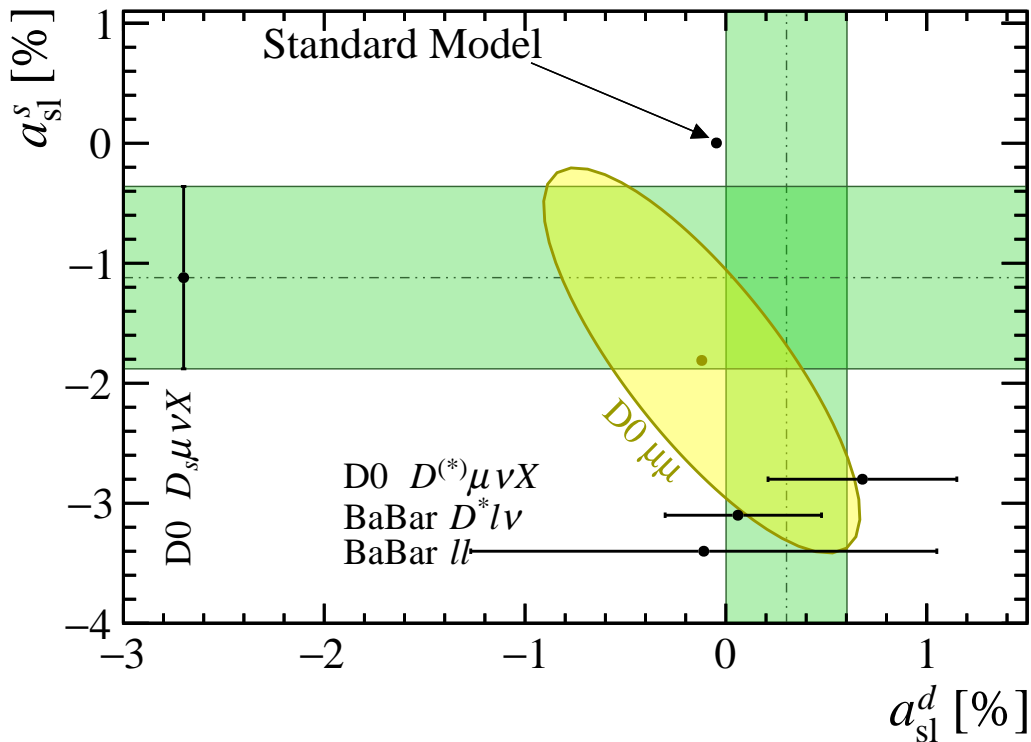


Figure 1.7: Overview of a_{sl}^d and a_{sl}^s measurements in August 2013, before the LHCb results. The black points represent separate measurements of a_{sl}^d or a_{sl}^s , and the 2011 D0 dimuon measurement is shown in the yellow ellipse. The green bands indicate the averages of measurements, excluding the D0 dimuon result.

In 2013, LHCb published a first measurement of a_{sl}^s using 1.0 fb^{-1} of data [48], and BaBar published a new measurement of a_{sl}^d in 2014 [49]. The new averages in September 2014, excluding the D0 dimuon result, are

$$\begin{aligned} a_{\text{sl}}^d &= (-0.05 \pm 0.24)\% \\ a_{\text{sl}}^s &= (-0.48 \pm 0.48)\%, \end{aligned} \quad (1.2.32)$$

and the B mixing landscape is summarized in Fig. 1.8. The picture that Fig. 1.8 sketches, allows a deviation from the SM prediction [50]. More measurements are needed to determine if there are contributions of new physics to CP violation in mixing in the neutral B systems. Measuring a_{sl}^d and a_{sl}^s using the full 3.0 fb^{-1} data set of LHCb collected in run 1 of the LHC is the main focus of this thesis.

1.2.8 Measuring a_{sl}^d and a_{sl}^s

In order to precisely measure CP violation in mixing in the neutral B systems (Eq. 1.2.23), one needs

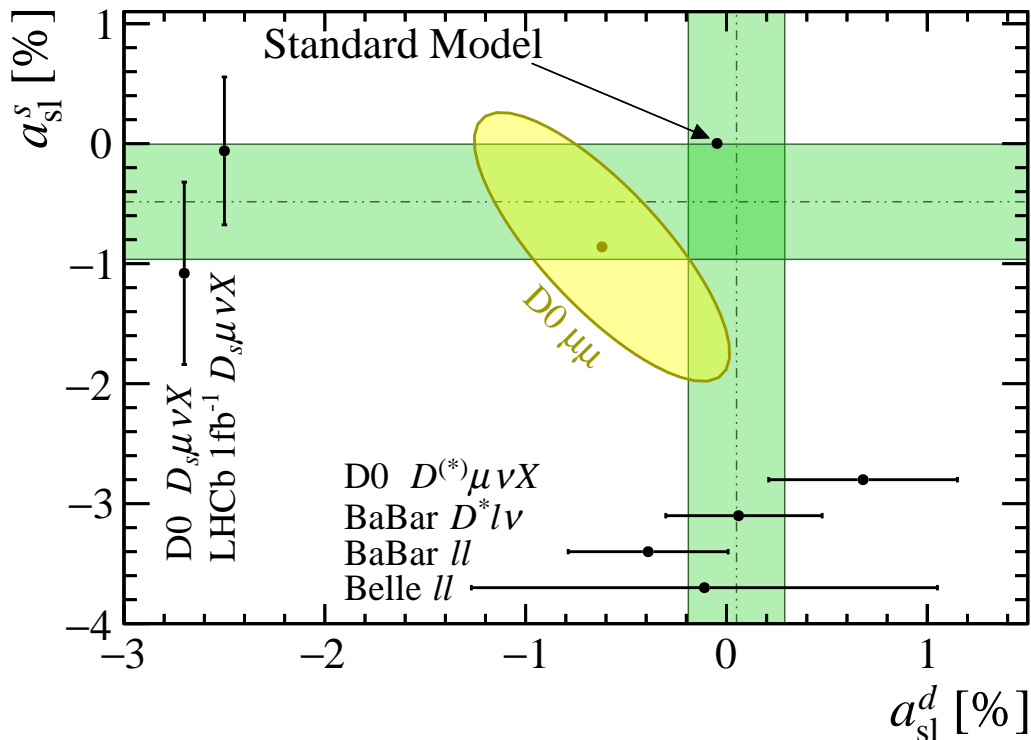


Figure 1.8: Overview of a_{sl}^d and a_{sl}^s measurements in September 2014, including the 1.0 fb^{-1} LHCb result on a_{sl}^s , but before the full run 1 LHCb results discussed in this thesis. The black points represent separate measurements of a_{sl}^d or a_{sl}^s , and the 2013 D0 dimuon measurement, where $\Delta\Gamma_d$ is fixed to the SM value, is shown in the yellow ellipse. The green bands indicate the averages of measurements, excluding the D0 dimuon result.

1. to produce and detect large amounts of B mesons,
2. to determine the flavour eigenstate at both production and the decay of the B meson,
3. to measure the decay time of the B meson to observe the time-dependent phenomenology of the mixing process.¹¹

A good candidate of a flavour-specific channel with a high branching fraction are Cabibbo-favoured semileptonic decays,

$$\begin{aligned}
 B^0 &\rightarrow D^-(\rightarrow K^+\pi^-\pi^-)\mu^+\nu_\mu & ; & & \bar{B}^0 &\rightarrow D^+(\rightarrow K^-\pi^+\pi^+)\mu^-\bar{\nu}_\mu \\
 B_s^0 &\rightarrow D_s^-(\rightarrow K^-K^+\pi^-)\mu^+\nu_\mu & ; & & \bar{B}_s^0 &\rightarrow D_s^+(\rightarrow K^+K^-\pi^+)\mu^-\bar{\nu}_\mu
 \end{aligned}
 \quad . \quad (1.2.33)$$

The B^0 decay is shown in Fig. 1.9. The charge of the muon and D meson identify the flavour eigenstate of the B meson at the time of decay. As a comparison their branching fractions are large compared to the hadronic decay modes [2],

$$\begin{aligned}
 \mathcal{B}(B_s^0 \rightarrow D_s^- \pi^+) &= (3.0 \pm 0.23) \times 10^{-3} \\
 \mathcal{B}(B_s^0 \rightarrow D_s^- l^+ \nu_l X) &= (8.1 \pm 1.3) \times 10^{-2} \\
 \mathcal{B}(B^0 \rightarrow D^- \pi^+) &= (2.52 \pm 0.13) \times 10^{-3} \\
 \mathcal{B}(B^0 \rightarrow D^- l^+ \nu_l X) &= (9.2 \pm 0.8) \times 10^{-2},
 \end{aligned}
 \quad (1.2.34)$$

and benefit from a high muon detection efficiency. The downside of semileptonic decays is that the neutrino is not detected. This prevents the full reconstruction of the B^0 mass peak used to discriminate against background. As a result the events are reconstructed inclusively, allowing for any number of additional particles X at the B vertex. In other words, there are contributions from other B decays to similar final states in our selected sample of events. These will be discussed in more detail in Chapters 4 and 5.

To determine the flavour of the B meson at production a method known as “tagging” is employed, in which the charge of the b quark at production is determined by studying the rest of the collision event [51]. The measured observable can then be written as

$$A_{CP}^{\text{meas, tagged}} = \frac{N(\bar{B}^0 \rightarrow B^0 \rightarrow f)(t) - N(B^0 \rightarrow \bar{B}^0 \rightarrow \bar{f})(t)}{N(\bar{B}^0 \rightarrow B^0 \rightarrow f)(t) + N(B^0 \rightarrow \bar{B}^0 \rightarrow \bar{f})(t)}, \quad (1.2.35)$$

¹¹Although a_{sl} is independent of time, the time dependence will become useful as we will see shortly.

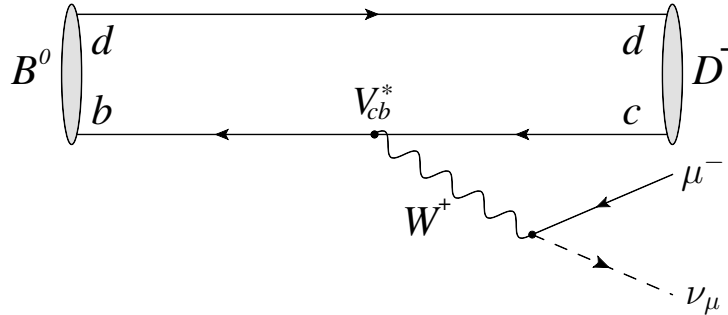


Figure 1.9: Feynman diagram of the semileptonic decay $B^0 \rightarrow D^- \mu^+ \nu_\mu$.

In an ideal measurement there are no detector effects, i.e. the asymmetry in observed yields N matches the theoretical asymmetry of transition probabilities P , or $A_{CP}^{\text{meas, tagged}} = A_{CP}^{\text{mix}}$ (Eq.1.2.23).

Due to the backgrounds in pp collisions, as well as incomplete reconstruction and mixing effects, the effective tagging efficiency is about 5% such that the statistical uncertainty would increase by a factor $1/\sqrt{\epsilon} = \sqrt{20}$. Instead, the B^0 and \bar{B}^0 initial states are added,

$$\begin{aligned} A_{CP}^{\text{meas}}(t) &= \frac{N(f, t) - N(\bar{f}, t)}{N(f, t) + N(\bar{f}, t)} \\ &= \frac{N(B^0 \rightarrow f, t) + N(\bar{B}^0 \rightarrow B^0 \rightarrow f, t) - N(\bar{B}^0 \rightarrow \bar{f}, t) - N(B^0 \rightarrow \bar{B}^0 \rightarrow \bar{f}, t)}{N(B^0 \rightarrow f, t) + N(\bar{B}^0 \rightarrow B^0 \rightarrow f, t) + N(\bar{B}^0 \rightarrow \bar{f}, t) + N(B^0 \rightarrow \bar{B}^0 \rightarrow \bar{f}, t)}, \end{aligned} \quad (1.2.36)$$

where f and \bar{f} respectively represent the final states of the B^0 and \bar{B}^0 decays as given in Eq. 1.2.33. This measured, untagged asymmetry A_{CP}^{meas} has contributions from the (unwanted) decays without oscillation $B^0 \rightarrow f$ and $\bar{B}^0 \rightarrow \bar{f}$. Including those probabilities from Eq. 1.2.22, and using $\cosh(\frac{1}{2}\Delta\Gamma t) \approx 1$ for simplicity, we find

$$\begin{aligned} A_{CP}^{\text{meas}}(t) &\approx \frac{(1 + \cos(\Delta mt)) + \left|\frac{p}{q}\right|^2(1 - \cos(\Delta mt)) - (1 + \cos(\Delta mt)) - \left|\frac{q}{p}\right|^2(1 - \cos(\Delta mt))}{(1 + \cos(\Delta mt)) + \left|\frac{p}{q}\right|^2(1 - \cos(\Delta mt)) + (1 + \cos(\Delta mt)) + \left|\frac{q}{p}\right|^2(1 - \cos(\Delta mt))} \\ &\approx \frac{(1 + a_{\text{sl}})(1 - \cos(\Delta mt)) - (1 - a_{\text{sl}})(1 - \cos(\Delta mt))}{2(1 + \cos(\Delta mt)) + (1 + a_{\text{sl}})(1 - \cos(\Delta mt)) + (1 - a_{\text{sl}})(1 - \cos(\Delta mt))} \\ &= \frac{a_{\text{sl}}}{2} - \frac{a_{\text{sl}}}{2} \cos(\Delta mt), \end{aligned} \quad (1.2.37)$$

where in the first step the approximation $|q/p|^2 \approx (1 - a_{\text{sl}})$ and $|p/q|^2 \approx (1 + a_{\text{sl}})$ are made, by using Eq. 1.2.23 and Eq. 1.2.24 and keeping only terms linear in a_{sl} . By summing up all initial states, the sensitivity of the measured asymmetry to a_{sl} is reduced by a factor 2 compared to Eq. 1.2.35, but it does not suffer from the tagging efficiency. In addition, the measured asymmetry now has a time-dependent behaviour on a_{sl} , and $A_{CP}^{\text{meas}}(t = 0) = 0$.

Imperfections in these measurements come from a possible difference in detection efficiency of the final state f with respect to \bar{f} , i.e. when $\epsilon(f) \neq \epsilon(\bar{f})$. In addition, in the pp collision events at the LHC there is no a-priori reason that there should be an equal amount of B^0 and \bar{B}^0 mesons produced: $N_P(B^0) \neq N_P(\bar{B}^0)$. This has to be taken into account in order to connect the observed asymmetry to a_{sl} . The observed yields N are now connected to the decay probabilities P as such,

$$\begin{aligned} N(B^0 \rightarrow f) &= N_P(B^0)\epsilon(f)P(B^0 \rightarrow f) \quad ; \quad N(\bar{B}^0 \rightarrow \bar{f}) = N_P(\bar{B}^0)\epsilon(\bar{f})P(\bar{B}^0 \rightarrow \bar{f}) \\ N(B^0 \rightarrow \bar{f}) &= N_P(B^0)\epsilon(\bar{f})P(B^0 \rightarrow \bar{f}) \quad ; \quad N(\bar{B}^0 \rightarrow f) = N_P(\bar{B}^0)\epsilon(f)P(\bar{B}^0 \rightarrow f). \end{aligned} \quad (1.2.38)$$

At this point it is useful to define the detection asymmetry,

$$A_{\text{det}} = \frac{\epsilon(f) - \epsilon(\bar{f})}{\epsilon(f) + \epsilon(\bar{f})}, \quad (1.2.39)$$

as well as the production asymmetry,

$$A_P = \frac{N_P(B^0) - N_P(\bar{B}^0)}{N_P(B^0) + N_P(\bar{B}^0)}, \quad (1.2.40)$$

such that we can write

$$\begin{aligned} \epsilon(f) &= \langle \epsilon \rangle (1 + A_{\text{det}}) & ; & & \epsilon(\bar{f}) &= \langle \epsilon \rangle (1 - A_{\text{det}}), \\ N_P(B^0) &= \langle N_P \rangle (1 + A_P) & ; & & N_P(\bar{B}^0) &= \langle N_P \rangle (1 - A_P), \end{aligned} \quad (1.2.41)$$

where $\langle \epsilon \rangle = \frac{1}{2}(\epsilon(f) + \epsilon(\bar{f}))$ and $\langle N_P \rangle = \frac{1}{2}(N_P(B^0) + N_P(\bar{B}^0))$ are constants that will drop out of the fraction in the asymmetry. Deriving an expression for A_{CP}^{meas} starting from Eq. 1.2.35 using the above relations between N and P (Eq. 1.2.38), we obtain

$$\begin{aligned} A_{CP}^{\text{meas}}(t) &\approx \frac{4A_{\text{det}} + 4A_P \cos(\Delta mt) + 2a_{\text{sl}} - 2a_{\text{sl}} \cos(\Delta mt)}{4 - 2a_{\text{sl}}(A_P - A_{\text{det}}) - 2a_{\text{sl}}(A_{\text{det}} - A_P) \cos(\Delta mt)} \\ &\approx A_{\text{det}} + \frac{a_{\text{sl}}}{2} + \left(A_P - \frac{a_{\text{sl}}}{2} \right) \cos(\Delta mt), \end{aligned} \quad (1.2.42)$$

where products of a_{sl} , A_P and A_{det} are dropped as they are expected to be small. The time-dependent asymmetry in the observed B^0 and \bar{B}^0 yields oscillates as a cosine with frequency Δm , amplitude $\left(A_P - \frac{a_{\text{sl}}}{2} \right)$ and offset $\left(A_{\text{det}} + \frac{a_{\text{sl}}}{2} \right)$. Note that besides the parameter of interest, a_{sl} , there are two unknowns: A_{det} and A_P . The detection asymmetry is the sum of all possible asymmetric detection effects as e.g. acceptance, material, trigger selection, tracking, and particle identification. In order to make a competitive measurement these corrections will have to be determined to at least the same permille-level precision as A_{CP}^{meas} , which is done with a variety of calibration samples. A thorough understanding of these effects is the most challenging aspect of measuring a_{sl}^d and a_{sl}^s . The production asymmetry can be determined simultaneously to a_{sl} by comparing the amplitude and the offset of Eq. 1.2.42. This is achieved using a decay-time-dependent fit. The treatment of background contributions, along with the full details on the a_{sl}^d analysis will be discussed in Chapter 4.

In the B_s^0 system the analysis strategy can be simplified due to the large value of the mixing frequency Δm_s with respect to the lifetime of the B_s^0 meson, allowing to perform a time-integrated analysis, i.e. measure the total yields $N(f)$ and $N(\bar{f})$ and integrate the probabilities in Eq. 1.2.22 over time. The integrated effect of the production asymmetry is diluted to a negligible level, although the detection asymmetry still has to be determined. The time integration for the B_s^0 system is further described in Appendix A. The observed yields have to be corrected for the background contributions from other B decays due to the inclusive reconstruction. Some backgrounds can contribute to the asymmetry due to a non-zero production asymmetry or a CP asymmetry, e.g. $B^- \rightarrow D_s^- \mu^+ X$ decays. These backgrounds will bias the measurement of a_{sl}^s either in the positive or negative direction, depending on the particle and decay channel. In summary, the relation between A_{CP}^{meas} and a_{sl}^s is as follows,

$$A_{CP}^{\text{meas}} = (1 - f_{\text{bkg}}) \frac{a_{\text{sl}}^s}{2} + f_{\text{bkg}} A_{\text{bkg}} + A_{\text{det}}, \quad (1.2.43)$$

where f_{bkg} is the total background fraction, and $f_{\text{bkg}}A_{\text{bkg}}$ is the total effect of the background asymmetry on the measurement. The measurement of a_{sl}^s will be described in Sec. 5.

2

The LHCb experiment

The data used to perform the measurements of a_{sl}^d and a_{sl}^s is collected by the LHCb experiment at the Large Hadron Collider (LHC). In the LHC, two beams of protons are accelerated in opposite directions and are made to collide at a centre-of-mass energy of 7 TeV in 2011 and 8 TeV in 2012. The amount of data collected by LHCb in these years corresponds to respectively 1 fb^{-1} and 2 fb^{-1} , adding up to a total of 3 fb^{-1} during run 1 of the LHC. In run 2 (2015-2018) the collisions take place at 13 TeV. The beams are made to collide in four interaction points, one of which is at point 8, where the LHCb experiment is located. In contrast to the other experiments at the LHC (ATLAS, CMS and ALICE), the proton-proton (pp) collisions in the LHCb detector are located on one side of the experimental hall, where the vertex locator (VELO) is placed. The reason for the conic and asymmetric setup of the LHCb experiment (see Fig. 2.1) is to study the decay products of beauty and charm hadrons, which exit the pp collision predominantly at small angles with respect to the beam axis. The LHCb experiment covers a polar angle domain $\theta \in [10, 250] \text{ mrad}$. This corresponds roughly to a pseudorapidity range of $\eta \in [2, 5]$, which is defined as

$$\eta = -\log \left[\tan \left(\frac{\theta}{2} \right) \right]. \quad (2.0.1)$$

The production of b hadrons at the LHC is dominated by gluon-gluon fusion and flavour excitation [52]. Due to the parton density distributions and large centre-of-mass energy of the colliding protons at the LHC, one of the two interacting partons in the colliding protons will generally have higher longitudinal momentum than the other, resulting in a boosted $b\bar{b}$ pair. The LHCb geometrical acceptance is optimized to include the resulting B particles. The LHCb detector, shown in Fig. 2.1, is described in detail in Ref. [53], and its performance during 2011 and 2012 evaluated in Ref. [54].

The sensitive detectors of LHCb cover a length (along the z -axis) of 20 meters, a width (x -axis) of about 12 meters, and a height (y -axis) of about 10 meters. LHCb is equipped with detectors to measure the particle momentum and the particle type. In addition, it includes a high vertex resolution detector in order to perform time-dependent B -decay measurements for CP violation studies. Finally, a trigger system selects interesting events online in order to reduce the data volume.

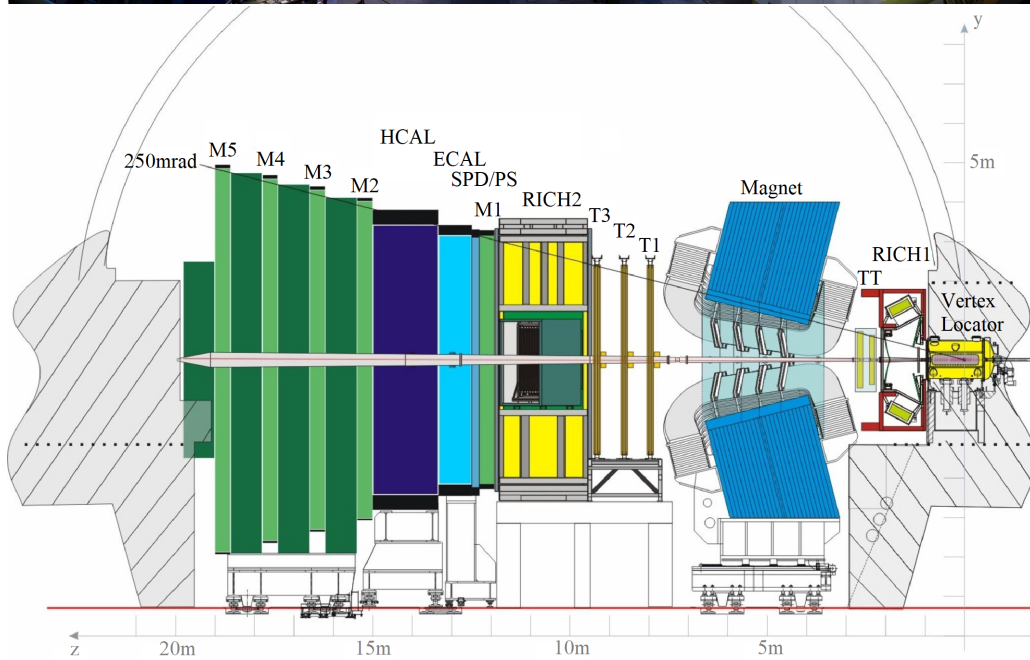


Figure 2.1: (top) The LHCb detector in the cavern at point 8 of the LHC. The VELO (not visible in the photograph) is positioned on the far right-hand side of the setup. Visible from right to left are the magnet yoke in blue, the three T stations, followed by the grey support structure of RICH2. The support structure of the calorimetry is coloured yellow. The figure is taken from Ref. [55]. (bottom) Schematic overview of the LHCb detector. The various subsystems are indicated by labels, including the three T stations (T1, T2 and T3), the two RICH detectors used for particle identification, and the five muon stations (M1 to M5). The figure is modified from Ref. [54].

This chapter describes the collision conditions in LHCb and the various subsystems that are used to collect the required information of the produced B mesons. The focus of the discussion lies on sources of potential detection charge asymmetries, relevant for the data analysis in this thesis.

2.1 The LHC and conditions at point 8

Before protons are injected into the LHC [56], they are accelerated and manipulated by a series of accelerators (see Fig. 2.2). A linear accelerator (LINAC2) accelerates protons from ionized hydrogen gas up to energies of 50 MeV, at which they enter the booster. This small quadrupole ring packs the protons together in six bunches of about 10^{11} protons per bunch, and accelerates them up to 1.4 GeV before injecting them into the Proton Synchrotron (PS). The PS is operational since 1959, and is one of CERN's oldest accelerators. It accelerates the protons in the bunches up to 25 GeV, and splits them into 72 bunches before injection into the Super Proton Synchrotron (SPS). The 7 km-circumference SPS is filled by four injections from the PS, and accelerates the protons to 450 GeV before injecting them into the two LHC storage rings. It takes about 5 minutes to fill each of the two LHC storage rings, which are 27 km in circumference. During the 2011 run, the

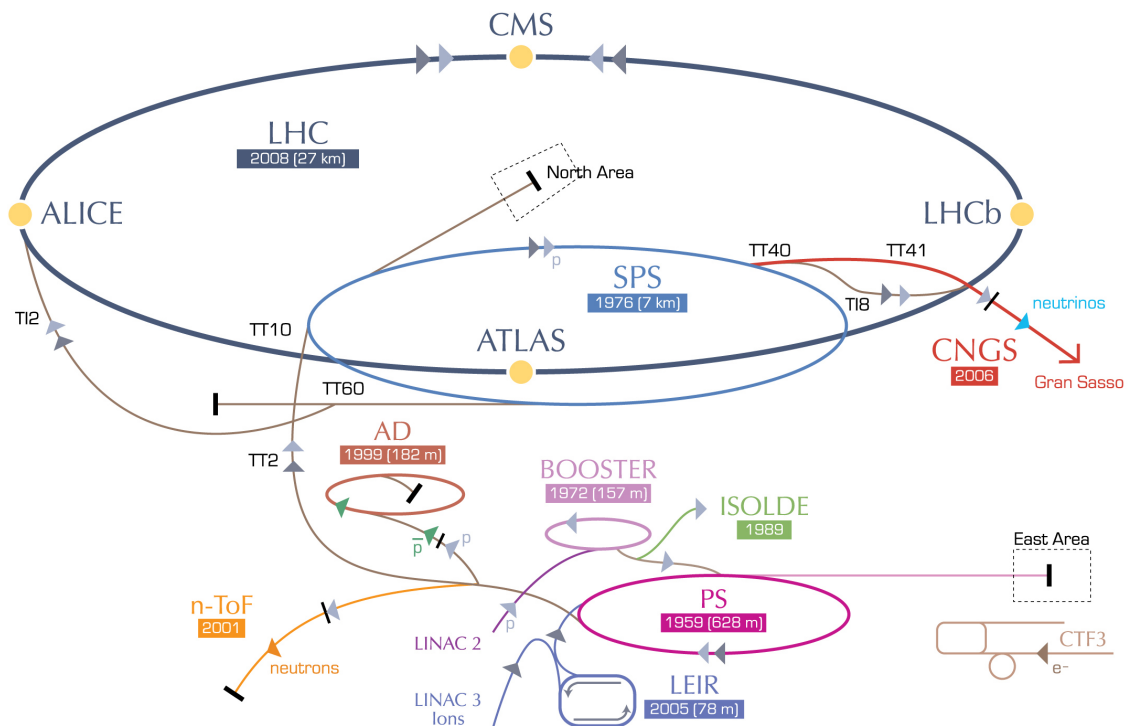


Figure 2.2: The LHC accelerator complex at CERN, modified from Ref. [57].

number of bunches in the LHC were increased in several steps to a maximum of 1300 bunches, with a 50 ns spacing in time between the bunches. In 2012 the LHC operated typically with 1300 bunches and the same bunch spacing was used. In run 2 the LHC operates mostly at the design bunch spacing of 25 ns, and with typically over 2500 bunches.

When full, the LHC accelerates both proton beams to 3.5 GeV (2011) or 4.0 GeV (2012) in about 15 minutes, while continuously squeezing the bunches together. When the beams are stable and at the desired energy, they are made to collide in the four interaction points and experimental data taking begins. Stable beams may survive in the LHC up to a day, although the beam current will steadily drop due to the pp collisions at the interaction points, as well as various beam loss mechanisms.

To reduce the overlap of multiple pp collisions in LHCb, the average number of pp interactions per bunch crossing is set to 1.8. This is accomplished, by a transverse beam offset, such that the bunches from the crossing beams do not completely cross each other. In order to keep the luminosity constant, the offset is continuously reduced as the beam current drops over time. This procedure is referred to as “luminosity levelling”. The resulting number of visible pp collisions per bunch crossing is on average $\mu_{\text{vis}} = 1.8$, corresponding to a luminosity of $4 \times 10^{32} \text{cm}^{-2} \text{s}^{-1}$ (see Fig. 2.3), and stable within 5% over one fill of the LHC. In fact, this is twice the nominal design luminosity of LHCb.

The angle under which the beams are made to collide is called the “crossing angle”, and has two contributions. The “external crossing angle” is controlled by LHC magnets,

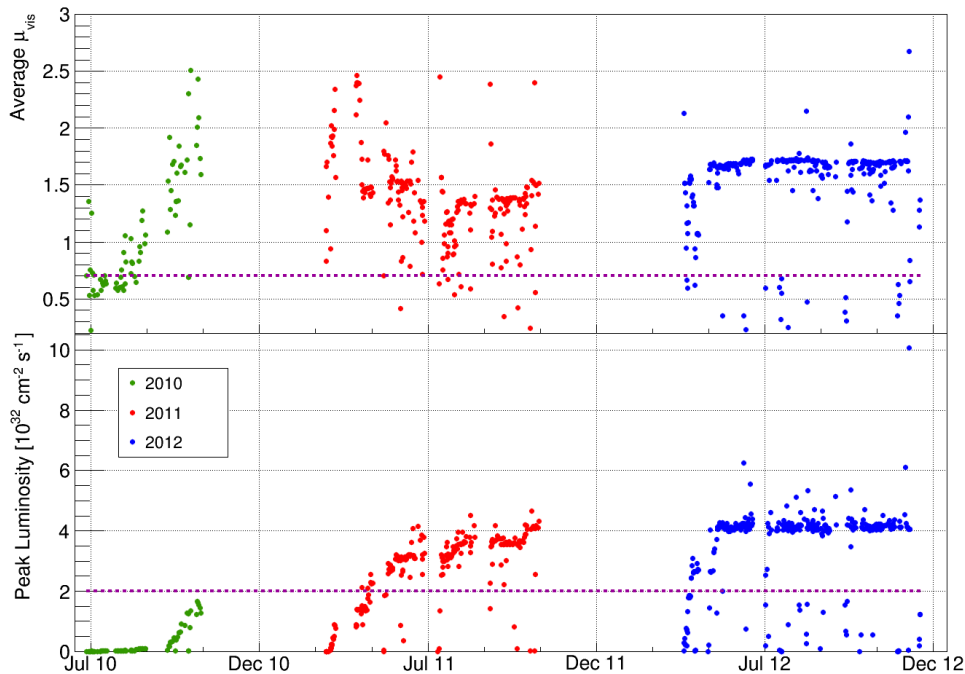


Figure 2.3: (top) The number of visible pp collisions, and (bottom) delivered instantaneous luminosity at the LHCb interaction point, over the course of run 1. The red dotted lines indicate the nominal design value. Figure is taken from Ref. [54].

and the “internal crossing angle” is controlled by the LHCb dipole magnet at +5 m and compensator magnets at −5 m along the z coordinate. The external angle in 2011 was $250\ \mu\text{rad}$ in the horizontal ($x - z$) plane, for both beams. In addition, the internal angle adds $\pm 270\ \mu\text{rad}$ for both beams, where the sign depends on the LHCb magnet polarity. This results in an effective horizontal beam-crossing angle in 2011 of $-20\ \mu\text{rad}$ for magnet polarity “up”, and $520\ \mu\text{rad}$ for magnet polarity “down”. In 2012, the external angle was set to zero such that the effective crossing angle was $\pm 236\ \mu\text{rad}$ per beam [58]. In addition, an external angle in the vertical plane of $100\ \mu\text{rad}$ was added to prevent parasitic collisions of bunches outside of the intended interaction region. The change in crossing angle provides an additional contribution to the transverse momentum of the particles, and affects the left-right distribution of particles in the LHCb detector. These are potential sources of charge asymmetries and depend on magnet polarity. This manifests itself as a difference between the absolute size of the measured detection asymmetries for the two magnet polarities in Chapter 3.

The b quarks that are created in the pp collisions quickly hadronize to form b hadrons, such as B^0 and B_s^0 . A possible charge asymmetry in the production (A_P) of a certain type of hadron may exist. This originates from the hadronic environment of the pp collision, and depends on the momenta of the b quarks. The model used in the LHCb simulation that describes the non-perturbative hadronization of b quarks into hadrons is the Lund string fragmentation model [59] (see Sec. 2.5). In this model, the b quarks are produced with a certain colour charge, which is connected to the beam fragments such that the overall system is colour neutral. Hence, the beam fragments exert a net force on the b quarks. This so-called “beam-drag” effect enhances the momentum of produced b hadrons, depending on the momenta of the other quarks that end up in the hadron. The production asymmetry of B^0 mesons is measured in Chapter 4. For B_s^0 mesons, the production asymmetry is washed out by the fast oscillations, and is negligible. Finally, for the various background modes in the analyses in this thesis, the production asymmetry is taken from external measurements.

The b hadrons decay typically within 7 mm in the LHCb lab frame, and the decay products of these hadrons are detected by the various subsystems of LHCb. These are divided into the track reconstruction detectors (Sec. 2.2) and particle identification detectors (Sec. 2.3).

2.2 Tracking of charged particles

The tracking of charged particles is provided by the Vertex Locator (VELO) and Tracker Turicensis (TT) before the dipole magnet, and three T stations after the magnet, which consist of a small inner tracker (IT) surrounded by a large-surface outer tracker (OT).

2.2.1 Magnet

The LHCb dipole magnet [60] consists of two 27-tonne coils and a 1450 tonne yoke, and provides an integrated magnetic field of 4 Tm. Combined with the excellent resolution of the tracking detectors, this allows to measure the momentum of particles with a relative precision in the range 0.5 – 0.8% for momenta from 2 to 100 GeV/ c , see Fig. 2.5 (left). The magnetic field points (mostly) along the vertical (y) direction (see Fig. 2.4), and bends particles of opposite charge towards opposite horizontal sides (x) of the detector. This causes any left-right asymmetry in the detector performance to be transformed into an asymmetry between particles of opposite charge. For this reason, detectors positioned after the magnet are more prone to cause a detection asymmetry between charge-conjugate final states. In order to mitigate these effects, the magnet polarity is regularly reversed during data taking, typically every two weeks. By taking the average of the results with both magnet polarities, the detection asymmetries caused by a left-right asymmetry will cancel, as long as an equal amount of data is taken with both polarities. In addition, the consistency of the results of both magnet polarities, corrected for detection asymmetries, can be verified. Furthermore, the magnetic field may bend particles outside of the sensitive LHCb acceptance, either towards the beam pipe (at low $|x|$) or outside of the tracking stations (at high $|x|$). Combined with a non-zero crossing angle, this can also introduce a charge asymmetry, which can depend on the magnet polarity. These detection asymmetries contribute to the tracking asymmetry, which is measured in Sec. 3.1.

For the reconstruction of charged tracks, knowledge of the size and direction of the magnetic field at each point in the detector is essential. The original field map was made from in-situ measurements in 2005, with about 500 000 measured points with steps of 80 mm along the x - and y -axes, and 100 mm along the z -axis, covering most of the LHCb acceptance. Due to slight movements of the detectors under influence of the magnetic field, it was necessary to correct the field map at the beginning of 2011. This was done by fitting

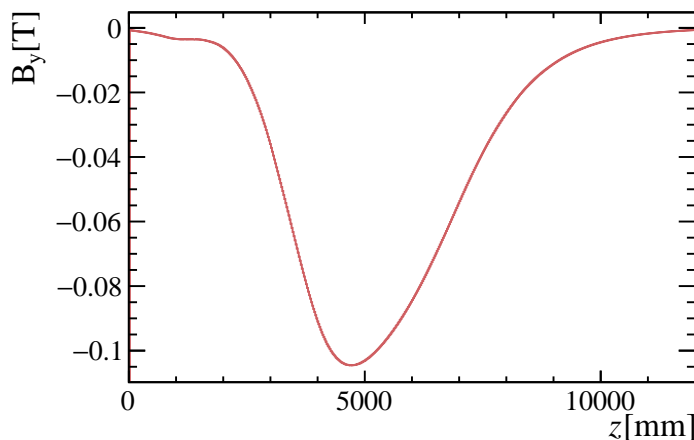


Figure 2.4: y -component of the magnetic field created by the dipole magnet, along z , at $x = y = 0$.

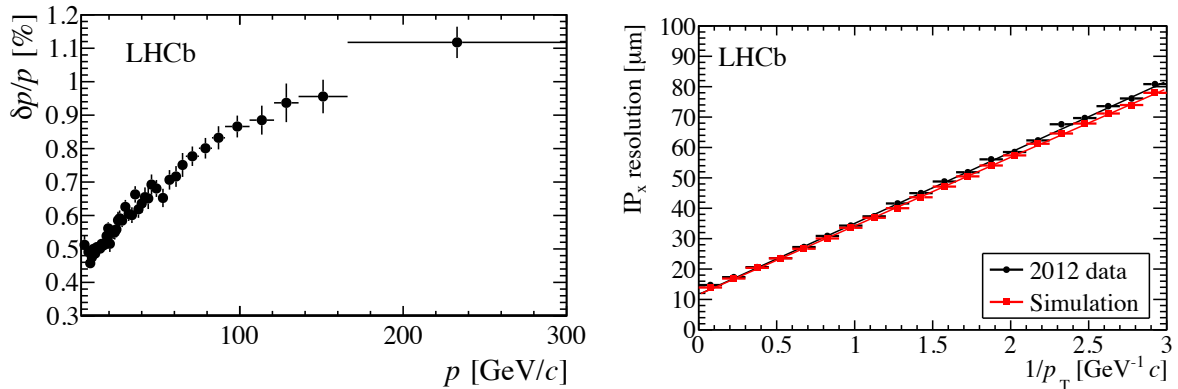


Figure 2.5: (left) Momentum resolution of long tracks as determined using $J/\psi \rightarrow \mu^+\mu^-$ decays, and (right) impact parameter resolution in x , obtained from prompt decays. The figures are taken from Ref. [54].

the orientation and overall scale of the original field map, to a new set of measurements acquired in a small region in the $y-z$ plane at fixed $x = 220$ mm. The measured magnetic field was found to be symmetric in x and identical, but of opposite sign, between magnet polarities to within 1 permille [61]. Hence, no significant charge asymmetry is expected to be caused by the magnetic field itself.

2.2.2 Vertex Locator

The VELO [62, 63] is the tracking detector that surrounds the pp collision point. It consists of 21 stations of two semicircular silicon-strip detectors, situated perpendicular to the beam direction (z) on the left and right side of the beam, as shown in Fig. 2.6. Each half-disc is a $300 \mu\text{m}$ thick sensor, and measures a combination of the r, ϕ coordinates, where r is the radial distance from the z -axis, and ϕ is the azimuthal angle. Depending on their polar angle θ , produced particles may pass through a different number of sensors, although at least three hits must be observed in order for the particle to be classified as “reconstructible”. The number of observed hits on a track in the VELO sensors directly affects the quality of the reconstructed track. The sensitive material of the sensors starts 8 mm away from the beam axis, allowing the first measurement point of a track to be close to the pp collision point. The VELO sensors are separated from the beam vacuum by a thin aluminium foil, called the RF foil, which sits as close as 5 mm from the beam axis. A traversing particle scatters on the RF foil before a first position measurement is made, which affects the impact parameter (IP) and decay-time resolution. The IP is the minimal distance of a particle to a vertex, and is an important discriminant for b -hadron decays. The VELO setup allows to have a primary vertex (PV) resolution of $13 \mu\text{m}$ in the transverse ($x-y$) plane and $71 \mu\text{m}$ along the beam axis (z) for PVs with 25 tracks, as well as an impact parameter (IP) resolution of less than $35 \mu\text{m}$ for tracks with $p_T > 1 \text{ GeV}/c$, see Fig. 2.5 (right). The decay-time resolution of b -hadrons is dominated by the error on the

secondary vertex, and is about 50 fs for the decay $B_s^0 \rightarrow J/\psi (\rightarrow \mu^+ \mu^-) \phi (\rightarrow K^+ K^-)$ [63].

The VELO and RF foil comprise about 0.23 radiation lengths, and combined with a different cross-section for K^+ and K^- with detector material, contributes to a kaon charge asymmetry which needs to be carefully calibrated. This is done in Sec. 3.2. For other particle types, the VELO is not expected to cause a significant charge asymmetry, since it is located before the magnet.

2.2.3 Tracker Turicensis

The Tracker Turicensis (TT) [53, 64] is a silicon detector situated just before the magnet. As it measures the last points on the track before the particle enters the magnet, it improves the momentum resolution by about 30%, and aids in the rejection of fake tracks. In addition, it is important in the reconstruction of long-lived neutral particles, such as

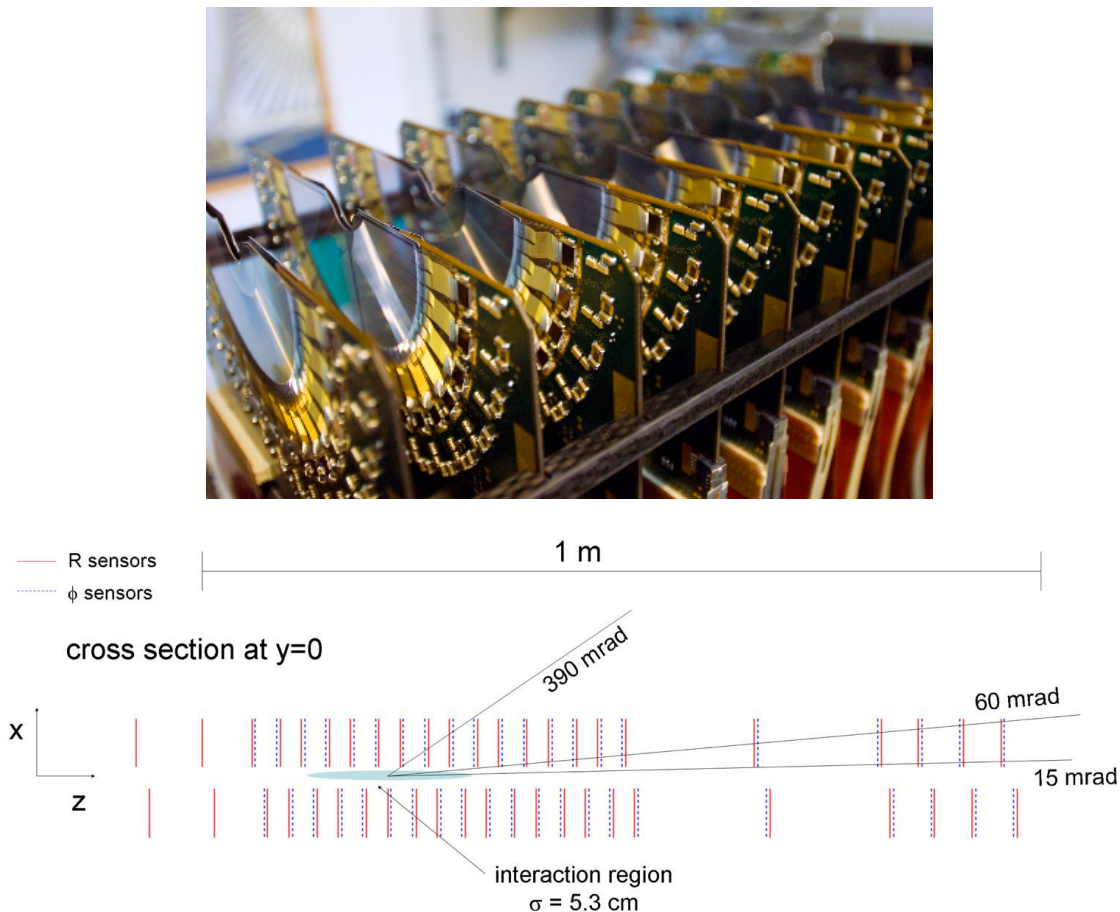


Figure 2.6: (top) Image of the VELO sensors, taken from Ref. [63]. (bottom) Schematic overview of the VELO half-disc sensors in the $x-z$ plane. The region where pp collisions occur is highlighted in blue. Particles emerging from the PV between a minimum (15 mrad) and maximum angle (390 mrad) pass through at least 3 VELO stations. The angle under which a particle hits the maximal possible amount of VELO sensors is 60 mrad. The figure is taken from Ref. [53].

the K_s^0 , that may decay outside of the VELO acceptance. The TT detector is 132.4 cm high and 138.6 cm to 157.2 cm wide, and consists of four layers of silicon strip detectors. The four detection layers along z measure stereo coordinates according to a 0° , -5° , $+5^\circ$, 0° angles with respect to the x axis, thus providing sensitivity to the non-bending y coordinate for pattern recognition. (see Fig. 2.7).

The TT detector may move slightly during magnet polarity reversal. It is therefore realigned after every such reversal, with a resulting hit resolution of about $50\ \mu\text{m}$, whereas the hit efficiency is 99.8%, as determined from hit residuals with fully reconstructed tracks.

2.2.4 Inner Tracker

The Inner Tracker (IT) [64,65], located downstream of the magnet, covers the inner region around the beam pipe of the three T stations, where the detector occupancy is highest (see also Fig. 2.7). Each station consists of four boxes of silicon-strip detectors, and each box consists of four layers in the same stereo arrangement as the TT detector. The hit resolution and efficiency is similar to that for the TT. The IT boxes closest to the magnet are found to move by about 5 mm in z due to the ramping of the magnetic field, and as such a different alignment is used for each magnet polarity.

In order to supply the IT with power, cooling and readout, cables and cooling ducts need to pass through the LHCb acceptance. These cables, and their support, are placed in a left-right asymmetric way (located mostly at negative x) and comprise about 0.05 radiation lengths per T station. They are the primary reason for a left-right material asymmetry, downstream of the magnet, and are clearly visible in Fig. 2.8. This contributes to a tracking asymmetry for charged hadrons, which is measured in Sec. 3.1.

2.2.5 Outer Tracker

The Outer Tracker (OT) [67,68] is a straw-tube gas detector, and covers the main area of the three T stations. Each station consists of four double layers of straws, arranged in the same stereo setup as the TT and IT (see Fig. 2.7). The OT measures 595 cm in x by 480 cm in y . It provides measurements of the position of ionizing particles by measuring the drift time of ions in the gas, in each of the 5-mm-wide straws. After alignment a hit resolution of about $200\ \mu\text{m}$ and hit efficiency of 99.2% are found, as determined from hit residuals with fully reconstructed tracks.

The maximal drift time in a single straw is larger than the bunch-crossing rate of 25 ns of the LHC. Therefore, a readout window of 75 ns (three clocks) is used. This makes the OT sensitive to signals from particles created in the previous and next bunch crossing, called spillover. Due to the 50 ns bunch spacing used in run 1, these contributions are limited with respect to a design operation of the LHC at 25 ns. On the other hand, the instantaneous luminosity was twice that of the nominal design, resulting in average channel occupancies in the OT of about 10% (17% for the modules close to the beam pipe). Since a straw can only fire once in each 75 ns window, a high occupancy can result in missing

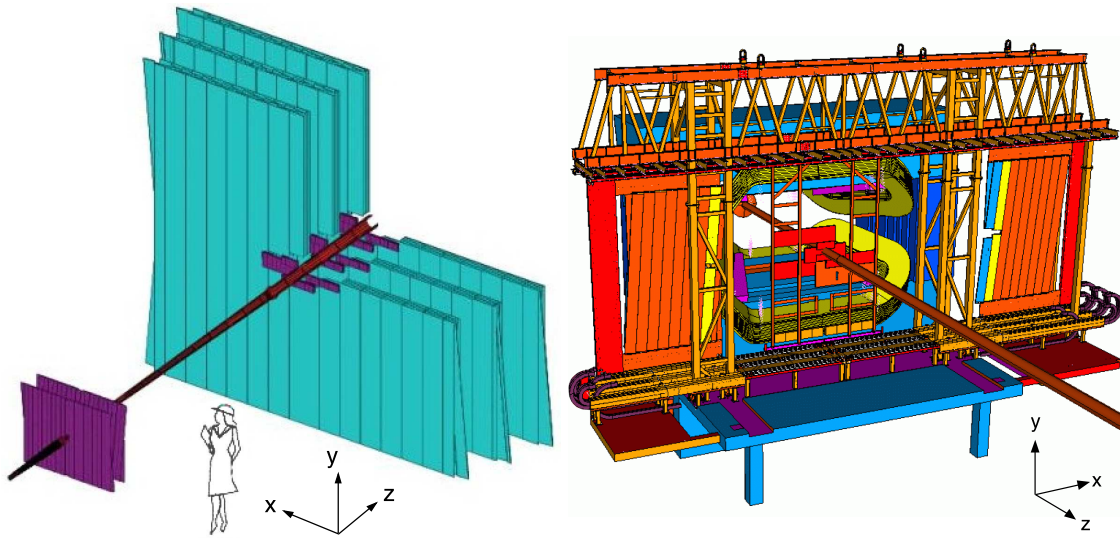


Figure 2.7: (left) Schematic overview of the silicon TT and IT in purple, and straw-tube OT in green. The beam pipe is also indicated in purple. The magnet in between the TT and the rest is left out. Visible are the four layers in the stereo configuration for each subdetector. (right) A view from the other side, where the two halves of the OT, left and right of the beam pipe, are pulled out for maintenance. The figure includes the support structures, the magnet coils in yellow, the magnet yoke in blue and the IT and OT in red. The support for the IT cables is also indicated in red. The figures are taken from Ref. [53].

hits or hits being attributed to the wrong tracks. As a result, a high detector occupancy increases the number of fake reconstructed tracks. In fact, most of the hits in the OT originate from secondary particles produced in the detector material, such as the beam pipe and its support, as well as material in the T stations themselves. For this reason the material distribution can lead to systematic track detection effects.

2.2.6 Material

When a particle travels through material inside the detector, it may undergo various interactions, which affect the track reconstruction efficiency. The first type of interaction is energy loss, caused by ionisation of the medium. The energy loss per unit length of traversed material, dE/dx , is described by the Bethe-Bloch function [2]. The second type are Coulomb interactions of the particle with the nuclei, called multiple scattering. This deflects the trajectory of the particle, and the associated material property is the radiation length X_0 . The distribution of the multiple scattering angle can be calculated using Molière theory [69], if the amount of material is well known. Finally, a particle may undergo inelastic nuclear interactions with the medium, creating secondary particles. A particle that undergoes a nuclear interaction is often not reconstructable. The nuclear cross-sections of particles with material differ significantly between particle species, as

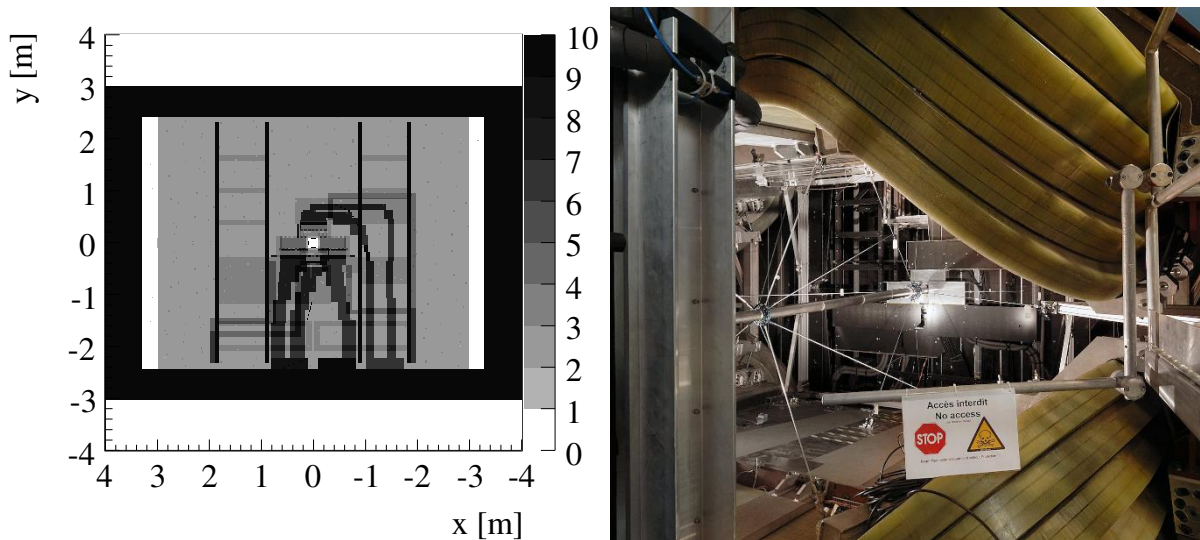


Figure 2.8: (left) Amount of material in the third T station (T3), expressed in units of radiation lengths X/X_0 . Visible are the support structures, cabling, cooling and the IT boxes. The figure is taken from Ref. [66]. (right) Image of the downstream view (towards higher z) through the dipole magnet. Clearly visible are the magnet coils in yellow. The beam pipe is visible inside, being held in place by metal support cables. Towards the end of the beam pipe, the first T station is visible. The IT boxes have a light-grey colour, while support for the cabling is darker grey. Positioned behind the IT are the black, horizontal OT modules. The figure is taken from Ref. [55].

shown in Fig. 2.9. Specifically, there is a difference in material cross-section between particles and antiparticles containing a strange quark, e.g. K^+ and K^- . This leads to a detection asymmetry of about 1% for charged kaons in LHCb, and will be calibrated carefully in Sec. 3.2.

In the track reconstruction, the first two effects — energy loss and multiple scattering — are taken into account. The amount of material traversed is calculated using the particle trajectory, and a detector model of LHCb using basic volumes (see Sec. 2.5). By weighing the various subdetectors, and comparing that against the corresponding weight in the simplified detector model, the error on the amount of material in the model can be estimated [70]. The largest uncertainties are found to be 6% for the VELO and RF foil, 5% for the cables and support structure of the IT, and about 10% for the beam pipe. In total, the uncertainty on the amount of material traversed by a particle in LHCb, before the calorimeters, is estimated to be about 10%. This affects the efficiency of the track reconstruction, and is a potential source for a charge asymmetry if the material is placed in an asymmetric way (as is the case for the IT cables).

2.2.7 Track reconstruction

The track reconstruction [70, 71] combines the individual measurements points provided by the tracking detectors described above, into a particle trajectory. The tracking detectors

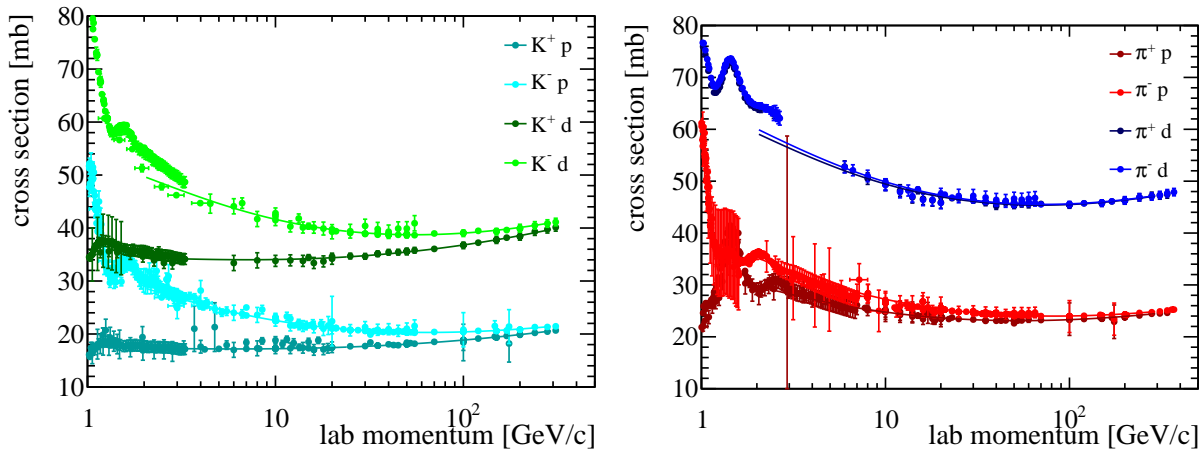


Figure 2.9: Nuclear cross sections of kaons (left) and pions (right) with protons and deuterium. The data and fits are taken from Ref. [2]. LHCb is sensitive to particles with momenta larger than 2 GeV. For kaons, large differences between K^+ and K^- are seen, while for pions these are negligible.

are positioned in a region where the magnetic field is low, and as such the tracks consist of two approximately straight-line segments, upstream (VELO + TT) and downstream (T stations) of the magnet, which are connected by a curved trajectory that passes through the magnet. These tracks are fitted to the individual hits using an extended Kalman filter. In the propagation to the z position of the next hit, the momentum is determined using the magnetic field map, and the energy loss due to interactions with the detector material in LHCb. In the estimation of the error of the next hit position, it takes into account multiple scattering.

Different types of tracks are defined in the LHCb reconstruction sequence, as shown in Fig. 2.10. VELO tracks have hits in the VELO detector only, upstream tracks have hits in the VELO and TT detectors, T tracks have only hits in the T stations, downstream tracks have hits in the TT and T stations, and long tracks have hits in the VELO, T stations, and optionally in the TT. Long tracks are the basis for most physics measurements. They are reconstructed with two algorithms. The first starts with a VELO track and adds T station hits within a search window, and subsequently extends the search to the T stations. The second matches VELO tracks directly to T tracks, which are constructed by using T station hits that are not used by the first algorithm. If hits from the TT detector match the track trajectory, they are then added. TT detector hits improve the momentum resolution, and allow to distinguish real tracks from combinations of hits that make a fake track. Typically, an event in which a b hadron is found contains 58 long tracks in 2011, and 74 long tracks in 2012. The higher multiplicity in 2012 is due to the larger production cross-section at the higher centre-of-mass energy, as well as the larger average number of visible pp collisions in LHCb.

All the tracks that are used in the analyses of Chapters 3, 4 and 5 are long tracks. The exception is Sec. 3.1, where partially reconstructed tracks are used in the determination of

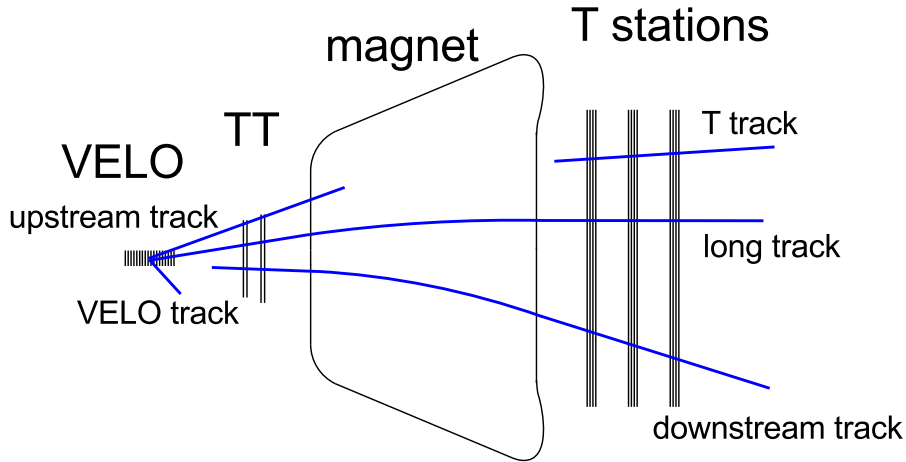


Figure 2.10: Illustration of the tracking detectors in LHCb, and the different types of tracks: VELO tracks, upstream tracks, T tracks, downstream tracks and long tracks. Figure is taken from Ref. [70].

the tracking efficiency and charge asymmetry.

The efficiency of the long track reconstruction is found to be 98% for momenta between 10 and 50 GeV/ c , and slightly decreases to 97% outside of that range (see Sec. 3.1). At lower particle momenta, this is due to multiple scattering¹. Higher momenta particles pass predominantly through the high-occupancy region around the beam pipe. A slight dependence of the tracking efficiency on the detector occupancy is found, indicating that a small asymmetry might be introduced if the occupancy is not left-right symmetric. This can be caused by a non-zero beam-crossing angle, or by the production of secondary particles due to asymmetrically placed detector material, and is determined in Sec. 3.1.

Other sources of a charge asymmetry in the track reconstruction can be due to dead detector channels and misalignment of modules, which change over time during the data taking in 2011 and 2012. Specifically after technical stops, where the left- and right halves of the TT and tracking stations can be moved out for maintenance, a realignment needs to be performed. In addition, detectors close to the magnet may slightly move when reversing the magnet polarity, resulting in a different alignment of the detector. The charge asymmetry due to the track reconstruction and related effects is measured in Sec. 3.1.

2.3 Particle identification

Particle identification (PID) of reconstructed particle tracks is required to distinguish between signal and background decays. Three types of detectors are used to determine the particle type: two ring-imaging Cherenkov detectors, the electromagnetic and hadronic calorimeters, and the muon stations.

¹The typical spread of the angle due to multiple scattering goes as $\sigma \propto \frac{1}{p}$ [2].

2.3.1 Ring-imaging Cherenkov detectors

The two ring-imaging Cherenkov detectors (RICH) [72, 73] use the Cherenkov light radiated by particles that travel faster than the speed of light in the radiator medium. This light is emitted in a cone, with an angle θ that depends on the velocity of the particle,

$$\cos(\theta) = \frac{1}{n\beta}, \quad (2.3.1)$$

where $\beta = v/c$, and n is the refractive index of the medium. Using a measurement of the Cherenkov angle which measures the velocity, and combined with the momentum of the track, the mass of the particle can be calculated. The RICH detectors serve to discriminate between pions, kaons and protons, as illustrated in Fig. 2.11 (right).

Three different radiators are used. In RICH1, located between the VELO and the TT, a 5 cm thick layer of silica aerogel is used, with $n = 1.03$, suited for PID up to momenta of 10 GeV/ c . The second radiator in RICH1 is C₄F₁₀ gas, with $n = 1.0014$, and provides PID up to momenta of 60 GeV/ c . RICH2 is positioned after the T stations, and is filled with CF₄ gas with $n = 1.0005$, providing PID up to momenta of 100 GeV/ c . The Cherenkov photons are reflected outside of the LHCb acceptance with a set of parabolic and straight mirrors, and are detected using hybrid photon detectors (HPDs), see Fig. 2.11. The parabolic mirrors are used to focus photons with the same angle into a ring in the HPD plane. The number of detected photons per track is about 20 in the C₄F₁₀ gas of RICH1, and 16 in RICH2, while the Cherenkov angle resolution is 1.6 mrad in the C₄F₁₀ gas of RICH1, and 0.7 mrad in RICH2. The distribution of reconstructed Cherenkov angles in RICH1 is shown in Fig. 2.11 (right), where the characteristic curves versus momentum for each particle type are seen.

The HPD response has some variation over time, and the individual HPDs are continuously calibrated. In addition, the refractive index of the medium depends on variables such as pressure and temperature, which may vary slightly over time, and regular calibrations are required. Improvements in the calibration methods were implemented during run 1. Finally, some HPDs may fail during data taking, and are either reset after a data-taking run, or replaced during technical stops. The reasons mentioned above can cause a change in identification efficiency, that is not necessarily symmetric between the left- and right detector halves, and varies over time. Changes in efficiency of up to a few percent have been observed. Therefore, some charge asymmetry is expected to be caused by PID requirements, which does not necessarily fully cancel when taking the average of the asymmetries of the two magnet polarities.

2.3.2 Calorimeters

The electronic and hadronic calorimeter (ECAL, HCAL) [74, 75] are primarily used for the identification of electrons, photons and π^0 particles, and online triggering of events with a large energy deposit. The ECAL and HCAL are barely used in the analyses in this thesis, since no such particles occur in the signal modes, and signal events are triggered

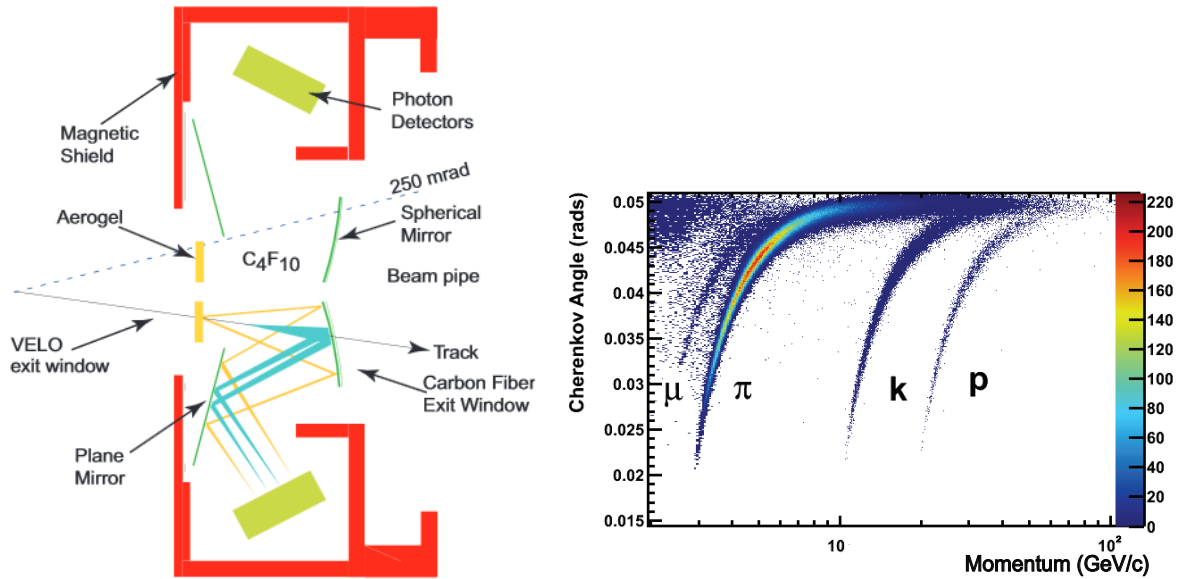


Figure 2.11: (left) Schematic cross-section of RICH1 in the y, z plane. The various components are indicated by labels. The mirrors that reflect the Cherenkov photons are visible in green, and the Cherenkov light of an example track is shown in blue. Figure is taken from Ref. [55]. (right) Reconstructed Cherenkov angle versus momentum for various particle types, in the C_4F_{10} radiator of RICH1. Figure is taken from Ref. [73].

by the muon stations. Positioned after RICH2, the calorimetry is built up of alternating layers of bulk material that induces particle showers, and scintillating material. Charged particles from the shower induce photons in the scintillating material, which are read out by photodetectors and provide a measure for the energy of the shower. The energy resolution is expressed as

$$\frac{\sigma(E)}{E} = \frac{a}{\sqrt{E}} \oplus b, \quad (2.3.2)$$

where E is expressed in GeV and \oplus indicates that both contributions should be added in quadrature. For the ECAL, $a = 10\%$ and $b = 1.5\%$, while for the HCAL $a = 80\%$ and $b = 10\%$. Just in front of the ECAL are the preshower (PS) and scintillating pad (SPD) detectors, which provide additional PID information by measuring the start of the shower.

2.3.3 Muon stations

Muons are the only particles that survive after the calorimeters, and as such muon identification is conceptually straightforward. The LHCb muon detector [76, 77] consists of five stations (M1-M5): one placed before, and four placed after the calorimeters. They use multi-wire proportional chambers (MWPCs) to detect the passage of particles. The width of the chambers increases towards the outside (large x) of the detector, to match the decrease in occupancy, as is visible in Fig. 2.12. These chambers are larger than the sensitive volume they contain. In order to decrease the insensitive regions in the $x - y$

plane, the chambers in one station are staggered at four different z -positions, which differ up to 30 cm. This changes the amount of material in front of the chambers at certain x, y positions and the covered solid angle (by about 1%), resulting in a different occupancy (up to a relative 30%) between the chambers. Since the shifts in z of the chambers are not the same between the left and right half of a station. This introduces a left-right asymmetry by construction, and introduces an asymmetry of the muon hardware-level trigger, as will be discussed in Sec. 2.4. This asymmetry is calibrated in Sec. 4.5.3.

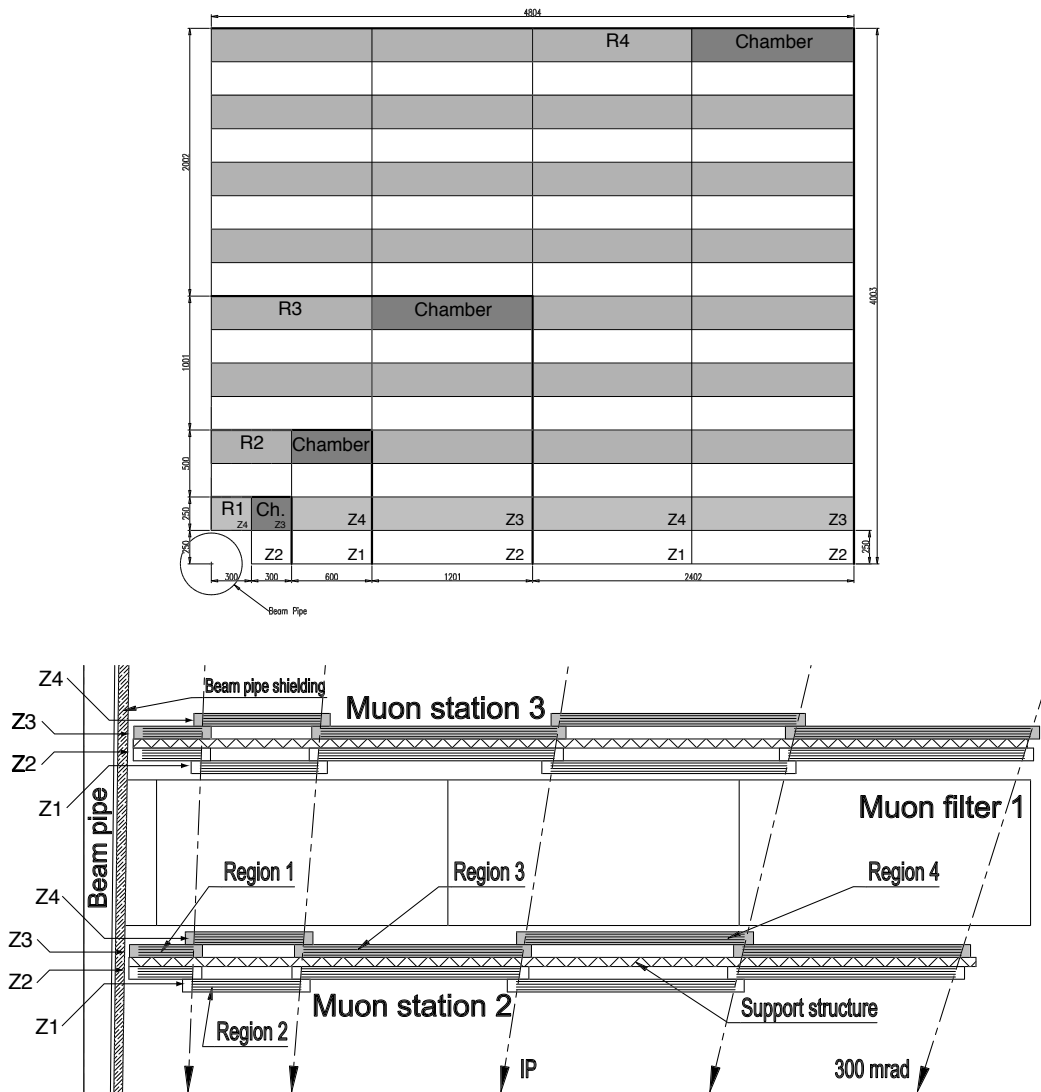


Figure 2.12: (top) x, y view of one quarter of M2. Indicated with the labels Z1-Z4 are the four different z -positions of the chambers. The rows marked in a grey shade are positioned behind the support structure, at Z3 or Z4. (bottom) View of muon stations M2 and M3 in the x, z plane at $y = 0$. Indicated are four different z -positions of the various chambers in one station. Both figures are taken from Ref. [76]

2.3.4 Particle ID

The identification of charged hadrons (π^\pm, K^\pm, p^\pm) is mostly provided using the RICH systems [54]. A likelihood for each particle hypothesis is assigned to each track, using the information from RICH1 and RICH2. The difference between the log-likelihood of two particle hypotheses, e.g. a particle being a kaon or a pion, is called $DLL_{K-\pi}$. A typical kaon PID requirement is $DLL_{K-\pi} > 5$, which is 85% efficient for kaons from $D^0 \rightarrow K^-\pi^+$ decays, and 97% efficient to reject pions from these decays (see Sec. 3.3). Stronger PID requirements give rise to larger inefficiencies, and thus potentially larger detection asymmetries.

Muon identification [78] is done by requiring hits in the muon stations around the (extrapolated) track. The stations used depend on the momentum of the track:

- $p < 6 \text{ GeV}/c$: M2 + M3 ,
- $6 < p < 10 \text{ GeV}/c$: M2 + M3 + (M4 or M5),
- $p > 10 \text{ GeV}/c$: M2 + M3 + M4 + M5 ,

based on the fact that low-momentum muons can be stopped in the material. Subsequently, a likelihood is constructed from the χ^2 value of a straight-line fit to the hits in the muon stations. The muon identification for a typical requirement of $DLL_{\mu-\pi} > 0$ has an efficiency in the range 0.96 – 0.99% depending on the (transverse) momentum, and a pion misidentification probability of about 1% dominated by $\pi \rightarrow \mu$ decays-in-flight.

The DLL variables from the RICH systems, muon system and calorimetry are added linearly to form more powerful DLL variables. These are used in the physics analyses in this thesis. In addition to the DLL variables, neural-net based PID variables are constructed using input from RICH1, RICH2, the muon system and the calorimetry, and take into account possible correlations between the various detector systems. These variables are referred to as **ProbNN**, and have a different performance as function of particle momentum. They are used for the reduction of backgrounds in Chapter 5. The charge asymmetry due to PID requirements is measured in Sec. 3.3.

2.4 Trigger

With an event size of approximately 100 kB and about 10 MHz of visible pp interactions in LHCb, the data bandwidth would exceed 1 TB/s, which is too much to store on disk. In order to reduce the data volume, interesting events are selected online using a trigger system [79]. The trigger performance in 2011 is documented in Ref. [80], and in 2012 in [81]. The trigger is divided into a hardware and a software stage. The hardware stage (called L0) reduces the bandwidth to a total of 1 MHz, and has a fixed latency of 4 μs to make a decision for each event. The most important systems used in the L0 trigger are the calorimeters and the muon stations. In the former, the decision is based on an estimation of the transverse energy deposit in the calorimeter. In the latter, it is based

on an estimation of the transverse momentum of a particle in the muon stations. In this thesis, only the muon-based hardware trigger (called L0Muon) is used, which uses about 400 kHz of bandwidth (out of the 1 MHz).

In each quadrant of the muon stations, the muon with the highest p_T is identified by searching for hits from M1 through M5 in a straight line, that roughly point towards the interaction region. The p_T is calculated from the transverse momentum kick of the track in the magnet, resulting in a relative p_T resolution is about 25%. If the estimated p_T exceeds the threshold of 1.48 GeV/c in 2011, or 1.76 GeV/c in 2012, the event is accepted. The efficiency of selecting b -hadron decays is about 95%, but steadily drops to about 70% below muon transverse momenta of 5 GeV/c. In 2011, the staggering in z of the muon chambers (Sec. 2.3.3) is not taken into account in the determination of the p_T . This overestimates the p_T of a muon with a positive or negative charge, depending on the magnet polarity, and increases the L0Muon efficiency for this charge at low p_T . This creates a significant charge asymmetry, which will be discussed in Sec. 3.4. In 2012, a fix was implemented and the charge symmetry associated with the muon hardware trigger is much smaller.

After the hardware trigger, a software trigger (called H1t) further reduces the bandwidth. The software trigger runs on the LHCb online computing system [82, 83] situated in the cavern at point 8, close to the LHCb detector but shielded from radiation by a concrete wall. The H1t is divided into two stages. The first stage (H1t1) reduces the rate to about 40 kHz in 2011, and has about 58 ms per event to make a decision. This allows for a partial event reconstruction, similar to the track reconstruction run offline, but with reduced search windows and no PID reconstruction. Candidates are selected based on their p_T , p , track quality and displacement from the primary vertex. In 2012, about 20% of the events that passed the hardware trigger were saved temporarily offline, to be processed by the software trigger at a later stage during the gaps between fills of the LHC [84]. This allowed more computing time per event, part of which was spent on an improved VELO reconstruction and a better agreement between the online and offline reconstruction. In addition, more disk space was available in 2012, which allowed a higher H1t1 output rate of 80 kHz.

Two H1t1 lines are used in the analyses in this thesis. The first (called H1t1TrackMuon) selects muon tracks from events that passed L0Muon and have $p > 8.0$ GeV/c and $p_T > 1.0$ GeV/c². This line has a rate of about 5 kHz in 2011, and an average signal efficiency of about 75% for $B^+ \rightarrow J/\psi K^+$ events. The second line (called H1t1TrackAllL0) selects all events that passed the hardware trigger, but demands more a stringent $p > 10$ GeV/c and $p_T > 1.7$ GeV/c. It has a rate of about 33 kHz in 2011 and a signal efficiency ranging from 60 – 95% depending on the B decay mode. The higher bandwidth in 2012 allows to loosen some these requirements, and increases the efficiency of H1t1TrackMuon to about 90%, and H1t1TrackAllL0 by a few percent.

Finally, the second software stage (H1t2) performs a full event reconstruction, and reduces the bandwidth to about 3 kHz in 2011 and 5 kHz in 2012. Events are selected by

²Although these criteria vary somewhat throughout the data-taking period, this is the most common configuration.

matching the decay topology to that of true 2, 3 or 4-body b -hadron decays that include a muon in the final state. The charge asymmetry due to the trigger is measured in Sec. 3.4.

2.5 Simulation

In the analyses in this thesis, simulated events are used to determine the selection efficiency as well as the size of various background contributions. In addition they are used to correct the momentum of partially reconstructed b -hadron decays, and to determine the size of a variety of possibly biasing effects.

Simulated pp collisions are generated using PYTHIA [85] with a specific LHCb configuration [86]. It is found that the charged particle multiplicities in PYTHIA 6 are underestimated by about 10 – 40%, depending on the bin of p_T of the tracks [87]. The agreement is better when using PYTHIA 8, but still depends on the region of phase space. For this reason, a combination of events generated with PYTHIA 6 and PYTHIA 8 is used for the simulated samples used in this thesis, and the performance is compared between these two versions.

Decays of hadronic particles are described by EVTGEN [88], in which final-state radiation is generated using PHOTOS [89]. The interaction of the generated particles with the detector is implemented using the GEANT4 toolkit [90] as described in Ref. [91]. A simulation of the response of the subdetectors in LHCb transforms the energy deposits in the active detector material into digital signals. These are then processed by an emulation of the hardware-level trigger, and an offline version of the software-level trigger, followed by a full event reconstruction identical to that for real data. Tracks are matched to the generated decays by matching the digital clusters, used to form the track, to the generated energy deposits created by GEANT4. This allows to compare reconstructed quantities to the generated quantities of the particles.

3

Detection asymmetries

The main challenge in the measurements of a_{sl}^d and a_{sl}^s is to quantify the charge asymmetry of the detection efficiency between the final states f and \bar{f} , given by

$$A_{\text{det}} = \frac{\epsilon(f) - \epsilon(\bar{f})}{\epsilon(f) + \epsilon(\bar{f})}. \quad (3.0.1)$$

In the a_{sl}^d analysis, the visible final states are $f = D^-(\rightarrow K^+\pi^-\pi^-)\mu^+$, and in the a_{sl}^s analysis $f = D_s^-(\rightarrow K^+K^-\pi^-)\mu^+$. Various parts of the detection process can contribute to the detection asymmetry. The size of these contributions are assessed with calibration samples; samples with high statistics that allow to measure particle detection efficiencies directly in data. The simulation is not guaranteed to describe the data at the precision required, which is $\mathcal{O}(0.1\%)$, but is a crucial tool to understand the asymmetry.

One can think of many causes of a detection asymmetry at permille-level precision. Local effects (e.g. an inefficient channel or a slightly higher bias voltage in a sensor) contribute to changes in efficiency in specific locations of the detector. On a larger scale, a misalignment of a module or even a whole station can contribute to a difference in left-right detector efficiency. Specific causes of detection inefficiencies and asymmetries are discussed in detail in Sec. 2. Most importantly, hadronic cross-sections of particles and antiparticles traversing detector material are not necessarily charge symmetric. In addition, a different amount of material traversed by particles of opposite charge, increases the probability of having a detection asymmetry. This can be caused by a left-right asymmetric placement of material in the detector setup, as is the case for cables connected to the IT. Finally, the crossing angle of the colliding beams in the LHCb interaction point directly affects the left-right occupancy in the detector, as discussed in Sec. 2.1.

The vertical magnetic dipole field bends positively and negatively charged particles to horizontally opposite directions. This transforms any difference between the detection efficiency on the left and right side of LHCb, downstream of the magnet, into a charge detection asymmetry. It is expected that these effects are dependent on where the particle passes through the detector, and therefore on the momentum and other kinematic variables. The strategy is to determine the detection asymmetries as a function of kinematic variables ($p_{\text{T}}, p, \eta, \phi$) using the calibration samples. These are used to determine the asymmetry of the signal samples, based on their kinematic distributions. Effectively, this is done by

applying event weights to the calibration samples, such that the kinematic distributions match those of the signal sample. Assuming the detection asymmetry only depends on these distributions, the detection asymmetry of the calibration sample then matches that of the signal sample, modulo statistical variations in these distributions.

A key feature of LHCb is the regular flip of the magnet polarity, such that charged particles predominantly traverse opposite sides of the spectrometer. As a net effect, the left-right asymmetries are expected to change sign, while constant terms such as the material cross-section differences will not, allowing to disentangle these contributions. The idea is to determine a_{sl}^d and a_{sl}^s separately for data taken with each magnet polarity, after correcting for detection asymmetries, and check for consistency of these results. After that, the arithmetic average over both magnet polarity samples is taken to reduce any possible left-right asymmetry that might remain.

The asymmetry due to two detection efficiencies that factorize can be approximated as

$$\begin{aligned} A_{\text{det}} &= \frac{\epsilon_1(f)\epsilon_2(f) - \epsilon_1(\bar{f})\epsilon_2(\bar{f})}{\epsilon_1(f)\epsilon_2(f) + \epsilon_1(\bar{f})\epsilon_2(\bar{f})} = \frac{(1 + A_{\text{det},1})(1 + A_{\text{det},2}) - (1 - A_{\text{det},1})(1 - A_{\text{det},2})}{(1 + A_{\text{det},1})(1 + A_{\text{det},2}) + (1 - A_{\text{det},1})(1 - A_{\text{det},2})} \\ &= \frac{A_{\text{det},1} + A_{\text{det},2}}{1 + A_{\text{det},1}A_{\text{det},2}} \approx A_{\text{det},1} + A_{\text{det},2} + \mathcal{O}(A^3). \end{aligned} \quad (3.0.2)$$

The individual efficiencies are expected to mostly factorize since they represent unrelated segments of the reconstruction and selection, and are determined with separate calibration samples. On top of that, the asymmetries are small, and any existing correlation is expected to not depend on the charge of the final state. Hence, the total detection asymmetry A_{det} is obtained as the sum of the individual asymmetries, as long as the product of the asymmetries is below the experimental sensitivity of the measurement ($\mathcal{O}(10^{-5})$). The total detection asymmetry is then

$$A_{\text{det}} = A_{\text{track}} + A_{\text{PID}} + A_{\text{trigger}}, \quad (3.0.3)$$

where A_{track} is the asymmetry due to tracking and related effects, A_{PID} is the asymmetry due to hadron PID criteria, and A_{trigger} is the asymmetry due to the trigger. In the a_{sl}^d analysis, only the muon triggers the event and A_{trigger} is called A_{μ} . In the a_{sl}^s analysis, the software-level trigger asymmetry is determined separately, which is called A_{Hlt} . A_{track} is further divided into charge-neutral pairs of the final-state tracks in the a_{sl}^d and a_{sl}^s analyses, $A_{\text{track}} = A_{\mu\pi} + A_{K\pi}$ (A_{KK} for a_{sl}^s), as illustrated in Fig. 3.1.

This chapter introduces the methods used in assessing various detection asymmetries, see Table 3.1 for an overview, including the decay modes that are used as calibration samples. The application of the detection asymmetry methods to the a_{sl}^d and a_{sl}^s measurements will be discussed in subsequent chapters.

3.1 The asymmetry of $\mu^+\pi^-$ pairs

The muon and the pion are almost identical particles in terms of mass ($m_{\mu^+} \approx 106$ MeV, $m_{\pi^+} \approx 140$ MeV). Therefore the tracking asymmetry of the $\mu^+\pi^-$ pair is believed to

Asymmetry	Decay modes	Chapter
$A_{\mu\pi}$	$B \rightarrow J/\psi X$ $D^{*+} \rightarrow D^0(\rightarrow K^-\pi^+\pi^-\pi^+)\pi^+$	3.1
$A_{K\pi}, A_{KK}$	$D^- \rightarrow K^+\pi^-\pi^-$ $D^- \rightarrow K_s^0(\rightarrow \pi^+\pi^-)\pi^-$	3.2
A_{PID}	$D^{*+} \rightarrow D^0(\rightarrow K^-\pi^+)\pi^+$	3.3
A_μ	$B \rightarrow J/\psi X$	3.4
A_{Hlt}	$B \rightarrow J/\psi X$ $D_s^- \rightarrow \phi(\rightarrow K^+K^-)\pi^-$	3.4.1
a_{sl}^d	$B^0 \rightarrow D^-(\rightarrow K^+\pi^-\pi^-)\mu^+\nu_\mu$ $B^0 \rightarrow D^{*-}(\rightarrow \bar{D}^0(\rightarrow K^+\pi^-)\pi^-)\mu^+\nu_\mu$	4
a_{sl}^s	$B_s^0 \rightarrow D_s^-(\rightarrow K^+K^-\pi^-)\mu^+\nu_\mu$	5

Table 3.1: Overview of the various detection asymmetries that are calculated with calibration samples in this chapter, including the decay modes that are used and a reference to the section. For comparison, the bottom two rows display the signal modes in the a_{sl}^d and a_{sl}^s analyses. Charge conjugate modes are implicitly included.

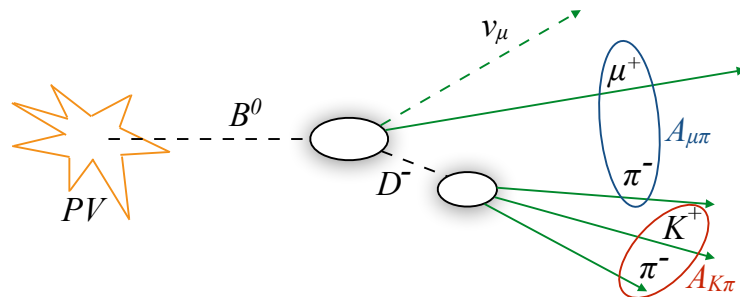


Figure 3.1: The detection asymmetry due to tracking is split up into two pairs of opposite-charge tracks, shown here for the $B^0 \rightarrow D^-\mu^+\nu_\mu X$ decay.

largely cancel when the kinematic distributions are in agreement. However, pions do undergo nuclear interactions with the detector material, so small differences in efficiency between detecting muons and pions can be expected. Since the charge asymmetry in the pion–nuclear cross-section is small, the asymmetry of $\mu^+\pi^-$ pairs,

$$A_{\mu\pi} = \frac{\epsilon(\mu^+\pi^-) - \epsilon(\mu^-\pi^+)}{\epsilon(\mu^+\pi^-) + \epsilon(\mu^-\pi^+)}, \quad (3.1.1)$$

is small. $A_{\mu\pi}$ is determined in two ways: first using a sample of muons to determine the tracking efficiency (Sec. 3.1.1) and assuming the pion behaves as a muon, and second using a sample of pions (Sec. 3.1.2) and assuming the muon behaves as a pion. A comparison between both methods is made in Sec. 3.1.3

3.1.1 The J/ψ tag-and-probe method

The J/ψ tag-and-probe method employs the large sample of $B \rightarrow J/\psi(\mu^+\mu^-)X$ decays that LHCb has collected, to measure the tracking efficiency of muons. The decays are triggered on a special calibration line, as is explained in detail in Ref. [92]. In total, about 300 000 decays are collected.

The event is triggered by the presence of a single muon. This “tag” muon is reconstructed as a long track and has a minimum p_T of 1.3 GeV/ c . In order to remove background tracks originating from the PV, the muon is required to originate from a secondary vertex by demanding that the Impact Parameter (IP) exceeds 0.5 mm, and the difference of the fit quality of the PV with and without the muon track is $\chi_{\text{IP}}^2 > 200$. The other muon from the J/ψ decay is called the “probe”, and is initially reconstructed without making use of hits in (part of) the tracking system. The tag and probe muons are required to combine into an invariant mass around the J/ψ mass, with a vertex quality of $\chi^2/\text{dof} < 5$. If the standard long-track-finding algorithm finds the partially reconstructed probe muon, the candidate is considered efficient, and flagged “pass”. Otherwise, it is flagged as “fail”. The long track is required to have $p > 5$ GeV/ c in order for the probe to be counted as efficient. The track finding efficiency of the subsystem that is not used in the partial reconstruction, is the fraction of candidates in the “pass” category, over the sum of “pass” and “fail”. Using the information of the precisely reconstructed tag track and the partially reconstructed probe track with less momentum precision, the invariant mass spectrum of the J/ψ is calculated. The efficiency fraction is obtained from the ratio of yields in a maximum likelihood fit to the J/ψ invariant mass peaks in both categories.

Three methods are used to probe the tracking efficiencies in various subsystems, called the “VELO”, “T-station” and “long” method. See Fig. 3.2 for an illustration.

The VELO method uses a downstream track (reconstructed in the TT and T-stations) to probe the VELO tracking efficiency. The downstream track is compared to reconstructed long tracks, and a long track is identified as coming from the same particle as the downstream track when 50% of the hits in the T-stations are the same. If such a long track is found, the event is considered “pass”. Otherwise, it is considered as “fail”.

The T-station method builds a probe candidate by making use of a stand-alone track reconstruction in the muon stations and combining these tracks with VELO segments, to test the efficiency of the T-stations. If a long track shares the same VELO segment and extrapolates to at least two of the same hits in the muon stations, they are identified as coming from the same particle, and the event is considered as “pass”.

The long method builds probe candidates by matching TT hits to muon tracks. A matching long track is found if at least 70% of muon hits are shared, and 60% of TT hits in case they exist. This directly probes the long track reconstruction efficiency, which requires only hits in the VELO and T-stations.

The total (long) tracking efficiency can also be found by multiplying the efficiency obtained from the VELO and T-station methods, assuming that the long tracking efficiency factorizes. Due to the smaller uncertainty, this is the default method used to determine the tracking efficiency and asymmetry, while the long method serves as a cross-check. Agreement within statistical errors between both methods is found. The invariant mass fits using the three methods described above are shown in Fig. 3.3, and the efficiencies are shown in Fig. 3.4. In 2012 the efficiency is slightly lower, which is partially attributed to the higher detector occupancy [92].

As discussed above, the track-finding efficiency is expected to depend on the kinematic properties of the probe track and detector occupancy. Therefore, the efficiencies are determined as a function of the probe momentum p , transverse momentum p_T , pseudorapidity η and projected azimuthal angle in the $x - y$ detector plane, ϕ , as well as the event track multiplicity. Details of the obtained efficiencies can be found in Ref. [92].

The charge asymmetry of the tracking efficiency is obtained by determining the tracking efficiency separately for probes with a positive and negative charge. It is defined as

$$A_{\text{track}} = \frac{\epsilon^+ - \epsilon^-}{\epsilon^+ + \epsilon^-}, \quad (3.1.2)$$

and is shown as a function of transverse momentum in Fig. 3.5. There is no evidence for a particular trend, and data taken in 2011 and 2012 display a comparable tracking asymmetry. However, around $p_T \approx 2.5 \text{ GeV}/c$ there is an indication for a magnet polarity-dependent effect.

The application of the J/ψ tag-and-probe method in the a_{sl}^d and a_{sl}^s analyses is to determine the asymmetry in the tracking efficiency of $\mu^+\pi^-$ pairs. First, the kinematic distributions of the positively charged probe track in the J/ψ sample are weighed to match those of the μ^+ in the signal sample, and similarly for the negatively charged probe track and the signal μ^- distributions. The tracking asymmetry of the signal muon is then determined as in Eq. 3.1.2. Second, the same procedure is followed to obtain the tracking asymmetry of the signal pion, assuming it behaves as a muon. Finally, the tracking asymmetry of $\mu^+\pi^-$ pairs is calculated as

$$A_{\mu\pi} = A_{\text{track}}^{\mu_{\text{sig}}} + A_{\text{track}}^{\pi_{\text{sig}}} = \frac{\epsilon_+^{\mu_{\text{sig}}} - \epsilon_-^{\mu_{\text{sig}}}}{\epsilon_+^{\mu_{\text{sig}}} + \epsilon_-^{\mu_{\text{sig}}}} - \frac{\epsilon_+^{\pi_{\text{sig}}} - \epsilon_-^{\pi_{\text{sig}}}}{\epsilon_+^{\pi_{\text{sig}}} + \epsilon_-^{\pi_{\text{sig}}}}, \quad (3.1.3)$$

where the superscripted μ_{sig} and π_{sig} indicate which particle was used to weigh the calibration sample. The signal pion asymmetry has an opposite sign, due to it having the opposite charge of the muon in the final state. The correlation between both weighed samples is obtained by calculating the kinematic overlap between the signal muon and pion, and is taken into account in the determination of the total statistical error.

An incomplete matching of the probe-track kinematic distributions to those of the signal tracks might be a potential source of bias on the result. It is investigated by varying the choice of binning used to match the kinematic distributions to those of the signal. The deviation with respect to the nominal result is assigned as a systematic error. The

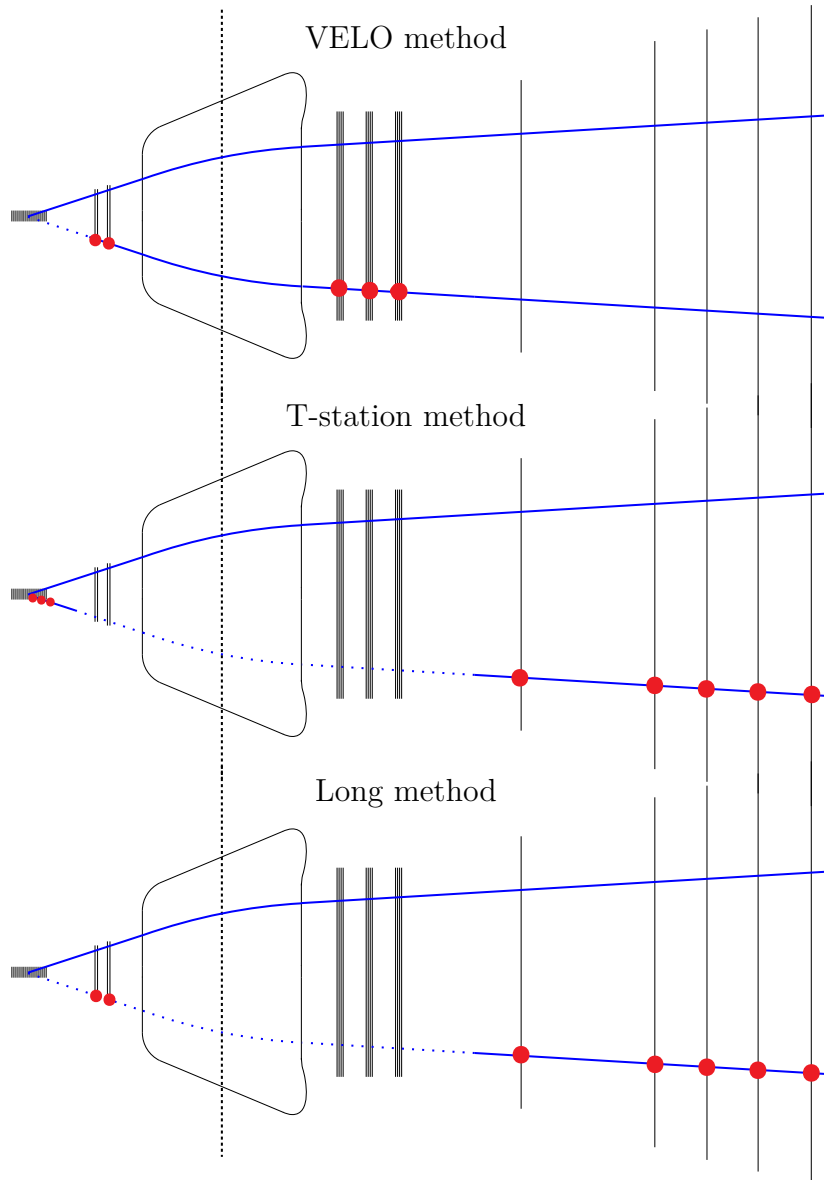


Figure 3.2: Illustration of the VELO, T-station and long methods for determining the tracking efficiency using the J/ψ tag-and-probe method. The red dots indicate hits that are used to form a partially reconstructed probe track candidate. The solid line represents the part of the track that is reconstructed. The figure is taken from Ref. [70].

size of this effect depends on the kinematic distributions of the signal, and is discussed in Chapters 4 and 5.

Alternatively, the $\mu^+\pi^-$ asymmetry is calculated by subtracting the amount of signal μ^+ candidates from the amount of signal π^- candidates in each bin of kinematic phase-space (p_T, η), and multiplying by the tracking asymmetry in that particular bin,

$$A_{\mu\pi} = \frac{1}{N_{\text{sig}} \sum_{\text{bins } i} (N_i^{\mu^+} - N_i^{\pi^-}) \times A_{\text{track}}^i, \quad (3.1.4)$$

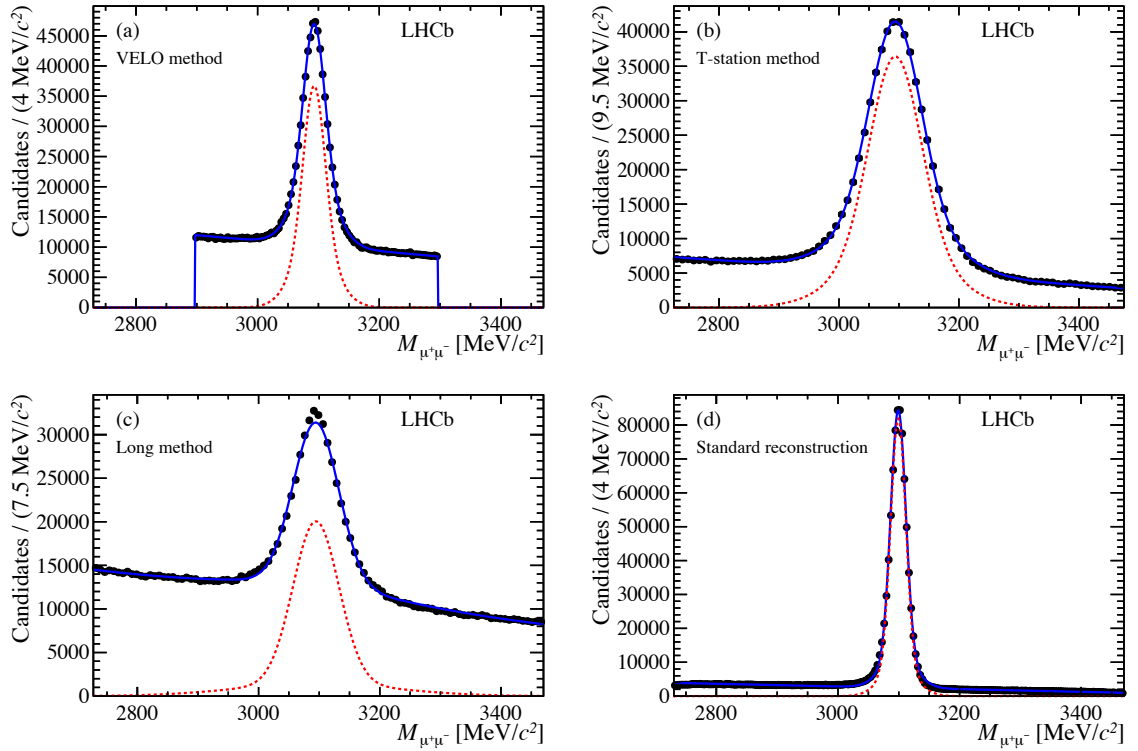


Figure 3.3: Fits to the J/ψ invariant mass used in the J/ψ tag-and-probe method, using the partially reconstructed probe track, in the (a) VELO method, (b) T-station method, and (c) long method. For comparison the J/ψ invariant mass fit where the probe is fully reconstructed is shown in the bottom right. The effect of the partial reconstruction on the momentum resolution is clearly visible by the wider peaks in (a), (b) and (c) compared to (d). Figure is taken from Ref. [92].

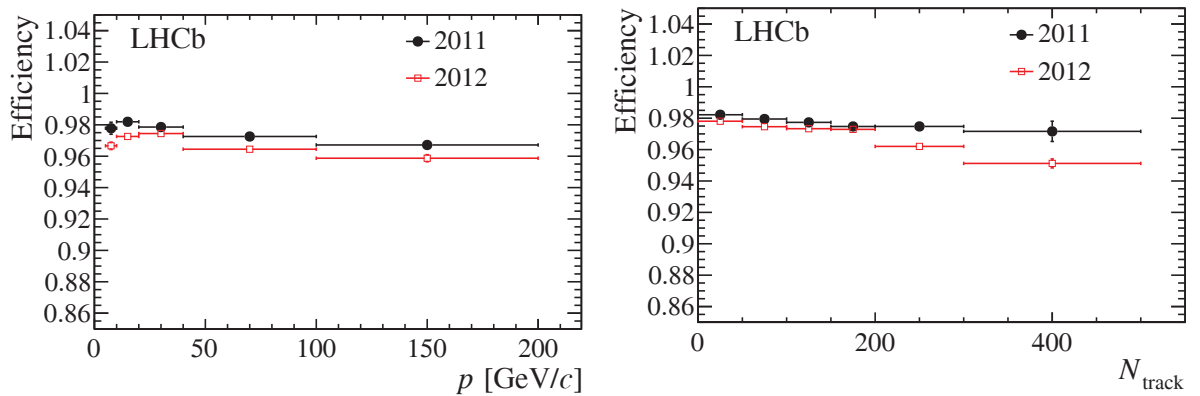


Figure 3.4: Tracking efficiency as determined with the J/ψ tag-and-probe VELO + T-station method, as a function of (left) momentum and (right) number of reconstructed tracks in the detector, split by data-taking year. Figures are taken from Ref. [54].

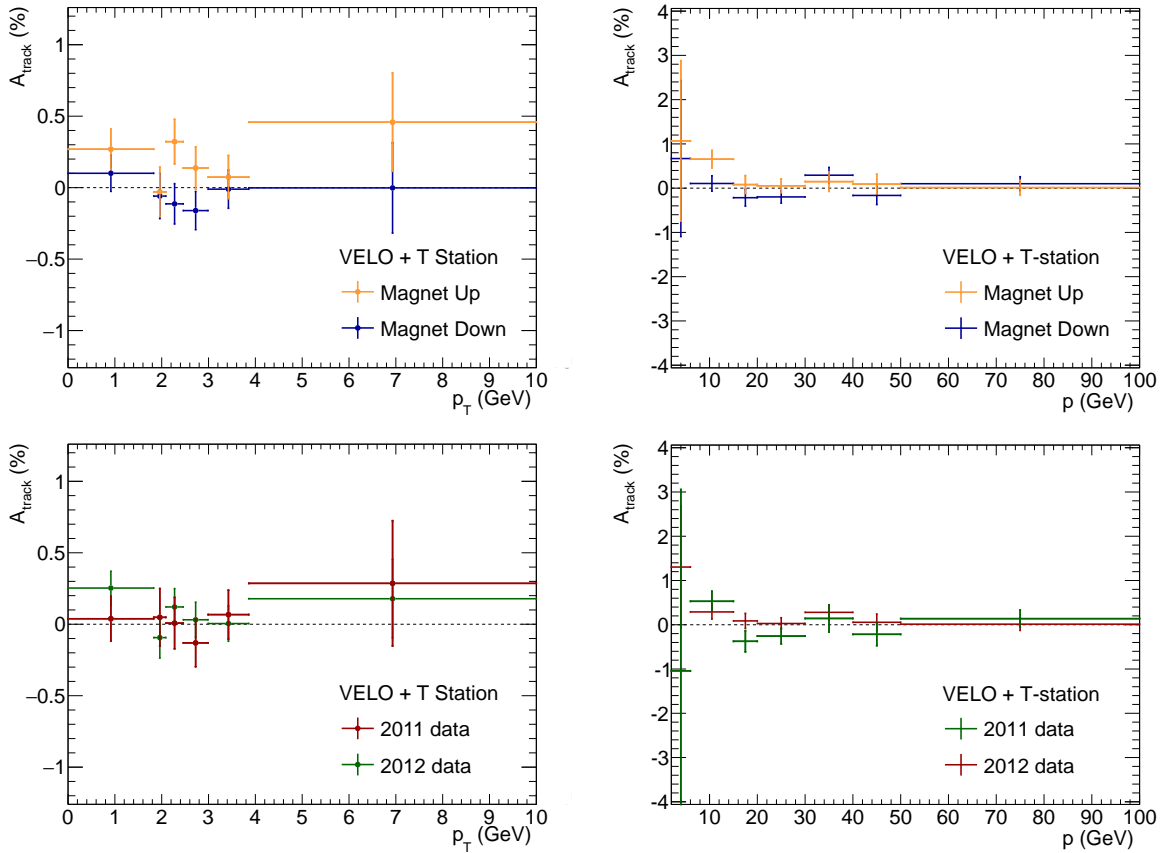


Figure 3.5: Tracking asymmetries determined using the J/ψ tag and probe method, split by (top) magnet polarity and (bottom) data-taking year, as a function of (left) p_T and (right) p .

where A_{track}^i is the tracking asymmetry as obtained in Eq. 3.1.2 in a specific bin, and N_{sig} is the total number of signal candidates. Both methods of determining the $\mu^+\pi^-$ asymmetry from the single-track asymmetry are found to be statistically compatible.

The resulting asymmetries for the a_{sl}^d and a_{sl}^s analyses are discussed in the appropriate sections in Chapters 4 and 5.

3.1.2 The D^* partial-and-full method

The second method uses partially reconstructed $D^{*+} \rightarrow D^0(\rightarrow K^-\pi^+\pi^-\pi^+)\pi^+$ decays to determine the charge asymmetry of reconstructing pions, and was also employed in an earlier measurement of a_{sl}^s by LHCb [48]. The method is described in detail in Ref. [93].

When requiring the D^{*+} to originate from the primary vertex (PV), there are enough kinematic constraints to form a peak in the invariant mass difference, $\Delta M = m(\pi^+D^0) - m(D^0)$, even when one of the pions from the D^0 decay is not reconstructed. The missing pion, called the “probe”, is any one of the π^+ or π^- from the D^0 decay. A maximum-likelihood fit to ΔM with a missing probe gives the total yield, while a fit to ΔM in the fully reconstructed case gives the “pass” yield. When fully reconstructed, the pion considered as “probe” is required to have $p > 2 \text{ GeV}/c$ and $p_T > 300 \text{ MeV}/c$ in order to

be counted as efficient. The efficiency is then the ratio of “pass” and “total”. The pion detection asymmetry is constructed by calculating the efficiency separately for a positively and negatively charged probe track, and using Eq. 3.1.2.

The background yield in the invariant mass fits is constrained by a fit to the same ΔM variable constructed using combinations of pions and kaons with a wrong charge sign to form the D^0 candidate, i.e. $D^0 \rightarrow K^+\pi^-\pi^+\pi^-$. These combinations are only formed by combinatorial background, plus a small contribution from D^0 mixing and doubly-Cabibbo-suppressed decays of a D^0 , which result in a real “wrong-sign” final state. This small contribution is taken into account by an additional component in the fit. An example of such a fit is shown in Fig. 3.6. In total, about 11 million partially reconstructed decays are found.

The charge asymmetry of the pion detection efficiency is measured as a function of momentum of the probe pion. In the case that the pion is not reconstructed, the momentum of the missing pion is inferred from a kinematic fit using the PV constraint, constraining the D^{*+} and D^0 mass to their world-average masses [94], and using the momenta of the other tracks. This decreases the momentum resolution, compared to that of a fully reconstructed pion. To determine the migration of the probe pions into neighbouring bins of momentum, a matrix is constructed by comparing the momentum of the pion in the fully reconstructed sample to the inferred momentum from the kinematic fit, assuming one pion is missing. Using this matrix, the effect of the worse pion momentum resolution is statistically unfolded, and the tracking asymmetry as function of p is obtained. Alternatively, the procedure can be done in bins of p_T . The pion charge asymmetry as function of p and p_T is shown in Fig. 3.7. The asymmetry split by magnet polarity goes up to about 0.5% and shows little features, although some evidence for a magnet-dependent

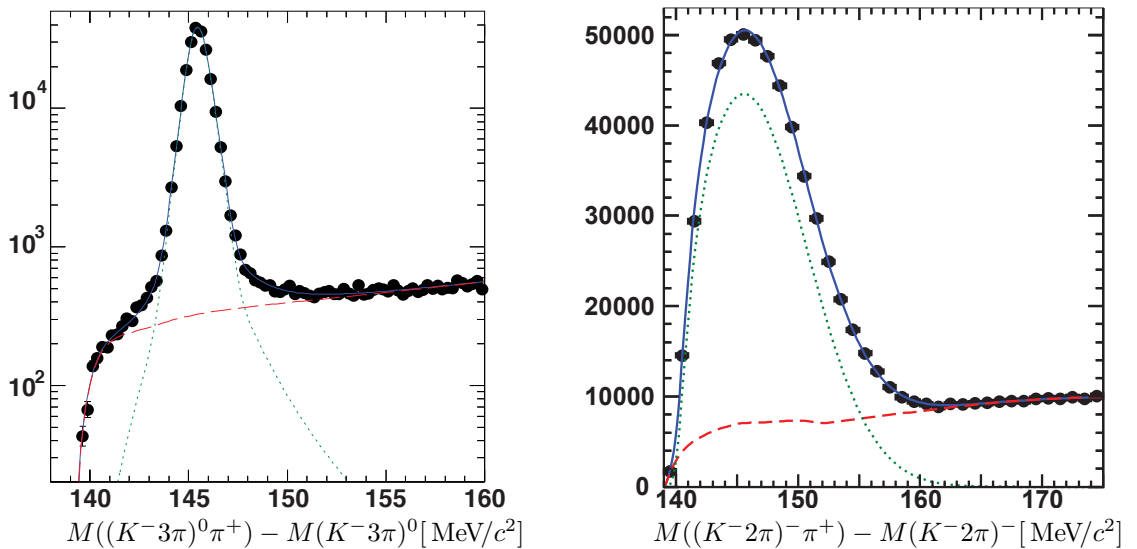


Figure 3.6: Example of fits to the (left) fully- and (right) partially-reconstructed D^{*+} decays in 2011 data, in the momentum range 15 – 20 GeV/ c . The reduced mass resolution of the partially reconstructed events still allows to determine the signal component.

cross-over point exists around $p \approx 40$ GeV/ c . In 2012 data, the pion asymmetry for momenta below 5 GeV/ c is somewhat larger than for 2011, which is partially attributed to the higher detector occupancy in 2012. The average of the magnet polarity split results is consistent with zero.

The $\mu^+\pi^-$ asymmetry is obtained from the charge-split efficiencies in the same way as the J/ψ method, see Eq. 3.1.3, only using a single-track pion asymmetry instead of that of a muon. The unfolding procedure requires the inversion of the migration matrix, and small variations might induce instabilities. Different matrix inversion regularization methods are used to assess a possible systematic bias.

Since a two-dimensional unfolding in p and p_T would become too complicated, only a one-dimensional binning in p is used when weighting the kinematic distributions of the probe pion. As a check, the weighting to signal data is repeated using the binning in p_T . The obtained values are compatible with the default method within their statistical error. The resulting $\mu^+\pi^-$ asymmetry in the a_{sl}^d and a_{sl}^s analyses will be described in the appropriate sections in Chapters 4 and 5.

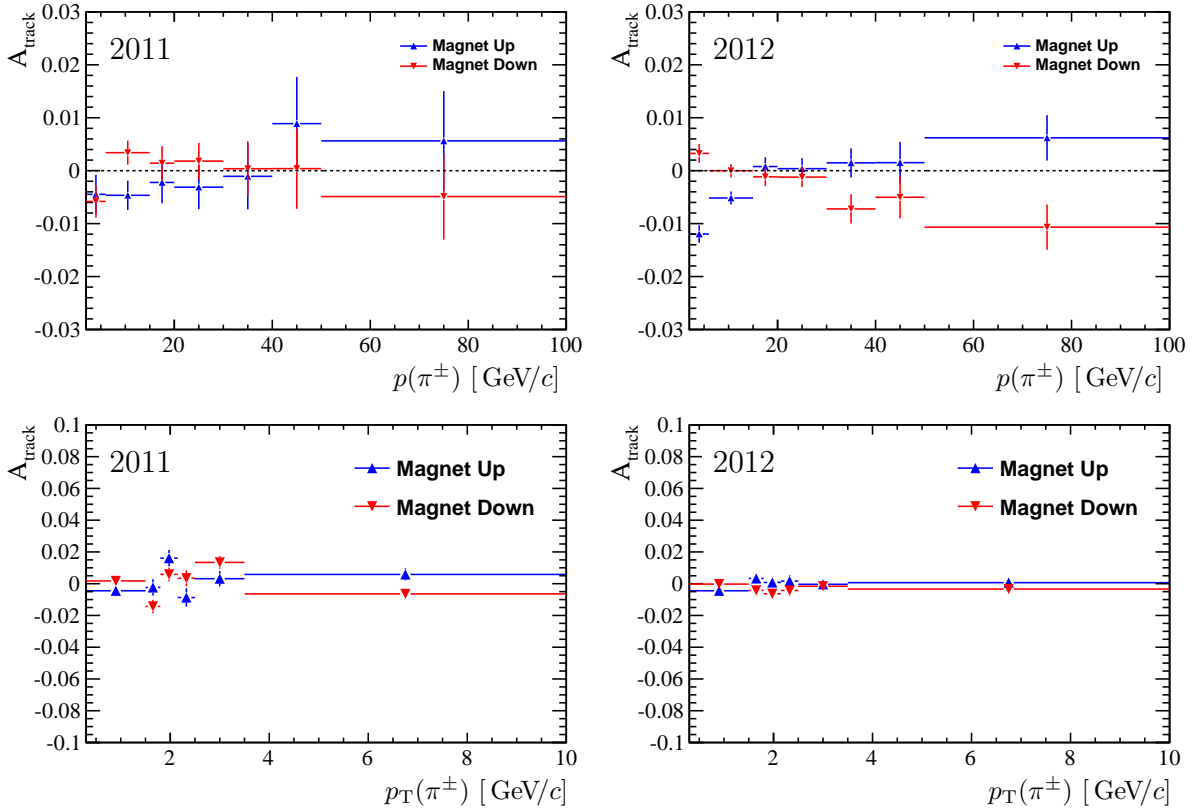


Figure 3.7: Tracking asymmetries as obtained with the D^* method in (left) 2011 data and (right) 2012 data, as a function of (top) p and (bottom) p_T .

3.1.3 Comparing the methods

The tracking asymmetries obtained with the J/ψ tag-and-probe method (Fig. 3.5) and D^{*+} partial-and-full method (Fig. 3.7) are similar, although some differences can be observed in the results split by magnet polarity. The J/ψ method requires at least part of the probe track to be reconstructed in a subdetector. This implies that the track must be in LHCb geometrical acceptance; the efficiency of which is thus not taken into account. When the particles originating from the PV have a symmetric angular spread, this does not affect the charge asymmetry. However, due to the non-zero beam-crossing angle an effect can be expected, as explained in Sec. 2. Especially due to the magnet polarity dependence of the horizontal beam-crossing angle in 2011, this effect can be different in size between magnet polarities. This might be responsible for the small difference between 2011 and 2012 data in Fig. 3.7, compared to the overlap in 2011 and 2012 data in Fig. 3.5. The effect that the acceptance has on the J/ψ tag-and-probe tracking asymmetry is determined with simulated events. These are weighed to match the angular spread observed in data, in order to take into account the effect of the beam-crossing angle. Depending on the kinematic distribution, the correction to the VELO + T station method is found to range from -0.05% to $+0.05\%$ with a statistical error of about 0.01% , but the correction is negligible in the magnet average.

On the other hand, the D^{*+} method correctly takes into account the acceptance asymmetry, but has limited precision for higher momenta. When a significant amount of momentum of the D^0 is carried by the missing pion, the mass resolution broadens and the uncertainty on the asymmetry increases. In addition, due to the one-dimensional unfolding any correlation between kinematic variables (e.g. p, η) is not taken into account in the procedure. This limits the sensitivity of the D^{*+} method. For these reasons a combination of both methods is made.

Pions are different than muons in the sense that they undergo nuclear interactions. The cross-section of π^+ and π^- on protons are slightly different, but the asymmetry in the cross-section with deuterium is almost negligible, as is shown in Fig. 2.9. Although various materials are used in the setup of the LHCb detector, one can reasonably assume that it is an isoscalar target, meaning that it consists of an equal amount of protons and neutrons. The most precise measurement of the cross sections with deuterium have been done in the 1970s [95–97]. The asymmetry in pion momenta ranging from 23 to 280 GeV/ c was found to be

$$1 - \frac{\sigma^{\pi^+d}}{\sigma^{\pi^-d}} = (0.14 \pm 0.09)\%. \quad (3.1.5)$$

As a rough estimate, about 20% of all charged pions undergo a hadronic interaction in the spectrometer, integrating the material from VELO up to RICH2. Assuming every hadronic interaction results in an inefficient reconstruction, this results in a charge asymmetry of $(0.03 \pm 0.02)\%$, but depends on the kinematic distribution of the sample. Using the kinematic distributions of the a_{SI}^d signal sample, the maximal effect is found to be 0.07%.

A more detailed study is done using simulation and a full material description of the LHCb detector. This also takes into account the non-isoscalar properties of the different

materials, and an asymmetry in the amount of material traversed by positive and negative pions depending on the magnet configuration. The total effect on the tracking asymmetry is found to range between -0.04% and $+0.03\%$ with a statistical error of about 0.01% , using the kinematic distributions of the a_{sl}^s signal sample. In the average over magnet polarities the effect is found to be negligible.

The combination of the J/ψ and D^{*+} methods is made by weighting the tracking asymmetries by their relative uncertainties, while correcting the J/ψ method for the acceptance and material effects. For large momenta of the probe track, the ΔM distribution in the D^* partial-and-full method becomes very broad and the extracted yield becomes more uncertain. Hence, the J/ψ method dominates in the combination of both methods at large momenta. The effect of the acceptance and material corrections on the combined $\mu^+\pi^-$ asymmetry depends on the signal kinematics, and will be discussed in Chapter 5, and a numerical comparison including material and acceptance corrections is made in Table 5.5.

3.2 The asymmetry of $K^+\pi^-$ pairs

The other charge-neutral pair in the final state of the a_{sl}^d analysis is the $K^+\pi^-$ pair. In contrast to pions, a sizeable difference in cross section with material is expected for K^+ and K^- mesons, as was discussed in Sec. 2.2.6. The charge asymmetry of the $K^+\pi^-$ pair is determined using prompt charm decays, as illustrated in Fig. 3.8. The idea is to obtain the charge asymmetry in $D^- \rightarrow K^+\pi^-\pi^-$ decays and subtract the asymmetry in $D^- \rightarrow K_s^0(\rightarrow \pi^+\pi^-)\pi^-$ decays. As is discussed below, the $K_s^0 \rightarrow \pi^+\pi^-$ decays have only a small detection asymmetry, such that in the subtraction the D^- production asymmetry and the π^- asymmetry cancel, and only the $K^+\pi^-$ asymmetry remains. The events are required to be triggered independently of the presence of the D^- daughter particles at the hardware level, to minimize a possible bias. Both decays can be triggered at the first software stage by the π^- originating directly from the D^- meson (two possibilities for the $K^+\pi^-\pi^-$ mode, only one for the $K_s^0\pi^-$ mode). This is called the “tag” pion. When the kinematic distributions of the D^- meson and triggered π^- meson are identical between the $K^+\pi^-\pi^-$ and $K_s^0\pi^-$ modes, any production and trigger asymmetry cancels in the difference of the observed asymmetry. This method has been used before in measurements of CP violation in D^0 mesons [98], and includes asymmetries due to acceptance, reconstruction, material and particle identification.

In the selection of the $D^- \rightarrow K^+\pi^-\pi^-$ and $D^- \rightarrow K_s^0\pi^-$ candidates, the tag pion has to satisfy $p_T > 1.6 \text{ GeV}/c$ as well as a pion PID requirement ($\text{DLL}_{K-\pi} < 0$). On the $K^+\pi^-$ pair used in the determination of the asymmetry, $p_T > 250 \text{ MeV}/c$ and $p > 2 \text{ GeV}/c$ is required on both tracks, as well as a kaon PID cut ($\text{DLL}_{K-\pi} > 7$) on the K^+ and pion PID cut ($\text{DLL}_{K-\pi} < 3$) on the π^- . The K_s^0 candidates are reconstructed from two long tracks, forcing the K_s^0 to have decayed inside the VELO. This happens in about a third of the K_s^0 decays. The detection asymmetry of K_s^0 candidates is small due to

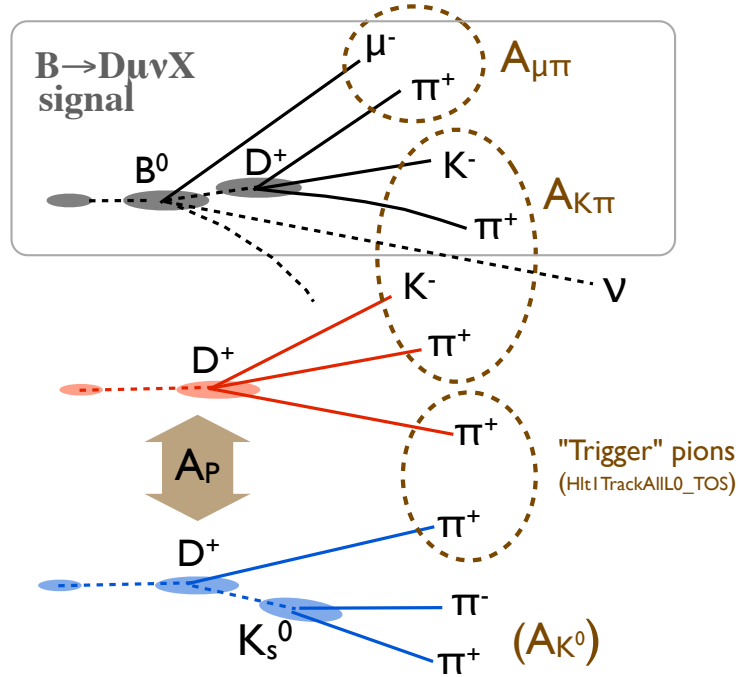


Figure 3.8: Illustration of the weighting procedure used in the determination of the $K^+\pi^-$ asymmetry (note the swapped signs in the illustration with respect to the text). The particles in the dashed circles from different decays are matched in their kinematic distributions. In addition, the kinematic distributions of the D^+ mesons are matched such that they have the same production asymmetry.

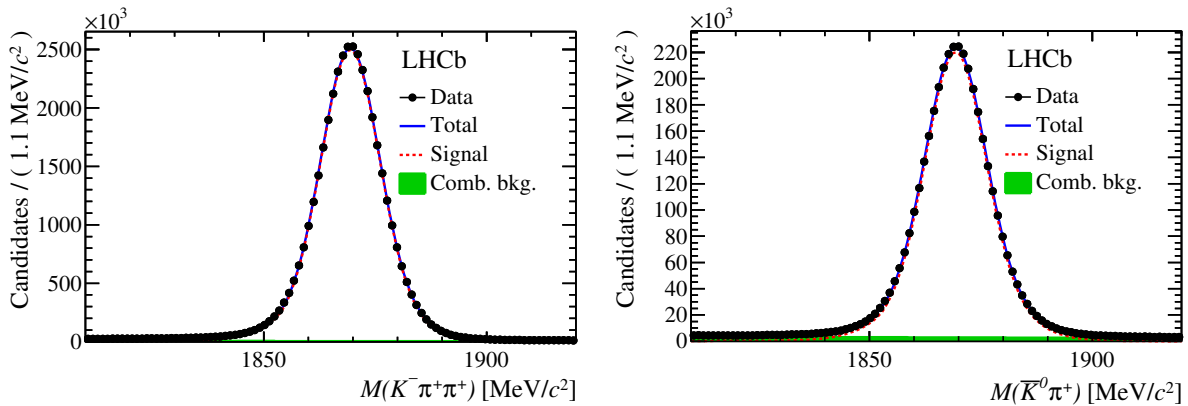
the charge-symmetric final state. However, the K_s^0 itself has a significant lifetime, such that material, CP -violating and mixing effects can create a charge asymmetry of the flavour eigenstates K^0 and \bar{K}^0 , as produced from the respective decays $D^- \rightarrow K^0\pi^-$ and $D^+ \rightarrow \bar{K}^0\pi^+$. The K_s^0 asymmetry due to all these effects has been extensively studied in Ref. [99] and is found to be $A_{K_s^0} = (-0.054 \pm 0.014)\%$. Finally, direct CP violation in these Cabibbo-favoured tree charm decays is expected to be small due to the large suppression of alternative diagrams, and is ignored. Taking the above into account, we are left with the $K^+\pi^-$ asymmetry

$$A_{K\pi} = \frac{\epsilon(K^+\pi^-) - \epsilon(K^-\pi^+)}{\epsilon(K^+\pi^-) + \epsilon(K^-\pi^+)} = A_{D^- \rightarrow K^+\pi^-\pi^-} - A_{D^- \rightarrow K_s^0\pi^-} - A_{K_s^0}, \quad (3.2.1)$$

where $A_{D^- \rightarrow K^+\pi^-\pi^-}$ and $A_{D^- \rightarrow K_s^0\pi^-}$ are determined from the charge asymmetry in the observed yields, while for $A_{K_s^0}$ the above value is used. The observed yields are obtained from a maximum-likelihood fit to the invariant mass, shown in Fig. 3.9. In total, about 50 million $D^- \rightarrow K^+\pi^-\pi^-$ decays and 3.5 million $D^- \rightarrow K_s^0\pi^-$ decays pass the selection. The measured asymmetries of the $D^- \rightarrow K^+\pi^-\pi^-$ and $D^- \rightarrow K_s^0\pi^-$ samples before

Table 3.2: The unweighed asymmetries of the $K^+\pi^-\pi^-$ and $K_S^0\pi^-$ data samples.

	$A_{K\pi\pi}[\%]$	$A_{K_S\pi}[\%]$
Total	1.82 ± 0.01	0.84 ± 0.06
2011, Up	2.36 ± 0.04	0.85 ± 0.18
2011, Down	1.52 ± 0.02	0.64 ± 0.15
2012, Up	2.10 ± 0.02	0.87 ± 0.09
2012, Down	1.52 ± 0.03	0.89 ± 0.09
2011 (linear av.)	1.94 ± 0.02	0.74 ± 0.12
2012 (linear av.)	1.81 ± 0.02	0.88 ± 0.07
Weighted av.	1.86 ± 0.01	0.85 ± 0.06

Figure 3.9: Fits to the invariant mass of the (left) $D^- \rightarrow K^+\pi^-\pi^-$ and (right) $D^- \rightarrow K_S^0\pi^-$ candidates, used in the determination of the $K^+\pi^-$ asymmetry. Figures are taken from Ref. [98].

any weighting procedure are shown in Tab. 3.2. A significant difference is observed in the asymmetries between the two magnet polarities. Part of this is explained by the magnet-dependent PID asymmetry introduced by the selection on these samples, which is determined with the method described in Sec. 3.3 and contributes about 0.1%. The rest is attributed mostly to the kaon material interaction asymmetry, but also includes effects from tracking, acceptance and amount of material traversed.

There are three weighting steps involved in the determination of the $K^+\pi^-$ asymmetry, illustrated by Fig. 3.8. The distributions that are matched to each other are described below. In addition, alternative variables are used in the weighting in order to determine the size of a potential bias due to the choice of variables.

First, the kinematic distributions of the K^+ and π^- (that is not used to trigger the event) of the $D^- \rightarrow K^+\pi^-\pi^-$ sample are matched to the kaon and pion in the signal sample. This is done by applying weights to the events in the $D^- \rightarrow K^+\pi^-\pi^-$ sample. Three variables are considered simultaneously: the p_T and pseudorapidity η distributions of the pion, and the p_T distribution of the kaon. Alternatively, the p_T and η distributions of the kaon, and p_T distribution of the pion are used.

The second weighting step consists of matching the ϕ distribution of the kaon in the $D^- \rightarrow K^+\pi^-\pi^-$ sample to that of the kaon in the signal sample. This weighting is found to not affect the distributions in the previous step. Alternatively, this step is left out.

Finally, weights are applied to the $D^- \rightarrow K_S^0\pi^-$ sample in order to match the $D^- \rightarrow K^+\pi^-\pi^-$ sample, in the distributions of p_T and η of the D^- , and the p_T of the trigger pion. This cancels the D^- production asymmetry and the π^- detection asymmetry in the $D^- \rightarrow K^+\pi^-\pi^-$ sample. Alternatively, the three variables whose distributions are matched are the p_T of the D^- , and the p_T and η of the π^- . Another variation of the weighting is done by using the ϕ angle of the D^- meson instead of η .

When using only the last weighting step — matching the $D^- \rightarrow K_S^0\pi^-$ sample to the $D^- \rightarrow K^+\pi^-\pi^-$ sample — and subtracting the K_S^0 asymmetry, the $K^+\pi^-$ asymmetry can be shown as a function of momentum of the kaon. This is done in Fig.3.10. A clear decrease in the absolute asymmetry as a function of momentum is observed, as is expected from the decreasing kaon interaction asymmetry as was shown in Fig. 2.9.

Using the alternative variables in the weighting steps described above, the potential bias due to the choice of these variables is determined. The deviation from the resulting $K^+\pi^-$ charge asymmetry using these alternative schemes, with respect to the result using the nominal variables, are assigned as systematic errors. The amount of material encountered in the VELO by tracks originating from a D^- meson that is promptly produced in the PV, might be somewhat different than that for tracks originating from $B^0 \rightarrow D^-$ decays. This effect is studied in simulation and found to be negligible. The resulting values for the asymmetries depend on the kinematic distributions of the $K^+\pi^-$ pair in the a_{sl}^d signal

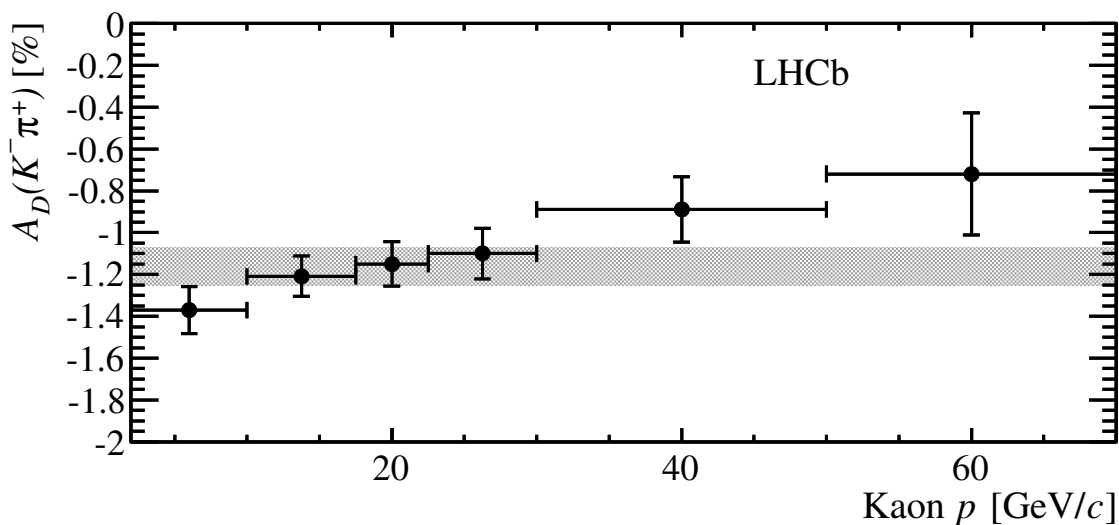


Figure 3.10: The $K^+\pi^-$ charge asymmetry as function of momentum of the kaon, averaged over both magnet polarities. Note the swapped signs in the figure with respect to the text. The shaded area is the average of the individual bins. The figure is taken from Ref. [98].

sample, and will be discussed in Chapter 4. In the a_{sl}^s analysis, the final state involves a K^+K^- pair instead. The next section describes how to use the above method to determine the K^+K^- asymmetry.

3.2.1 The asymmetry of K^+K^- pairs

If the kinematic distributions of a K^+K^- pair nearly overlap, such as in $D_s^- \rightarrow \phi\pi^-$ decays where the ϕ decays as $\phi \rightarrow K^+K^-$, the K^+K^- asymmetry is expected to be very small. For other decays to a $K^+K^-\pi^-$ final state, i.e. $D_s^- \rightarrow K^{*0}K^-$, where $K^{*0} \rightarrow K^+\pi^-$, and non-resonant decays, this is not necessarily the case.

In order to determine the K^+K^- asymmetry, the first weighting step in the $K^+\pi^-$ asymmetry method — which matches the distributions of the $K^+\pi^-$ pair in the $D^- \rightarrow K^+\pi^-\pi^-$ decay to the signal distributions — is replaced by only weighting the kaon from the $D^- \rightarrow K^+\pi^-\pi^-$ sample to the kaon in the signal with the same sign (SS) as the D_s^+ meson. The distributions that are required to match are the p_T and η of the kaon. This procedure is then repeated for the opposite-sign (OS) kaon. The second step — where the azimuthal angles ϕ of the kaons are matched — is skipped. Finally, the third step that matches the kinematic distributions of the D^- mesons in the $D^- \rightarrow K^+\pi^-\pi^-$ and $D^- \rightarrow K_s^0\pi^-$, is identical. The K^+K^- asymmetry is calculated as

$$A_{KK} = A_{K\pi}^{\text{OS}} - A_{K\pi}^{\text{SS}}.$$

In the determination of the statistical error, the large correlation (93% – 99%) between $A_{K_{OS}}$ and $A_{K_{SS}}$ is taken into account. Any residual pion asymmetry from the unweighed π^- in the $D^- \rightarrow K^+\pi^-\pi^-$ sample is likely to be small in the magnet-average result. As a check, an additional weighting step is done for the pion by matching the distributions in the samples used for $A_{K_{OS}}$ and $A_{K_{SS}}$ to those of the pion in the a_{sl}^s signal sample. The effect is found to be around $\pm 0.03\%$ for data taken with a given magnet polarity, and is included as a systematic error to the magnet separate results. It is found to be negligible in the magnet average. Due to the large overlap between the $A_{K_{OS}}$ and $A_{K_{SS}}$ samples, the effect of $A_{K_s^0}$ on the K^+K^- asymmetry is estimated to be smaller than 10^{-5} and neglected. The K^+K^- asymmetry depends on the signal kinematic distributions, and will be further discussed in Chapter 5.

3.3 Hadron identification asymmetry

In the stripping and offline selection, particle identification (PID) criteria are placed on the D^- (D_s^-) daughter particles. The efficiency of these selection criteria depend on the performance of RICH1 and RICH2, which can vary depending on the position and momentum of the particles as discussed in Chapter 2. As a consequence, a charge asymmetry could be created by the PID requirements.

The possible asymmetries introduced by the PID criteria in the a_{sl}^d and a_{sl}^s signal selections are measured using a large sample of $D^0 \rightarrow K^-\pi^+$ decays that originate from

a $D^{*-} \rightarrow D^0\pi^-$ decay. The pions and kaons from the D^0 decay are required to have $p_T > 1.2 \text{ GeV}/c$ and $p > 2 \text{ GeV}/c$. The charge of the pion in the D^{*-} decay identifies the charges of the kaon and pion from the D^0 decay, without requiring input from PID-sensitive variables. This allows to determine the efficiency of a cut on PID variables on the kaon or pion in an unbiased way. The total yield can be obtained by performing a maximum-likelihood fit to the invariant mass difference of the D^{*-} and D^0 candidates. This is shown in Fig. 3.11 (left).

This fit is used to calculate signal weights for the events using the *sPlot* method [100]. This method allows to subtract combinatorial background in kinematic distributions of signal candidates. As the efficiencies depend on the kinematic properties of the particles, the sample is split up into bins in n kinematic variables. For each bin, the efficiency is determined as the sum of signal weights for events where the particle passes the PID criterium, over the total signal weights in this bin. The efficiencies obtained with this method are discussed in Ref. [73], and shown in Fig. 3.11 for two typical PID criteria. The efficiency of correct identification using standard PID criteria is about 95% for momenta between 10 and 40 GeV/c , but drops quickly above or below this range. For tighter PID requirements the drop is significantly faster. Hence, a larger PID asymmetry is expected for particles with very high or low momenta.

In order to calculate the PID efficiency of signal particles, the n -dimensional histogram is used as a look-up table, and an iteration over all signal events is made to determine the total PID efficiency for that signal particle. The charge asymmetries of the hadron PID efficiencies are defined as

$$A_{\text{PID}} = \frac{\epsilon_{\text{PID}}(D_{(s)}^+) - \epsilon_{\text{PID}}(D_{(s)}^-)}{\epsilon_{\text{PID}}(D_{(s)}^+) + \epsilon_{\text{PID}}(D_{(s)}^-)}, \quad (3.3.1)$$

and are shown in Fig. 3.12 and Fig. 3.13 as a function of momentum for PID criteria that are used in the a_{sl}^s analysis. The variation of the asymmetry displays opposite behaviour for

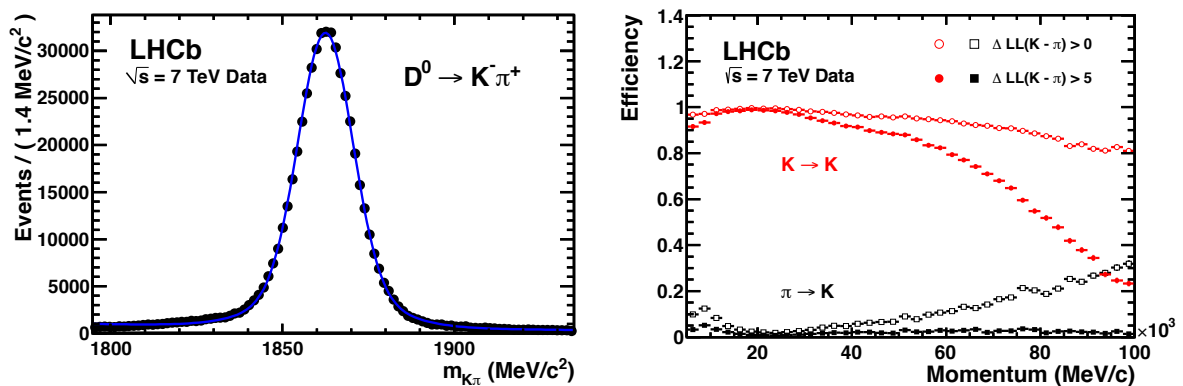


Figure 3.11: (left) A fit to the $D^0 \rightarrow K^- \pi^+$ invariant mass, used to determine signal weights and PID efficiencies. (right) Kaon (mis)identification efficiency for two typical PID criteria. Figures are taken from Ref. [73].

the two magnet polarities around $p = 40 \text{ GeV}/c$, and diverges rapidly above $p = 60 \text{ GeV}/c$. This is the momentum range in which most sensitivity in the PID variables originates from RICH2, which is positioned after the magnet. This effect increases with stronger PID requirements. The amount of signal candidates in the a_{sl}^d and a_{sl}^s analyses with momenta in this highly-asymmetric range is small. In addition, the average asymmetry of both magnet polarities remains close to zero.

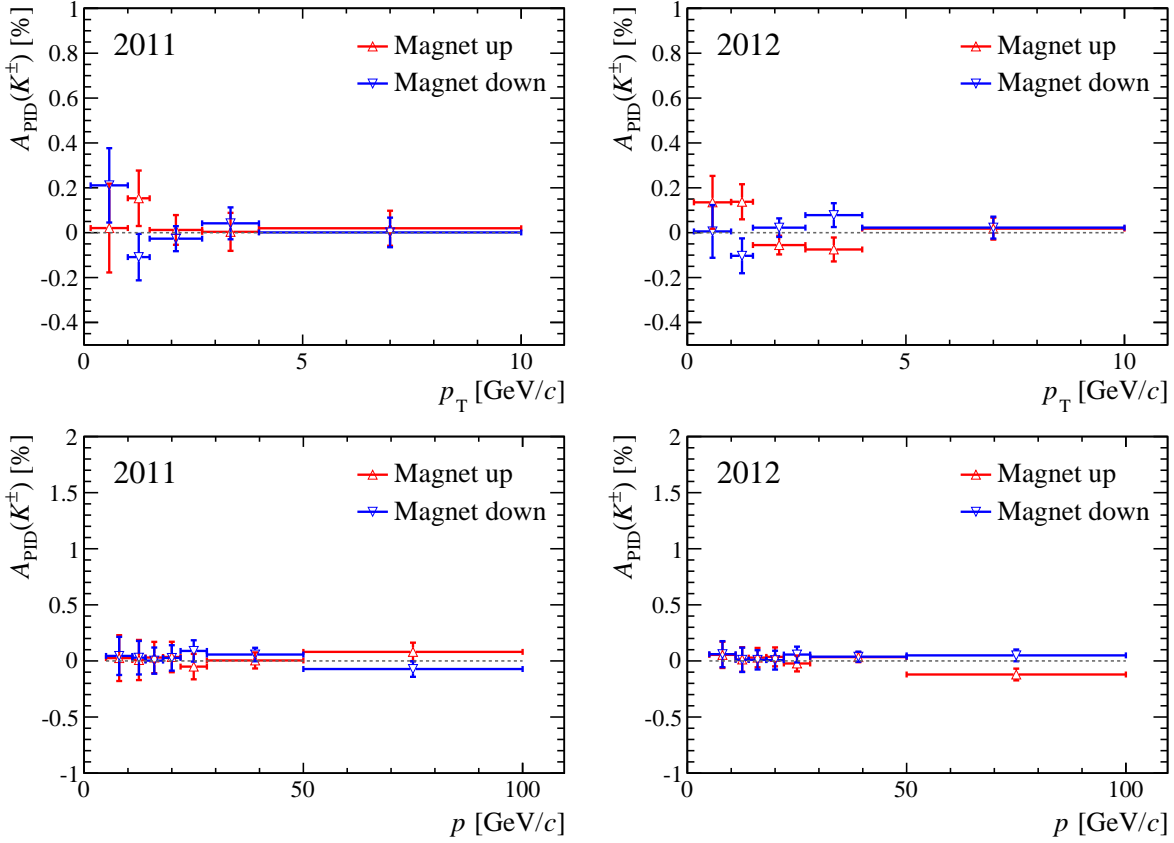


Figure 3.12: Kaon PID asymmetry as function of (top) momentum and (bottom) transverse momentum in (left) 2011 and (right) 2012 for PID criteria used in the a_{sl}^s analysis (see Sec. 5), with the loose PID selection that is used for the $D_s^- \rightarrow \phi\pi^-$ resonant decay region ($\text{DLL}_{K-\pi} > -5$ and $\text{ProbNNK} > 0.1$).

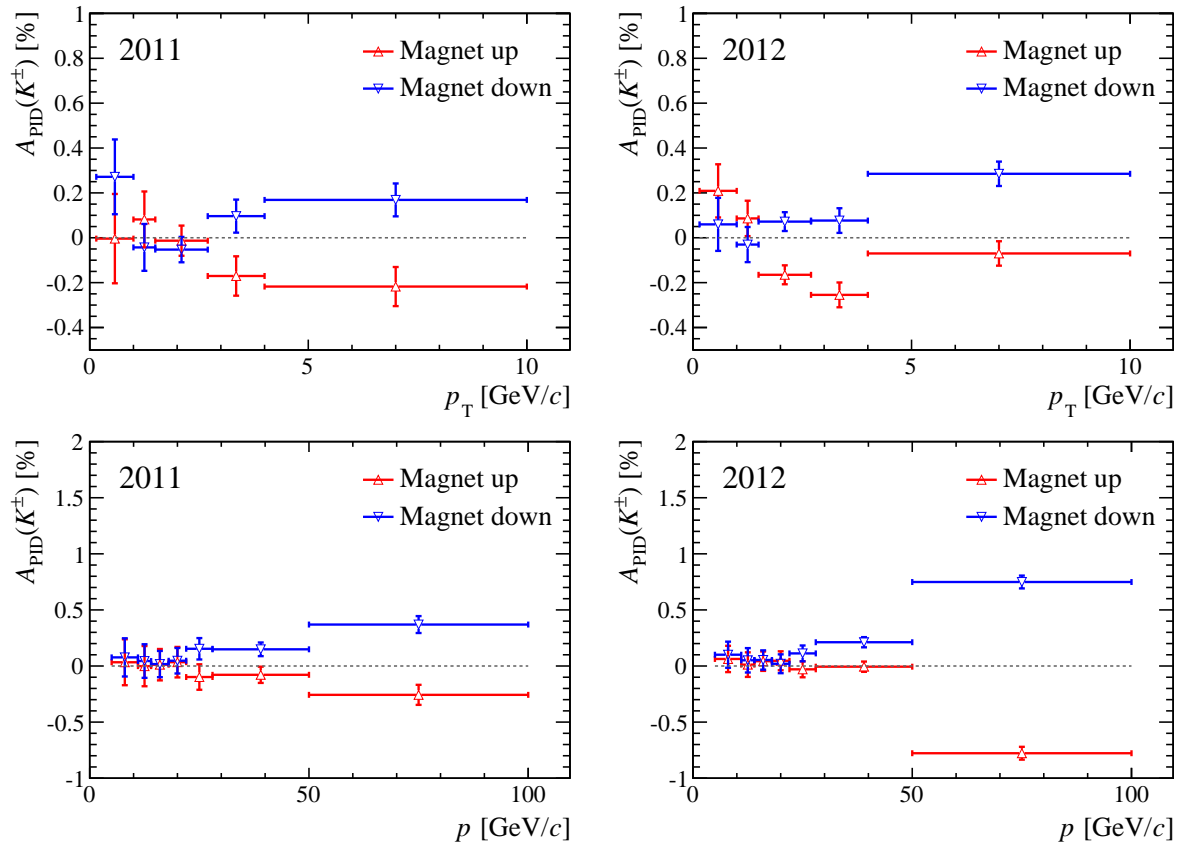


Figure 3.13: Kaon PID asymmetry as function of (top) momentum and (bottom) transverse momentum in (left) 2011 and (right) 2012 for PID criteria used in the a_{s1}^s analysis (see Sec. 5), with the more stringent selection that is used for the decay region outside of the $D_s^- \rightarrow \phi\pi^+$ resonance ($\text{DLL}_{K-\pi} > 4$ and $\text{ProbNNK} > 0.15$).

The PID efficiency of a signal candidate is determined by multiplying the PID efficiencies for the individual final-state particles (e.g. K^+ , π^+ , π^-). Since the same samples are probed when determining the individual efficiencies, the statistical error of the combination is correlated. Therefore a toy method is used to determine the overall statistical uncertainty. To do this, the efficiencies in each bin of the n -dimensional histograms are independently varied, by drawing a random value from a Gaussian distribution with a width equal to the error on the efficiency. The new efficiency histograms are used to redetermine the total PID asymmetry. This procedure is repeated 100 times, and the standard deviation of these values is taken as the statistical error.

A possible bias due to the choice of binning is determined by varying the binning, as well as changing the binning variables to both 2-dimensional and 3-dimensional schemes in p_T , p , η and ϕ . The maximal difference with respect to the nominal result is taken as a systematic error. In addition, a possible bias might originate from the usage of the *sPlot* method, and is investigated as follows.

As described above, the efficiencies are calculated from the ratio of signal weights, which are determined with the *sPlot* method. These weights depend on the signal shape

used in the fit to the invariant mass distributions. However, the invariant mass shape is affected by the kinematic properties of the particles. For the result on the asymmetry, this effect is expected to be small since the kinematic distributions of the charge-conjugate final state are almost identical. Nonetheless, in order to test the validity of the *sPlot* method an alternative method is used. Here the data is first divided into kinematic bins, after which a fit is performed in each bin to obtain the “pass” and “fail” yields and efficiencies. The resulting differences between both methods varies between -0.02% and $+0.02\%$ depending on the kinematic bin, which is included in the systematic uncertainties.

3.4 Trigger and muon PID asymmetry

The semileptonic final states used in the a_{sl}^d and a_{sl}^s analyses are mainly triggered by the muon. The efficiency of triggering on the signal muon (TOS) is determined with a J/ψ tag-and-probe method, similar to the method used for the tracking asymmetry, but in this case both muons are fully reconstructed as long tracks offline and the samples have a negligible overlap. The event is triggered on one muon which acts as the “tag”, while the trigger information on the “probe” muon is used to determine the trigger and muon PID efficiency. Candidate J/ψ decays are obtained from loosely selected $B \rightarrow J/\psi X$ decays in order to suppress backgrounds directly originating from the PV, and the event is triggered on the tag muon by the muon system (L0Muon, see Chapter. 2.4). Both muons are required to have $p > 6 \text{ GeV}/c$ and $p_{\text{T}} > 1.2 \text{ GeV}/c$ and minimum $\chi_{\text{IP}}^2 > 4$. They should form a J/ψ vertex with $\chi^2/\text{ndf} < 4$ which should be significantly detached from the PV, and the resulting momentum vector should have a $p_{\text{T}} > 500 \text{ MeV}/c$ and point towards the PV within an angle $\cos(\phi) > 0.99$. Another track is loosely combined with this vertex to form a B candidate.

This selects about 30 million events in total. The requirements that are probed by this method are the muon hardware trigger, the first software-stage trigger (H1t1TrackMuon) and the muon identification requirement ($\text{DLL}_{\mu-\pi} > 0$), given that the probe track is reconstructed as a long track. An event is categorized as “pass” if the probe track meets all the requirements, and as “fail” if it does not. The muon trigger- and PID asymmetry is defined as

$$A_{\mu} = \frac{\epsilon_{\mu}^{+} - \epsilon_{\mu}^{-}}{\epsilon_{\mu}^{+} + \epsilon_{\mu}^{-}}, \quad (3.4.1)$$

and from now on referred to as the muon asymmetry.

The efficiencies are determined from the ratio of pass to total yields, obtained from a binned maximum-likelihood fit to the J/ψ invariant mass, shown in Fig. 3.14. The shape used for the fit is the sum of a Crystal Ball (CB) function and a Gaussian function. The CB is a Gaussian function with a power-law tail on the left side, with a continuous and smooth transition. It is defined as

$$f_{\text{CB}}(x, \alpha, n, \mu, \sigma) = N \cdot \begin{cases} e^{-\frac{(x-\mu)^2}{2\sigma^2}}, & \text{for } \frac{x-\mu}{\sigma} > \alpha \\ A \cdot (B - \frac{x-\mu}{\sigma})^{-n}, & \text{for } \frac{x-\mu}{\sigma} \leq \alpha, \end{cases} \quad (3.4.2)$$

where $A = \left(\frac{n}{|\alpha|}\right)^n \cdot e^{-\frac{|\alpha|^2}{2}}$ and $B = \frac{n}{\alpha} - |\alpha|$. Here N is the normalization factor, x is the invariant mass, μ is the mean, σ the Gaussian width, α is the point where the shape changes from Gaussian to a power-law tail in units of σ , and n is the decay strength of the power-law tail. The tail on the left side is required to describe radiative energy losses of the tracks, while the two Gaussian functions allow to describe two different contributions to the momentum resolution, typically from tracks traversing either through the IT or the OT. The Gaussian and CB share the same parameter for the mean. The CB tail parameters α and n are fixed from a fit to simulated events without background, but are varied within their error to determine the systematic bias of this choice on the muon asymmetry. The shape used for the background is a first-order Chebychev polynomial, the parameters of which are found to be less correlated with the CB tail parameters than an exponential background shape. The fit is performed simultaneously for positive and negative “pass” candidates, sharing all free parameters but the normalization. The same is done for the “fail” candidates. The results of the fits for 2012 data are shown in Fig. 3.14.

The muon asymmetry is reconstructed from the separate charge efficiencies, and is shown in Fig. 3.15. From the top row it is immediately clear that the muon asymmetry in 2011 for each magnet polarity is large, and diverges at low p_T . This is due to a misalignment in the L0 muon trigger, as discussed in Sec. 2.4. Due to the misalignment, the p_T of the muon calculated in the hardware trigger (LOMuon) is underestimated for one charge. This decreases the efficiency of the trigger for that charge, and induces a charge asymmetry for low transverse momenta. Demanding a higher minimum p_T would solve this problem, but since the p_T resolution in the hardware trigger is so much worse than that of the offline reconstructed p_T of the track, this effect is smeared out over a large range of offline p_T values. Instead, the full 2011 data is used to calibrate the positions of the pads in the muon stations, after which the hardware trigger is emulated using the offline-reconstructed track parameters, using the correct positions of the pads. A look-up table is created with the correct values for the hardware-trigger p_T . This look-up table is

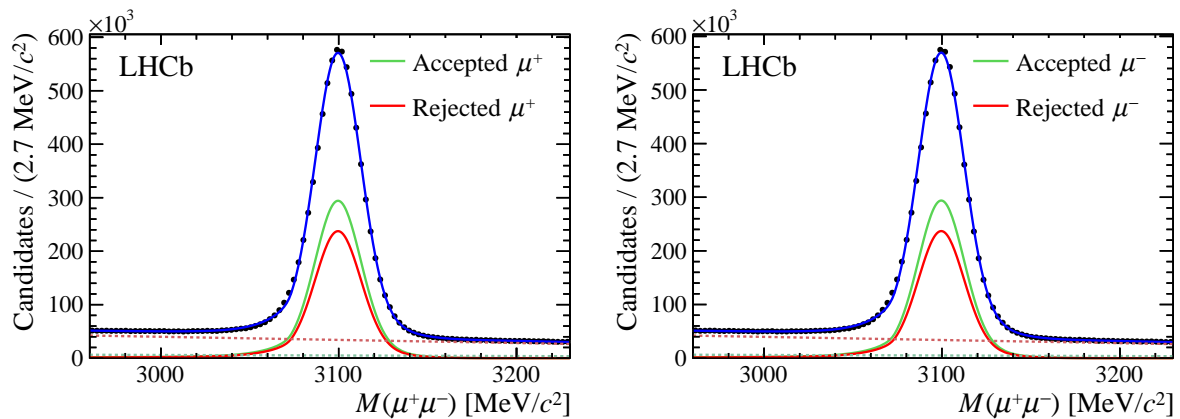


Figure 3.14: Fits to the J/ψ invariant mass in 2012 data, used to measure the muon asymmetry. The “pass” and “fail” contributions are projected, split up for a (left) positive charge and (right) negative charge of the probe track.

applied to the data, and a slightly higher cut of $p_{T, \text{LOMuon}} > 1640 \text{ MeV}/c$ is made to obtain similar efficiencies for both charges. This is shown in the second row of Fig. 3.15.

In 2012 data the LOMuon p_T is calibrated from the start, using the first few run numbers, which are excluded from the data in the a_{sl}^d and a_{sl}^s analyses. Hence, no look-up table is constructed offline. The resulting charge asymmetry is shown in the bottom row of Fig. 3.15. The effect as function of p_T and p is larger than the corrected 2011 data, which is explained by the difference in the procedure and the fact that not the whole 2012 data was used for a correction a-posteriori. Around $p = 40 \text{ GeV}/c$ the sign of the asymmetry for each magnet polarity flips. This roughly corresponds to the momentum at which most of the tracks that are either in the left- or right side of the detector before the magnet, stay on that side after the magnet. The potential sources of asymmetry described in

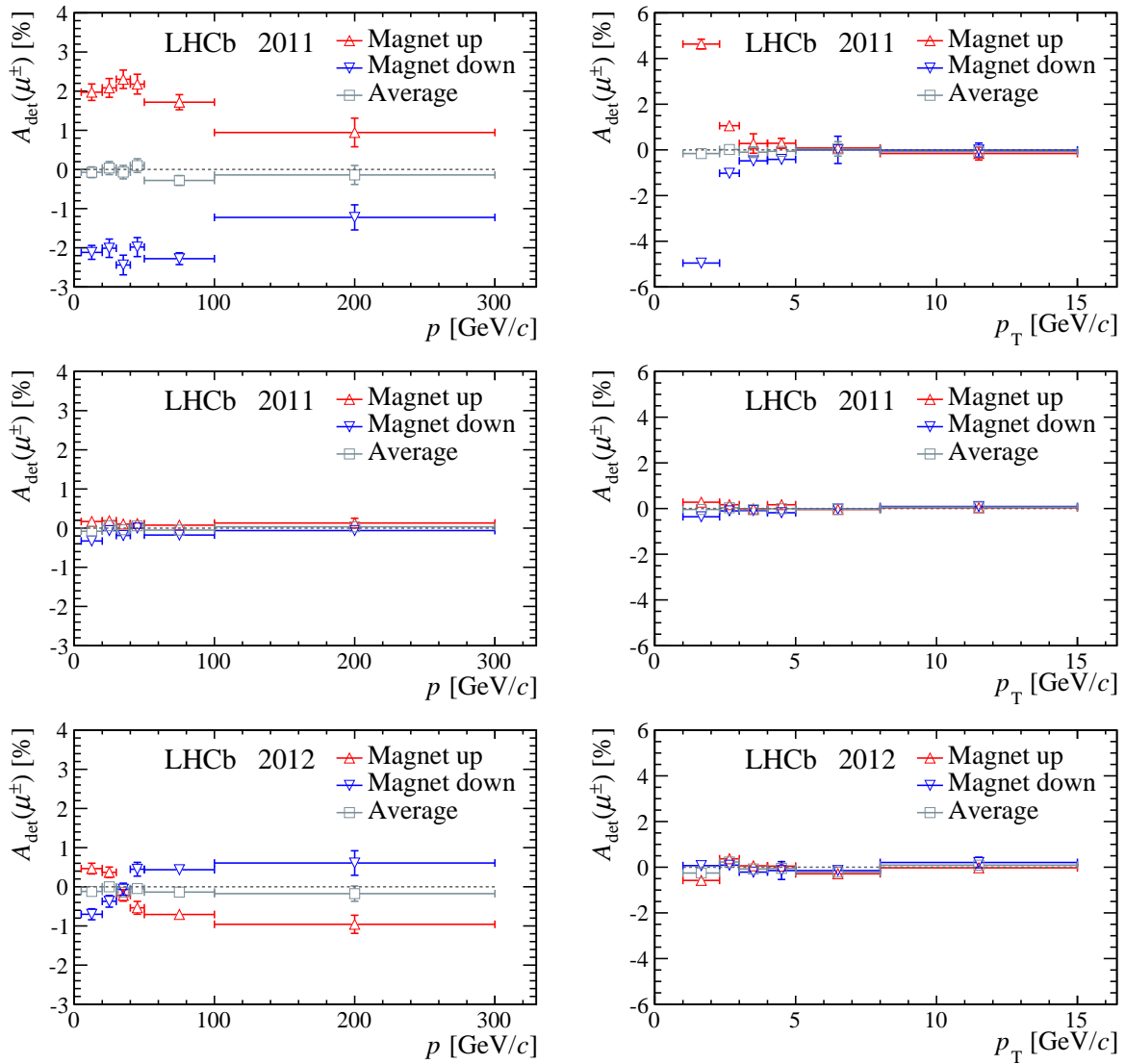


Figure 3.15: The muon asymmetry in bins of momentum (left) and p_T (right), for 2011 data without (top) and with (middle) L0 look-up table applied, and (bottom) calibrated 2012 data.

Sec. 2.3.3 are expected to be the same size but of opposite sign for each magnet polarity. This is observed when averaging over magnet polarities, which is consistent with zero in all situations.

The kinematic distributions of the probe muon in the $B \rightarrow J/\psi X$ sample are matched to those of the muon in the signal in the a_{sl}^d and a_{sl}^s analyses. This is done by weighting in bins of kinematic variables. The resulting asymmetries will be discussed in Chapters 4 and 5. In the a_{sl}^d and a_{sl}^s signal samples, there is an additional requirement at the second software-trigger level for the event to be triggered on the muon topological lines, described in Chapter 2. The possible asymmetry in this requirement has been determined using the overlap in triggered events of the two, three- and four-body lines, and found to be zero with a precision of 0.020%. This is added as a systematic uncertainty on the results.

In the a_{sl}^s analysis, the Hlt1 trigger requirement consists of two lines, in order to increase the signal efficiency. How the asymmetry of the combination is determined is discussed in the next section.

3.4.1 Asymmetry of two trigger lines

In the measurement of a_{sl}^s a combination of the software-level muon trigger (`Hlt1TrackMuon`) on the muon, and the general software-level single-track trigger (`Hlt1TrackAllL0`) on all the four final-state tracks, is used. Therefore, the total muon and trigger asymmetry is split up into two steps. First, the muon asymmetry as described in the previous section is determined, for the hardware-level trigger and muon PID requirement only. In addition, the efficiency of the requirement for the muon to have triggered on either of the first software-level trigger lines, is determined with respect to the hardware trigger and muon PID requirement. The asymmetry is shown in Fig. 3.16 for 2012 data. From the figure it is clear that the software trigger requirement contributes little to the total muon asymmetry.

The efficiency of the general software-level trigger line on the other three tracks (`Hlt1TrackAllL0`) is determined using a sample of prompt $D_s^- \rightarrow \phi(\rightarrow K^+ K^-)\pi^-$ decays. This sample is required to be triggered independently of the signal (i.e., on the rest of the event) at the hardware level, to minimize a possible bias due to the hardware trigger. The final-state hadrons are required to have $p_T > 500 \text{ MeV}/c$ and $p > 5 \text{ GeV}/c$. Two out of three final-state tracks function as “tag”, while the third track functions as the “probe”. Fits to the D_s^- invariant mass result in the single-track efficiencies for this software trigger line for kaons and pions, and the charge asymmetries for kaons and pions are shown in Fig. 3.17.

Both software trigger lines share similarities in the selection requirements, as discussed in Sec. 2.4. Therefore a large fraction of signal events is triggered on both lines — up to 80% — especially since the muon may trigger both lines. In order to calculate the combined efficiency of triggering on one or more final-state tracks, the software trigger efficiencies of muons, pions and kaons of both charges are split up in bins of kinematic variables. These histograms are then used as a look-up table for the signal tracks in the a_{sl}^s analysis. In each event a combination of all track efficiencies is made, while taking the

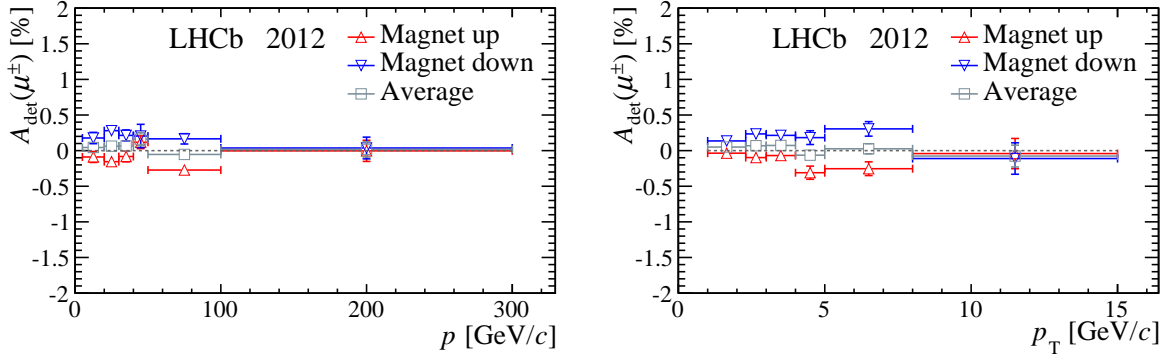


Figure 3.16: Charge asymmetry of either the software-level muon trigger or general single-track trigger on the muon, with respect to the muon hardware trigger and PID criterium, in 2012 data, as a function of (left) p and (right) p_T . The asymmetries are determined with the J/ψ tag-and-probe method.

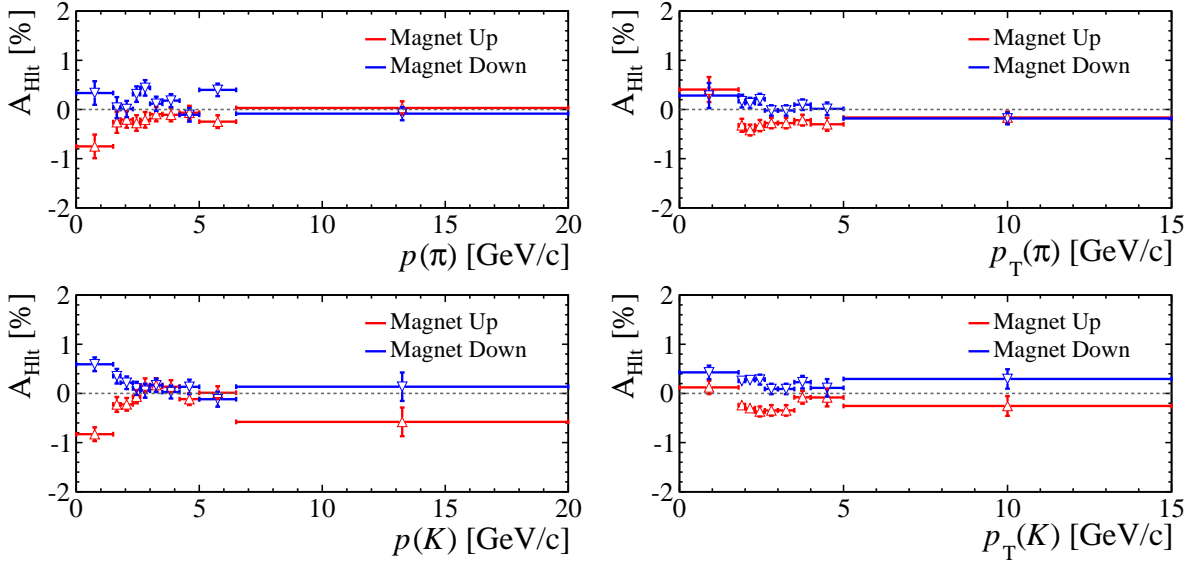


Figure 3.17: Charge asymmetry of the general single-track software trigger for hadrons in 2012 data, as a function of (left) p and (right) p_T . Displayed are (top) pion probe tracks and (bottom) kaon probe tracks as determined with the D_s^- sample.

possibility of being triggered by multiple tracks into account. A sum over all events is done as follows,

$$\begin{aligned}
 \varepsilon_{B_s^0} = \sum_i^{N_{\text{evts}}} & \left(\varepsilon_{K^+}^i + \varepsilon_{K^-}^i + \varepsilon_{\pi^-}^i + \varepsilon_{\mu^+}^i - \varepsilon_{K^+}^i \varepsilon_{K^-}^i - \varepsilon_{K^+}^i \varepsilon_{\pi^-}^i - \varepsilon_{K^+}^i \varepsilon_{\mu^+}^i \right. \\
 & - \varepsilon_{K^-}^i \varepsilon_{\pi^-}^i - \varepsilon_{K^-}^i \varepsilon_{\mu^+}^i - \varepsilon_{\pi^-}^i \varepsilon_{\mu^+}^i + \varepsilon_{K^+}^i \varepsilon_{K^-}^i \varepsilon_{\pi^-}^i + \varepsilon_{K^+}^i \varepsilon_{K^-}^i \varepsilon_{\mu^+}^i \\
 & \left. + \varepsilon_{K^+}^i \varepsilon_{\pi^-}^i \varepsilon_{\mu^+}^i + \varepsilon_{K^-}^i \varepsilon_{\pi^-}^i \varepsilon_{\mu^+}^i - \varepsilon_{K^+}^i \varepsilon_{K^-}^i \varepsilon_{\pi^-}^i \varepsilon_{\mu^+}^i \right), \quad (3.4.3)
 \end{aligned}$$

where i runs over all signal events. The charges in Eq. 3.4.3 are reversed for the \bar{B}_s^0

efficiency. The software trigger asymmetry is then

$$A_{\text{HIt}} = \frac{\varepsilon_{B_s^0} - \varepsilon_{\bar{B}_s^0}}{\varepsilon_{B_s^0} + \varepsilon_{\bar{B}_s^0}}. \quad (3.4.4)$$

The statistical uncertainty on A_{HIt} is determined by varying the efficiency histograms within their error, similar to what is done for the hadronic PID asymmetry in Sec. 3.3. Variations in the binning and binning variables are made in order to determine a possible bias originating from the choice of binning. The resulting asymmetry and uncertainties for the a_{sl}^s signal sample is discussed in Sec. 5.4.

4

CP violation in mixing of B^0 mesons

The amount of *CP* violation in mixing of B^0 mesons is quantified by the parameter a_{sl}^d . The LHCb measurement of a_{sl}^d described in this chapter is published in Ref. [101]. The definition of this phenomenological parameter is given in Sec. 1.2.8, and the methods used to determine the detection asymmetries are described in Sec. 3.

4.1 Method

The B^0 decays are reconstructed in two semileptonic decay channels,

- $B^0 \rightarrow D^{*-} \mu^+ \nu_\mu X$, with $D^{*-} \rightarrow \bar{D}^0 \pi^-$ and $\bar{D}^0 \rightarrow K^+ \pi^-$,
- $B^0 \rightarrow D^- \mu^+ \nu_\mu X$, with $D^- \rightarrow K^+ \pi^- \pi^-$

and their charge-conjugate modes, where X represents any number of additional particles that are not explicitly reconstructed in the decay, in addition to the neutrino (which is always missing and explicitly stated in the decay channel). The decay topologies are illustrated in Fig. 4.1. As mentioned in Sec. 1.2.8 the non-reconstruction of these additional particles results in a broad B^0 invariant mass peak. Backgrounds like $B^+ \rightarrow D^- \pi^+ \mu^+ \nu_\mu$ therefore contribute to the signal sample, where in this case $X = \pi^+$. The detailed selection of the signal sample is described in Sec. 4.2. The contributions from various backgrounds are determined in Sec. 4.3.

The value of a_{sl}^d and the production asymmetry A_P are determined from the untagged yields of charge-conjugate signal candidates as a function of the B^0 decay time as discussed in Sec. 1.2.8. The resulting measured asymmetry is repeated here for convenience,

$$A_{\text{meas}}(t) = \frac{N(f, t) - N(\bar{f}, t)}{N(f, t) + N(\bar{f}, t)} \approx A_{\text{det}} + \frac{a_{\text{sl}}^d}{2} + \left(A_P - \frac{a_{\text{sl}}^d}{2} \right) \cos(\Delta m_d t), \quad (4.1.1)$$

where f and \bar{f} are determined by the charge of the final state muon, and the yields N are determined from fits to the invariant mass of the D^- and D^+ candidates. The B^0 lifetime is corrected for the missing momentum in the reconstruction using so-called k -factors. This is discussed in Sec. 4.4. In this analysis, the candidates are weighted such that the

kinematic distribution of the highest-momentum pions match those of the muons, in order to minimize the $\mu^+\pi^-$ detection asymmetry. The determination of the remaining detection asymmetry A_{det} using the methods described in Chapter 3 is the focus of Sec. 4.5. This is followed by the measured values of a_{sl}^d and the production asymmetry A_P in Sec. 4.6, and a discussion of the systematic uncertainties in Sec. 4.7.

4.2 Selection

The analysis makes use of the full LHCb data set obtained during run 1 of the LHC. The data set corresponds to integrated luminosities of 1.0 fb^{-1} at a centre-of-mass energy of 7 TeV obtained in 2011, and 2.0 fb^{-1} at 8 TeV obtained in 2012. Since A_P depends on the hadronic environment, it is expected to be slightly different between both data-taking periods, and is thus reported for each year individually.

The recording of the event is triggered by the signal muon at the hardware- and the first software level. In the second software level the topology of the B^0 decay is required to be consistent with that of a multibody B^0 decay. The demands made in these trigger lines are described in more detail in Sec. 2.4. In the offline selection, standard quality requirements are made on the reconstructed tracks and vertex to form D^- or D^{*-} candidates. These are then combined with a muon of opposite charge to form a good-quality B^0 vertex. All final-state tracks should be inconsistent with originating from the primary vertex. A further selection is applied to reduce the background that is visible in the D^- or \bar{D}^0 invariant mass distribution. This background is also referred to as combinatorial background, and

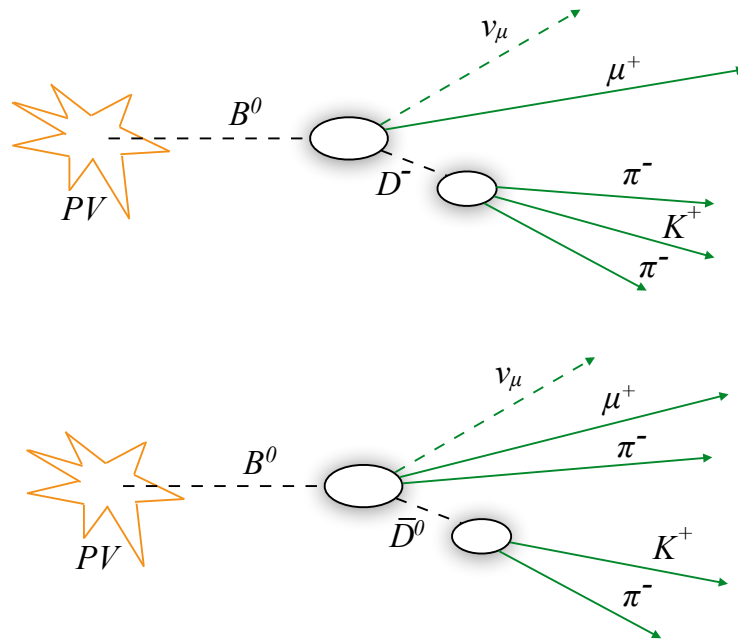


Figure 4.1: Decay topologies of the two signal decay modes.

dominates in the D^- or \bar{D}^0 candidate invariant mass distribution left and right of the signal peak. A tight window is applied to the reconstructed invariant mass difference between the D^{*-} and the \bar{D}^0 candidates in the $B^0 \rightarrow D^{*-} \mu^+ \nu_\mu X$ mode, to remove combinatorial background contributions. In the $B^0 \rightarrow D^- \mu^+ \nu_\mu X$ mode, the combinatorial background is reduced by requiring that the D^- vertex is downstream of the B^0 vertex. The most important requirements are summarized in Table 4.1.

4.2.1 Removal of identifiable backgrounds

Decays of $B \rightarrow J/\psi X$ form a source of background when one of the muons from the $J/\psi \rightarrow \mu^+ \mu^-$ decay is misidentified as a pion, and combined with the other particles in the decay to form a fake $D^{(*)\pm}$ candidate of a signal event. Fortunately, this background is easily identified by applying the muon mass hypothesis to the reconstructed pions, and looking at the invariant mass of either of the pions combined with the muon. This is shown in the left plot of Fig. 4.2 for a limited mass range that includes the J/ψ mass. If the invariant mass of the $\mu^\pm \pi^\mp$ pair is around the J/ψ mass $[3070 - 3150] \text{ MeV}/c^2$ and the pion candidate has hits in the muon stations, the candidate is rejected. This veto reduces the total background by about 4% in the D^- mode, and 1% in the D^{*-} mode.

A similar identifiable background originates from $\Lambda_b^0 \rightarrow \Lambda_c^+ \mu^- X$ decays, followed by

Table 4.1: Most important selection requirements on the data, on top of the trigger requirement. The PID DLL variables are explained in Sec. 2.

	Variable	$B^0 \rightarrow D^{*-} \mu^+ \nu_\mu X$	$B^0 \rightarrow D^- \mu^+ \nu_\mu X$
Offline cuts	$M(D^{(*)\pm} \mu^\mp)$	$[3.0, 5.2] \text{ GeV}/c^2$	$[3.0, 5.2] \text{ GeV}/c^2$
	$M(D^{*-}) - M(\bar{D}^0)$	$[144, 147] \text{ MeV}/c^2$	-
	$\tau(D^{0,\pm})$	$> 0.1 \text{ ps}$	$> 0.1 \text{ ps}$
	$\log(\text{IP}/\text{mm}) D^{0,\pm}$	> -3.0	> -3.0
	$z(D^0) - z(B^0)$	-	$> 0.0 \text{ mm}$
	J/ψ veto	See text	See text
	Λ_c^+ veto	-	See text
Calibration cuts	p all tracks	$> 3 \text{ GeV}/c$	$> 3 \text{ GeV}/c$
	p (μ^\pm and higher p_T π^\pm)	$> 6 \text{ GeV}/c$	$> 6 \text{ GeV}/c$
	p_T (lower p_T π^\pm)	$> 300 \text{ MeV}/c$	$> 300 \text{ MeV}/c$
	$p_T(K^\pm)$	$[300, 7000] \text{ MeV}/c$	$[300, 7000] \text{ MeV}/c$
	$p_T(\mu^\pm)$	$> 1.2 \text{ GeV}/c$	$> 1.2 \text{ GeV}/c$
	p_T (higher p_T π^\pm)	$> 1.2 \text{ GeV}/c$	$> 1.2 \text{ GeV}/c$
PID cuts	$\text{DLL}_{K-\pi}(K^\pm)$	> 7	> 7
	$\text{DLL}_{K-\pi}$ (lower p_T π^\pm)	< 3	< 3
	$\text{DLL}_{K-\pi}$ (higher p_T π^\pm)	< 10	< 4
	$\text{DLL}_{\mu-\pi}(\mu^\pm)$	> 0	> 0

$\Lambda_c^+ \rightarrow pK^-\pi^+$, and the proton is misidentified as a pion, such that the Λ_c^+ decay products form a $D^{(*)-}$ candidate. Again the proton mass hypothesis is applied to the pions, and $pK^-\pi^+$ candidates with an invariant mass around the Λ_c^+ mass [2260 – 2310] MeV/ c^2 are rejected if the pion satisfies a tight proton PID requirement ($DLL_{p-\pi} > 10$), as shown in the left plot of Fig. 4.2. This veto reduces the background by about 5%. In the D^{*-} sample the contribution of this background is small, and a veto is not applied.

Simulation studies (Sec. 4.3) indicate that combinatorial background in the D^- or \bar{D}^0 invariant mass mostly originates from real b -hadron decays and not from the PV, such that they have a short reconstructed D^- or \bar{D}^0 decay time. Figure 4.3 shows the background-subtracted decay-time distribution of D^- and \bar{D}^0 candidates in black, and for candidates in the mass sidebands around the D^- and \bar{D}^0 signal peak in red. A minimum decay time of 0.1 ps is required to reduce the contribution of this background, in particular in the $B^0 \rightarrow D^-\mu^+\nu_\mu X$ mode.

Finally, there is a contribution from real D^- or \bar{D}^0 mesons that do not originate from a b -hadron decay but from the PV, and are combined with a random muon. These so-called prompt backgrounds peak in the invariant D^- or \bar{D}^0 invariant mass, but point back to the PV instead of a secondary vertex. Simulation studies of inclusive D decays (Sec. 4.3.2) show the size of this contribution to be about 1%. In data, part of this contribution can be identified using the impact parameter (IP) of the D^- of same-sign combinations $D^\mp\mu^\mp$, as shown in Fig. 4.4 (left). These combinations have an enhanced relative contribution of prompt candidates. From the number of same-sign combinations this contribution is estimated to be about 0.2% with respect to the total amount of right-sign signal events. Another contribution of prompt candidates originates from real D^- or \bar{D}^0 mesons combined with a muon that originates from a semileptonic decay of the other charmed hadron in the

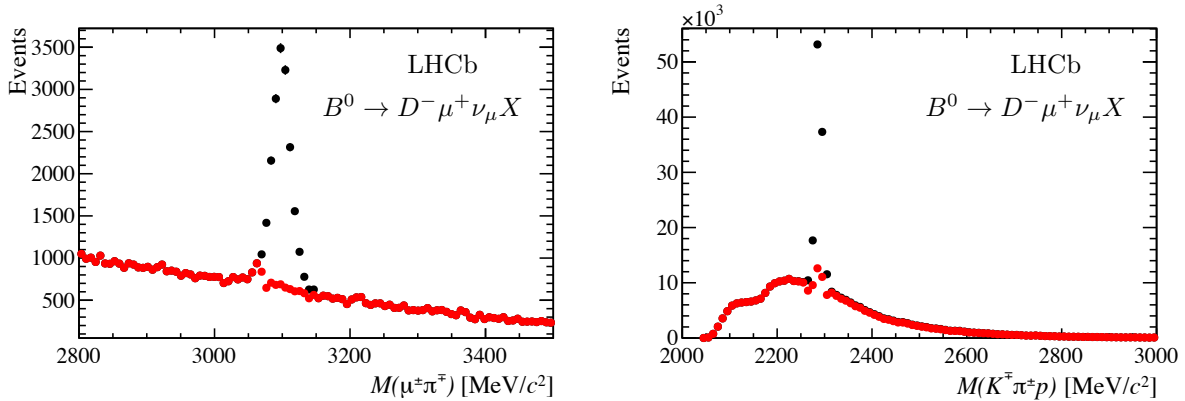


Figure 4.2: The invariant mass distributions of (left) the muon and the highest-momentum pion and (right) the $K^+\pi^-\pi^-$ combination where the lowest-momentum pion has the proton hypothesis, for candidates in the sideband of the $B^0 \rightarrow D^-\mu^+\nu_\mu X$ data, (black) before and (red) after the corresponding veto. The candidates that fall within the (left) J/ψ and (right) Λ_c^+ mass window are removed if they satisfy muon-like resp. proton-like PID for the pion in question. Note that not all candidates fall inside the mass range of the left plot.

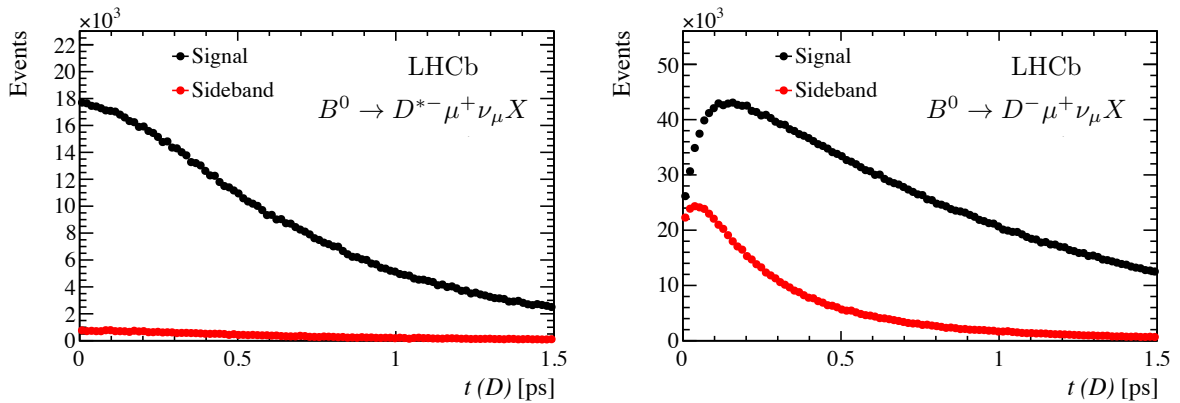


Figure 4.3: Reconstructed decay time of sideband-subtracted signal events in black, and events in the D^0 or D^- mass sidebands in red, for (left) the $B^0 \rightarrow D^{*-}\mu^+\nu_\mu X$ and (right) the $B^0 \rightarrow D^-\mu^+\nu_\mu X$. Due to the requirement that the D^- vertex should be downstream of the B^0 vertex in the $B^0 \rightarrow D^-\mu^+\nu_\mu X$ mode, the lower decay time is affected by the decay-time resolution.

$c\bar{c}$ -event. In that case, the muon has the right sign. From a fit to the $\log(\text{IP})$ distribution, shown in Fig. 4.4 (right), the total contribution of prompt charm backgrounds in the right-sign data is estimated to be about 0.7%. The prompt charm contribution is reduced to a negligible level of 0.1% when demanding $\log(\text{IP}/\text{mm}) > -3.0$ for the D^- or \bar{D}^0 .

The calibration samples used to determine the detection asymmetries have certain (kinematic) constraints in their respective selection, described in the appropriate sections. In order to match the requirements of these samples with the signal samples, additional

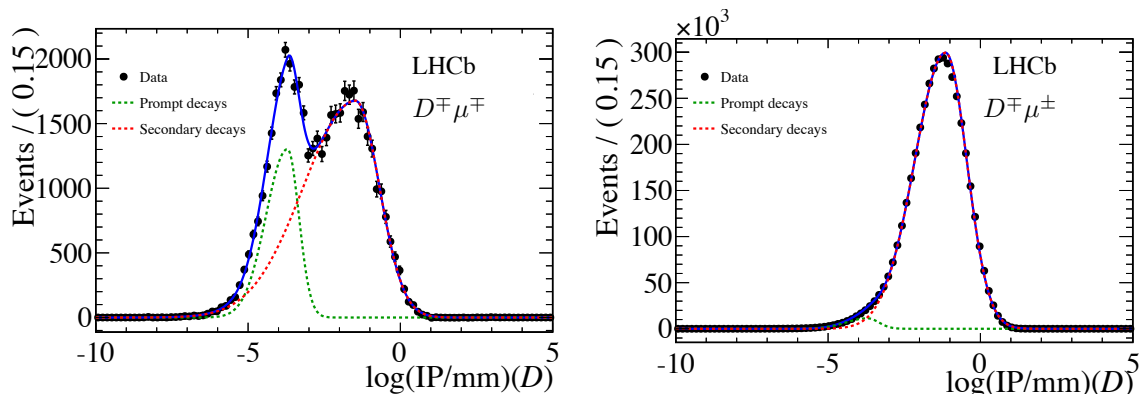


Figure 4.4: Logarithm of the impact parameter (IP) of the D^- in (left) the same-sign $D^\mp\mu^\mp$ data sample, and (right) the right-sign $B^0 \rightarrow D^-\mu^+\nu_\mu X$ data. The result of the fit is overlaid, where the green line represents prompt D^- decays, the red line represents secondary D^- decays and the blue line is the total. In the fit to the right-sign data, the prompt shape is fixed to that of the wrong-sign data.

cuts on the momenta and PID of the final-state particles are made. These are also listed in Table. 4.1.

4.2.2 Mass fit and signal yields

The signal yields after all selection steps are determined with a fit to the invariant mass distributions of the D^- and \bar{D}^0 in data, and are given in Table 4.2. The D^- mode contains about six times more candidates than the D^{*-} mode. Note that these yields still include peaking background contributions from other b -hadron decays to real D^- and \bar{D}^0 mesons. The D^- and \bar{D}^0 invariant mass shapes are modelled with the sum of a Crystal Ball function (Eq. 3.4.2) and a second Gaussian function, with a shared mean. The combinatorial background is described with an exponential function. The fits to the combined 2011 and 2012 data and both magnet polarities are shown in Fig. 4.5. The fits to the individual data samples are shown in Appendix. B.

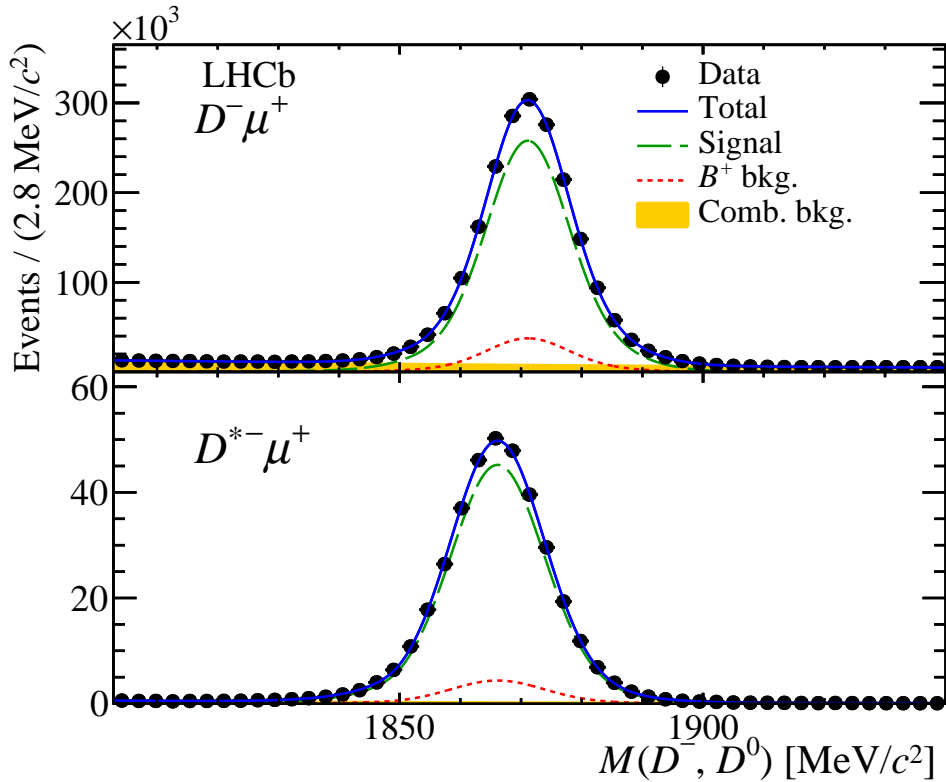


Figure 4.5: The invariant mass distributions of (top) the D^- candidates in the $B^0 \rightarrow D^- \mu^+ \nu_\mu X$ and (bottom) the \bar{D}^0 candidates in the $B^0 \rightarrow D^{*-} \mu^+ \nu_\mu X$ mode. The fit shape is overlaid. The contribution of D^- or \bar{D}^0 candidates corresponding to the peaking B^+ background (see Sec. 4.3.2) is projected as the red curve.

Table 4.2: Signal yields for the $B^0 \rightarrow D^{*-}\mu^+\nu_\mu X$ and $B^0 \rightarrow D^-\mu^+\nu_\mu X$ samples for the two magnet polarities and the two data-taking periods, obtained from fits to the D^- and \bar{D}^0 invariant mass distributions, after all selection cuts. The bottom two rows indicate the effective signal yield after applying $\mu\pi$ weights, as described in Sec. 4.5.

Channel	2011 Up	2011 Down	2012 Up	2012 Down	Total
$B^0 \rightarrow D^{*-}\mu^+\nu_\mu X$	53 089	71 462	179 411	168 005	471 967
$B^0 \rightarrow D^-\mu^+\nu_\mu X$	352 705	477 661	1 187 579	1 103 893	3 121 838
$B^0 \rightarrow D^{*-}\mu^+\nu_\mu X$ (eff.)	40 020	54 208	140 515	131 647	366 389
$B^0 \rightarrow D^-\mu^+\nu_\mu X$ (eff.)	226 153	306 205	768 088	714 399	2 014 845

4.3 Simulation and background studies

Simulated events with 2011 and 2012 data-taking conditions are generated using the software described in Sec. 2.5. They are used to determine the contribution of backgrounds in the data sample (Sec. 4.3.3), to calculate the k -factors for the correction of the B^0 lifetime (Sec. 4.4.1) and to verify the time-dependent fit (Sec. 4.4).

4.3.1 Signal simulation

Signal samples of $B^0 \rightarrow D^{*-}\mu^+\nu_\mu X$ and $B^0 \rightarrow D^-\mu^+\nu_\mu X$ decays are generated. The additional particles in the final state can originate from higher charmed resonances, $B^0 \rightarrow D^{(*)\pm}\tau$ decays with $\tau \rightarrow \mu X$, and non-resonant higher multiplicity decays which have additional pions in the final state. Therefore, the samples are enriched by including contributions from such decays. The absolute branching ratios used in the creation of these “cocktail” samples come from Ref. [94], and isospin symmetry is assumed to determine the branching ratios of yet unmeasured decay modes. In the $B^0 \rightarrow D^-\mu^+\nu_\mu X$ mode cocktail, exclusive $B^0 \rightarrow D^-\mu^+\nu_\mu$ decays contribute 44%, while decays of B^0 through higher charmed resonances contribute 46%, and are dominated by the $B^0 \rightarrow D^{*-}(\rightarrow D^-\{\pi^0, \gamma\})\mu^+\nu_\mu$ decay (33%). Tauonic decay modes (with $\tau \rightarrow \mu X$) contribute 5%, and non-resonant decays with higher multiplicity contribute 2%.

In contrast, the $B^0 \rightarrow D^{*-}\mu^+\nu_\mu X$ mode cocktail is dominated by the lowest-multiplicity $B^0 \rightarrow D^{*-}(\rightarrow \bar{D}^0\pi^-)\mu^+\nu_\mu$ decay, with 83%. Higher charmed resonances contribute 6%, tau decays with 4% and higher multiplicity modes with 6%. A comparison between the kinematic distributions of the B^0 candidates of data and simulation is shown in Fig. 4.6, where a good agreement is observed.

In total, 60 million $B^0 \rightarrow D^{*-}\mu^+\nu_\mu X$ events, and 30 million $B^0 \rightarrow D^-\mu^+\nu_\mu X$ events are generated. The overall efficiency due to acceptance, trigger and signal selection criteria is found to be 0.25% for the $B^0 \rightarrow D^-\mu^+\nu_\mu X$ mode and 0.20% for the $B^0 \rightarrow D^{*-}\mu^+\nu_\mu X$ mode, with statistical uncertainties of $\mathcal{O}(0.001\%)$. This includes the statistical error degradation due to the application of event weights in the data sample, in order to match

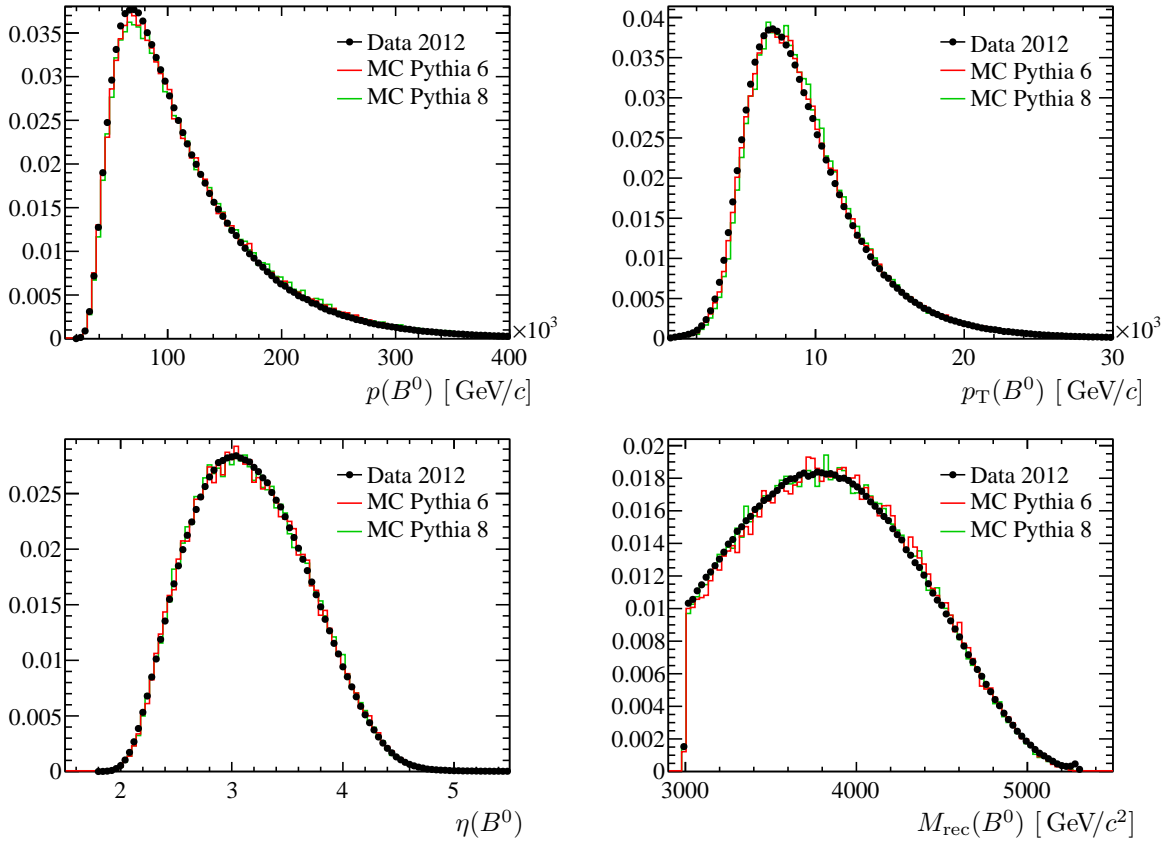


Figure 4.6: The normalized kinematic distributions of the reconstructed B^0 candidate in the $B^0 \rightarrow D^- \mu^+ \nu_\mu X$ mode for data and simulation (MC), for both versions of PYTHIA. A similar agreement between data and simulation is found for the $B^0 \rightarrow D^{*-} \mu^+ \nu_\mu X$ mode.

the pion kinematic distributions to those of the muon, as explained in Sec. 4.5.

4.3.2 Contributions from peaking backgrounds

In order to investigate the various sources of background involving real D mesons, two samples of 15 million of both $D^- \rightarrow K^+ \pi^- \pi^-$ and $D^{*-} \rightarrow \bar{D}^0 (\rightarrow K^+ \pi^-) \pi^-$ decays are generated, which include D^- and \bar{D}^0 mesons from b -hadron decays. After full selection has been applied, 84% (83%) of all candidates in the D^{*-} (D^-) mode match to generated signal decays. Most background events originate from real b hadrons decaying to D^- or \bar{D}^0 , and are dominated by semileptonic B^+ decays. These decays are hard to reduce since they peak in the D^- or \bar{D}^0 invariant mass. The B^+ contribution is discussed in Sec. 4.3.3 and has a separate component in the decay-time fit. Another significant background is combinatoric D^- or \bar{D}^0 candidates from real b -hadron decays, that involve a fake track. This background appears as combinatorial background in the D^- or \bar{D}^0 invariant mass distribution, which is also treated as a dedicated component in the decay-time fit.

The contribution from $B^0 \rightarrow D^{(*)-} \pi^+ X$ with a $\pi^+ \rightarrow \mu^+ \nu_\mu$ decay-in-flight, as well as

$B^0 \rightarrow D^{(*)-} D_{(s)}^{(*)+} X$ decays where the $D_{(s)}^{(*)+}$ decays semileptonically, contribute $(0.9 \pm 0.4)\%$ to both signal modes. They have the right sign combination, and are treated as signal decays. Due to additional missing momentum a reduction in time resolution is expected, especially for the latter. This effect is studied in Sec. 4.7.2.

The contribution from (Cabibbo-suppressed) B_s^0 decays is about $(1.5 \pm 0.5)\%$ in both modes, and is not modelled. Its effect is considered as a systematic uncertainty, and is described in Sec. 4.7. Finally, the contribution of $\bar{A}_b^0 \rightarrow D^{*-} \mu^+ \nu_\mu X$ decays is estimated in Sec. 4.7.2 and considered as a source of systematic error. Other sources of real D^{*-} or D^- mesons are found to be negligible.

4.3.3 Determination of the B^+ fraction

The dominant contribution of other b -hadron decays to the signal sample originates from B^+ decays. A cocktail of semileptonic B^+ decays is generated to determine the size of this contribution after all selection steps. The branching ratios of contributing decays are determined in the same way as those of the signal cocktails (using Ref. [94] and isospin). The B^+ mesons are forced to decay to a $D^- (\rightarrow K^+ \pi^- \pi^-)$ or a $\bar{D}^0 \rightarrow K^+ \pi^-$, including resonant states. The latter includes $B^+ \rightarrow D^{*-} \mu^+ \nu_\mu X$ decays. In total, 22.5 million $B^+ \rightarrow D^0 \mu^+ \nu_\mu X^+$ events and 10 million $B^+ \rightarrow D^- \mu^+ \nu_\mu X^+$ events are generated.

Under (u, d) isospin symmetry the production rates of B^+ and B^0 are equal. With this assumption, the relative fraction of B^+ events in the data can be obtained from the selection efficiencies and the total branching fractions of the decays present in the B^0 and B^+ cocktails. These are summarized in Table 4.3, with the first error is due to the known error on the measured branching fractions, and the second is due to the change in central value when varying the branching ratios of the yet unmeasured decays by a factor two. The B^+ fractions in the signal data after selection is defined as

$$f_{B^+} = \frac{N_{B^+}}{N_{B^0} + N_{B^+}}, \quad (4.3.1)$$

and are found to be

$$\begin{aligned} f_{B^+}(B^0 \rightarrow D^{*-} \mu^+ \nu_\mu X \text{ mode}) &= (8.8 \pm 2.0 \pm 1.0)\%, \\ f_{B^+}(B^0 \rightarrow D^- \mu^+ \nu_\mu X \text{ mode}) &= (12.7 \pm 2.1 \pm 0.6)\%, \end{aligned} \quad (4.3.2)$$

where the first uncertainty is due to the branching fractions, and the second is due to the efficiency variations between PYTHIA 6 and PYTHIA 8.

The estimated B^+ fractions are verified in data using the corrected mass to distinguish between B^0 and B^+ decays. The corrected mass is defined as

$$M_{\text{corr}} = \sqrt{M(D^{(*)-} \mu^+)^2 + |p_{\text{T,missing}}|^2 + |p_{\text{T,missing}}|}, \quad (4.3.3)$$

where $p_{\text{T,missing}}$ represents the transverse momentum of an additional massless particle originating from the B^0 vertex, such that the reconstructed B^0 flight direction points back to the PV. For the dominant signal modes, which miss only a neutrino, this correction

Table 4.3: The total branching ratios corresponding to the generated cocktails. The first uncertainty comes from the measured uncertainties on the individual branching fractions present in the cocktail. The second uncertainty comes from varying the branching ratios of yet unmeasured decays. The last column displays the selection efficiency. For the $B^+ \rightarrow D^{*-}\mu^+\nu_\mu X$ sample, this efficiency contains the fraction of \bar{D}^0 mesons that originated from a D^{*-} decay.

Cocktail sample	Branching fraction	Efficiency
Signal $B^0 \rightarrow D^{*-}\mu^+\nu_\mu X$	$(4.07 \pm 0.20 \pm 0.08)\%$ $\times \mathcal{B}(D^0 \rightarrow K^-\pi^+)$	0.163%
Signal $B^0 \rightarrow D^-\mu^+\nu_\mu X$	$(4.95 \pm 0.23 \pm 0.08)\%$ $\times \mathcal{B}(D^- \rightarrow K^+\pi^-\pi^-)$	0.240%
Bkg $B^+ \rightarrow D^{*-}\mu^+\nu_\mu X$	$(10.33 \pm 0.41 \pm 0.10)\%$ $\times \mathcal{B}(D^0 \rightarrow K^-\pi^+)$	0.006%
Bkg $B^+ \rightarrow D^-\mu^+\nu_\mu X$	$(0.97 \pm 0.16 \pm 0.08)\%$ $\times \mathcal{B}(D^- \rightarrow K^+\pi^-\pi^-)$	0.178%

works better than for the B^+ background, which involves at least one additional massive particle. Therefore the corrected mass is expected to be lower for the B^+ background than for the signal modes. The distributions of the corrected mass are shown in Fig. 4.7. A fit to data is performed using template shapes for B^+ and B^0 fixed from simulation, and the shape of the combinatorial background obtained from the corrected mass of wrong-sign $D^\pm\mu^\pm$ combinations. The B^+ fractions obtained are $(16.1 \pm 0.1)\%$ for the $B^0 \rightarrow D^-\mu^+\nu_\mu X$ mode, and $(8.0 \pm 0.2)\%$ for the $B^0 \rightarrow D^{*-}\mu^+\nu_\mu X$ mode, where the errors are the statistical errors from the fit only. The errors on the template shapes are not taken into account. In addition, components in the fit that are not modelled (i.e. other b -hadron decays) contribute a few percent. When considering the possible systematic effects, the B^+ fractions obtained from data are compatible with Eq. 4.3.2.

4.4 Decay-time model

The decay time of the B^0 candidates is calculated via the measured decay length L between the production vertex (primary vertex) and the decay vertex (secondary vertex),

$$t_{\text{rec}} = \frac{M_{B^0} L}{p_{B^0} c}, \quad (4.4.1)$$

where M_{B^0} is the world-average B^0 mass taken from Ref. [2], and p_{B^0} is the momentum of the B^0 candidate as obtained from the reconstructed final-state particles. This momentum is biased due to the missing neutrino and possibly other particles in the reconstruction, and is therefore corrected using a so-called k -factor method.

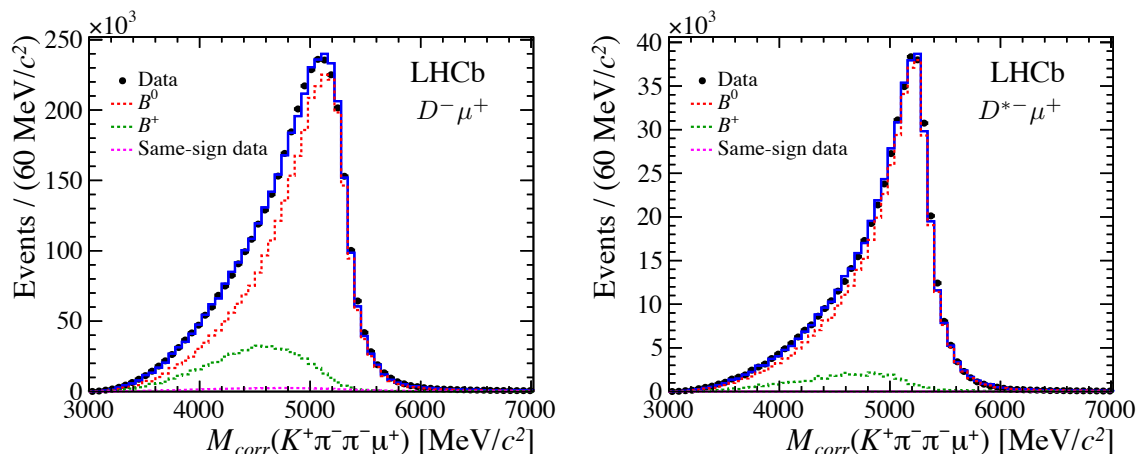


Figure 4.7: Corrected B mass in (left) the $B^0 \rightarrow D^- \mu^+ \nu_\mu X$ sample and (right) the $B^0 \rightarrow D^{*-} \mu^+ \nu_\mu X$ sample. Distributions from data are shown in black points. A fit to the data is done, using shapes for the B^0 and B^+ components as obtained from simulated samples, including a shape for the combinatorial background as obtained from same-sign combinations in data.

4.4.1 Determination of the k -factors

In order to correct the B^0 momentum in the decay-time model, a correction factor, called a k -factor, is constructed using the simulated events,

$$k = \frac{p_{\text{rec}}}{p_{\text{true}}}, \quad (4.4.2)$$

where p_{rec} is the reconstructed momentum of the B^0 , and p_{true} is the generated momentum. The distributions of the k -factors for both decay modes are shown in the top row of Fig. 4.8. No significant dependence of the k -factor distribution on the true B^0 decay time is found, as is shown in Fig. 4.9 (left).

The dependence of the average k -factor on the reconstructed B^0 mass is shown in Fig. 4.9 (right). It can be described with a second-order polynomial,

$$\langle k \rangle(M_{\text{rec}}) = p_0 + p_1 \left(\frac{M_{\text{rec}}}{M_{B^0}} - 1 \right) + p_2 \left(\frac{M_{\text{rec}}}{M_{B^0}} - 1 \right)^2, \quad (4.4.3)$$

where $p_{0,1,2}$ are the fit parameters, M_{rec} is the reconstructed B^0 mass and $\langle k \rangle(M_{\text{rec}})$ is the fitted average k -factor. The reconstructed decay time of each candidate is multiplied with $\langle k \rangle(M_{\text{rec}})$,

$$t_{\text{corr}} = \langle k \rangle(M_{\text{rec}}) t_{\text{rec}}. \quad (4.4.4)$$

The corrected decay time, t_{corr} , corresponds on average to the real decay time. This is shown in Fig. 4.10, where the good overlap of t_{corr} with t_{true} is visible. The small discrepancy at decay times < 1 ns is irrelevant due to a decay-time window of $[1,15]$ ps that is applied later on in the fit.

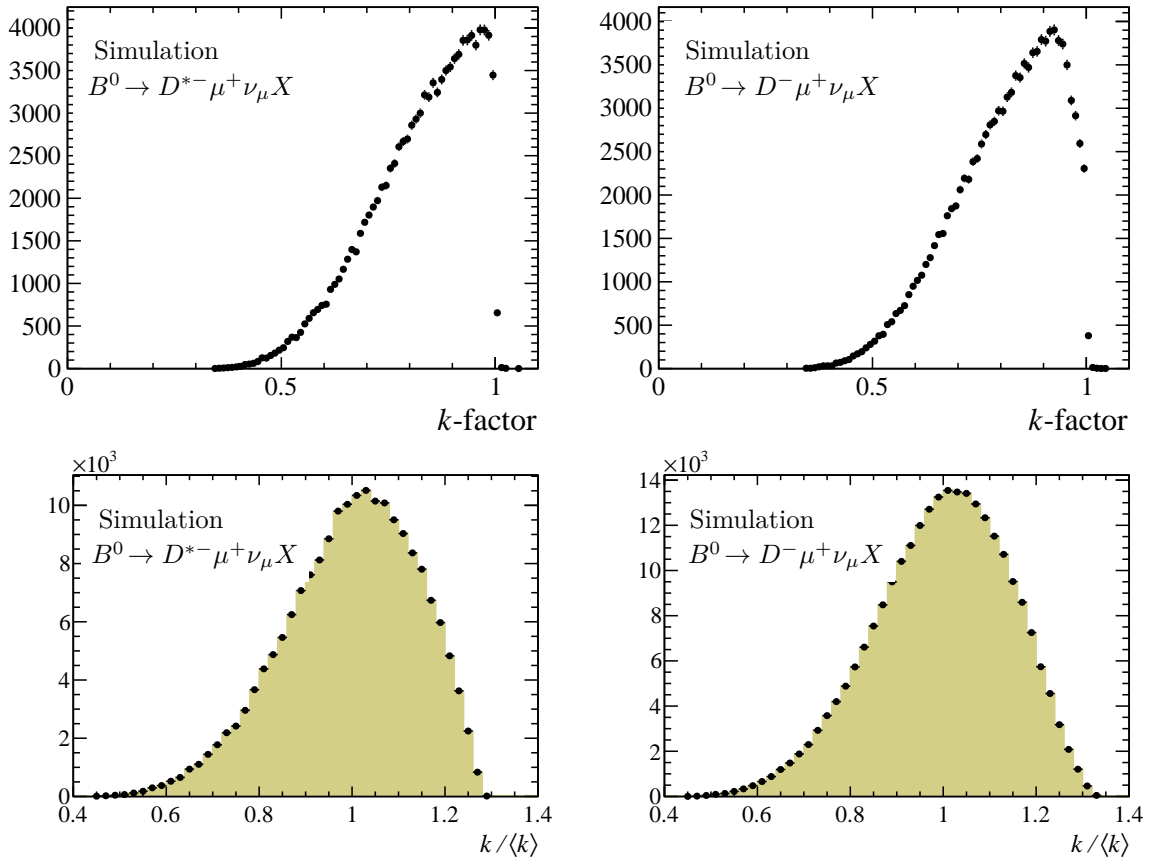


Figure 4.8: The normalized distribution of (top) the k -factors, and (bottom) the corrected k -factors, as obtained from simulation, for (left) the $B^0 \rightarrow D^{*-}\mu^+\nu_\mu X$ mode and (right) the $B^0 \rightarrow D^-\mu^+\nu_\mu X$ mode.

4.4.2 Decay-time resolution

Experimentally, there are two sources of uncertainty that smear the decay time in Eq. 4.4.1. The first originates from the error on the decay length L , dominated by the error on the secondary vertex position. The second comes from the uncertainty on the B^0 momentum, which is dominated by the spread in k -factors. As these two sources of uncertainty are uncorrelated the total error is given by

$$\sigma_t = \sqrt{\left(\frac{M}{pc}\sigma_L\right)^2 + \left(t\frac{\sigma_p}{p}\right)^2}, \quad (4.4.5)$$

where the first contribution results in a constant offset, and the second contribution increases linearly with time. These effects can be seen in simulation. Figure 4.11 shows the mean and width of the decay-time resolution as function of the true decay time. The decay-time resolution is obtained by fitting a single Gaussian function to the difference in true and reconstructed decay times in each time bin. The mean of the decay time resolution as function of true decay time is flat and close to zero. The width of the

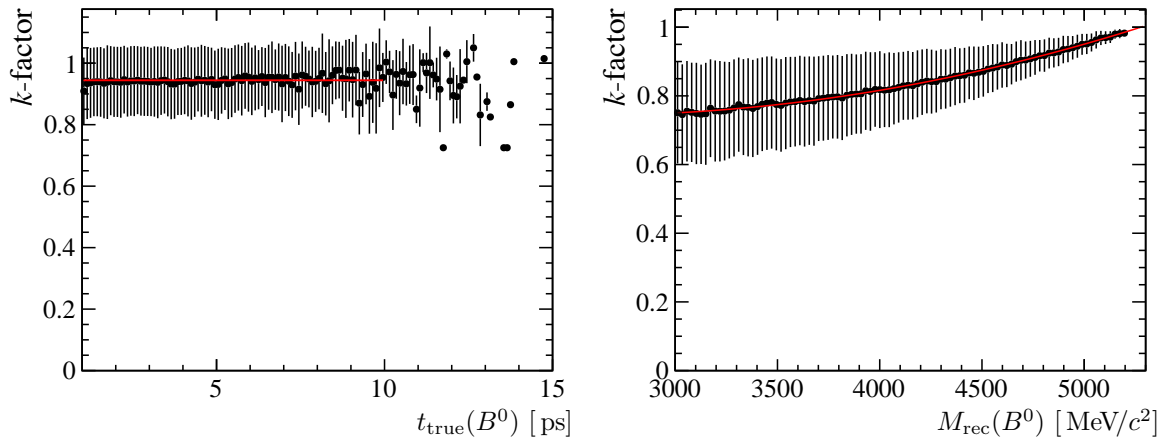


Figure 4.9: The k -factor distribution of the $B^0 \rightarrow D^- \mu^+ \nu_\mu X$ mode, as function of (left) the true B decay time, and (right) the reconstructed B^0 mass, with the second-order polynomial fit overlaid. The error bars represent the spread of the k -factor distribution in each bin. Similar distributions are obtained for the $B^0 \rightarrow D^{*-} \mu^+ \nu_\mu X$ mode.

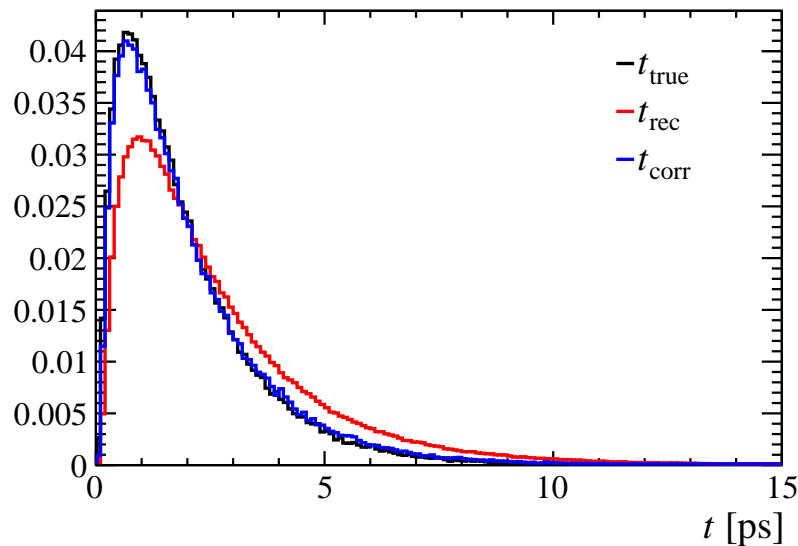


Figure 4.10: Decay-time distributions in signal simulation for t_{true} , t_{rec} and t_{corr} .

Gaussian increases linearly with the true decay time, and there is a barely visible offset at $t = 0$ due to the uncertainty on the decay length. The size of this offset is determined from simulation. To separately determine the resolution due to the decay length, the reconstructed decay time using the *true* B^0 momentum is compared to the true decay time, shown for both $B^0 \rightarrow D^{*-} \mu^+ \nu_\mu X$ and $B^0 \rightarrow D^- \mu^+ \nu_\mu X$ modes in Fig. 4.12. No bias is observed, and the average resolution is about 70 fs.

The uncertainty on the momentum dominates the error on the decay time above 0.4 ps,

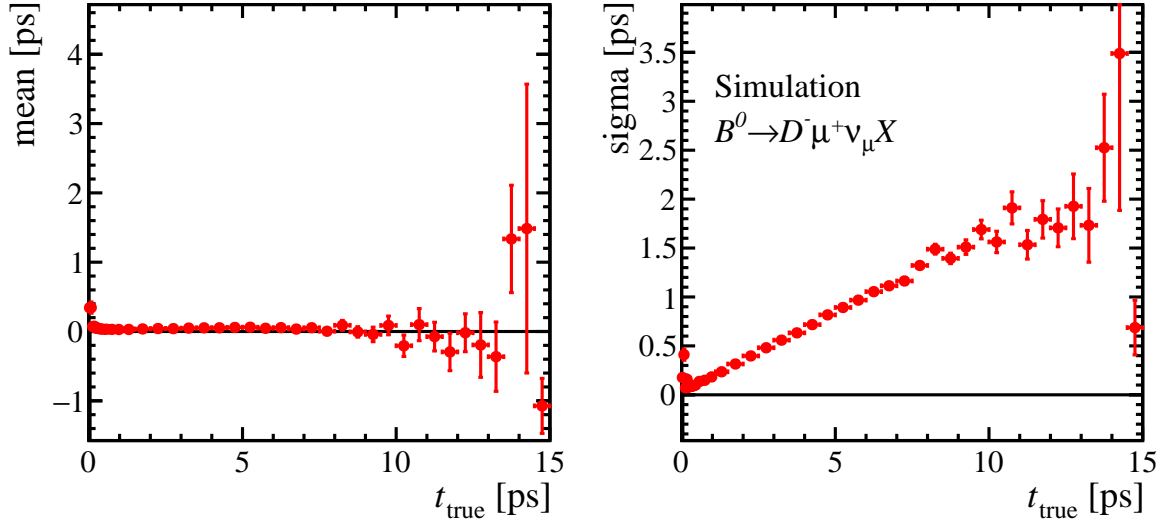


Figure 4.11: (left) The mean and (right) the width of the decay-time resolution in simulation, as determined from single Gaussian fits to $t_{\text{rec}} - t_{\text{true}}$, as a function of t_{true} , for the $B^0 \rightarrow D^- \mu^+ \nu_\mu X$ mode. Similar behaviour is observed for the $B^0 \rightarrow D^{*-} \mu^+ \nu_\mu X$ mode.

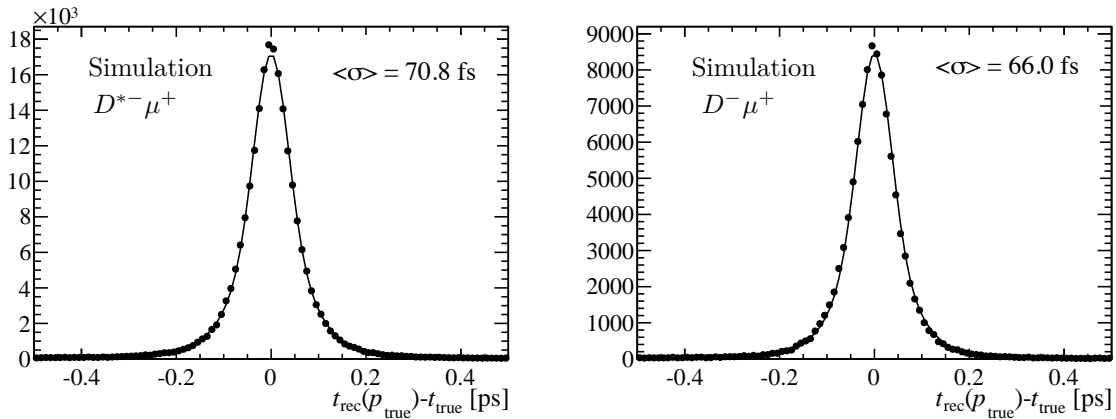


Figure 4.12: Decay-time resolution in simulation when taking the true B^0 momentum for both modes. To avoid any bias from a decay-time acceptance (Eq. 4.4.11), only events with a decay time above 2.0 ps are used. A triple Gaussian function is fitted to the data. The weighted average resolution of the three Gaussian functions is indicated in the plots.

and originates from the spread in k -factors,

$$\frac{\Delta p}{p} = k_{\text{corr}} - 1, \quad (4.4.6)$$

where k_{corr} is the k -factor corrected for the average k -factor as function of the reconstructed B^0 mass,

$$k_{\text{corr}} = \frac{k}{\langle k \rangle (M_{\text{rec}})}. \quad (4.4.7)$$

The distribution of the corrected k -factor behaves more symmetric than the original k -factors, as shown in Fig. 4.8.

4.4.3 Signal model

The number of decays to final states f and \bar{f} can be written as (Eq.1.2.42)

$$\begin{aligned} N(f, t) &= \mathcal{N} e^{-t/\tau_d} \left(1 + A_{\text{det}} + \frac{a_{\text{sl}}^d}{2} + \left(A_P - \frac{a_{\text{sl}}^d}{2} \right) \cos(\Delta m_d t) \right), \\ N(\bar{f}, t) &= \mathcal{N} e^{-t/\tau_d} \left(1 - A_{\text{det}} - \frac{a_{\text{sl}}^d}{2} - \left(A_P - \frac{a_{\text{sl}}^d}{2} \right) \cos(\Delta m_d t) \right), \end{aligned} \quad (4.4.8)$$

where \mathcal{N} is a normalization factor, and τ_d is the lifetime of the B^0 meson. The above is implemented in a two-dimensional fit, with t and the charge of the final-state muon (f or \bar{f}) as dimensions, and t is the true decay time.

Two convolutions are done in order to take into account the decay-time resolution. The first is due to the error on the decay length, which is taken into account by analytically convolving the decay time in Eq. 4.4.8 with a triple Gaussian resolution function $R(t')$ obtained from the fit in Fig. 4.12, denoted as

$$\mathcal{P}_{L\text{-conv}}(f, t) = N(f, t - t') \otimes R(t'). \quad (4.4.9)$$

The second contribution is due to the spread of the k -factors, and is multiplicative in the decay time itself (see Eq. 4.4.5). This convolution is done by dividing the true decay time in Eq. 4.4.8 by the corrected k -factor k_{corr}^i , and summing the decay-time distribution over all bins i of the corrected k -factor distribution, weighted by the normalized probability (i.e. the bin height, $F(k_{\text{corr}}^i)$). Finally, for the correct normalization one has to multiply the number of events by the Jacobian, $dt_{\text{true}}/dt_{\text{rec}} = k_{\text{corr}}^i$. To summarize, the convolution with the k -factor distribution is done as

$$\mathcal{P}_{k\text{-conv}}(f, t) = \sum_i N(f, t/k_{\text{corr}}^i) k_{\text{corr}}^i F(k_{\text{corr}}^i). \quad (4.4.10)$$

The decay-time acceptance of LHCb is discussed in Appendix. A. The shape used to describe the decay-time acceptance is

$$a(t) = (1 - e^{-(t-t_{\text{shift}})/\alpha})(1 + \beta t), \quad (4.4.11)$$

where t_{shift} , α and β describe, respectively, the acceptance “turn-on” time, the strength of the turn-on, and the upper acceptance shape factor. This simple description does not accurately describe the data below decay times of 1 ps, hence the nominal fit is only performed in the range [1, 15] ps.

To summarize, the full time-dependence of the signal is described by

$$\mathcal{P}(f, t) = \mathcal{N} \times \sum_i \left([N(f, t/k_{\text{corr}}^i - t') \otimes R(t')] k_{\text{corr}}^i F(k_{\text{corr}}^i) \times a(t) \right) \quad (4.4.12)$$

where $\otimes R(t')$ is the first, analytic convolution with the decay-length resolution, and \mathcal{N} is a normalization factor which is left free in the fit. Since the B^0 lifetime is highly correlated with β , the lifetime is fixed to the B^0 lifetime from Ref. [94]. Furthermore, in the fit to data A_{det} is fixed from external inputs (see Sec. 4.5), and Δm_d is fixed to the world-average value [94].

4.4.4 Simulation studies

The simulated signal samples described in Sec. 4.3 are used to test the signal decay-time model (Eq. 4.4.12). The fit of Eq. 4.4.12 to the corrected decay time in the simulated $B^0 \rightarrow D^- \mu^+ \nu_\mu X$ sample is performed, and shown in Fig. 4.13. The resulting fit parameters are shown in Table 4.4. No significant bias on the values of a_{sl}^d or A_P is observed.

The correlations between the fitted parameters are shown in Table 4.5. The correlation between the physical parameters a_{sl}^d and A_P is found to be small. The correlation between the acceptance parameters t_{shift} and α is sizeable. Therefore, t_{shift} is fixed in the fit to

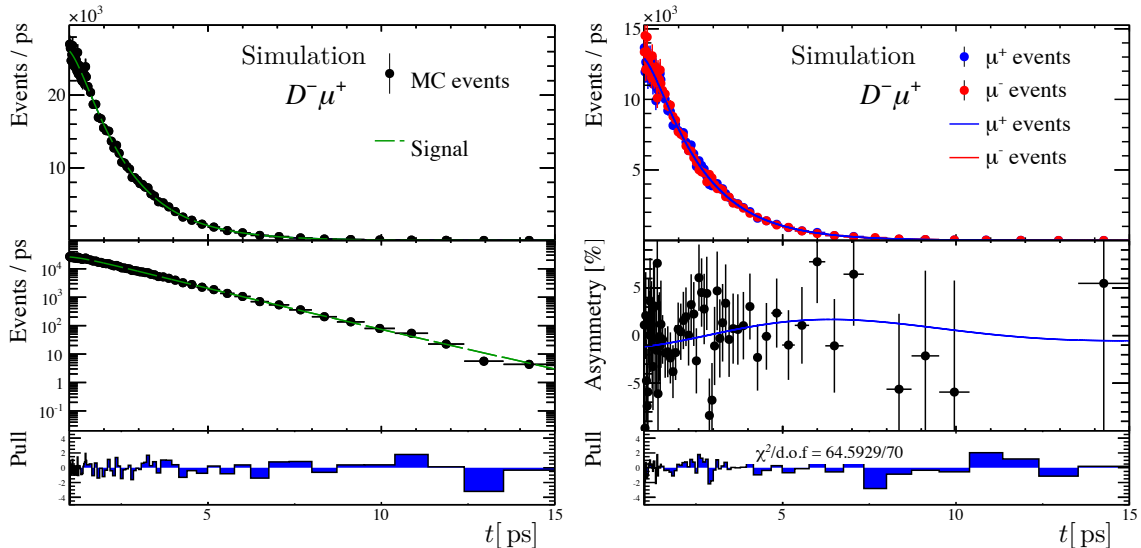


Figure 4.13: Fit to the decay-time distribution in signal simulation for the $B^0 \rightarrow D^- \mu^+ \nu_\mu X$ mode. (left) Projection of the decay time, (right) projection of the charge asymmetry. The distribution of the fit residual divided by the error is shown below.

Table 4.4: Fit results of the time-dependent fit to the simulated $B^0 \rightarrow D^- \mu^+ \nu_\mu X$ signal sample.

Parameter	Value
α	0.554 ± 0.094
β	-0.036 ± 0.003
t_{shift}	0.197 ± 0.139
a_{sl}^d	0.012 ± 0.011
A_P	-0.006 ± 0.008

Table 4.5: Correlation matrix of the time-dependent fit of the simulated $B^0 \rightarrow D^- \mu^+ \nu_\mu X$ signal sample.

	α	β	t_{shift}	a_{sl}^d	A_P
α	1.00	-0.59	0.96	0.00	0.00
β		1.00	-0.45	-0.01	0.00
t_{shift}			1.00	0.00	0.00
a_{sl}^d				1.00	0.05
A_P					1.00

data to the value obtained from the fit to simulation. Finally, the correlation between the acceptance parameters and a_{sl}^d and A_P is small. This is not surprising, since the acceptance is not expected to be different between the charge-conjugate final states. It also indicates that the choice of the acceptance shape does not have a significant influence on the final result.

4.4.5 Background models

As discussed in Sec. 4.3.2, the background is dominated by B^+ decays and combinatorial background originating from real b -hadron decays. Contributions from other decays are negligible or treated as a systematic uncertainty. The background due to B^+ decays behaves similar to the signal decays; the main difference being that the B^+ mesons do not mix. The decay time is described by an exponential decay multiplied with a lower decay-time acceptance function,

$$\begin{aligned} \mathcal{P}_{B^+}(f, t) &= \mathcal{N}_{B^+} e^{-t/\tau_{B^+}} (1 + A_{\text{det}} + A_{P,B^+}) (1 - e^{-(t-t_{\text{shift},B^+})/\alpha_{B^+}}), \\ \mathcal{P}_{B^+}(\bar{f}, t) &= \mathcal{N}_{B^+} e^{-t/\tau_{B^+}} (1 - A_{\text{det}} - A_{P,B^+}) (1 - e^{-(t-t_{\text{shift},B^+})/\alpha_{B^+}}), \end{aligned} \quad (4.4.13)$$

where the normalization \mathcal{N}_{B^+} is fixed to the signal normalization multiplied by the B^+ fraction (Eq. 4.3.2). For simplicity of the model, no convolution for the decay-time resolution is made and there is no explicit term for the upper-decay-time acceptance. Instead, these effects are absorbed in the parameter for the lifetime, τ_{B^+} , and the acceptance

parameters t_{shift,B^+} and α_{B^+} , which are fixed from a fit to simulated decays. This is motivated by the fact that the lifetime of the B^+ meson is not of interest in this analysis. The fit of Eq. 4.4.13 to the simulated B^+ sample is shown in Fig. 4.14.

The detection and production asymmetry of the B^+ contribution cannot be disentangled due to the lack of mixing, so both are determined from external input. The detection asymmetry is taken to be the same as for the signal data; even though there is at least one additional particle missing in the decay, the kinematic spectra of the reconstructed final-state particles are nearly identical. The production asymmetry is taken from an LHCb measurement using $B^+ \rightarrow J/\psi K^+$ decays, where a charge asymmetry $A_{\text{meas}}(J/\psi K^+) = (-1.3 \pm 0.1)\%$ is measured [102]. Correcting for the measured direct CP asymmetry $A_{CP}(B^+ \rightarrow J/\psi K^+) = (0.3 \pm 0.6)\%$ [94] and kaon detection asymmetry of $(-1.0 \pm 0.2)\%$ [103], results in

$$A_{P,B^+} = (-0.6 \pm 0.6)\% . \quad (4.4.14)$$

Due to the publication status at the time of this analysis, this is the number that is used. However, it is worth noting that at the time of this thesis an update can be made. The average from Ref. [94] can be updated with a new LHCb measurement of the B^+ production asymmetry using $B^+ \rightarrow \bar{D}^0 \pi^+$ decays. A value of $A_{P,B^+} = (-0.47 \pm 0.29)\%$ is obtained when averaging over the two centre-of-mass energies [104].

The combinatorial background in the \bar{D}^0 and D^- invariant mass-distributions originates largely from real B^0 decays (see Sec. 4.3.2). This can be seen in the decay-time distribution and mixing asymmetry of the D^- sidebands, shown in Fig. 4.15. The sideband regions

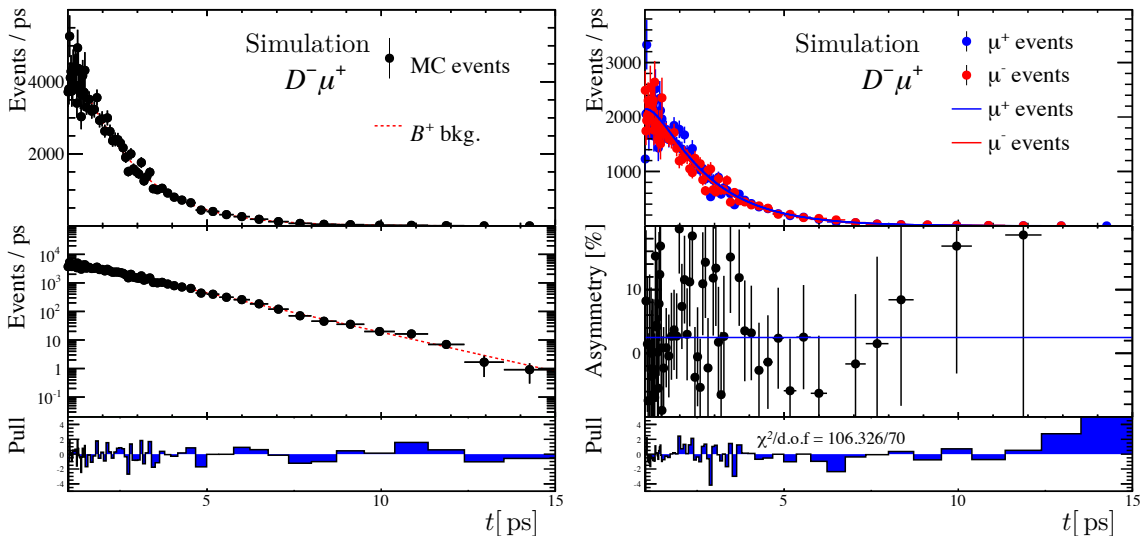


Figure 4.14: Fit to the decay-time distribution of the simulated B^+ background for the $B^0 \rightarrow D^- \mu^+ \nu_\mu X$ mode. (left) Projection of the decay time, (right) projection of the charge asymmetry. The distribution of the fit residual divided by the error is shown below.

are defined as $M(D^-) < 1840 \text{ MeV}/c^2$ and $M(D^-) > 1900 \text{ MeV}/c^2$. In order to display the mixing asymmetry, the initial state is determined using flavour tagging [51] to distinguish between mixed and unmixed decays. The time-dependent behaviour of the asymmetry between mixed and unmixed decays shows the characteristic oscillation from B^0 . The model used for the decay time of the combinatorial background (sideband background) is

$$\begin{aligned} N_{\text{sb}}(f, t) &= \mathcal{N}_{\text{sb}} e^{-t/\tau_{\text{sb}}} (1 + A_{\text{det, sb}} + A_{P, \text{sb}} \cos \Delta m_d t) (1 - e^{-(t-t_{\text{shift, sb}})/\alpha_{\text{sb}}}) , \\ N_{\text{sb}}(\bar{f}, t) &= \mathcal{N}_{\text{sb}} e^{-t/\tau_{\text{sb}}} (1 - A_{\text{det, sb}} - A_{P, \text{sb}} \cos \Delta m_d t) (1 - e^{-(t-t_{\text{shift, sb}})/\alpha_{\text{sb}}}) . \end{aligned} \quad (4.4.15)$$

Since it is unclear what the detection asymmetry of the various contributing modes would be, these decays are not used to determine a_{sl}^d . Instead, the parameters for the detection and production asymmetry, $A_{\text{det, sb}}$ and $A_{P, \text{sb}}$, are left free in the fit. In addition, the lifetime parameter τ_{sb} is a free parameter in the fit, to effectively take into account effects from the decay-time resolution and upper decay-time acceptance. The fit of Eq. 4.4.15 to the sidebands in the data is shown in Fig. 4.16. The fraction of combinatorial background is determined from the D^- or \bar{D}^0 invariant-mass distribution. The invariant-mass model is described in Sec. 4.2.2.

4.4.6 Full model

The model that is fit to the data is the three-dimensional fit in either D^- or \bar{D}^0 mass depending on the signal channel, the B^0 candidate decay time and the charge of the muon. The full model is the sum of the signal, the B^+ and the combinatorial background models described above. As discussed in Sec. 4.3.2 the contribution from other decays is either negligible or small enough to have an insignificant effect on the final results.

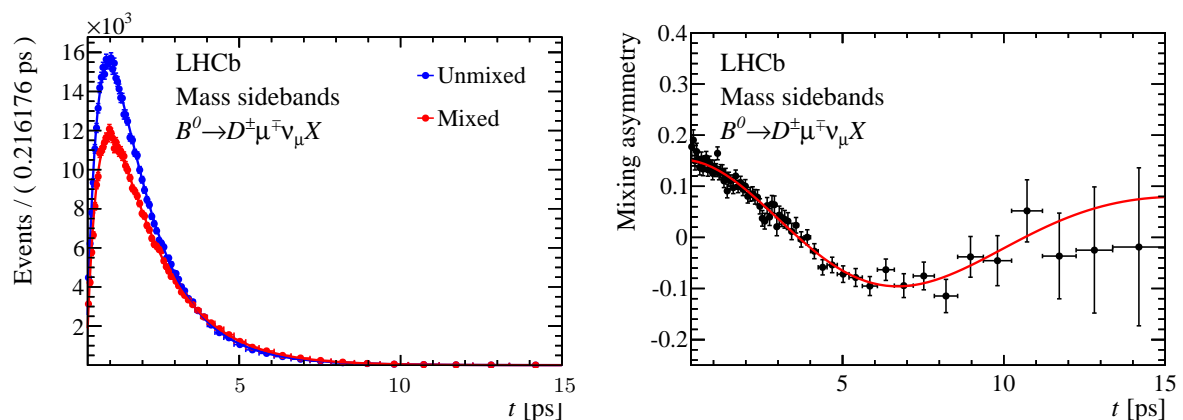


Figure 4.15: (left) Decay-time distribution of the sidebands in data for unmixed ($B^0 \rightarrow B^0$ and $\bar{B}^0 \rightarrow \bar{B}^0$) and mixed ($B^0 \rightarrow \bar{B}^0$ and $\bar{B}^0 \rightarrow B^0$) decays. (right) Their final state mixing asymmetry. The shape used to fit the data (Eq. 4.4.15) is superimposed.

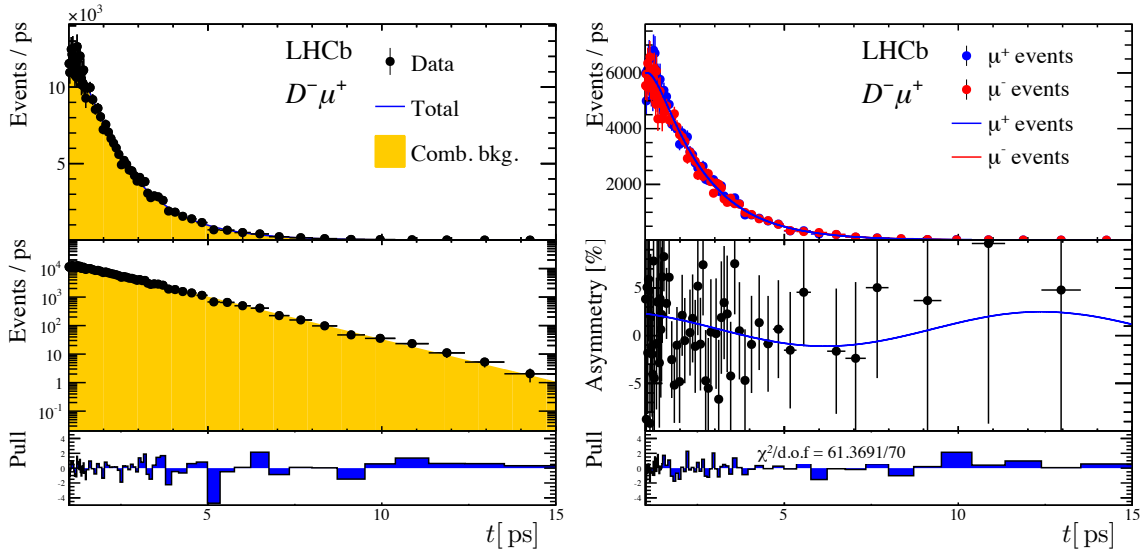


Figure 4.16: Fit to the decay-time distribution in sideband data for the $B^0 \rightarrow D^- \mu^+ \nu_\mu X$ mode. (left) Projection of the decay time, (right) projection of the charge asymmetry. The distribution of the fit residual divided by the error is shown below.

4.5 Detection asymmetries

This section is dedicated to the detection asymmetries, using the methods from Chapter 3. In the a_{sl}^d analysis they are grouped into three subsections. First, the asymmetry of the $\mu^+ \pi^-$ pair where π^- is the pion with the highest momentum, and the asymmetry of the $K^+ \pi^-$ pair where π^- is the pion with the lowest momentum are discussed. This is sketched by Fig. 4.17. Finally, the asymmetry from the muon trigger and PID is discussed.

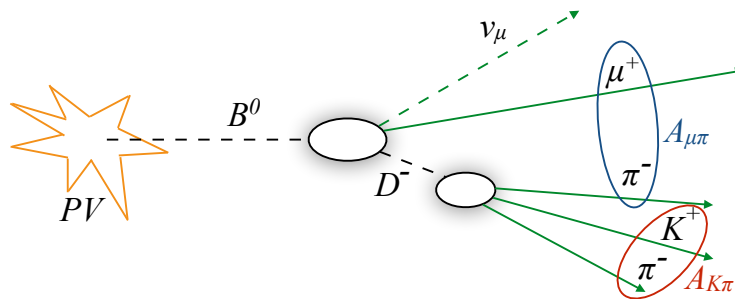


Figure 4.17: The detection asymmetry is split up into two pairs of opposite-charge tracks, shown here for the $B^0 \rightarrow D^- \mu^+ \nu_\mu X$ decay.

4.5.1 The $\mu^+\pi^-$ asymmetry

Section 3.1 describes two methods to determine the $\mu^+\pi^-$ tracking asymmetry, $A_{\mu\pi}$. The first is the J/ψ tag-and-probe method, which was still under development at the time when the a_{sl}^d analysis was performed. The other method is the D^* partial-and-full method, which was used in an earlier LHCb analysis of a_{sl}^s [48]. Using only the latter would result in a large systematic uncertainty. Therefore, an alternative approach to correcting the $\mu^+\pi^-$ asymmetry is chosen. Event weights are assigned such that the kinematic distributions of the highest-momentum pion in the $B^0 \rightarrow D^{*-}\mu^+\nu_\mu X$ and $B^0 \rightarrow D^-\mu^+\nu_\mu X$ signal samples match those of the signal muon. As motivated in Sec. 3.1 the tracking asymmetry of the charge-neutral $\mu^+\pi^-$ pair is expected to be zero when their kinematic distributions are the same. Figures 4.18 and 4.19 display the kinematic distributions of both particles where the background is subtracted using the *sPlot* method [100]. The pion is softer in momentum than the muon. The weights are obtained by dividing the kinematic distributions of both particles. The weights are then normalized by multiplying them with

$$w_{\text{eff}} = \frac{\sum_i w_i}{\sum_i w_i^2}, \quad (4.5.1)$$

where w_{eff} gives the statistical reduction of the original sample. In the $B^0 \rightarrow D^-\mu^+\nu_\mu X$ sample, a weighting in p_T is found to be sufficient, while in the $B^0 \rightarrow D^{*-}\mu^+\nu_\mu X$ sample a two-dimensional weighting in p_T and η is used. Figures 4.18 and 4.19 show how well the kinematic distributions overlap before and after weighting. The weighting reduces the effective signal yields by about 35% in the $B^0 \rightarrow D^-\mu^+\nu_\mu X$ mode, and 25% in the $B^0 \rightarrow D^{*-}\mu^+\nu_\mu X$, as shown in Table 4.2.

The residual tracking asymmetry due to the small remaining difference in the kinematic distributions is determined with the J/ψ tag-and-probe method (Sec. 3.1.1). It is found to be

$$A_{\mu\pi} = (0.00 \pm 0.02)\%, \quad (4.5.2)$$

and is considered as a systematic error on a_{sl}^d and A_P in both signal channels.

The potential asymmetry due to the hadronic pion interaction is estimated as described in Sec. 3.1.3. The upper limit resulting from the simulation study is 0.07%, and is assigned as a systematic error.

In addition, the asymmetry of the PID cut on the highest-momentum pion is determined with the method described in Sec. 3.3. The results, split by signal mode and magnet polarity, are shown in Table 4.6.

4.5.2 The $K^+\pi^-$ asymmetry

The asymmetry of the $K^+\pi^-$ pair, $A_{K\pi}$, is determined using calibration charm decays $D^- \rightarrow K^+\pi^-\pi^-$ and $D^- \rightarrow K_S^0(\rightarrow \pi^+\pi^-)\pi^-$ with the method described in Sec. 3.2. It is calculated as $A_{K^+\pi^-\pi^-} - A_{K_S^0\pi^-} - A_{K_S^0}$, where the kinematic distributions of the calibration samples are weighted, and $A_{K_S^0} = (-0.054 \pm 0.014)\%$.

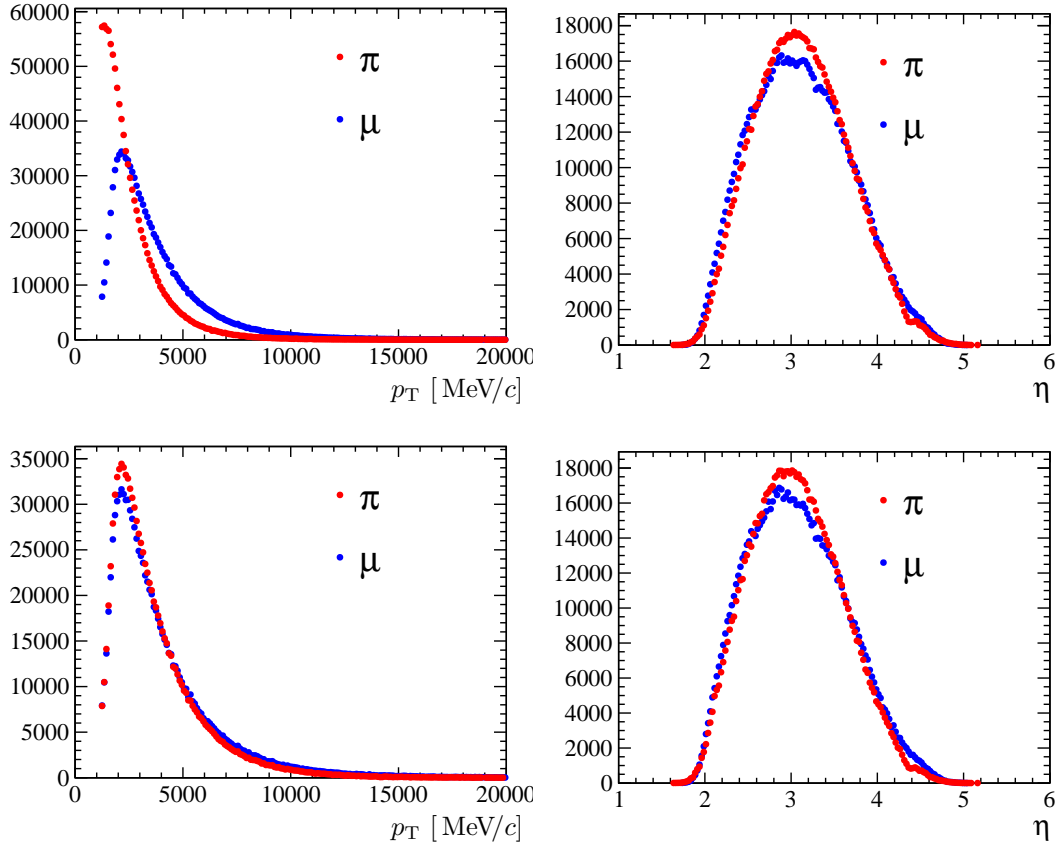


Figure 4.18: Distributions of (left) p_T and (right) pseudorapidity η of the muon compared to the highest-momentum pion for $B^0 \rightarrow D^- \mu^+ \nu_\mu X$ data sample collected in 2011, (top) before and (bottom) after weighting the pion p_T distribution to match that of the muon. The distributions in 2012 data are similar.

Table 4.6: Asymmetry [%] of the PID cut on the highest- p_T pion in the a_{sl}^d analysis, for each data-taking year and magnet polarity.

A_{PID} [%]	Magnet up	Magnet down
2011 D^-	-0.05 ± 0.01	0.05 ± 0.01
2011 D^{*-}	-0.27 ± 0.01	0.09 ± 0.01
2012 D^-	-0.03 ± 0.01	0.00 ± 0.01
2012 D^{*-}	-0.04 ± 0.01	-0.04 ± 0.01

The $K^+ \pi^- \pi^-$ and $K_S^0 \pi^+$ asymmetries are significantly affected by the weighting procedure used to match the kinematic distributions between calibration and signal samples, although the average of the magnet polarities varies only by about 0.1% (0.3%) in the $B^0 \rightarrow D^- \mu^+ \nu_\mu X$ ($B^0 \rightarrow D^{*-} \mu^+ \nu_\mu X$) mode. The resulting asymmetries are displayed in Table 4.7.

In the $B^0 \rightarrow D^{*-} \mu^+ \nu_\mu X$ mode the difference of the $K^+ \pi^-$ asymmetry between the two

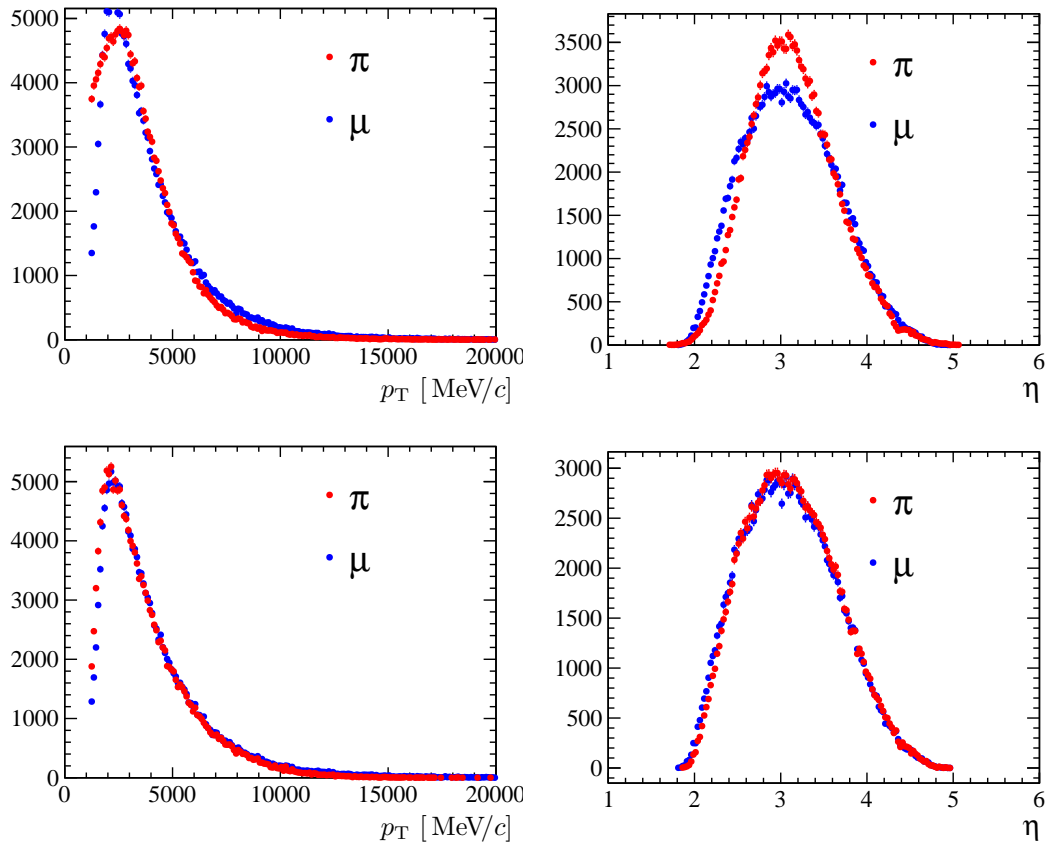


Figure 4.19: Distributions of (left) p_T and (right) pseudorapidity η of the muon compared to the leading pion for $B^0 \rightarrow D^{*-} \mu^+ \nu_\mu X$ data sample collected in 2011, (top) before and (bottom) after weighting the pion p_T and η distributions to match those of the muon. The distributions in 2012 data are similar.

magnet polarities is larger than that in the $B^0 \rightarrow D^- \mu^+ \nu_\mu X$ mode. This is because the pion in the $D^{*-} \rightarrow \bar{D}^0 \pi^-$ decay is very soft in momentum. This enhances the asymmetry due to PID criteria, as well as the asymmetry due to the material cross section and amount of material traversed. In order to determine the size of possible biases, the weighting procedure is varied as outlined in Sec. 3.2, and the fit models are varied. Any differences are assigned as a systematic error, of which the quadratic sum equates to 0.066% for the $B^0 \rightarrow D^- \mu^+ \nu_\mu X$ mode, and 0.098% for the $B^0 \rightarrow D^{*-} \mu^+ \nu_\mu X$ mode. The PID criterium on the kaon in the signal selection is the same as that of the calibration samples, such that no additional PID asymmetry on the $K^+ \pi^-$ pair needs to be evaluated.

4.5.3 The muon trigger and PID asymmetry

The detection asymmetry due to the muon trigger and PID, A_μ , is determined using the method outlined in Sec. 3.4. The selection on the muon that is probed is the hardware- and lower software-level trigger, as well as the muon PID criterium. The events in the calibration sample are weighted such that the kinematic distributions match those in the

Table 4.7: The weighted asymmetries for the $D^- \rightarrow K^+\pi^-\pi^-$ and $D^- \rightarrow K_s^0\pi^-$ modes, and the resulting value of $A_{K\pi}$ for the $B^0 \rightarrow D^-\mu^+\nu_\mu X$ and $B^0 \rightarrow D^{*-}\mu^+\nu_\mu X$ modes, where the K_s^0 asymmetry is taken into account.

	$A_{K\pi\pi}$ [%]	$A_{K_s\pi}$ [%]	$A_{K\pi}$ [%]
$B^0 \rightarrow D^-\mu^+\nu_\mu X$			
2011, Magnet up	2.25 ± 0.06	0.73 ± 0.23	1.58 ± 0.23
2011, Magnet down	1.61 ± 0.02	0.60 ± 0.19	1.07 ± 0.20
2012, Magnet up	2.09 ± 0.02	0.87 ± 0.13	1.27 ± 0.13
2012, Magnet down	1.57 ± 0.03	0.65 ± 0.13	0.97 ± 0.13
$B^0 \rightarrow D^{*-}\mu^+\nu_\mu X$			
2011, Magnet up	2.60 ± 0.00	0.70 ± 0.22	1.95 ± 0.22
2011, Magnet down	0.44 ± 0.01	0.50 ± 0.18	-0.01 ± 0.19
2012, Magnet up	2.33 ± 0.08	0.96 ± 0.12	1.42 ± 0.15
2012, Magnet down	0.74 ± 0.07	0.54 ± 0.12	0.25 ± 0.14

signal. The weighted asymmetries are summarized in Table 4.8. The observed difference between data-taking years is described in Sec. 3.4, and the asymmetry averaged over magnet polarities is consistent with zero. Since the kinematic distributions of the muon are identical between the $B^0 \rightarrow D^{*-}\mu^+\nu_\mu X$ mode and $B^0 \rightarrow D^-\mu^+\nu_\mu X$ modes, the muon asymmetry is expected to be the same within statistical variations of the signal sample, which is indeed the case. For the 2011 data, the look-up-table is applied to remove the bias from the p_T estimate of the L0 trigger, as discussed in Sec. 3.4.

The size of potential biases due to the choice of binning in the weighting procedure, as well as the choice of fit model, are determined by varying these choices, as discussed in Sec. 3.4. Any observed difference is assigned as a systematic uncertainty. The quadratic sum of these effects is included in Table 4.8.

 Table 4.8: Muon asymmetries in the α_{sl}^d analysis due to the trigger and muon PID [%]. The first error is the statistical error on the J/ψ samples, and the second is the total systematic error.

A_μ [%]	Magnet up	Magnet down
2011 D^-	$0.35 \pm 0.08 \pm 0.02$	$-0.23 \pm 0.08 \pm 0.03$
2011 D^{*-}	$0.31 \pm 0.08 \pm 0.03$	$-0.21 \pm 0.07 \pm 0.02$
2012 D^-	$-0.04 \pm 0.05 \pm 0.01$	$-0.03 \pm 0.05 \pm 0.01$
2012 D^{*-}	$-0.06 \pm 0.05 \pm 0.02$	$-0.02 \pm 0.05 \pm 0.01$

4.5.4 Summary

A summary of the detection asymmetries A_{det} is shown in Table 4.9. The total effect is calculated as the sum of the individual detection asymmetries, and used as input in the fits to the time-dependent decay rates.

Table 4.9: Overview of the detection asymmetries [%]. The errors are the statistical errors due to the size of the calibration samples only.

$A_{\text{det}} [\%]$	$B^0 \rightarrow D^- \mu^+ \nu_\mu X$	$B^0 \rightarrow D^{*-} \mu^+ \nu_\mu X$
2011 Magnet up		
A_{PID}	-0.05 ± 0.01	-0.27 ± 0.01
$A_{K\pi}$	1.58 ± 0.24	1.95 ± 0.22
A_μ	0.35 ± 0.08	0.31 ± 0.08
total	1.88 ± 0.25	1.99 ± 0.23
2011 Magnet down		
A_{PID}	0.05 ± 0.01	0.09 ± 0.01
$A_{K\pi}$	1.07 ± 0.20	-0.01 ± 0.19
A_μ	-0.23 ± 0.08	-0.21 ± 0.07
total	0.88 ± 0.21	-0.13 ± 0.20
2012 Magnet up		
A_{PID}	-0.03 ± 0.01	-0.04 ± 0.01
$A_{K\pi}$	1.27 ± 0.13	1.42 ± 0.15
A_μ	-0.04 ± 0.05	-0.06 ± 0.05
total	1.20 ± 0.14	1.32 ± 0.16
2012 Magnet down		
A_{PID}	0.00 ± 0.01	-0.04 ± 0.01
$A_{K\pi}$	0.97 ± 0.13	0.25 ± 0.14
A_μ	-0.03 ± 0.05	-0.02 ± 0.05
total	0.95 ± 0.14	0.20 ± 0.15

4.6 Results

Taking into account the detection asymmetries as discussed in Sec. 4.5, the simultaneous fit to the D^- (\bar{D}^0) mass, B^0 decay time and muon charge, described in Sec. 4.4, is applied to the data. The data is binned in each dimension, as is allowed due to the large size of the data sample. The fits are performed on the data for each magnet polarity and data-taking year, and are shown in Appendix B. Figure 4.20 shows the time-dependent decay rates for both modes, as well as the charge asymmetry, for both data-taking years and magnet polarities combined. The obtained values for a_{sl}^d and A_P are shown in Table 4.10. The correlation between a_{sl}^d and A_P in the fits is small.

The combination of the individual values of a_{sl}^d is made by performing an arithmetic (unweighted) average of the results for each magnet polarity. Then, an average over the two data-taking years is made, weighted by the respective luminosity. Finally, a weighted

average is made over the two signal channels. This results in

$$\begin{aligned}
 B^0 \rightarrow D^- \mu^+ \nu_\mu X : a_{\text{sl}}^d &= (-0.19 \pm 0.21 \pm 0.30)\% \\
 B^0 \rightarrow D^{*-} \mu^+ \nu_\mu X : a_{\text{sl}}^d &= (0.77 \pm 0.45 \pm 0.34)\% \\
 \text{Combined} : a_{\text{sl}}^d &= (-0.02 \pm 0.19 \pm 0.30)\%
 \end{aligned} \tag{4.6.1}$$

where the first error is the combined statistical error resulting from the fits, and the second error is the systematic error resulting from the studies done in the next section. The systematic error is assumed to be fully correlated between the $B^0 \rightarrow D^- \mu^+ \nu_\mu X$ mode and $B^0 \rightarrow D^{*-} \mu^+ \nu_\mu X$ mode. The production asymmetry is found to be

$$\begin{aligned}
 A_P(7 \text{ TeV}) &= (0.66 \pm 0.26 \pm 0.22)\% \\
 A_P(8 \text{ TeV}) &= (0.48 \pm 0.15 \pm 0.17)\%,
 \end{aligned} \tag{4.6.2}$$

where A_P is shown for each centre-of-mass energy separately, due to the expected dependence. A discussion of these results is given in Chapter 6.

4.7 Systematic uncertainties

The largest systematic uncertainty is due to the limited size of the calibration samples used in the determination of A_{det} . This error is included in the systematic uncertainty on a_{sl}^d .¹ The determination of the statistical error on A_{det} is described in Sec. 4.5, along with the systematic error. The propagation of these uncertainties to a_{sl}^d and A_P is done by generating a sample using the nominal decay-time model, with enough events to be able to neglect effects due to statistical fluctuations. Fits to this large simulated sample with the same model are then applied, only with the parameter of interest varied by plus or minus its error. The deviation of the obtained values of a_{sl}^d and A_P is taken as a systematic uncertainty.

¹This is in contrast to the a_{sl}^s analysis in the next chapter, where the statistical uncertainty on A_{det} is included in the total statistical uncertainty on a_{sl}^s . This follows from the different approaches made in these analyses.

Table 4.10: Results of the nominal fits to data in [%], for the four subsamples of both signal modes.

Data Sample	$B^0 \rightarrow D^- \mu^+ \nu_\mu X$		$B^0 \rightarrow D^{*-} \mu^+ \nu_\mu X$	
	a_{sl}^d	A_P	a_{sl}^d	A_P
2011 Magnet Down	0.45 ± 0.54	1.09 ± 0.37	2.63 ± 1.18	0.92 ± 0.80
2011 Magnet Up	-1.94 ± 0.62	0.25 ± 0.0043	-1.29 ± 1.35	0.28 ± 0.93
2012 Magnet Down	0.40 ± 0.34	0.78 ± 0.24	1.80 ± 0.74	1.54 ± 0.52
2012 Magnet Up	-0.39 ± 0.33	0.00 ± 0.23	-0.18 ± 0.72	0.18 ± 0.50
All	-0.19 ± 0.21	0.47 ± 0.14	0.77 ± 0.45	0.79 ± 0.31

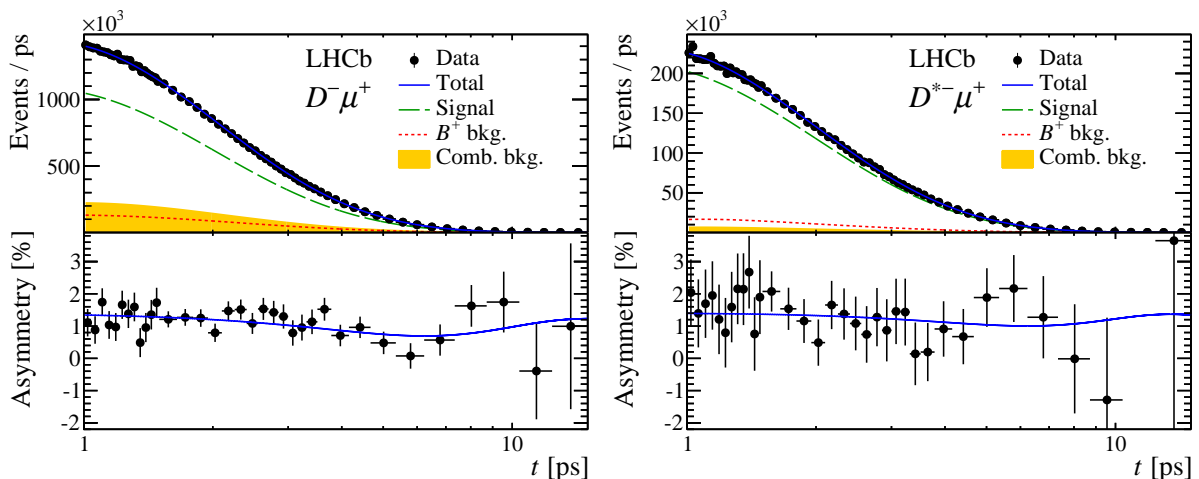


Figure 4.20: Decay rate and charge asymmetry versus decay time for (left) the $B^0 \rightarrow D^- \mu^+ \nu_\mu X$ sample and (right) the $B^0 \rightarrow D^{*-} \mu^+ \nu_\mu X$ sample. The data from the two data-taking years and magnet polarities are combined and the fit results are overlaid. The number of bins in the asymmetry plots is reduced for clarity. The visible asymmetry in these plots is fully attributed to the non-zero detection and production asymmetries (not to a non-zero value of a_{sl}^d).

The second largest source of systematic error is due to the modelling of the B^+ background, and is determined in Sec. 4.7.1. Errors due to other backgrounds are determined in Sec. 4.7.2. Systematic biases from the k -factor approach are studied in Sec. 4.7.3, and other sources of systematic uncertainty in the fit model are determined in Sec. 4.7.4. A breakdown of all systematic errors on a_{sl}^d and A_P is shown in Table 4.11.

4.7.1 B^+ background

Since the B^+ background is almost indistinguishable from the signal, its fraction and the parameters of its decay-time model are fixed in the nominal fit. The uncertainty on the B^+ production asymmetry is obtained from external measurements (see Sec. 4.4.5), and found to be $A_{P,B^+} = (-0.6 \pm 0.6)\%$. Varying A_{P,B^+} within its uncertainty in the fit to the large simulated sample results in a systematic error of 0.12% on a_{sl}^d and 0.06% on A_P .

There are a few additional uncertainties regarding the B^+ background that are considered. The uncertainty on the fraction of the B^+ background is propagated to a_{sl}^d and A_P using the method with the large simulated sample described above, resulting in an uncertainty of 0.03% on a_{sl}^d . The parameters of the B^+ decay-time acceptance are determined from a fit to simulated events as described in Sec. 4.4.5. The uncertainties on these parameters are due to the simulated sample size, and are varied simultaneously in the fit to the large simulated sample, taking into account the correlations between the parameters. The effect is found to be negligible. The nominal decay-time description of the B^+ background is simplified by ignoring the convolutions with the k -factors and decay length error, and absorbing these effects in the other parameters. Using a decay-time

model for the B^+ background similar to that of the signal is limited by the statistical power of the simulated B^+ sample. The k -factors obtained from the simulated B^+ sample are shown in Fig. 4.21 (left). The fit to signal data using the complete description for the B^+ background, including k -factor convolution and upper decay-time acceptance, results in a value for a_{sl}^d that differs by 0.02% from the nominal fit. This is taken as a systematic error.

4.7.2 Other backgrounds

There are two significant background contributions present in the simulation cocktail of Sec. 4.3 that do not have a separate decay-time model. The first is the contribution of B_s^0 decays (for instance from $B_s^0 \rightarrow D_s^- D^+$, with $D_s^- \rightarrow \phi \mu^- \nu$ decays), contributing about 2% to the signal. The fast oscillations from the B_s^0 mixing are completely washed out by the poor decay-time resolution of the partially reconstructed decays. Therefore, the time-dependent decay rates are similar to that of the B^+ component, but without any production asymmetry (see also Appendix A). To assess the effect of this contribution, the high-statistics sample is fitted with an additional component describing the B_s^0 contribution, with a fixed fraction of 2%. The assigned systematic error is 0.03%.

The second background to consider are the $B^0 \rightarrow DDX$ -type decays where D is any charm meson, which contribute $(0.9 \pm 0.4)\%$ to the total, and are treated as signal decays. They have a smaller k -factor due to the larger number of missing particles. The relatively large uncertainty on this fraction could affect the uncertainty on the k -factor distribution. The effect this has on the measurement of a_{sl}^d is determined by varying the fraction of

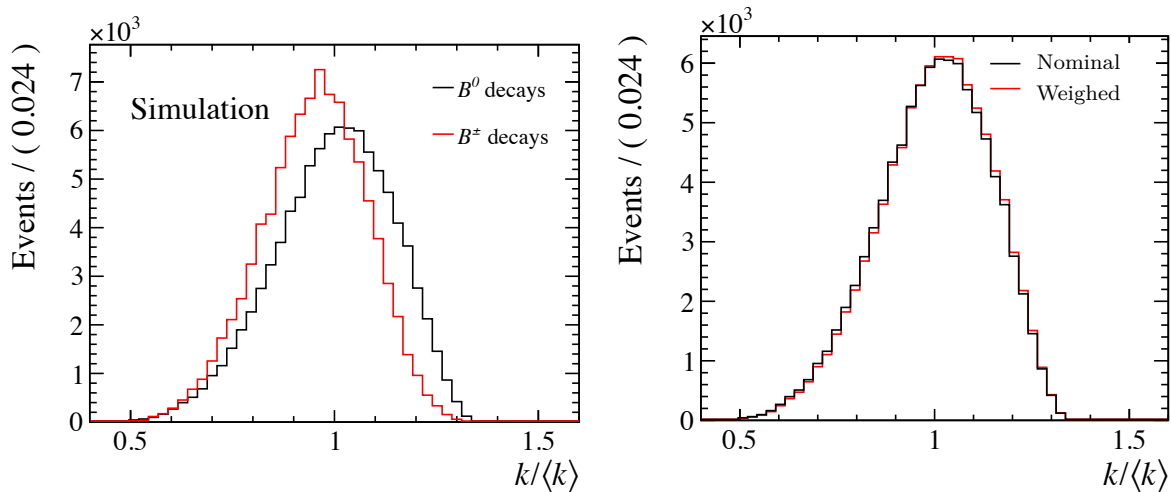


Figure 4.21: (left) Difference of the corrected k -factor distributions obtained from B^0 decays and B^+ decays. (right) Comparison of the default corrected k -factor distribution (“nominal”) with the corrected k -factor distribution obtained when first applying weights to the simulated sample to match the momentum distribution in simulation to that in data, using fully reconstructed $B^+ \rightarrow J/\psi K^+$ decays (“weighed”).

another decay with many missing particles, namely $B^0 \rightarrow D^* \tau X$, by 2% when determining the k -factor. The effect on a_{sl}^d is found to be negligible.

A last source of potential backgrounds are baryonic decays of the type $\Lambda_b^0 \rightarrow D^{(*)+} \mu^- \bar{\nu}_\mu X$, where X represents any neutral baryonic state. Simulated events of this type of decays were not available at the time of this analysis, and are not included in the cocktail described in Sec. 4.3. Instead, their contribution is estimated using various measurements available. The fraction of background from $\Lambda_b^0 \rightarrow D^{(*)+} \mu^- \bar{\nu}_\mu X$ decays is estimated to be roughly 2% using the ratio of Λ_b^0 to B^0 production cross sections [105], simulated efficiencies, and the branching ratio of $\Lambda_b^0 \rightarrow D^0 p \pi^-$ relative to that of $\Lambda_b^0 \rightarrow \Lambda_c^+ \pi^-$ decays [106]. The Λ_b^0 production asymmetry is estimated to be $(-0.9 \pm 1.5)\%$, determined from the raw asymmetry observed in $\Lambda_b^0 \rightarrow J/\psi p K^-$ [107] and subtracting kaon and proton detection asymmetries. The uncertainty on the Λ_b^0 production asymmetry results in a systematic uncertainty on a_{sl}^d of 0.07%.

4.7.3 Uncertainties on the k -factor

The decay-time model relies on a good description of the k -factors, which are obtained from simulation. A possible mismodelling of the production and/or decay models in the simulation could have an effect on the decay-time fit.

The production model is tested by comparing the momentum spectra of beauty mesons in data and simulation. This is done using the fully reconstructed decay mode $B^+ \rightarrow J/\psi K^+$. Weights are obtained as a function of $p(B^+)$ in order to match the momentum distribution of the simulated B^+ mesons to that of the data. These weights are then applied to the B^0 signal simulation and new k -factors are determined. This is shown in Fig. 4.21 (right). The effect of using this data-weighted variation of the k -factor histogram on a_{sl}^d and A_P is found to be negligible.

Concerning the decay model, the contribution of the various decays in the signal simulation cocktail to the k_{corr} histogram is shown in Fig. 4.22. The branching ratios assumed for the various decays in this cocktail have an uncertainty [94]. In the $B^0 \rightarrow D^- \mu^+ \nu_\mu X$ cocktail, about 44% of events originate from $B^0 \rightarrow D^- \mu^+ \nu_\mu$ decays which has an absolute error on the branching fraction of about 2.5%. Another 44% comes from $B^0 \rightarrow D^{*-} \mu^+ \nu_\mu$ decays (where $D^{*-} \rightarrow D^- X$) or higher resonances, of which the error on the branching ratio is about 2%. In order to take into account other yet unknown decays, both fractions are separately increased by 10% in the determination of alternative k -factors. The deviation when using these alternative k -factors on the value of a_{sl}^d is found to be about 0.02% for the $B^0 \rightarrow D^- \mu^+ \nu_\mu X$ mode, and negligible for the $B^0 \rightarrow D^{*-} \mu^+ \nu_\mu X$ mode.

4.7.4 Other fit-related systematic uncertainties

The mixing frequency Δm_d is assumed from the world-average value [94], and is fixed in the fit for both the signal mode and the sidebands. The error on the world average is

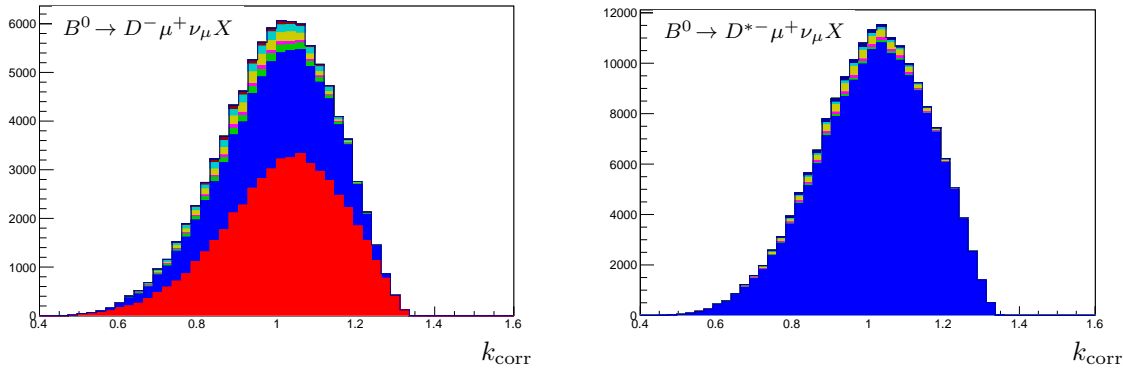


Figure 4.22: (left) Contribution of the various resonant decay modes to the k -factor distribution in the simulated D^- sample. The contribution from $B^0 \rightarrow D^- \mu^+ \nu_\mu X$ decays is highlighted in red, that of $B^0 \rightarrow D^{*-} (\rightarrow D^- \{\pi^0, \gamma\}) \mu^+ \nu_\mu$ in blue, while contributions from other resonances, tau decays and non-resonant decays are stacked on top. (right) The same composition plot for the D^* sample, where the contribution from $B^0 \rightarrow D^{*-} (\rightarrow \bar{D}^0 \pi^-) \mu^+ \nu_\mu$ is indicated in blue.

0.004 ps⁻¹, and the error is propagated to a_{sl}^d and A_P using the high-statistics simulated sample described above. The effect on a_{sl}^d is 0.02%.

A possible mismodelling of the lower decay-time acceptance might affect the measurement. The effect is estimated by changing the starting point of the decay time in the fit from 1.0 ps to 0.4 ps in the fit to data. The turn-on effect of the acceptance now plays a more important role. This is reflected in a reduced error for the acceptance turn-on parameters α and t_{shift} , and the change in their correlation. The value for the upper acceptance parameter β remains unchanged. The sensitivity to a_{sl}^d is similar, although the error on A_P somewhat decreases. This is because for B^0 decay times close to zero, the measured asymmetry (Eq. 4.1.1) is proportional to $A_P + A_{\text{det}}$. The change in central value of a_{sl}^d is negligible, but the effect on A_P is 0.07%. In addition, the effect of a quadratic upper-decay-time acceptance model is tested, which is of the form $1 + \beta t + \gamma t^2$ (c.f. Eq. 4.4.11), as used in studies of $B_s^0 \rightarrow J/\psi \phi$ in LHCb [28]. A sample is generated from the signal model using the quadratic shape, where $\beta = 0.003$ and $\gamma = -0.002$, while a fit is applied with the nominal decay-time acceptance. The deviation of a_{sl}^d is found to be 0.03%.

The flight-distance resolution used to convolve the decay-time model of the signal in Sec. 4.4.3 is obtained from a triple-Gaussian fit to the simulation. In order to test the effect of an underestimated flight-distance resolution, the widths of the triple-Gaussian are doubled. Even in this very conservative test, no significant change in the obtained values for a_{sl}^d or A_P is observed.

The model for the fit to the D^- (\bar{D}^0) mass distribution is the sum of a Crystal Ball function with a Gaussian function, as described in Sec. 4.2. Any effect of mismodelling the mass shape is expected to be similar for both charge-conjugate final states, such that the effect on a_{sl}^d is negligible. Nevertheless, the impact of the choice of parametrization is

determined by using an alternative fit model using the sum of two Gaussian shapes. The effect on a_{sl}^d and A_P is found to be negligible. Furthermore, the choice of binning in decay time and D^- or D^{*-} mass is varied, and found to have a negligible effect on a_{sl}^d and A_P .

Finally, the errors on all fixed fit parameters that are not mentioned above are varied within plus or minus one times their error. Their effect on a_{sl}^d is determined with the high-statistics method, and listed in Table 4.11.

Table 4.11: Overview of all contributions to the systematic uncertainty on a_{sl}^d and A_P . Entries marked with “-” are found to be negligible. When different from the $B^0 \rightarrow D^- \mu^+ \nu_\mu X$ mode, the value for the $B^0 \rightarrow D^{*-} \mu^+ \nu_\mu X$ mode is given in parentheses. The contributions from the individual detection asymmetries are multiplied by two (see Eq. 4.1.1) to estimate the effect on a_{sl}^d , while the effect of the total detection asymmetry on a_{sl}^d and A_P is estimated with a high-statistics simulated sample, as explained in the text.

Source of uncertainty	a_{sl}^d	A_P (7 TeV)	A_P (8 TeV)
B^+ background:			
B^+ production asymmetry	0.12	0.06	0.06
B^+ fraction	0.03	0.01	0.01
B^+ acceptance	-	-	-
B^+ decay time model	0.02	0.01	0.01
Other backgrounds:			
B_s^0 component	0.03	0.01	0.01
A_b^0 component	0.07	0.03	0.03
$B^0 \rightarrow D^{(*)-} D_s^+$ decays	-	-	-
k-factor distribution	0.02 (0.01)	0.01 (-)	0.01 (-)
Knowledge of Δm_d:	0.02	0.01	0.01
Other fit related systematics:	0.04 (0.03)	0.07	0.07
Detection asymmetry:	0.26 (0.30)	0.20 (0.21)	0.14 (0.17)
$A_{K\pi}$			
Statistical uncertainty	0.16(0.18)	0.15 (0.14)	0.09(0.10)
Systematic uncertainty	0.13 (0.20)	0.07 (0.10)	0.07 (0.10)
A_μ			
Statistical uncertainty	0.06	0.06	0.03
Systematic uncertainty	0.06	0.03	0.03
A_{PID}	0.07	0.04	0.04
$A_{\mu\pi}$	0.04	0.02	0.02
Quadratic sum	0.30 (0.34)	0.22 (0.23)	0.17 (0.20)

4.7.5 Further consistency checks

The results for magnet polarity up and down are expected to be statistically compatible, when taking into account the detection asymmetries. Due to the large correlation of the systematic uncertainties, only the statistical error from the fit and the statistical component of the error on the detection asymmetry are considered, and added in quadrature. The comparison is shown in Fig. 4.23. In the 2011 data, the compatibility of a_{sl}^d is around two standard deviations. This discrepancy reduces to a little over one standard deviation for the larger-statistics 2012 sample. The production asymmetry is compatible in all scenarios. It should be noted that the size of some systematic uncertainties on the detection asymmetries depend on the magnet polarity. An example is the variation of binning in the weighting step of the $K^+\pi^-$ asymmetry. This is not taken into account in this comparison, and might explain the differences between the results for magnet polarity up and down.

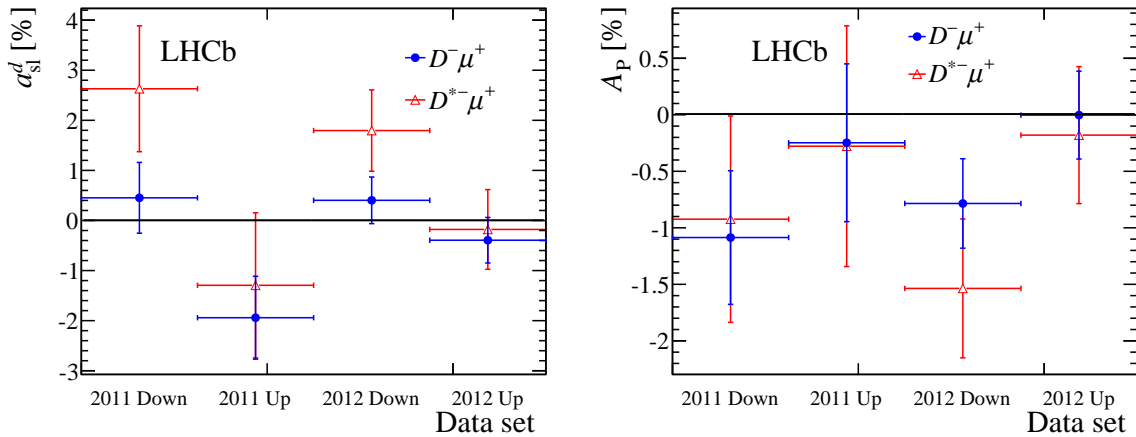


Figure 4.23: Results for (left) a_{sl}^d and (right) A_P on samples divided by year and magnetic field polarity. In blue is the $B^0 \rightarrow D^- \mu^+ \nu_\mu X$ mode, in red the $B^0 \rightarrow D^{*-} \mu^+ \nu_\mu X$ mode.

A check is done on the $B^0 \rightarrow D^- \mu^+ \nu_\mu X$ sample by placing fiducial cuts where the muon asymmetry is large. Large asymmetries occur in momentum regions where muons of one charge are bent out of the geometrical acceptance, depending on the magnet polarity. In addition, the region where muons of one charge pass through different quadrants of the muon stations (e.g. from left to right) is removed. The regions are defined as

$$\begin{aligned}
 &|p_x| < 0.317(p - 3400 \text{ MeV}/c), \\
 &|p_x| < 600 \text{ MeV}/c \quad \text{or} \quad |p_x| > 1100 \text{ MeV}/c,
 \end{aligned} \tag{4.7.1}$$

and remove about 10% of data. The resulting values for A_P are compatible with the nominal results. The values for a_{sl}^d are compatible within their statistical error.

It is possible that the detection asymmetries are affected by changes in software or hardware over periods of time. Therefore, the data are split up into seven run periods over 2011 and 2012. The detection asymmetries are found to be stable over these periods. The nominal fit is repeated for each period, and the values of a_{sl}^d are found to be stable as

well, as shown in Fig. 4.24 (left). Furthermore, in case there is more than one PV in the event, it is possible that the B decay is associated to the wrong PV and the decay time is biased. Therefore, the data are split up into events with one, two and more than two PVs. The decay-time distributions are found to be very similar, and the values of a_{sl}^d and A_P are consistent, as shown in Fig. 4.24 (right). These consistency checks give confidence in the result and show that the systematic uncertainty is correctly estimated.

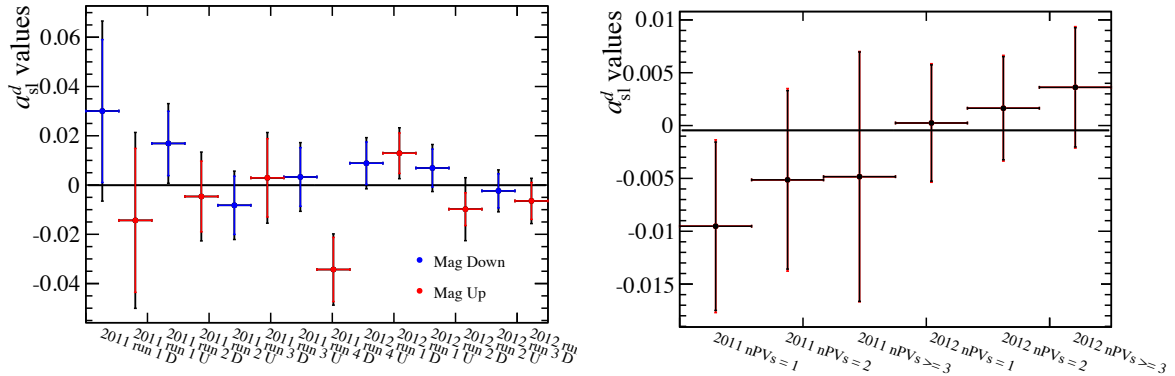


Figure 4.24: Results of a_{sl}^d using the $B^0 \rightarrow D^- \mu^+ \nu_\mu X$ mode, split up into (left) run blocks and (right) number of PVs.

5

CP violation in mixing of B_s^0 mesons

This chapter details the analysis of *CP* violation in mixing of B_s^0 mesons, which is quantified by the parameter a_{sl}^s . This measurement is published in Ref. [108]. The definition of this parameter is outlined in Sec. 1.2.8, and the measurement employs the techniques from Sec. 3 to determine the detection asymmetries.

5.1 Method

The B_s^0 decays are reconstructed in the decay channel

$$B_s^0 \rightarrow D_s^- \mu^+ \nu_\mu X \quad \text{with} \quad D_s^- \rightarrow K^- K^+ \pi^-$$

and their charge-conjugate modes, where the X represents any number of additional particles — besides the neutrino — that are not explicitly reconstructed in the decay. The decay topology is illustrated by Fig. 5.1, and is similar to the a_{sl}^d analysis as the only difference is that the $D^- (\rightarrow K^+ \pi^- \pi^-)$ is replaced by $D_s^- (\rightarrow K^+ K^- \pi^-)$. Also, here in the a_{sl}^s analysis the non-reconstruction of the additional particles results in a broad invariant mass peak for the B_s^0 candidates.

In contrast to the a_{sl}^d analysis, due to the fast mixing frequency Δm_s the time-dependent effect washes out and it is sufficient to measure the time-integrated asymmetries (see Sec. 1.2.8). The measured asymmetry in the charge-conjugated signal candidates is

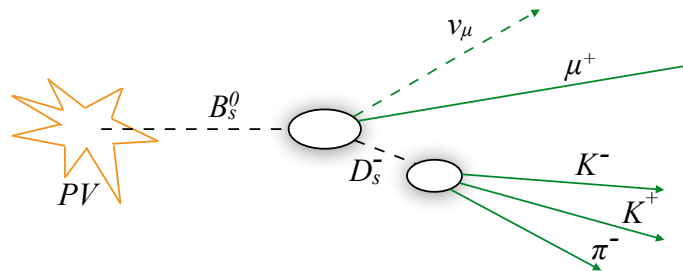


Figure 5.1: Decay topology of the a_{sl}^s signal decay mode.

corrected for the effect of backgrounds and for the detection asymmetry in order to obtain a_{sl}^s , as in Eq. 1.2.43. It is rewritten here for convenience,

$$A_{\text{meas}} = \frac{N(D_s^- \mu^+) - N(D_s^+ \mu^-)}{N(D_s^- \mu^+) + N(D_s^+ \mu^-)},$$

$$a_{\text{sl}}^s = \frac{2}{1 - f_{\text{bkg}}} (A_{\text{meas}} - A_{\text{det}} - f_{\text{bkg}} A_{\text{bkg}}) \quad (5.1.1)$$

Here, f_{bkg} is the fraction of peaking backgrounds that dilute the measurement of a_{sl}^s , and A_{bkg} is the total (production + physics) asymmetry of these backgrounds that can bias the value of a_{sl}^s . The selection of data is described in Sec. 5.2, where non-peaking backgrounds are reduced. The contribution of peaking backgrounds, originating from other b -hadron decays, is determined in Sec. 5.3, the relevant detection asymmetries are discussed in Sec. 5.4 and the results are shown in Sec. 5.5.

5.2 Selection

Similar to the a_{sl}^d analysis, this analysis makes use of the full LHCb dataset obtained during run 1 of the LHC. This equals integrated luminosities of 1.0 fb^{-1} at a centre-of-mass energy of 7 TeV obtained in 2011, and 2.0 fb^{-1} at 8 TeV obtained in 2012.

The event is required to be triggered by the muon from the semileptonic B_s^0 decay on the hardware level. At the first software stage, the event is required to be triggered by the muon only (`Hlt1TrackMuon`), or any of the tracks using a more stringent trigger (`Hlt1TrackAllL0`). At the second software stage, the decay topology of the reconstructed B_s^0 candidate is required to be consistent with a b -hadron decay. The precise requirements made in the trigger are described in Sec. 2.4.

In the offline selection, standard quality requirements on the reconstructed tracks and vertices are made to form B_s^0 signal candidates. Similar as in the a_{sl}^d analysis, the final-state tracks are required to not point back to the primary vertex, in order to reduce backgrounds from promptly produced particles. An additional selection is made to reduce various sources of backgrounds, some of which are similar to those in the a_{sl}^d analysis. The decay $D_s^- \rightarrow K^+ K^- \pi^-$ can occur through resonant states, which are treated separately in this analysis.¹ The dominant resonances are the $\phi(1020) \rightarrow K^+ K^-$ and the $K^*(892) \rightarrow K^+ \pi^-$ decays, which are visible in the invariant mass of two-daughter combinations, as shown in Fig. 5.2. Three regions in this so-called Dalitz plane of the $D_s^- \rightarrow K^+ K^- \pi^-$ decay are selected:

- $\phi\pi$: Invariant mass of the $K^+ K^-$ pair within $\pm 20 \text{ MeV}/c^2$ of the narrow ϕ mass of $1020 \text{ MeV}/c^2$,
- K^*K : Invariant mass of the $K^+ \pi^-$ pair within $\pm 90 \text{ MeV}/c^2$ of the broader K^* mass of $892 \text{ MeV}/c^2$,

¹In the a_{sl}^d analysis, there is a large overlap between resonances in the $D^- \rightarrow K^+ \pi^- \pi^-$ decay, and they are not separated.

- NR : non-resonant, i.e. all remaining phase space ,

which have different amounts of background, as well as different kinematic distributions for the daughter $K^+K^-\pi^-$ particles. Therefore, the selection is optimized separately for each of the three regions. The largest signal-to-background ratio is obtained in the $\phi\pi$ region, followed by the K^*K region. Since the sample contains less background, the $\phi\pi$ region has looser PID requirements compared to the selection used for the K^*K and NR regions.

The value for a_{sl}^s will be determined separately for each magnet polarity, data-taking year and Dalitz region, and checked for consistency between these twelve values. Then, the raw asymmetry and various detection asymmetries will be averaged, and combined to obtain the overall value for a_{sl}^d .

5.2.1 Removal of identifiable backgrounds

Contributions from backgrounds under the D_s^- invariant mass peak are further reduced with specific selection criteria. Most of these backgrounds originate from misidentification of the kaon that has the same sign as the D_s^- candidate. These identifiable background contributions can be visualized by using the momentum asymmetry of this kaon (here K^-) with respect to the other two particles,

$$\beta = \frac{p_{K^+} + p_{\pi^-} - p_{K^-}}{p_{K^+} + p_{\pi^-} + p_{K^-}}. \quad (5.2.1)$$

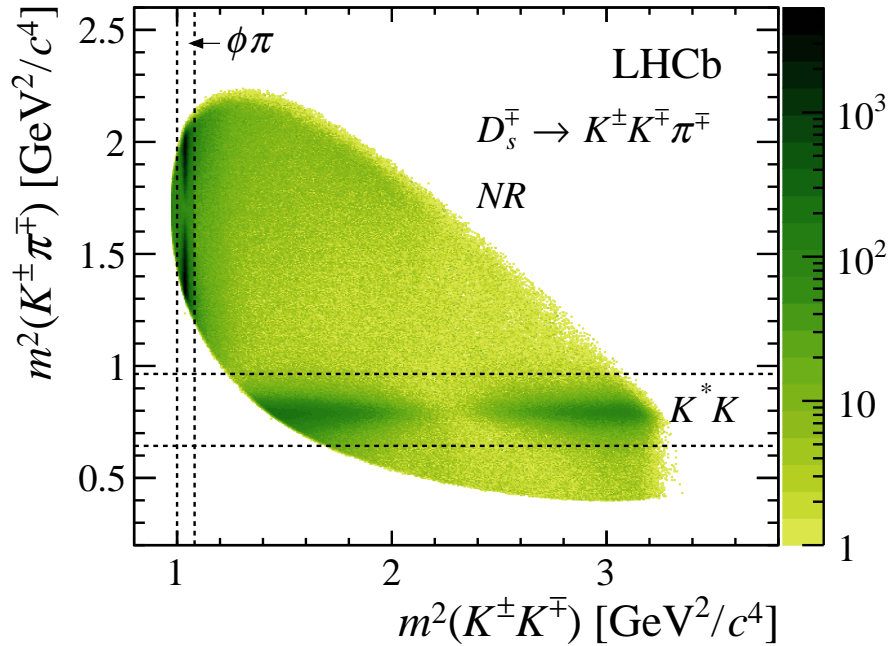


Figure 5.2: Dalitz plot of the $D_s^- \rightarrow K^- K^+ \pi^-$ decay for selected $D_s^- \mu^+$ candidates, with the three selection regions indicated. To suppress combinatorial background, a narrow invariant mass window, between 1950 and 1990 MeV/c^2 , is required for the D_s^- candidates in this plot.

When looking at the invariant mass $M_{K^-K^+\pi^-}$ versus β for all D_s^- candidates, the contributions from misidentified K^- backgrounds have a well-defined dependence on β , while correctly identified candidates have no dependence on β . The D_s^- candidate invariant mass is different for either the correct hypothesis m_{K^-} or an alternative wrong hypothesis m_{alt} . This difference can be parametrized as

$$M_{K^-K^+\pi^-}^2 - M_{\text{alt}}^2 \approx (m_{K^-}^2 - m_{\text{alt}}^2) \frac{2}{1 - \beta}, \quad (5.2.2)$$

which follows from relativistic mechanics, and where an approximation is made for $m/p \ll 1$ for all final-state particles. M_{alt}^2 is the D_s^- candidate mass under a mass hypothesis m_{alt} of the K^- candidate.

The left column of Fig. 5.3 shows these plots for the three different Dalitz regions. The signal is seen as a band around 1970 MeV/ c^2 , and the correctly identified but Cabibbo-suppressed $B_s^0 \rightarrow D^-(K^-K^+\pi^-)\mu^+\nu_\mu$ decays are visible in these plots around 1870 MeV/ c^2 .

The reduction of the non-peaking backgrounds is optimized using simulated events, combined with studies on data using the sidebands around the D_s^- peak. In general, misidentified backgrounds are reduced by requiring an additional neural-net-based PID cut on the same-sign kaon for all three Dalitz regions. Specific backgrounds are reduced further by applying a veto under certain mass hypotheses, as is done in the a_{sl}^d analysis in Sec. 4.2. A list of veto criteria that are applied is summarized in Table 5.1.

In all modes there is a clear contribution from misidentified $\bar{A}_b^0 \rightarrow A_c^+(p^-K^+\pi^-)\mu^+\nu_\mu$ decays. These decays are especially abundant in the K^*K and NR samples. They are reduced by applying a tight PID cut on the kaon with the same sign as the D_s^- , when the invariant mass of the D_s^- candidate under the proton hypothesis for the kaon, $M(K_p^-K^+\pi^-)$, is within 27 MeV/ c^2 of the \bar{A}_c^- mass. The subscript p^- denotes which particle was misidentified.

In the K^*K and NR samples the contribution from misidentified $B^0 \rightarrow D^-(\pi^-K^+\pi^-)\mu^+\nu_\mu$ decays is removed by applying a similar a cut if the invariant mass

Table 5.1: Summary of the applied vetoes used to reduce specific non-peaking backgrounds under the D_s^+ mass peak, in order of appearance in the text. The subscript of a particle denotes the (misidentified) mass hypothesis that is applied.

Veto	Veto if	Applied to
$A_c^+ \rightarrow p_K K \pi$	$K^+ \text{ DLL}_{p-K} > 0.0$ and $2261 < m(K_p^+ K^- \pi^+) < 2315 \text{ MeV}/c^2$	$\phi\pi$
$A_c^+ \rightarrow p_K K \pi$	$K^+ \text{ DLL}_{p-K} > -15.0$ and $2261 < m(K_p^+ K^- \pi^+) < 2315 \text{ MeV}/c^2$	K^*K, NR
$D^+ \rightarrow \pi_K K \pi$	$K^+ \text{ DLL}_{K-\pi} < 30.0$ and $ m(K_\pi^+ K^- \pi^+) - 1870 < 20 \text{ MeV}/c^2$	K^*K, NR
$D^*(\rightarrow D^0(\rightarrow K \pi_K \pi \pi))$	$K^+ \text{ DLL}_{K-\pi} < 7.0$ and $m(K_\pi^+ K^-) < 800 \text{ MeV}/c^2$	K^*K, NR
$D^*(\rightarrow D^0 \pi_K)$	$m(K_\pi^+ K^- \pi^+) - m(K^- \pi^+) < 175 \text{ MeV}/c^2$	K^*K, NR
$D^*(\rightarrow D^0 \pi_K)$	$m(K^+ K_\pi^- \pi^+) - m(K^+ \pi^+) < 175 \text{ MeV}/c^2$	K^*K, NR
$D \rightarrow K^*(892)^0(\rightarrow K \pi_K) \pi$	$K^+ \text{ DLL}_{K-\pi} < 8.0$ and $ m(K_\pi^+ K^-) - 892 < 25 \text{ MeV}/c^2$	K^*K, NR
$J/\psi \rightarrow \mu_\pi \mu$	π^+ in muon stations, $3042 < m(\pi_\mu^+ \mu^-) < 3147 \text{ MeV}/c^2$	$\phi\pi, K^*K, NR$
$J/\psi \rightarrow \mu_K \mu$	K^+ in muon stations, $3042 < m(K_\mu^+ \mu^-) < 3147 \text{ MeV}/c^2$	K^*K, NR
$D^{*+} \rightarrow D^0(K^+ K^-) \pi^+$	$135 < m(K^+ K^- \pi^+) - m(K^+ K^-) < 152 \text{ MeV}/c^2$	NR

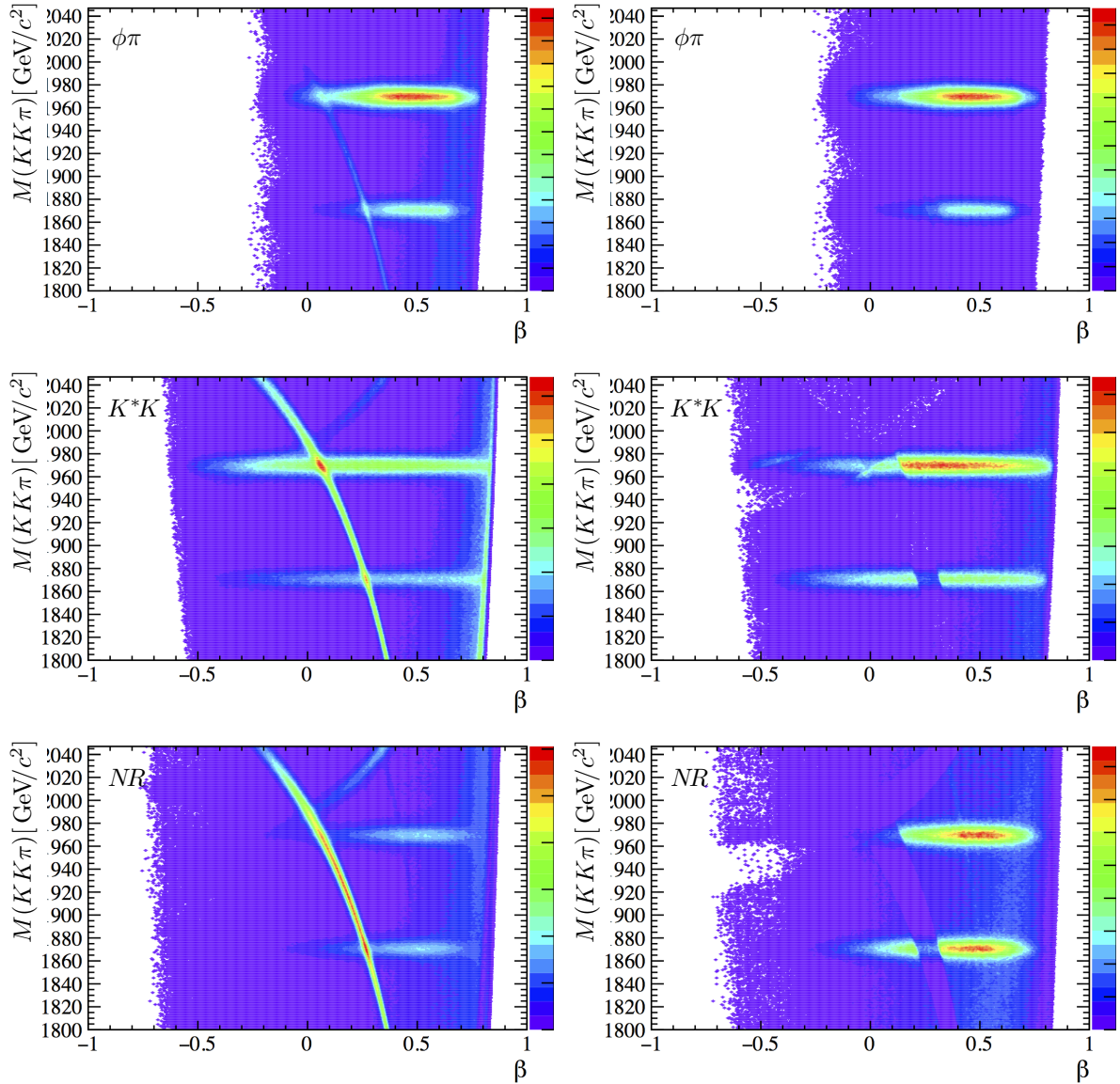


Figure 5.3: $M_{K^+K^-\pi^+}$ versus the momentum asymmetry of the same-sign kaon, β (Eq. 5.2.1), for (top) the $\phi\pi$ region, (middle) the K^*K region, and (bottom) NR region, (left) before and (right) after the vetoes in Table 5.1 and the neural-net-based PID criterium. The horizontal bands correspond to the correctly identified D_s^- and (Cabibbo-suppressed) D^- decays, while the downward-curving and upward-curving bands in the plots correspond to the misidentified \bar{L}_c^- and D^- backgrounds, respectively. The contribution from $D^{*-} \rightarrow D^0(\rightarrow K^+\pi^-\pi^+\pi^-)\pi^-$ decays is seen as a faint band on the right side of the plots.

$M(\pi^- K^- K^+ \pi^-)$ is within $20 \text{ MeV}/c^2$ of the D^- mass. This contribution is not visible in the $\phi\pi$ sample. The contribution of these \bar{A}_c^- and D^- backgrounds after these vetoes is found to be negligible for the K^*K and NR regions, and of subpercent level in the $\phi\pi$ region.

The (faint) band on the right of the spectra of Fig. 5.3 is due to the contribution of partially reconstructed backgrounds, and mainly consists of $B \rightarrow D^{*-}(\rightarrow D^0(\rightarrow K^+ \pi^- \pi^+ \pi^-) \pi^-_s) \mu^+ \nu_\mu$ decays where a pion is misidentified as a kaon. About half of this background is removed by the general neural-net-based PID criterium. In the K^*K and NR regions, these candidates are reduced further by removing events where the invariant mass of the $K^- K^+$ pair, under the $K^- \pi^+$ mass hypothesis, falls below $800 \text{ MeV}/c^2$ and the PID of the K^+ is not incompatible with that of a pion. Furthermore, events where the misidentified kaon is the soft π^- that comes directly from a D^{*-} decay are removed by applying a cut on the invariant mass difference $M(K^\pm_{\pi^\pm} K^\mp \pi^-) - M(K^\mp \pi^-) < 175 \text{ MeV}/c^2$ for both kaons.

Further backgrounds originate from $K^{*0}(\rightarrow K^- \pi^+) \pi^-$ final states where the π^+ is misidentified as a K^+ . These are removed if the $K^- K^+$ combination under the $K^- \pi^+$ mass hypothesis is within $25 \text{ MeV}/c^2$ of the $K^{*0}(892)$ mass, and the PID of the K^+ is compatible with that of a pion.

Another background originates from $B \rightarrow J/\psi X$ decays, where one muon is associated with the semileptonic decay, and the other muon is misidentified as a pion or kaon and forms a D_s^- candidate with particles from the rest of the decay. They are removed by a veto on the invariant mass of $\mu^+ K^-$ or $\mu^+ \pi^-$ pair (under the $\mu^+ \mu^-$ mass hypothesis) if it is within $50 \text{ MeV}/c^2$ of the known J/ψ mass, and the pion/kaon has hits in the muon stations.

Finally, in the NR region a contribution containing correctly identified $D^{*-} \rightarrow D^0(\rightarrow K^- K^+) \pi^-$ decays are found. These are removed by a veto on the mass difference $M(K^- K^+ \pi^-) - M(K^- K^+)$ to not be within $7 \text{ MeV}/c^2$ of the $D^{*-} - D^0$ mass. The momentum asymmetry plots after the vetoes are shown in the right column of Fig. 5.3. The dark bands indicate the successful removal of \bar{A}_c^- and D^- backgrounds due to these vetoes.

The fits with full selection applied, but without the vetoes, are shown in Fig. 5.4. Before the vetoes, the background in the invariant mass is not quite flat, mostly due to the misidentified D^- background. Therefore, an additional component is added in these fits, to the right of the D_s^- signal peak, shown in grey. The result of the fits after applying the vetoes from Table 5.1 are shown in Fig. 5.7. Moreover, studies done on simulated events show that the shape of the background under the D_s^- mass peak can be described by a first-order Chebychev function. Hence, possible remaining backgrounds are absorbed in the combinatorial background component of the fit model. The size of this component is determined independently for $B_s^0 \rightarrow D_s^- \mu^+ \nu_\mu$ and $\bar{B}_s^0 \rightarrow D_s^+ \mu^- \bar{\nu}_\mu$ candidates, to allow for potential charge asymmetric effects in the background.

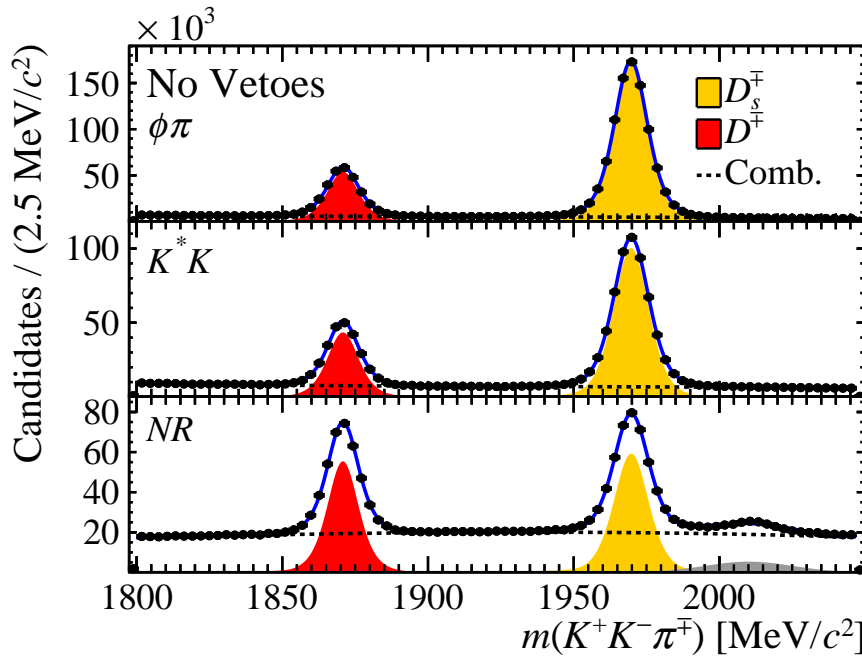


Figure 5.4: Fits to the D_s^\mp invariant mass, for the sum of $B_s^0 \rightarrow D_s^- \mu^+ \nu_\mu$ and $\bar{B}_s^0 \rightarrow D_s^+ \mu^- \bar{\nu}_\mu$ candidates, separately for the three Dalitz regions, after full selection but without applying the vetoes from Table 5.1. Both magnet polarities and data-taking years are added. The D_s^\mp signal yield is indicated in yellow, while the D^\mp yield is indicated in red. In order to take into account the contribution from backgrounds, the Chebychev function is changed from first-order to second-order, and an additional Gaussian function is added to account for D^+ decays in grey.

5.2.2 Peaking backgrounds

Similar to the a_{sl}^d analysis, a significant fraction of background originates from real D_s^- mesons, and are included in the fitted signal yields. The various contributing decays are studied in detail in Sec. 5.3.

The contribution of promptly produced D_s^- mesons is estimated using a fit to the logarithm of the IP distribution in the data, where the shape of the distribution from simulated prompt D_s^- decays is used. This is shown in Fig. 5.5. The contribution of prompt D_s^- candidates is reduced to about 0.1% by placing a cut at $\log(\text{IP}/\text{mm}) > -3$, and can safely be ignored.

Contributions from other b -hadron decays have at least one additional track in the final state, and thus a lower reconstructed B_s^0 mass. Even more discriminating is the corrected B_s^0 mass, as was defined in Eq. 4.3.3. Reconstructed and corrected mass distributions for simulated signal decays, as well as various other simulated b -hadron decays, are shown in Fig. 5.6. A cut is placed at $M_{\text{corr}} > 4200 \text{ MeV}/c^2$ to reduce these backgrounds without losing too much signal candidates. Finally, a cut on the minimum (transverse) momenta of the final-state particles is made in order to match the cuts made on the calibration samples, which are used to determine the detection asymmetries. The most important

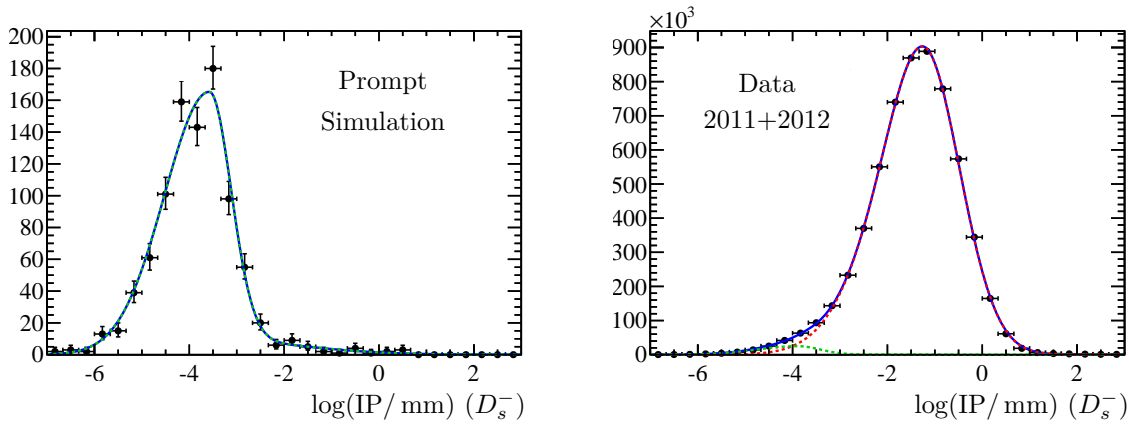


Figure 5.5: Logarithm of the impact parameter of the D_s^- candidates in (left) simulation of prompt $D_s^+ \rightarrow K^- K^+ \pi^+$ decays, and (right) in data. The fit shapes are overlaid. In data the shapes are fixed from the fit to the simulated samples: in green the prompt charm contribution (as obtained from the left plot), and in red the signal contribution.

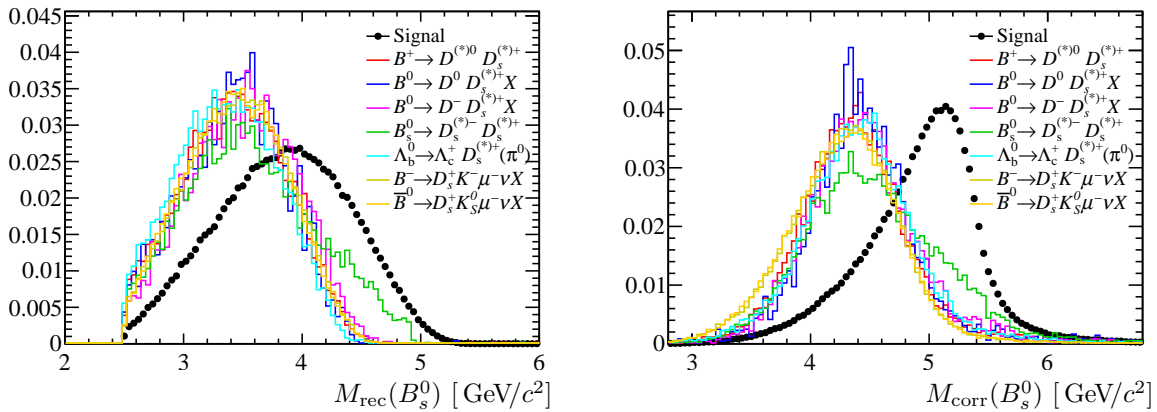


Figure 5.6: (left) Reconstructed and (right) corrected mass of the simulated B_s^0 signal candidates, and various backgrounds in simulation.

cuts made in the selection are summarized in Table 5.2. The total selection efficiency of these backgrounds will be described in Sec. 5.3.

5.2.3 Fit strategy and measured asymmetry

The measured asymmetry is obtained by performing a fit to the D_s^- invariant mass, separately for each Dalitz region. A wide D_s^- mass window of $[1800, 2047] \text{ MeV}/c^2$ is used (see Fig. 5.4) in order to constrain the combinatorial background component. This window includes a peak from Cabibbo-suppressed but correctly identified D^- decays around $1870 \text{ MeV}/c^2$. The signal D_s^- peak, as well as the D^- peak are modelled with a double-sided Hypatia function [109], which consists of a Gaussian core with asymmetric

Table 5.2: Most important selection criteria applied to the a_{s1}^s signal sample. The definitions of the PID variables `DLL` and `ProbNNk` are explained in Sec. 2.3.4. The “same-sign” kaon is the kaon with the same charge as the D_s^- . If the “applied to” field is empty, the cut is applied to all three Dalitz regions.

	Variable	Cut	Applied to
Offline cuts	$D_s^- \log(\text{IP}/\text{mm})$	> -3.0	
	$B_s^0 M_{\text{corr}}$	$> 4200 \text{ MeV}/c^2$	
	$B_s^0 M_{\text{rec}}$	$< 5200 \text{ MeV}/c^2$	
	$D_s^- M_{\text{rec}}$	$\in [1800, 2047] \text{ MeV}/c^2$	
Calibration cuts	muon p_T	$> 1.2 \text{ GeV}/c$	
	muon p	$> 6.0 \text{ GeV}/c$	
	kaons p_T	$> 300 \text{ MeV}/c$	
	kaons p	$> 2.0 \text{ GeV}/c$	
	pion p_T	$> 400 \text{ MeV}/c$	
	pion p	$> 5.0 \text{ GeV}/c$	
PID cuts	muon <code>DLL$_{\mu-\pi}$</code>	> 0	
	kaons <code>DLL$_{K-\pi}$</code>	> -5.0	$\phi\pi$
	kaons <code>DLL$_{K-\pi}$</code>	> 4.0	K^*K, NR
	same-sign kaon <code>ProbNNk</code>	> 0.1	$\phi\pi$
	same-sign kaon <code>ProbNNk</code>	> 0.15	K^*K, NR
	pion <code>DLL$_{K-\pi}$</code>	< 10.0	K^*K, NR
Veto	See Table 5.1		

tails. These tails are an effective parametrisation of the varying mass resolution on a per-event basis. The parameters that describe the tails are fixed from a fit to the data of both magnet polarities and data-taking years combined. The background is modelled with a first-order Chebychev polynomial.

A simultaneous fit to the D_s^- and D_s^+ invariant mass is performed, and the asymmetry between the D_s^- and D_s^+ yields is a parameter in the fit. Separate parameters are used for a possible asymmetry in the D^- and D^+ yields and in the combinatorial background. The mean of the D_s^- and D_s^+ peaks, as well as the mean of the D^- and D^+ peaks are allowed to vary independently to allow for a shift in invariant mass due to misalignment effects.

The fits to the invariant mass, split up by Dalitz region, are shown in Fig. 5.7. The fits to the data split up by magnet polarity and data-taking year are shown in Appendix C. The total D_s^\pm yields after the full selection are shown in Table 5.3. The $\phi\pi$ region contains the most candidates, while the K^*K and NR regions contribute respectively a half and a third of that amount.

The measured asymmetries are shown in Table 5.3. The combination is made by adding the three Dalitz regions with weights. The weights for each Dalitz region are obtained from the combined statistical error on the measured asymmetry and detection asymmetries, and are 0.61 for the $\phi\pi$ region, 0.25 for the K^*K region and 0.14 for the NR region. The

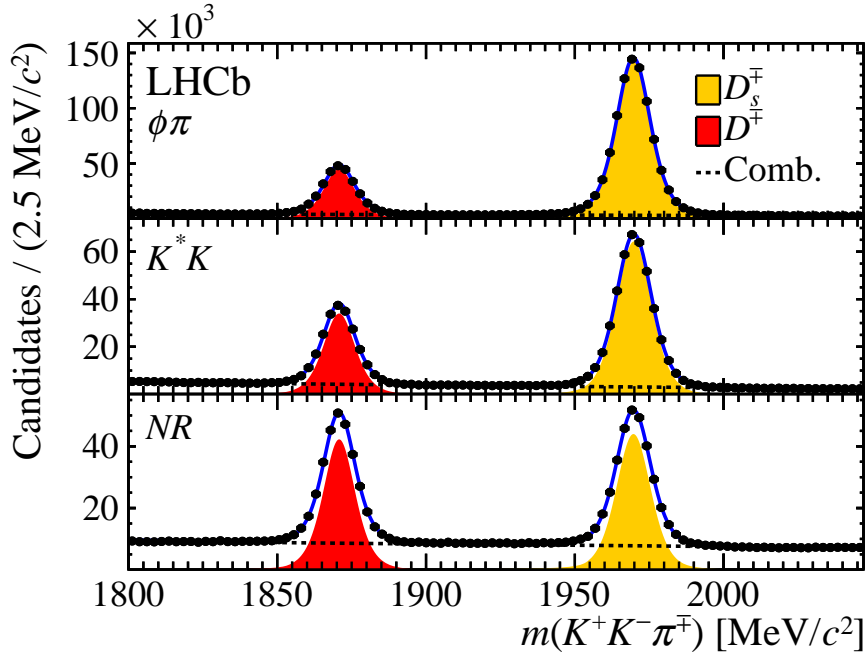


Figure 5.7: Fits to the D_s^\mp invariant mass, for the sum of $B_s^0 \rightarrow D_s^- \mu^+ \nu_\mu$ and $\bar{B}_s^0 \rightarrow D_s^+ \mu^- \bar{\nu}_\mu$ candidates, separately for the three Dalitz regions, after full selection. Both magnet polarities and data-taking years are added. The D_s^\mp signal yield is indicated in yellow, while the D^\mp yield is indicated in red.

Sample	Dalitz region		
	$\phi\pi$	K^*K	NR
Yields			
2011 Magnet up	113 442	52 650	35 417
2011 Magnet down	156 104	72 436	48 787
2012 Magnet up	325 005	148 359	101 288
2012 Magnet down	304 151	139 139	94 943
A_{meas} [%]			
2011 Magnet up	1.54 ± 0.32	1.31 ± 0.49	1.24 ± 0.65
2011 Magnet down	-1.97 ± 0.27	-1.13 ± 0.41	-1.56 ± 0.55
2012 Magnet up	0.28 ± 0.19	0.41 ± 0.29	1.16 ± 0.38
2012 Magnet down	0.01 ± 0.19	-0.12 ± 0.30	0.01 ± 0.40

Table 5.3: Yields and measured asymmetries in % including their statistical uncertainties, as obtained from fits to the invariant mass of D_s^- and D_s^+ candidates, separately for each Dalitz region, magnet polarity and data-taking year.

sum over Dalitz regions is followed by an arithmetic average of the two magnet polarities, and a weighted average of the two data-taking years, resulting in

$$A_{\text{meas}} = (0.11 \pm 0.09)\%. \quad (5.2.3)$$

A possible mismodelling of the mass peak might be a source of bias in the measured asymmetry. This is checked by performing a study using a sum of a double-sided Crystal Ball function (Eq. 3.4.2) and a Gaussian, instead of the Hypatia function for the signal shape, which is found to describe the data equally well. In order to quantify the difference in the fitted yields with both shapes, without double-counting the statistical error, events are generated using the alternative shape for the signal, and the nominal shape for the backgrounds. When the nominal fit is applied to these generated events, only a small bias on A_{meas} of 0.02% is observed in the NR region. This bias is most likely due to a correlation with the asymmetric combinatorial background. In addition, the fixed tail parameters of the signal shape are varied within their uncertainty. The resulting deviations from the nominal values for A_{meas} are negligible for the $\phi\pi$ region, and between 0.00% and 0.02% for the K^*K and NR regions. In the combination of all data, a total systematic error of 0.018% on the measured asymmetry is assigned to all these effects.

5.3 Simulation and peaking backgrounds

In order to study the signal and background composition, simulated events are generated. They are used to determine the relative contributions of the various backgrounds that are included in the measured asymmetry, which enter explicitly in the determination of a_{sl}^s (Eq. 5.1.1). The composition of the simulated samples is discussed below, after which the contributions of the backgrounds to the measurement of a_{sl}^s are discussed.

5.3.1 Signal simulation

The signal sample consists of 20 million B_s^0 mesons that are forced to decay to a $D_s^- \mu^+ \nu_\mu X$ final state, including resonances. The D_s^- is forced to decay to $K^- K^+ \pi^-$ using a phase-space model that includes the known resonances. Absolute branching ratios are obtained from Ref. [94], resulting in a contribution of 23% to the total sample for $B_s^0 \rightarrow D_s^- \mu^+ \nu_\mu$ decays. Contributions from B_s^0 decays to higher charmed resonances, for which $X = \gamma, \pi^0, \pi^+ \pi^-$, contribute 72% to the sample, and are dominated by $B_s^0 \rightarrow D_s^{*-} \mu^+ \nu_\mu$ decays. Decays involving a B_s^0 decaying semileptonically to a τ^+ , which in turn decays as $\tau^+ \rightarrow \mu^+ \bar{\nu}_\tau \nu_\mu$, contribute about 5%.

5.3.2 Contributions from peaking backgrounds

The contributions of various backgrounds that peak in the D_s^- mass, will dilute the sensitivity of the measured asymmetry to a_{sl}^s . These contributions are estimated using a cocktail of simulated $D_s^- \rightarrow K^+ K^- \pi^-$ decays. This includes decays from A_b^0, B^+ ,

\bar{B}^0 and B_s^0 . After full selection, 85% of the candidates originate from the signal decay $B_s^0 \rightarrow D_s^- \mu^+ \nu_\mu X$. About 6% of the candidates originate from combinatorial D_s^- decays. About 1.5% originates from misidentified $B_s^0 \rightarrow D_s^- \mu^+ \pi^+ K^+ X$ decays, or real $B_s^0 \rightarrow D_s^-$ transitions where the muon originates from a semileptonic decay of another b hadron. These decays behave similar to the signal, in the sense that they are sensitive to CP violation in the B_s^0 mixing process.

The dominant source of peaking backgrounds contains b -hadron decays into two charmed mesons, in which a D_s^+ is produced from the virtual W^+ and the other charmed hadron decays semileptonically. Combined, these doubly-charmed backgrounds contribute about 10% to the selected candidates. Finally, there is a contribution of about a percent from $B^+ \rightarrow D_s^- \mu^+ K^- \nu_\mu X$ and $B^0 \rightarrow D_s^- \mu^+ \bar{K}^0 \nu_\mu X$ decays.

The dominant backgrounds described above contain additional particles with respect to the $B_s^0 \rightarrow D_s^- \mu^+ \nu_\mu X$ signal mode. Their contribution is already reduced by the momentum cut on the muon and the cut on the corrected B_s^0 mass as shown in Fig. 5.6. Dedicated simulated samples containing at least 5 million events are generated for each of these modes to determine the selection efficiencies.

The production rates of the different b hadrons with respect to the B_s^0 meson are quantified by the b -hadron fractions [105, 110],

$$\begin{aligned} f_u/f_s &= f_d/f_s = 3.86 \pm 0.22 \\ f_{\Lambda_b^0}/f_s &= 2.34 \pm 0.31, \end{aligned} \quad (5.3.1)$$

where f_u is the production rate of B^+ mesons, f_s is the production rate of B_s^0 mesons, f_d is the production rate of B^0 mesons and $f_{\Lambda_b^0}$ is that of Λ_b^0 mesons. In the determination of $f_{\Lambda_b^0}/f_s$, the p_T -dependent production rate in Ref. [105] is taken into account. The branching ratios of these modes are taken from Ref. [94]. The relative selection efficiencies, production rates and branching ratios are summarized in Table 5.4. Besides diluting the measured asymmetry, these backgrounds can have a charge asymmetry, which would bias the measured value of a_{sl}^s . The asymmetry in these backgrounds is determined below.

5.3.3 Asymmetries in the background modes

The B^+ production asymmetry was determined in Sec. 4.4.5 to be $A_{P,B^+} = (-0.6 \pm 0.6)\%$, with the largest uncertainty originating from the measured CP asymmetry of $A_{CP}(B^+ \rightarrow J/\psi K^+) = (0.3 \pm 0.6)\%$. The B^0 background asymmetry originates from both the production asymmetry and a_{sl}^d . Both are taken from the a_{sl}^d analysis described in Chapter 4. The time-integrated asymmetries are diluted due to the B^0 oscillations, that go as $\cos(\Delta m_d t)$ for A_{P,B^0} , and as $1 - \cos(\Delta m_d t)$ for $a_{\text{sl}}^d/2$ (see Eq. 1.2.42). Using the values of the lifetime and Δm_d from Ref. [94] and the decay-time acceptance from Eq. 4.4.11 this results in a dilution factor of 0.36 on A_{P,B^0} and 0.64 on $a_{\text{sl}}^d/2$. Adding both effects, and averaging over the statistically compatible centre-of-mass energies, the result is

$$A_{\text{bkg},B^0}^{\text{eff}} = (-0.18 \pm 0.13)\%. \quad (5.3.2)$$

Table 5.4: Branching fractions (\mathcal{B}), efficiency ratios ($\varepsilon_{\text{sig}}/\varepsilon_{\text{bkg}}$), background-over-signal ratio ($f_{\text{bkg}}/f_{\text{sig}}$) and effective asymmetries for the different background sources. The branching fractions are obtained from Ref. [94]. The signal branching fraction is $\mathcal{B} = (7.9 \pm 2.4)\%$. The b -hadron fractions from the pp collision are $f_u/f_s = f_d/f_s = (3.86 \pm 0.22)$ [110] and $f_{\Lambda_b^0}/f_s = (2.34 \pm 0.31)$ [105].

Mode	\mathcal{B} [%]	$\mathcal{B}(c \rightarrow \mu)$ [%]	$\varepsilon_{\text{sig}}/\varepsilon_{\text{bkg}}$	$f_{\text{bkg}}/f_{\text{sig}}$ [%]	A_{bkg} [%]
$B^+ \rightarrow D^{(*)0} D_s^{(*)+} X$	7.9 ± 1.4	6.5 ± 0.1	4.34	5.8 ± 1.1	-0.6 ± 0.6
$B^0 \rightarrow D^0 D_s^{(*)+} X$	5.7 ± 1.2	6.5 ± 0.1	4.08	4.4 ± 1.0	-0.18 ± 0.13
$B^0 \rightarrow D^- D_s^{(*)+} X$	4.6 ± 1.2	16.1 ± 0.3	6.41	5.6 ± 1.5	-0.18 ± 0.13
$B_s^0 \rightarrow D_s^{(*)-} D_s^{(*)+}$	4.5 ± 1.4	8.1 ± 0.4	3.68	1.0 ± 0.3	–
$\Lambda_b^0 \rightarrow \Lambda_c^+ D_s^{(*)+} X$	$10.3^{+2.1}_{-1.8}$	4.5 ± 1.7	4.51	3.0 ± 1.4	$+0.5 \pm 0.8$
$B^- \rightarrow D_s^+ K^- \mu^- \nu X$	0.061 ± 0.010	–	2.43	1.3 ± 0.2	0.6 ± 0.6
$\bar{B}^0 \rightarrow D_s^+ K_s^0 \mu^- \nu X$	0.061 ± 0.010	–	2.89	1.1 ± 0.2	0.18 ± 0.13

The asymmetry of the $B_s^0 \rightarrow D_s^- D_s^+$ background has a negligible contribution from a production asymmetry in the time-integrated analysis, due to the fast oscillation frequency Δm_s . Furthermore, due to charge-symmetric final state, the total contribution from CP violation (or A_P) in this mode is negligible, and this background only dilutes the raw asymmetry.

The production asymmetry of Λ_b^0 baryons is estimated using the combined CP and production asymmetry of $A_{\text{meas}}(\Lambda_b^0 \rightarrow J/\psi p^+ K^-) = (-0.1 \pm 0.7)\%$ [111]. Correcting for the CP asymmetry in this decay, which is estimated to be $A_{CP}(\Lambda_b^0 \rightarrow J/\psi p^+ K^-) = (-0.6 \pm 0.3)\%$ [107, 112], this becomes

$$A_{P, \Lambda_b^0} = (+0.5 \pm 0.8)\%. \quad (5.3.3)$$

A paper containing new LHCb measurements of the production asymmetry of B^0 , B_s^0 , B^+ and $\bar{\Lambda}_b^0$ mesons, using alternative decay channels, is currently undergoing review [113]. They are statistically compatible with the values used in this section, but the uncertainties are larger compared to those determined in this section. In addition, a measurement of the $\bar{\Lambda}_b^0$ production asymmetry using semileptonic decays in LHCb is currently ongoing. The expected uncertainty on these measurements is about 0.3%.

5.3.4 Effect on a_{sl}^s

The total fraction of each background is calculated using the relative production rates, branching ratios, and relative selection efficiencies as obtained from the dedicated simulated samples. They are summarized in Table 5.4, and add up to a dilution of the raw asymmetry of

$$f_{\text{bkg}} \equiv \sum_i f_{\text{bkg}}^i = (18.4 \pm 6.0)\%. \quad (5.3.4)$$

The asymmetries in the background modes are shown in the last column of Table 5.4, and add up to a bias on a_{sl}^s of

$$f_{\text{bkg}} A_{\text{bkg}} \equiv \sum_i f_{\text{bkg}}^i A_{\text{bkg}}^i = (-0.023 \pm 0.031)\%. \quad (5.3.5)$$

5.4 Detection asymmetries

This section is dedicated to the detection asymmetries, using the methods from Chapter 3. Four contributions are discerned: the $\mu^+\pi^-$ asymmetry, the K^+K^- asymmetry, the trigger asymmetry and the asymmetry due to PID criteria.

5.4.1 The $\mu^+\pi^-$ asymmetry

In contrast to the a_{sl}^d analysis, both the J/ψ tag-and-probe method and the D^* partial-and-full methods from Sec. 3.1 are employed. The asymmetry arising from the different kinematic distributions of the μ^+ and π^- is covered by the combination of these two methods. This means that no weights are applied to match the π^- kinematic distributions to those of the μ^+ . Again, any tracking asymmetry is expected to disappear when both distributions are equal. The $\mu^+\pi^-$ asymmetry is calculated from either method by using the difference in the kinematic distributions of the μ^+ and π^- , as outlined in Sec. 3.1. The overlap of the signal muon and pion distributions is shown in Fig. 5.8, and slightly depends on the Dalitz region.

The results of both methods are compared in Table 5.5, where the simulation studies described in Sec. 3.1.3 are used to assign an additional systematic error due to different material cross-sections between muons and pions, and a different amount of material that is traversed by particles of either charge, depending on the magnet polarity. The J/ψ tag-and-probe method is corrected for the limited acceptance of the muons. Both methods are in good agreement.

The total $\mu^+\pi^-$ asymmetry used to correct A_{meas} is calculated by taking the weighted average of both methods, using only the statistical error when calculating the weights. In the magnet-average result, the systematic errors and correction to the J/ψ method, resulting from the simulation studies, are much smaller. Hence, no correction is applied and only a systematic error is assigned, which is 0.02% for all Dalitz regions, magnet polarities and data-taking years combined. The resulting values for the $\mu^+\pi^-$ tracking asymmetry are shown together with all other asymmetries at the end of this section in Table 5.10.

5.4.2 The K^+K^- asymmetry

The kaon detection asymmetry is of the order of a percent due to a difference in cross-sections of incident K^+ and K^- onto the detector material, as discussed in Sec. 3.2. However, when constructing an asymmetry of K^+K^- pairs, the asymmetry is expected

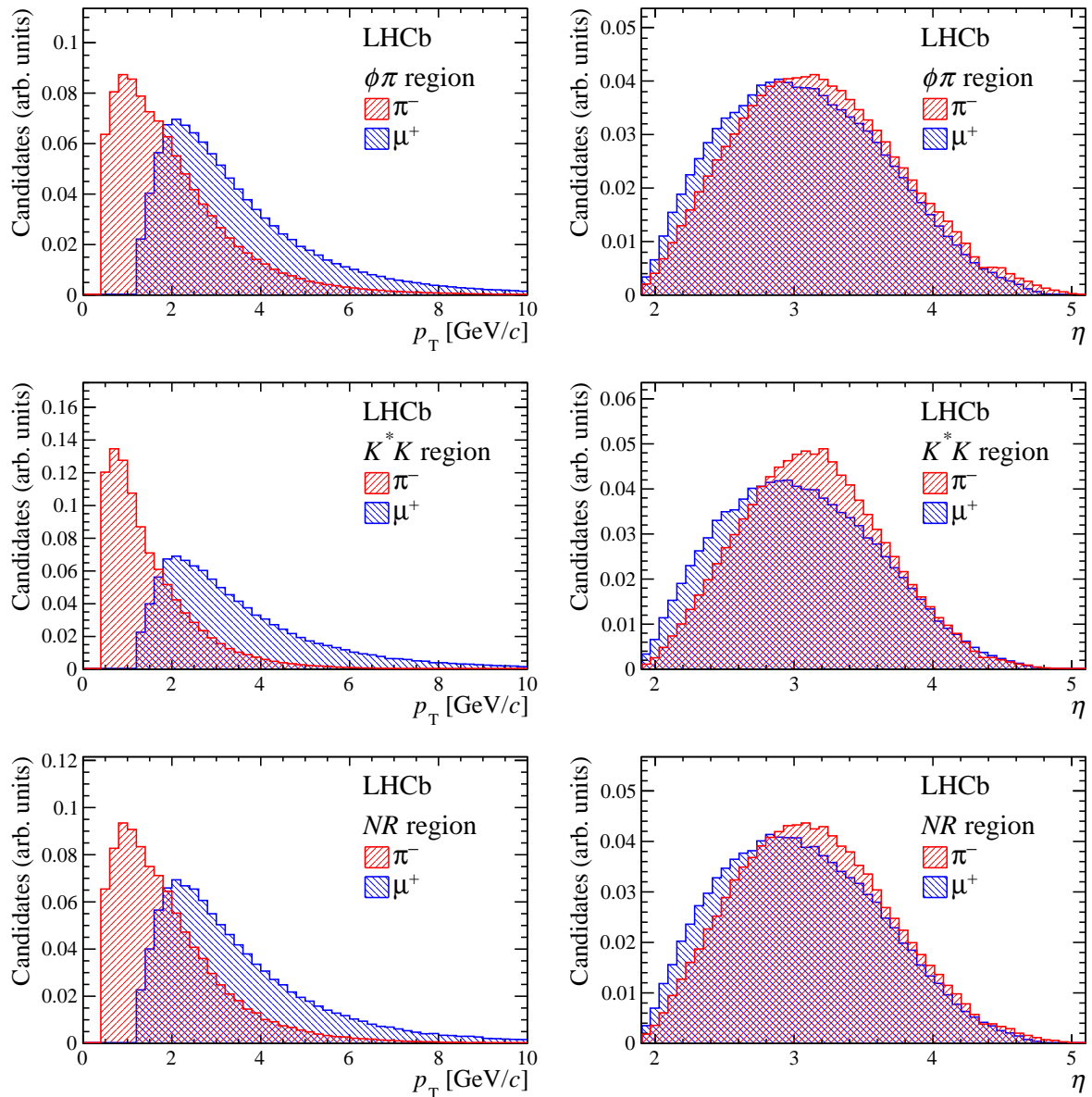


Figure 5.8: The background-subtracted p_T and η distributions of the final-state pion and muon. For these histograms all data including both years and both magnet polarities are combined.

to cancel if there is perfect kinematic overlap between the kaons. The overlap of the kinematic distributions of the kaon with the same sign (SS) and opposite sign (OS) as the D_s^- are shown in Fig. 5.9, and is in general very good. In the $\phi\pi$ region the kinematic distributions are nearly identical, as they come from the same resonance ($\phi(1020)$) and due to the small available phase space in this decay. In the other two regions the difference between the distributions is somewhat larger.

The K^+K^- asymmetry is calculated using the method from Sec. 3.2.1, and the resulting values are shown in Table 5.6. In the $\phi\pi$ region the asymmetry is small, due to the good kinematic overlap. In the other regions it is found to be somewhat larger. The total

Table 5.5: Asymmetry comparison of J/ψ and D^* method, split by magnet polarity, in percent. The first error is statistical, the second systematic. Simulation studies are performed to assign additional systematic errors, and to correct the J/ψ method in order to make a comparison in terms of the absolute difference and the difference in number of standard deviations $N(\sigma)$.

	D^* method	J/ψ method	Difference	$N(\sigma)$
2011, Magnet up				
$\phi\pi$	$0.26 \pm 0.26 \pm 0.08$	$0.27 \pm 0.15 \pm 0.14$	-0.01 ± 0.34	-0.03
K^*K	$0.46 \pm 0.46 \pm 0.10$	$0.25 \pm 0.16 \pm 0.13$	0.21 ± 0.51	0.41
NR	$0.30 \pm 0.29 \pm 0.09$	$0.27 \pm 0.16 \pm 0.13$	0.03 ± 0.37	0.08
2011, Magnet down				
$\phi\pi$	$-0.19 \pm 0.20 \pm 0.09$	$-0.28 \pm 0.13 \pm 0.17$	0.09 ± 0.31	0.29
K^*K	$-0.34 \pm 0.34 \pm 0.11$	$-0.25 \pm 0.14 \pm 0.15$	-0.09 ± 0.41	-0.22
NR	$-0.23 \pm 0.24 \pm 0.09$	$-0.21 \pm 0.14 \pm 0.13$	-0.02 ± 0.32	-0.06
2012, Magnet up				
$\phi\pi$	$0.26 \pm 0.14 \pm 0.09$	$0.15 \pm 0.10 \pm 0.14$	0.11 ± 0.24	0.46
K^*K	$0.46 \pm 0.23 \pm 0.12$	$0.14 \pm 0.11 \pm 0.14$	0.32 ± 0.31	1.03
NR	$0.31 \pm 0.16 \pm 0.10$	$0.12 \pm 0.11 \pm 0.13$	0.19 ± 0.25	0.76
2012, Magnet down				
$\phi\pi$	$-0.27 \pm 0.13 \pm 0.10$	$-0.24 \pm 0.10 \pm 0.15$	-0.03 ± 0.24	-0.13
K^*K	$-0.46 \pm 0.22 \pm 0.13$	$-0.24 \pm 0.10 \pm 0.18$	-0.22 ± 0.33	-0.67
NR	$-0.32 \pm 0.16 \pm 0.10$	$-0.22 \pm 0.10 \pm 0.15$	-0.10 ± 0.26	-0.38

systematic error resulting from the studies described in Sec. 3.2.1 is 0.034% when taking the average over the Dalitz regions, magnet polarities and data-taking years.

Table 5.6: K^+K^- asymmetry for the three Dalitz regions, obtained by weighing the calibration samples to the signal kaon kinematic distributions .

Sample	A_{KK} per Dalitz region [%]		
	$\phi\pi$	K^*K	NR
2011 Magnet up	0.010 ± 0.002	-0.043 ± 0.008	-0.059 ± 0.012
2011 Magnet down	0.010 ± 0.002	-0.003 ± 0.009	-0.031 ± 0.012
2012 Magnet up	0.015 ± 0.002	-0.057 ± 0.009	-0.086 ± 0.012
2012 Magnet down	0.001 ± 0.002	0.004 ± 0.009	-0.005 ± 0.012

5.4.3 PID asymmetry

In contrast to the a_{sl}^d analysis, the kaon PID criteria using DLL variables are softer in the selection of data (see Table 5.2) than they are in the determination of the K^+K^-

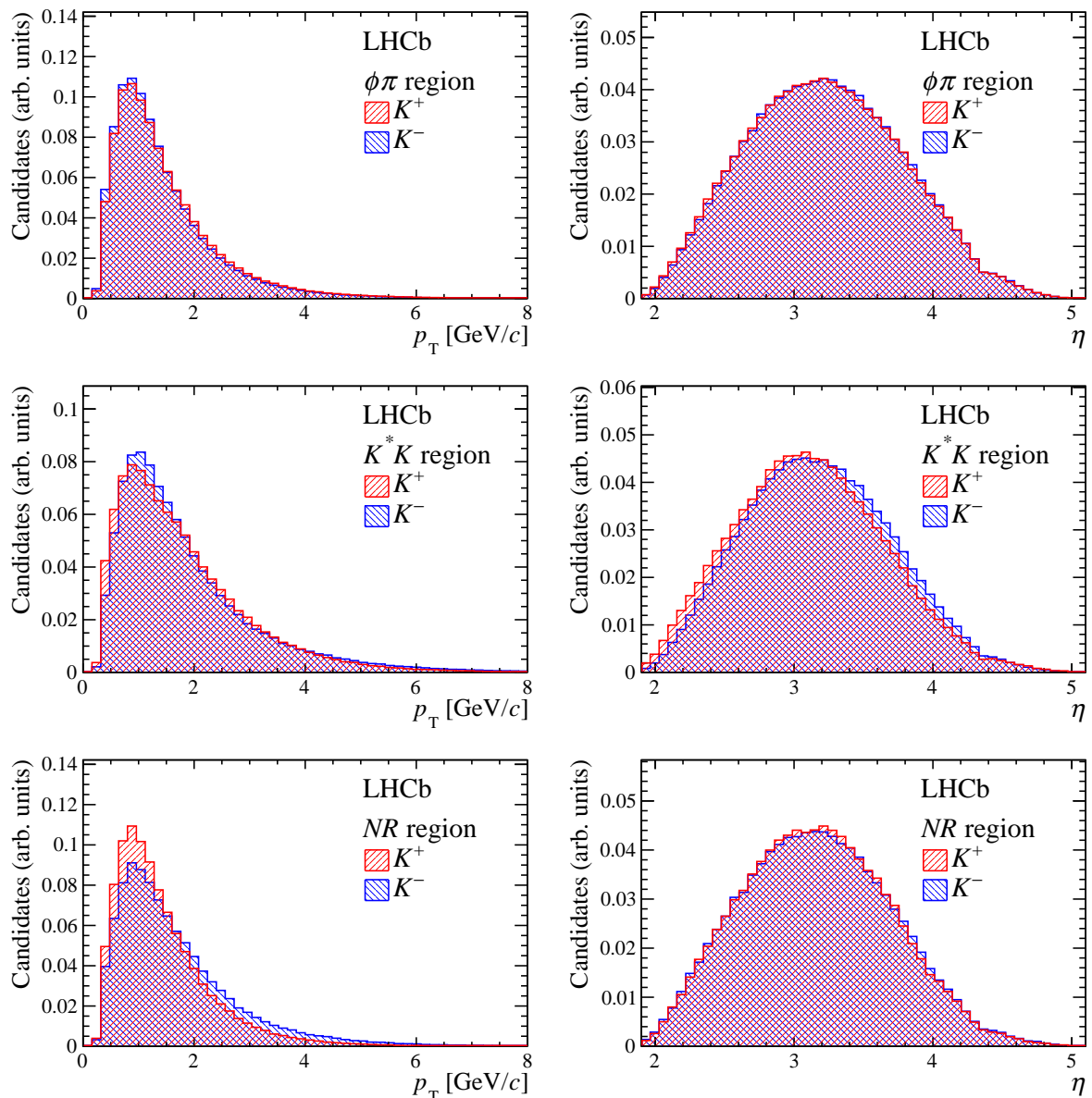


Figure 5.9: The background-subtracted p_T and η distributions of the final-state kaons. For these histograms all data including both years and both magnet polarities are combined.

asymmetry (Sec. 5.4.2). Therefore, the asymmetry due to PID in the calibration samples that are used to determine the K^+K^- asymmetry, are corrected for. These corrections are determined using the method of Sec. 3.3, based on $D^{*-} \rightarrow D^0(\rightarrow K^-\pi^+)\pi^-$ decays. The size of these corrections to A_{KK} is negligible in the $\phi\pi$ region, and are small (ranging from -0.03% up to 0.05%) in the other regions, due to the two oppositely-charged kaons. These corrections are already included in Table 5.6.

The PID asymmetry of the signal selection due to the PID criteria is determined separately. In addition to the cut on the kaon log-likelihood variable DLL, a cut is made on the neural-net variable `ProbNN` of the same-sign kaon. On the pion, a loose DLL cut is made

for the K^*K and NR regions. This is not done for the $\phi\pi$ region.² Besides these global PID requirements, the vetoes of the identifiable backgrounds in Sec. 5.2 require strong PID requirements for specific mass regions in the data. The asymmetries of these vetoes are determined by using the same method of Sec. 3.3, and only sampling the kinematic distributions of the data that lie within the specific mass region that is relevant to that veto. The resulting asymmetries are large, but the overall effect is small since they only apply to a small part of the data.

The total PID asymmetry is determined by summing the individual PID asymmetries of the selections on the various particles in the final state. The large correlations between the different asymmetries, when obtained from the same calibration sample, are taken into account. In the sum, the asymmetries of the vetoes are weighed by the amount of data they apply to. The dominant contribution originates from the global PID cuts on the kaons and reaches up to 6%, although it largely cancels due to the contribution of the other kaon in the final state. The total PID asymmetries are shown in Table 5.7, including the systematic errors described in Sec. 3.3.

Table 5.7: Total PID asymmetry, split up by year and Dalitz region, including the statistical error.

Sample	A_{PID} per Dalitz region [%]		
	$\phi\pi$	K^*K	NR
2011 Magnet up	0.01 ± 0.05	0.08 ± 0.07	0.06 ± 0.08
2011 Magnet down	-0.01 ± 0.04	-0.11 ± 0.06	-0.07 ± 0.07
2012 Magnet up	0.01 ± 0.03	0.04 ± 0.04	0.01 ± 0.05
2012 Magnet down	-0.01 ± 0.03	-0.14 ± 0.04	-0.07 ± 0.05

5.4.4 The trigger and muon PID asymmetry

The asymmetry of the muon hardware-level trigger and PID is determined using a tag-and-probe method using $B \rightarrow J/\psi X$ decays (see Sec. 3.4). The resulting asymmetries are shown in Table 5.8. Unlike the a_{sl}^d analysis, no look-up-table has been used to correct the bias due to the p_T estimate in the hardware-level trigger. Hence, the trigger asymmetries in the 2011 data for this analysis are larger than those for the a_{sl}^d analysis. After correcting the raw asymmetry for the trigger asymmetry, this choice should not make a difference in the obtained value for a_{sl}^s , for each magnet polarity and data-taking year. Also, the magnet-average asymmetries are compatible with zero, ensuring that the averaged result for a_{sl}^s is unaffected by this choice.

In contrast to the a_{sl}^d analysis, the asymmetry from the software-level trigger is treated separately, as was described in Sec. 3.4.1. This is because a combination of two software triggers is used: one using the muon (`Hlt1TrackMuon`), and another triggering on any of

²A description of the DLL and ProbNN variables is made in Sec. 2.3.4.

Sample	A_μ per Dalitz region [%]		
	$\phi\pi$	K^*K	NR
2011 Magnet up	1.10 ± 0.06	1.02 ± 0.06	1.01 ± 0.06
2011 Magnet down	-1.17 ± 0.07	-1.09 ± 0.05	-1.13 ± 0.05
2012 Magnet up	0.06 ± 0.04	0.09 ± 0.04	0.03 ± 0.04
2012 Magnet down	-0.12 ± 0.04	-0.13 ± 0.04	-0.18 ± 0.04

Table 5.8: Muon trigger and PID asymmetries, without the software-level trigger requirement, including the statistical errors only. In 2011 no look-up-table was applied to correct for the hardware-level p_T effect.

the four final-state tracks (`Hlt1TrackAllL0`). The resulting asymmetries are shown in Table 5.9, which also contains the corresponding systematic uncertainties. In addition, the second-level software trigger adds a systematic error of 0.020%, the same as in the a_{sl}^d analysis.

Table 5.9: The combined software-level trigger asymmetries in the a_{sl}^s sample, for each Dalitz region, split up by magnet polarity and data-taking year. The uncertainties are statistical only.

Sample	A_{Hlt} per Dalitz region [%]		
	$\phi\pi$	K^*K	NR
2011 magnet up	-0.04 ± 0.02	-0.05 ± 0.02	-0.04 ± 0.01
2011 magnet down	0.12 ± 0.03	0.14 ± 0.03	0.11 ± 0.02
2012 magnet up	-0.04 ± 0.02	-0.05 ± 0.02	-0.04 ± 0.01
2012 magnet down	0.10 ± 0.01	0.11 ± 0.01	0.09 ± 0.01

5.4.5 Total detection asymmetry

The combinations of the detection asymmetries for both magnet polarities and data-taking years are shown in Table 5.10. The systematic errors on the magnet-average results are significantly smaller than those for the individual magnet polarities, as discussed in the above sections.

5.5 Results

The measured asymmetries of Table 5.3 are corrected for the detection- and background asymmetry, as per Eq. 5.1.1. The dilution factor due to the background acts as a multiplicative factor to both the central value and the errors. This factor is calculated

Table 5.10: Detection asymmetries in % for both magnet polarities and data-taking years combined, for each Dalitz region, including statistical error. The last column is the average over the three Dalitz regions. For $A_{\mu\pi}$ the average of the D^* and J/ψ methods is used. A_μ is the muon hardware trigger and PID asymmetry, while A_{Hit} is the combined software-level trigger asymmetry. The detection asymmetries are uncorrelated between each other, and assumed to be fully correlated between Dalitz regions. In the last column, the second error is the combined systematic error.

A_{det}	$\phi\pi$	K^*K	NR	Average
$A_{\mu\pi}$	-0.01 ± 0.05	0.00 ± 0.06	0.00 ± 0.05	$-0.01 \pm 0.05 \pm 0.04$
A_{KK}	0.01 ± 0.00	-0.03 ± 0.00	-0.05 ± 0.01	$-0.01 \pm 0.00 \pm 0.03$
A_{PID}	-0.00 ± 0.02	0.04 ± 0.03	0.02 ± 0.03	$0.01 \pm 0.02 \pm 0.02$
A_μ	-0.03 ± 0.02	-0.03 ± 0.02	-0.07 ± 0.02	$-0.03 \pm 0.02 \pm 0.02$
A_{Hit}	0.00 ± 0.01	0.01 ± 0.01	0.00 ± 0.01	$0.00 \pm 0.01 \pm 0.01$
Total	-0.03 ± 0.06	-0.01 ± 0.07	-0.09 ± 0.06	$-0.03 \pm 0.06 \pm 0.06$

from the value of f_{bkg} in Sec. 5.3, and is

$$\frac{2}{1 - f_{\text{bkg}}} = 2.45 \pm 0.18 \quad (5.5.1)$$

Using the detection asymmetries from Table 5.10 and the background fraction and asymmetry of Sec. 5.3.4, the resulting values of a_{sl}^s with their statistical error are shown in Table 5.11. In contrast to the a_{sl}^d analysis, the statistical errors represent the quadratic sum of the statistical errors on both A_{meas} and on the detection asymmetries A_{det} . The individual contributions to the total statistical errors are shown in Table 5.11.

Figure 5.10 is a graphical representation of the values of a_{sl}^s , including each of the twelve data sets. They are found to be compatible within statistical fluctuations. Since the non-peaking backgrounds and detection asymmetries can vary significantly between Dalitz regions, an additional consistency check is made. Using only the uncorrelated statistical errors, the difference of the combined value of a_{sl}^s in the $\phi\pi$ region, $(0.16 \pm 0.25)\%$, with the value in the combined K^*K and NR regions, $(0.76 \pm 0.39\%)$, is 1.5 standard deviations. A further consistency check between Dalitz regions is done using prompt $D_s^- \rightarrow K^+K^-\pi^-$ decays, of which LHCb has recorded almost a factor 10 more events in run 1 compared to $B_s^0 \rightarrow D_s^-(\rightarrow K^+K^-\pi^-)\mu^+\nu_\mu$ decays. This mode can be used to measure the D_s^- production asymmetry, which should be independent of the D_s^- Dalitz region. The D_s^- production asymmetry is indeed found to be consistent [114].

The combination of the various Dalitz regions, magnet polarities and data-taking years, including statistical and systematic errors, is summarized in Table 5.12. In order to take into account the error on the background dilution factor, the systematic error due to $A_{\text{meas}} + A_{\text{det}}$ is multiplied by the sum of the dilution factor plus its error, in order to obtain the total systematic error on a_{sl}^s . The final result is

$$a_{\text{sl}}^s = (0.39 \pm 0.26 \pm 0.20)\%, \quad (5.5.2)$$

Table 5.11: Values of a_{sl}^s in % for each Dalitz region, magnet polarity and data-taking year, as obtained using Eq. 5.1.1. The values shown are statistical only. These values are graphically represented by Fig. 5.10.

	2011, Up	2011, Down	2012, Up	2012, Down	Total
$\phi\pi$	0.95 ± 0.87	-2.07 ± 0.74	0.55 ± 0.52	0.37 ± 0.52	0.16 ± 0.31
K^*K	0.52 ± 1.27	0.10 ± 1.08	0.91 ± 0.76	0.26 ± 0.77	0.50 ± 0.45
NR	0.43 ± 1.65	-0.82 ± 1.40	3.02 ± 0.97	0.62 ± 1.01	1.22 ± 0.59
Average	0.77 ± 0.72	-1.36 ± 0.62	0.98 ± 0.44	0.38 ± 0.44	0.39 ± 0.26

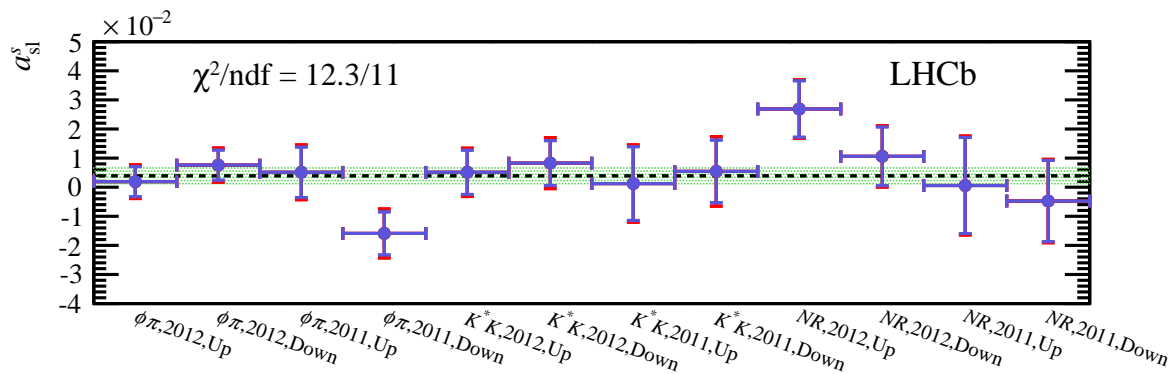


Figure 5.10: The values of a_{sl}^s for all Dalitz regions, magnet polarities and data-taking years separately. The blue error bar indicates the statistical error, while the red error bar in addition takes into account magnet-dependent systematic effects. The black dashed line indicates the value of the nominal combination, the error of which is displayed by the green-dotted region.

where the first error is the combination of statistical errors on the measured asymmetry and detection asymmetries, and the second error is the total systematic error. A discussion of this result is done in Chapter 6.

Table 5.12: Overview of contributions in the determination of a_{sl}^s , averaged over Dalitz regions, magnet polarities and data-taking periods, with their statistical and systematic uncertainties. All numbers are in percent. The central value of a_{sl}^s is calculated according to Eq. 5.1.1. The uncertainties are added in quadrature and multiplied by $2/(1 - f_{\text{bkg}})$, which is the same for all twelve subsamples, to obtain the uncertainties on a_{sl}^s .

Source	Value	Stat. uncert.	Syst. uncert.	
A_{meas}	0.11	0.09	0.02	
$-A_{KK}$	0.01	0.00	0.03	
$-A_{\mu\pi}$	0.01	0.05	0.04	
$-A_{\text{PID}}$	-0.01	0.02	0.03	
$-A_{\mu}$	0.03	0.02	0.02	
$-A_{\text{Hlt}}$	0.00	0.01	0.02	
$-f_{\text{bkg}} A_{\text{bkg}}$	0.02	-	0.03	+
$(1 - f_{\text{bkg}})a_{\text{sl}}^s/2$	0.16	0.11	0.08	
$2/(1 - f_{\text{bkg}})$	2.45	-	0.18	\times
a_{sl}^s	0.39	0.26	0.20	

6

The measurements of a_{sl}^d and a_{sl}^s in this thesis provide an improved understanding of CP violation in mixing of B mesons. The current experimental status is summarized in Sec. 6.1, followed by a discussion of other potential sources of CP violation that may contribute to the D0 dimuon anomaly besides the mixing parameters a_{sl}^d and a_{sl}^s in Sec. 6.2. Finally, Sec. 6.3 evaluates the potential of the measurements presented in this thesis with future improvements.

6.1 The picture after LHCb run 1

The measurements of a_{sl}^d and a_{sl}^s are the most precise measurements of these parameters to date, and both are found to be compatible with the SM. Figure 6.1 displays all current measurements in the a_{sl}^d versus a_{sl}^s plane, which is an update of Fig. 1.8, where the LHCb measurements are now added in red. The world averages of the individual measurements of a_{sl}^d and a_{sl}^s are

$$\begin{aligned} a_{\text{sl}}^d &= (0.02 \pm 0.20)\% \\ a_{\text{sl}}^s &= (0.17 \pm 0.30)\%. \end{aligned} \tag{6.1.1}$$

The correlation between the LHCb measurements is $\rho = +0.13$, due to common systematic effects in the muon detection asymmetry, and the contribution of the B^0 background in the a_{sl}^s analysis [108]. This results in a correlation between the world-averaged values of $\rho = +0.07$. The world averages of a_{sl}^d and a_{sl}^s are only marginally compatible with the D0 dimuon result, with a p -value of 0.5%. This indicates that the observed D0 dimuon anomaly cannot be explained by new physics in CP violation in mixing alone. It might be a statistical fluctuation, or caused by other contributions that are not yet taken into account, as will be discussed in the following.

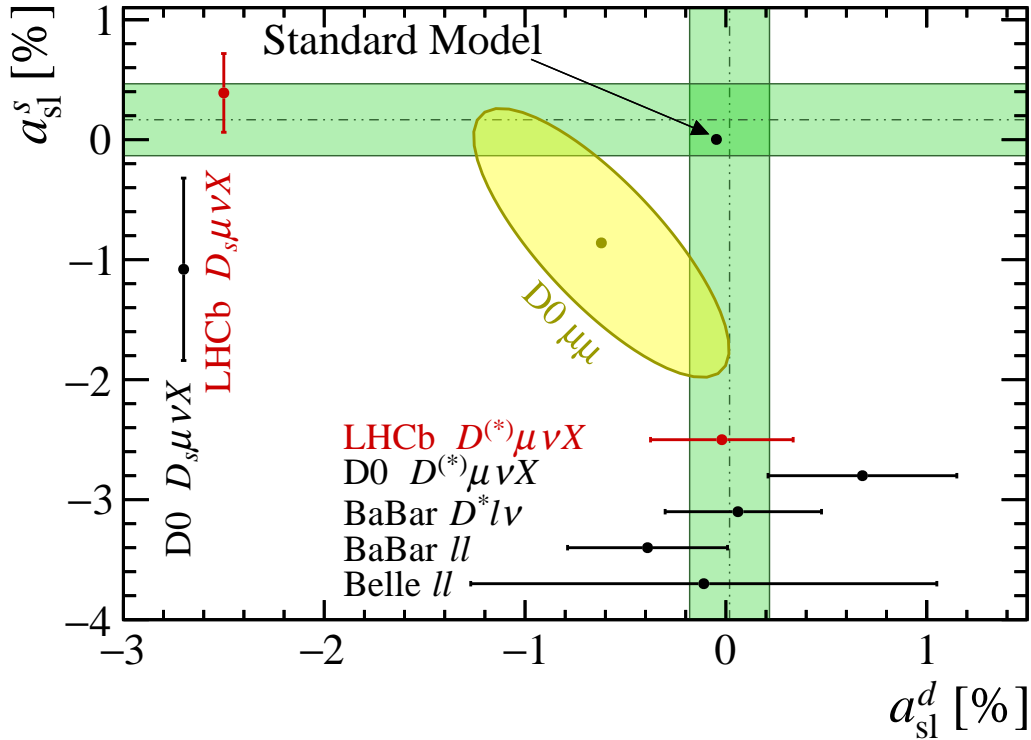


Figure 6.1: Overview of a_{sl}^d and a_{sl}^s measurements after the run-1 LHCb results presented in this thesis, indicated with red points. The black points represent the other individual measurements of a_{sl}^d or a_{sl}^s . The D0 dimuon measurement is shown in the yellow ellipse. The green bands indicate the averages of measurements, excluding the D0 dimuon result.

6.2 Thoughts about the dimuon anomaly

The D0 dimuon measurement is obtained by counting events in which two same-sign muons are present, and calculating the corresponding charge asymmetry $A_{\mu\mu}$ (see Eq. 1.2.31). The motivation for this measurement is primarily due to the contribution of a_{sl}^d and a_{sl}^s to $A_{\mu\mu}$, but since no explicit reconstruction of a B -meson decay is done, there are additional contributions to $A_{\mu\mu}$ that need to be considered.

In the 2011 D0 result [45], contributions from backgrounds and detection asymmetries are taken into account. The contribution from b -hadron decays that can also produce a same-sign dimuon final state without mixing, such as $b \rightarrow c$ decays as e.g. $B^0 \rightarrow D^- (\rightarrow K^0 \mu^- \bar{\nu}_\mu) \pi^+$ decays (while the other b -hadron decays semileptonically), is also included. These decays contribute equally to the number of $\mu^+ \mu^+$ and $\mu^- \mu^-$ final states, and dilute the sensitivity of $A_{\mu\mu}$ to a_{sl}^d and a_{sl}^s .

Other contributions to $A_{\mu\mu}$ have been considered since the 2011 D0 result was published. In Ref. [46] the potential contribution from CP violation in the interference between mixing and decay in the B^0 and B_s^0 systems is estimated. This can contribute to $A_{\mu\mu}$ when one b hadron decays semileptonically, while the other decays as e.g. $B_{(s)}^0 \rightarrow D_{(s)}^+ D_{(s)}^-$, where

the $D_{(s)}^-$ meson subsequently decays semileptonically. Due to CP violation in interference, $P(B_{(s)}^0 \rightarrow D_{(s)}^+ D_{(s)}^-)(t) \neq P(\bar{B}_{(s)}^0 \rightarrow D_{(s)}^- D_{(s)}^+)(t)$ resulting in a charge asymmetry. These contributions depend on the values of Δm , $\Delta\Gamma$ and the amount of CP violation in interference in these decays given by $\sin(2\beta_{(s)})$ [3]. The integrated contributions are found to be negligible for the B_s^0 system due to the small value of $\sin(2\beta_s)$ and the dilution due to the high mixing frequency Δm_s . The contribution of CP violation in interference of B^0 mesons is taken into account by the D0 collaboration in the 2013 update [47] as follows. Since experimentally only an upper bound on the value of $\Delta\Gamma_d$ exists, the SM value is used. This results in a 3.6σ deviation from the SM prediction. However, there is ample room for new-physics contributions to $\Delta\Gamma_d$, for instance through decays such as $B^0 \rightarrow \tau^+ \tau^-$ [115]. When allowing the values of a_{sl}^d , a_{sl}^s and $\Delta\Gamma_d$ free in the fit to the observed $A_{\mu\mu}$, the discrepancy with the SM predictions of a_{sl}^d , a_{sl}^s and $\Delta\Gamma_d$ reduces to 3.0σ , with large correlations between the parameters.

In addition, decays where direct CP violation can be expected, but is not yet measured, can contribute to $A_{\mu\mu}$. An example is the decay $B^+ \rightarrow \bar{D}^0(\rightarrow \mu^- X)D^+$. The SM contribution of such decays is expected to be negligible [46], but new-physics contributions can enhance this effect. The same argument holds for decays where no sizeable direct CP violation is expected in the SM, such as in semileptonic decays of b - and c -hadrons [116, 117]. Such new-physics contributions might also explain the D0 dimuon anomaly.

The possibility of other (SM or new physics) contributions to $A_{\mu\mu}$ that would have been overlooked cannot be excluded. Unfortunately, LHCb is unable to measure the like-sign dimuon asymmetry, mainly due to possible production asymmetries originating from the pp collisions (as opposed to the $p\bar{p}$ collisions at the Tevatron). However, the currently unmeasured contributions mentioned above can be investigated by LHCb. One idea is to constrain the amount of CP violation in mixing using existing measurements of CP violation in interference [118]. Assuming that new physics contributions to the phase of $\Gamma_{12,s}$ are negligible, and new-physics contributions to penguin diagrams in $B_s^0 \rightarrow J/\psi \phi$ are negligible [119, 120], the contribution of new physics to the CP -violating phase in $b \rightarrow c\bar{c}s$ transitions, called ϕ_s , should be the same as the new physics contribution to ϕ_{12} in a_{sl}^s [121]. Since the phase ϕ_s is measured to be consistent with zero in decays such as $B_s^0 \rightarrow J/\psi \phi$ [28] and $B_s^0 \rightarrow D_s^- D_s^+$ [122], this constrains the size of new physics contributions to ϕ_{12} . Combined with the world-average values for $\Delta\Gamma_s$ and Δm_s (Eq. 1.2.27 and 1.2.28) this results in an estimate of

$$a_{\text{sl}}^s = (0.004 \pm 0.075)\%, \quad (6.2.1)$$

and the LHCb measurement of a_{sl}^s can potentially be used to measure other sources of CP violation, such as the direct CP violation in semileptonic B_s^0 decays, which was assumed to be zero in the analyses in this thesis. Another suggestion made in Ref. [118] is to use this method to measure direct CP violation in Cabibbo-favoured charm decays using the measurement of a_{sl}^s , which were also assumed to be negligible. However, this is not

straightforward due to the extensive use of charm hadron decays as calibration modes throughout this thesis. Possibly in the future, one can rely on simulation studies to model the detection asymmetries with enough accuracy to make this possible.

6.3 Future prospects

The SM prediction for a_{sl}^d and a_{sl}^s (Eq. 1.2.29) is much more precise than the experimental measurements presented in this thesis. This implies that — even though CP violation in mixing is unlikely to fully explain the D^0 dimuon anomaly — there is a potential that new-physics contributions to the mixing process exist. In order to confirm or exclude whether this is the case, a large improvement in the experimental uncertainty on a_{sl}^d and a_{sl}^s is required. The largest source of uncertainty for the a_{sl}^d and a_{sl}^s analyses is the statistical error on the signal sample. This can be improved upon with future data and by including other decay channels.

6.3.1 Additional charm decay channels

A possibility is including more decay modes of the D^- (\bar{D}^0) and D_s^- mesons, for example $D_s^- \rightarrow \pi^- \pi^+ \pi^-$ ($\mathcal{B} = 1.1\%$) decays, which do not suffer from kaon material interactions. This mode has a branching fraction that is about 1/5 of the total $D_s^- \rightarrow K^+ K^- \pi^-$ branching fraction, and would naively increase the number of a_{sl}^s signal decays by a factor 1.2. In addition, the $\bar{D}^0 \rightarrow K^+ \pi^- \pi^+ \pi^-$ mode could be considered for the a_{sl}^d analysis. This mode has a branching fraction of 8.1% which is twice that of the $\bar{D}^0 \rightarrow K^+ \pi^-$ mode. The downside of these many-body final states is that each additional track suffers from a reconstruction inefficiency. The combined probability for a track to be within LHCb acceptance, to not have a hadronic interaction with the detector material and to be efficiently reconstructed depends on the kinematic distributions of the particle, and is roughly estimated to be about 70%. Taking that into account, the amount of a_{sl}^d signal decays when adding $\bar{D}^0 \rightarrow K^+ \pi^- \pi^+ \pi^-$ decays increases by a factor 1.2.

Finally, charm decays involving one or more neutral final-state particles have significant branching fractions. Decays involving a K_s^0 suffer from a reduced reconstruction efficiency due to the additional track from the $K_s^0 \rightarrow \pi^+ \pi^-$ decay, and the branching ratio of these decays is 70%. In addition, only 1/3 of the K_s^0 mesons decay inside the VELO, which is required for the reconstruction of a K_s^0 with two long tracks. The detection asymmetry for neutral kaons is already used in Sec. 3.2, and has been studied in Ref. [99]. Taking the above into account, adding $D_s^- \rightarrow K^- K_s^0$ ($\mathcal{B} = 1.5\%$) decays to the a_{sl}^s analysis naively increases the amount of signal decays by a factor 1.1. In decays involving a π^0 or γ , the reconstruction of a narrow invariant mass peak is more challenging since neutral particles have a worse momentum resolution. However, for decays involving a π^0 , such as $D^{*-} \rightarrow \bar{D}^0 (\rightarrow K^+ \pi^- \pi^0) \pi^-$, the delta-mass peak ($m_{D^{*-}} - m_{\bar{D}^0}$) is still narrow enough to separate the signal from the background [123]. The efficiency of reconstructing a π^0 candidate is estimated to be about 50% [124]. Adding the $\bar{D}^0 \rightarrow K^+ \pi^- \pi^0$ mode

($\mathcal{B} = 14.2\%$) to the a_{sl}^d analysis would naively provide a factor of 1.3 increase in signal yield.

Adding these additional charm decay channels also requires to understand the background contributions in all of these, as well as measuring potential sources of detection asymmetries. If this is understood, potentially the total signal statistics in a_{sl}^s can be increased by a factor of 1.3, and in the a_{sl}^d analysis by a factor 1.4. This does not, however, provide a significant improvement to the final result, as can be seen in Table 6.1. Hence, this approach is not considered further.

6.3.2 Additional beauty decay channels

Other semileptonic decays of B^0 and B_s^0 mesons that include a D^- (D^{*-}) or D_s^- meson in the final state, for instance through higher resonances, are already included in the analyses in this thesis. Semileptonic decays that do not decay to charm hadrons are Cabibbo-suppressed and have a low branching ratio [2], so these will not be considered further. However, one could consider using the fully-reconstructible modes $B_{(s)}^0 \rightarrow D_{(s)}^- \pi^+$ (without a neutrino in the final state) to measure CP violation in mixing. These modes have been used at LHCb to measure the mixing frequencies Δm_d [125] and Δm_s [126]. The narrow $B_{(s)}^0$ invariant mass peak will allow to distinguish signal decays from backgrounds peaking in the $D_{(s)}^-$ mass. Decays of $B^0 \rightarrow D^- \pi^+$ are not flavour specific, and contributions from CP violation in interference in this decay [127] should be taken into account. In appendix D this contribution to the untagged CP asymmetry is estimated, and found to be negligible. However, the $B_{(s)}^0 \rightarrow D_{(s)}^- \pi^+$ branching fractions are an order of magnitude smaller, the hardware-level trigger efficiency is about 30% lower for hadrons than for muons [80], and it is more difficult to determine the hardware-level trigger detection asymmetry. This is partly due to the low granularity of the calorimeters. These modes would provide an independent measurement of a_{sl}^d and a_{sl}^s , with different detection asymmetries and backgrounds. The results will, however, not be competitive in terms of statistics.

6.3.3 Reducing errors due to calibration samples

The second- and third-largest errors originate from the statistical and systematic error on the calibration samples. The statistical error can be improved upon with additional methods or channels for determining detection asymmetries (such as was done for the J/ψ tag-and-probe and D^{*-} partial-and-full methods for the tracking asymmetry in the a_{sl}^s analysis). There are on-going efforts to study the use of new methods to measure the detection asymmetries. One example is to use $D^{*-} \rightarrow \bar{D}^0 (\rightarrow K^+ \pi^-) \pi^-$ decays where one of the tracks from the \bar{D}^0 decay is only required to be reconstructed in the VELO. Such a method could be used to determine the long tracking efficiency of the rest of the detector. This is useful as the charge asymmetry caused by the VELO is small. Several advantages are that the “probe” track is not required to be in the acceptance of the muon stations — as is the case with the J/ψ tag-and-probe method — and the VELO track

adds a constraint that allows for a narrow partially reconstructed invariant mass peak — which is not the case for the D^{*-} partial-and-full method. A reduction of the systematic error on the detection asymmetries might be possible when the individual contributions of all possible detector effects are better understood. This would allow for a more optimal decision of the variables and bins used in the weighting of the calibration samples, or an improved selection to remove events that are expected to have a large detection asymmetry.

6.3.4 Reducing errors due to backgrounds

The next largest contribution to the error on a_{sl}^d and a_{sl}^s is the contribution from peaking backgrounds. In the a_{sl}^d analysis this is mostly due to the error on the production asymmetry of the B^+ , which is determined from external measurements and contributes 0.12% to the total systematic error. As already mentioned in Sec. 4.4.5, this error can be halved when using an updated LHCb measurement employing $B^+ \rightarrow \bar{D}^0 \pi^+$ decays [104]. The largest uncertainty on the asymmetry of the peaking background modes in the a_{sl}^s analysis, is due to the A_b^0 production asymmetry. This is currently being measured at LHCb with improved precision, as already mentioned in Sec. 5.3.2. In order to reduce the error on the background fraction f_{bkg} , the branching fractions of the signal and background modes have to be measured more precisely. These are measured at the B -factories [2] and are difficult to improve upon at a hadron collider. Higher-precision measurements of these branching fractions could be performed at Belle II experiment in Tsukuba, Japan, which starts data-taking in 2018.

A further improved estimate of the contribution from peaking backgrounds could be made by performing a fit to a parameter that has some distinguishing power between signal and background, using template distributions for signal and every type of background (obtained e.g. from simulated events). A first attempt of this method was made as a cross-check of the B^+ fraction, using the corrected B^0 mass, in Sec. 4.3.3. In the LHCb analysis of semileptonic $B^0 \rightarrow D^{*-} \tau^+ \nu_\tau$ decays, this method was successfully applied by modelling the missing B^0 mass, muon energy, and q^2 of the decay for each background type [128]. Such a method would allow to determine the background fractions directly from data. Potentially this method could even measure the asymmetry in these backgrounds directly.

6.3.5 Beyond run 1

Adding additional data taken during run 2 (2015-2018) of the LHC will reduce all statistical errors. The plan is to collect at least 5 fb^{-1} at a centre-of-mass energy of $\sqrt{s} = 13 \text{ TeV}$. The $b\bar{b}$ production cross-section at this energy is about twice that of run 1 [129]. In addition, a real-time alignment and calibration is implemented [130], which increases online performance, and an upgraded computing infrastructure and revised trigger setup [131] allows for a rate of 12.5 kHz of events written to storage (compared to 5 kHz in 2012), a significant amount of which is dedicated to charm decays. Using all data at the end of run

2, this would result in a factor of 4.3 more signal events for both a_{sl}^d and a_{sl}^s . Due to the increased bandwidth for charm decays, this number is likely to be even higher for most of the calibration channels.

After 2018 the LHCb detector will be upgraded [132] to be able to deal with luminosities of $2 \times 10^{33} \text{ cm}^{-2}\text{s}^{-1}$ or above, corresponding to an average number of visible pp interactions per bunch crossing of $\mu_{\text{vis}} = 5.2$ [133]. In order to deal with the larger detector occupancy, the sensors in the VELO will be replaced by a pixel-based silicon detector. In addition, the IT and OT will be replaced with a scintillating-fibre detector called the SciFi, with fibres and channels that are $250 \mu\text{m}$ wide (compared to the 5-mm-wide OT straws). The TT will be replaced with a finer-grained silicon-strip detector called Upstream Tracker (UT). Finally, the hardware-level trigger will be completely removed in order to avoid the 1 MHz readout bottleneck, and all detector electronics will be replaced and read out at 40 MHz [134]. The plan is to collect a total of 50 fb^{-1} with the upgraded LHCb detector. This would naively increase the amount of signal and calibration data by a factor 30 with respect to the analyses in this thesis.

Using the estimates for the errors described above, possible future measurements of LHCb are indicated in Table 6.1 and Fig. 6.2. In the run-2 estimate, a reduction of statistical errors on both the signal and calibration samples are taken into account, as well as a reduction in the systematic uncertainty of a factor 2 due to a better understanding of the detection asymmetries, and additional calibration methods. In the LHCb upgrade estimate, this is chosen to be a factor 10 smaller than the current analyses. The correlation between the a_{sl}^d and a_{sl}^s measurements is chosen to be the same as for the measurements in this thesis, $\rho = +0.13$. As can be observed in Fig. 6.2, an evidence or discovery of new physics is well possible with these future updates, while being compatible with the current measurements.

6.4 Closing remarks

The measurements of a_{sl}^d and a_{sl}^s presented in this thesis improve our understanding of the anomaly that was present in 2013. No significant evidence for new-physics contributions to B -meson mixing is seen yet. Due to the statistical limitations of the measurements, exciting improvements can be expected after run 2 and after the upgrade of LHCb, which

	a_{sl}^d [%]	a_{sl}^s [%]
run 1	0.39 ± 0.36	-0.02 ± 0.33
run 1+	± 0.34	± 0.31
run 2	± 0.17	± 0.16
Upgrade	± 0.06	± 0.06

Table 6.1: Potential measurement errors of a_{sl}^d and a_{sl}^s by LHCb after the considerations explained in the text.

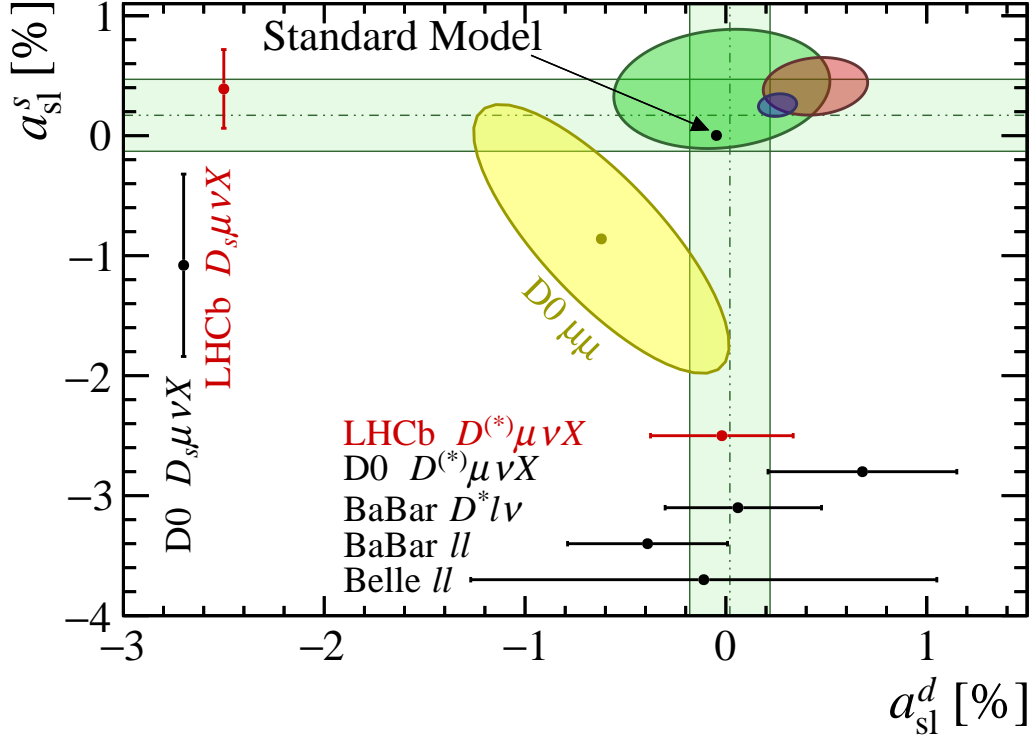


Figure 6.2: Future prospects of the a_{sl} analyses at LHCb overlaid on Fig. 6.1. The two-dimensional combination of the measurements provided in this thesis are indicated by the green ellipse. A possible result including run-2 data is indicated in red, where the central value is (arbitrarily) chosen such that the combined result is 3σ away from the SM. Finally, the possible result after including LHCb upgrade data is indicated in the purple ellipse, with the central value chosen to be 5σ away from the SM, indicating a discovery. The borders of the ellipses show the 68% confidence level intervals with two degrees of freedom.

have the potential to claim a new-physics discovery.

The role of a_{sl} in the future search for new physics will be complementary to analyses with a higher precision to the phase of M_{12} , such as CP violation in interference in $B_s^0 \rightarrow J/\psi \phi$ decays. Together, constraints on new-physics contributions from other sources can be made, such as a non-SM contribution to $\Delta\Gamma_d$ from $B^0 \rightarrow \tau^+ \tau^-$ decays, which are very difficult to reconstruct. In addition, the measurements of a_{sl} require a precise understanding of the LHCb detector, in particular its detection asymmetries, for which this thesis shows that they can be controlled with sufficient precision.

Appendices



A

Time integration of the a_{sl}^s analysis

The idea to perform a time-integrated analysis for a_{sl}^s stems from the 1 fb^{-1} analysis of LHCb [48]. The idea is as follows. In order to properly integrate the transition probabilities in Eq. 1.2.22 over time, including the detector effects as in Eq. 1.2.38 we first multiply the probabilities by the detector time acceptance $\epsilon_t(t)$ which represents the time-dependent part of the detection efficiency. This effect is expected to be equal for B_s^0 and \bar{B}_s^0 so it was not considered before. However, it will not drop out of the asymmetry here due to the time integral. The time acceptance can be parametrized by

$$\epsilon_t(t) = \frac{[1 + \beta(t - t_0)][a(t - t_0)]^n}{1 + [a(t - t_0)]^n}, \quad (\text{A.0.1})$$

where the parameters $a = 1.382$, $n = 1.771$, $t_0 = 0.07742 \text{ ps}$ and $\beta = -0.0494$ are found from a fit to simulated B_s^0 decays. The shape of the time acceptance, shown in Fig. A.1, has a turn-on at low decay times due to the requirement that the decay vertex of the B_s^0 meson is significantly displaced with respect to the point at which the B_s^0 was created, the primary vertex (PV). The slow fall-off at larger decay times is due a decrease in reconstruction efficiency for tracks far away from the central axis in the VELO. Going through the calculation of Eq. 1.2.42 again, we find

$$\begin{aligned} A_{CP}^{\text{meas}} &\approx A_{\text{det}} + \frac{a_{\text{sl}}}{2} - \left(A_P + \frac{a_{\text{sl}}}{2} \right) \frac{\int_{t=0}^{\infty} e^{-\Gamma t} \cos(\Delta m t) \epsilon_t(t) dt}{\int_{t=0}^{\infty} e^{-\Gamma t} \cosh(\frac{\Delta \Gamma t}{2}) \epsilon_t(t) dt} \\ &\approx A_{\text{det}} + \frac{a_{\text{sl}}}{2} - \left(A_P + \frac{a_{\text{sl}}}{2} \right) \frac{0.001}{0.73}, \end{aligned} \quad (\text{A.0.2})$$

where the same approximations are used as before, but keeping the time-dependent cosh term this time, since it deviates slightly from one at larger times in the B_s^0 system. In the computation of the integrals the latest combination of experimental values for $\Delta m_s = 17.8 \hbar \text{ ps}^{-1}$, $\Gamma_s = 1/1.5 \text{ ps}^{-1}$ and $\frac{\Delta \Gamma_s}{\Gamma_s} = 0.12$ are used [2]. This means that any existing production asymmetry will be diluted by $\sim 10^3$. Since both a_{sl}^s and A_P are expected to be small, this is below the expected experimental precision and we can safely ignore this term in a time-integrated analysis.¹

¹Note that if we try the same for the B^0 system, i.e. using $\Delta m_d = 0.51 \hbar \text{ ps}^{-1}$, $\Gamma_d \approx \Gamma_s$ and $\Delta \Gamma_d \approx 0$ the ratio of integrals becomes 0.5.

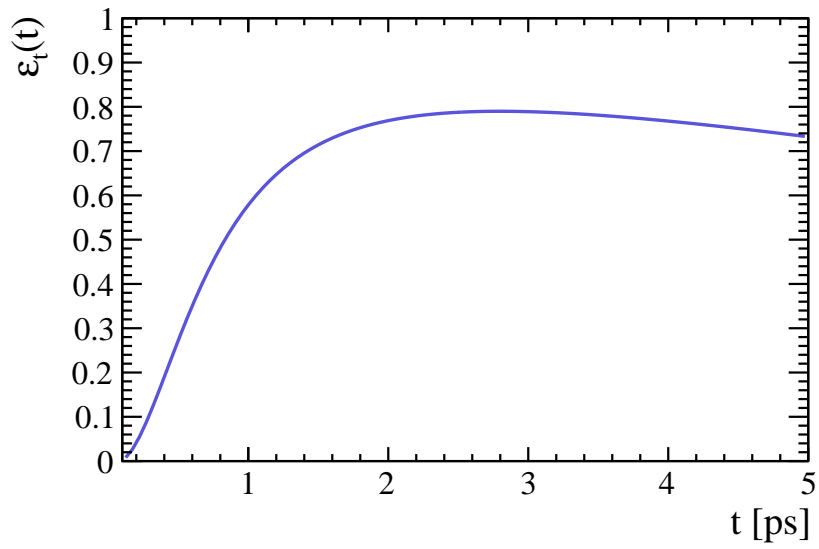


Figure A.1: The lifetime acceptance of B mesons in LHCb (Eq. A.0.1).

B

Additional material in the a_{sl}^d analysis

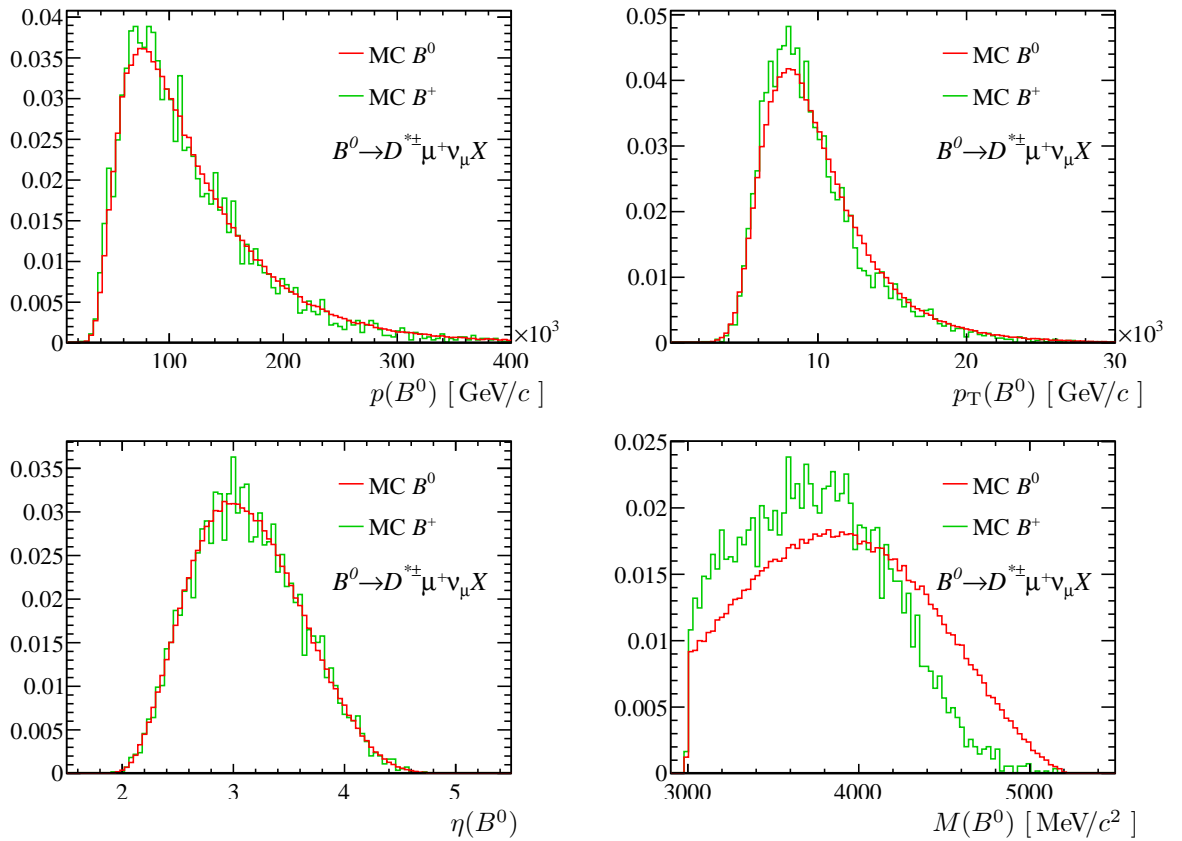


Figure B.1: The momentum distributions of the reconstructed B candidate in the $B^0 \rightarrow D^{*\pm} \mu^+ \nu_\mu X$ mode for signal and B^+ background in simulation (MC).

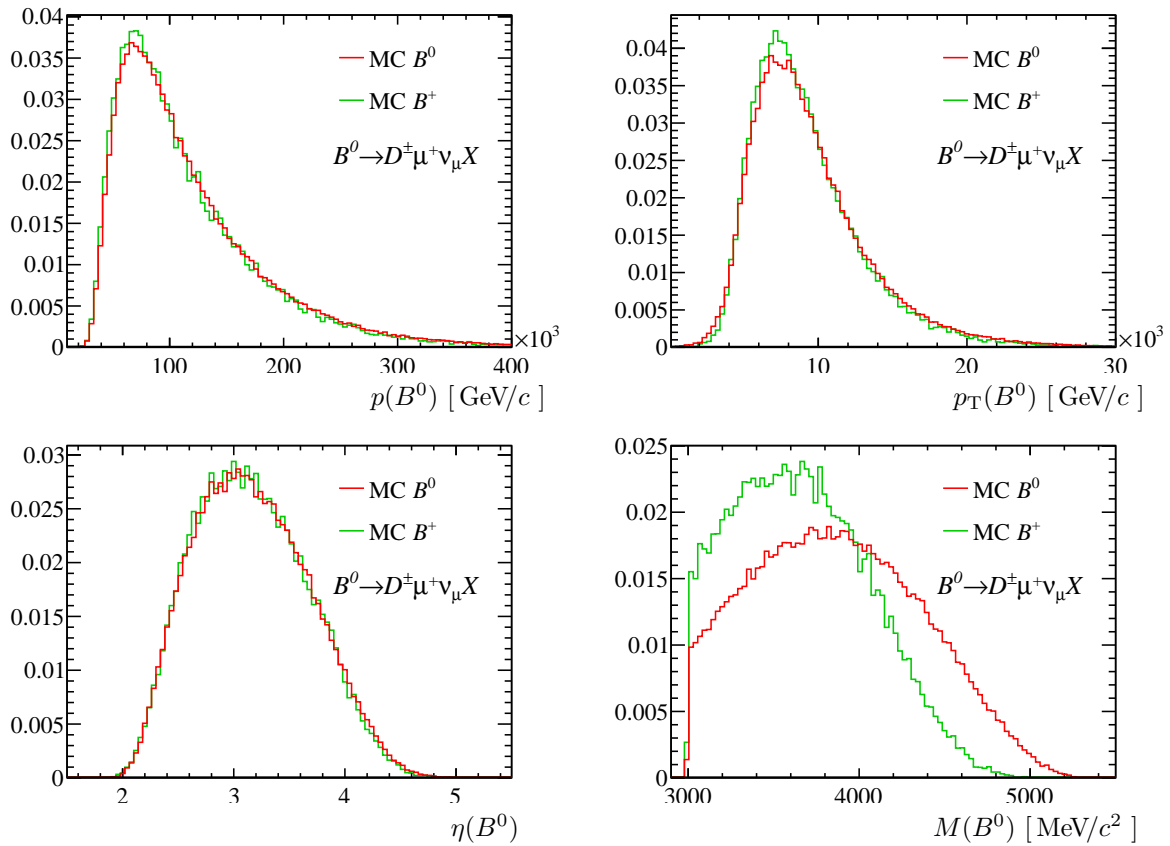


Figure B.2: The momentum distributions of the reconstructed B candidate in the $B^0 \rightarrow D^+ \mu^+ \nu_\mu X$ mode for signal and B^+ background in simulation (MC).

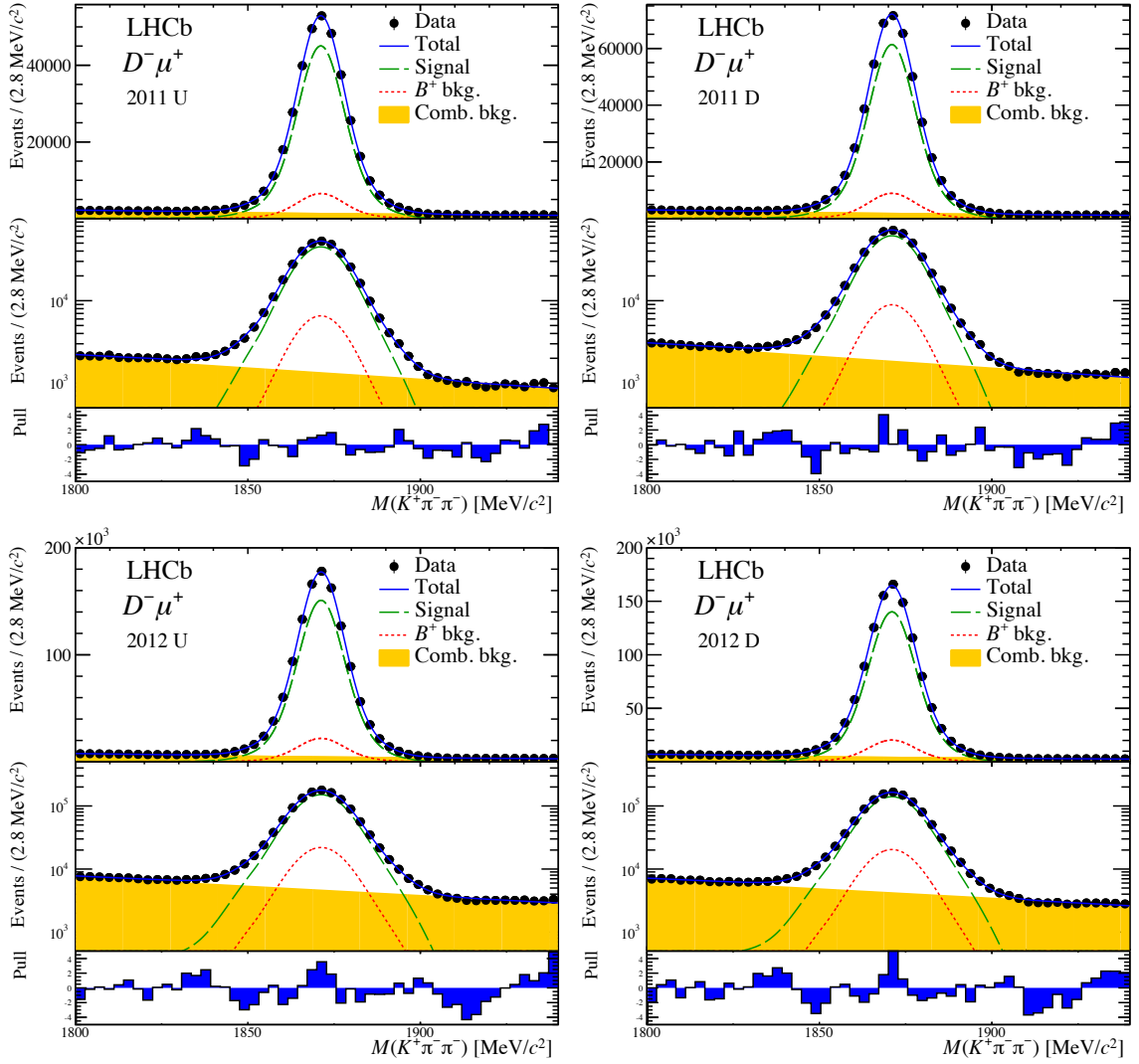


Figure B.3: Projection of the D^- invariant mass in the nominal fit to (top) 2011 and (bottom) 2012 data, with magnet polarity (left) up (U) and (right) down (D), in the $B^0 \rightarrow D^- \mu^+ \nu_\mu X$ sample. The distribution of the fit residual divided by the error (pull) is shown below.

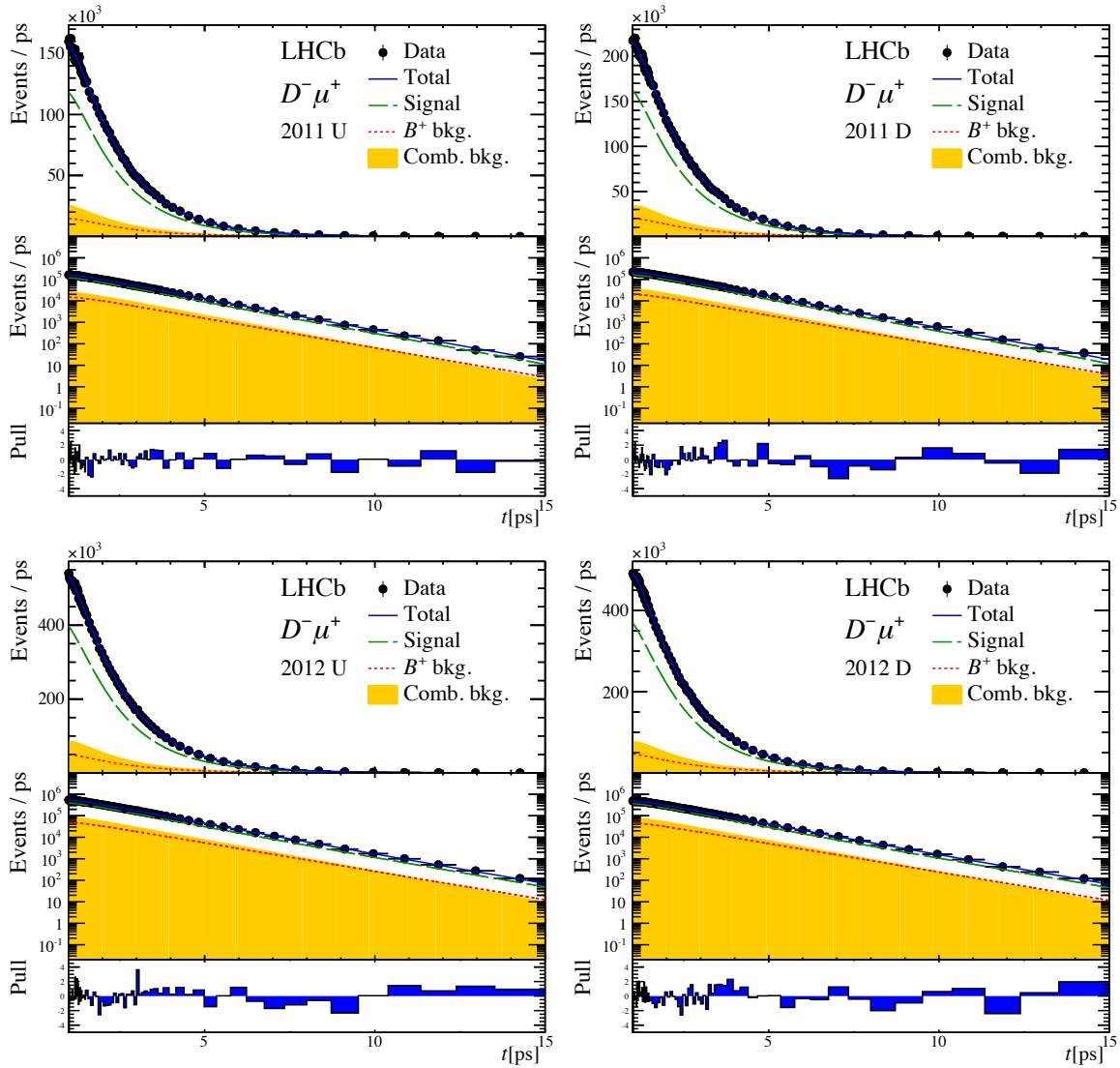


Figure B.4: Projection of the B^0 decay time in the nominal fit to (top) 2011 and (bottom) 2012 data, with magnet polarity (left) up (U) and (right) down (D), in the $B^0 \rightarrow D^- \mu^+ \nu_\mu X$ sample. The distribution of the fit residual divided by the error (pull) is shown below.

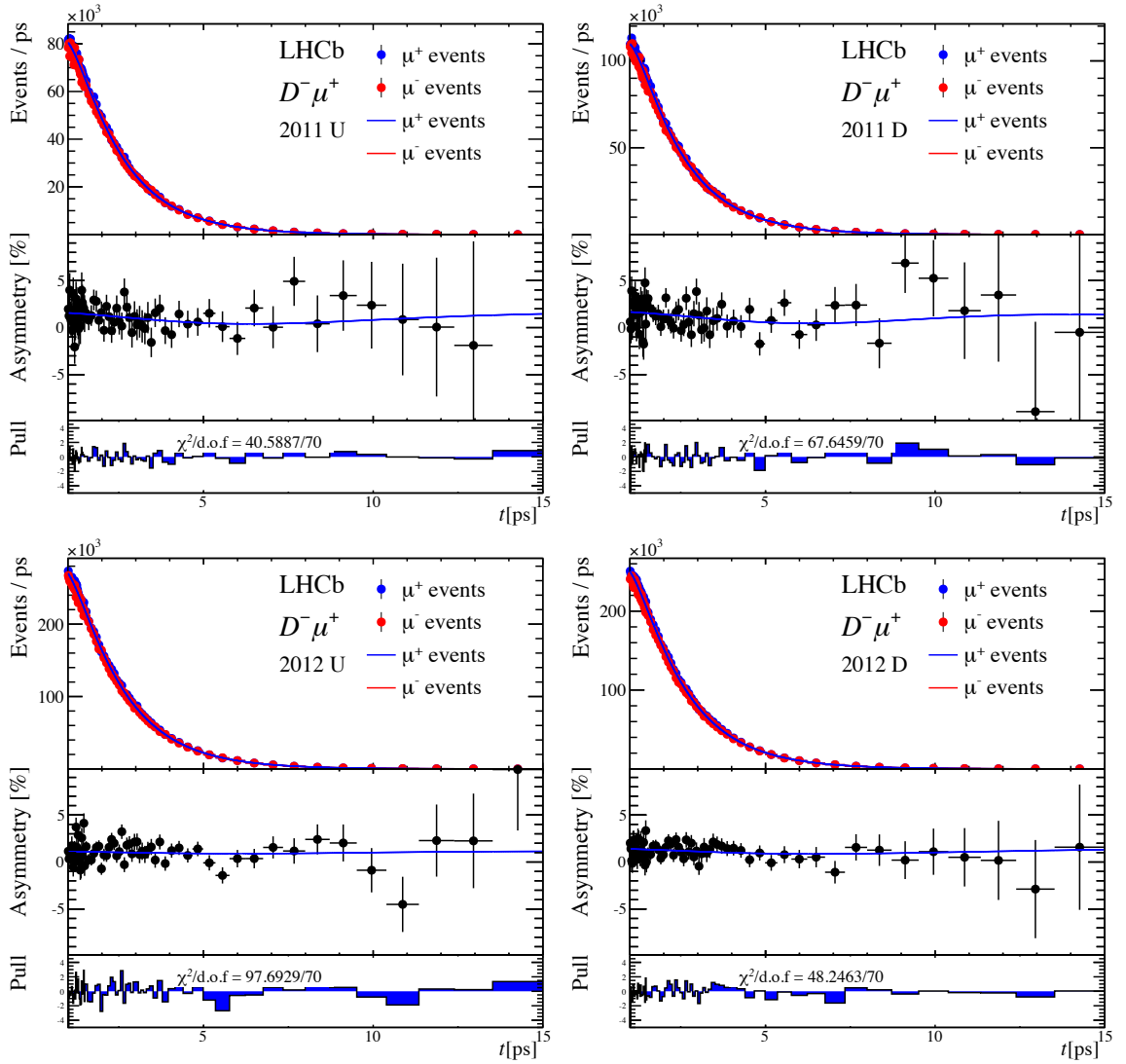


Figure B.5: Projection of the charge asymmetry in the nominal fit to (top) 2011 and (bottom) 2012 data, with magnet polarity (left) up (U) and (right) down (D), in the $B^0 \rightarrow D^- \mu^+ \nu_\mu X$ sample. The distribution of the fit residual divided by the error (pull) is shown below.

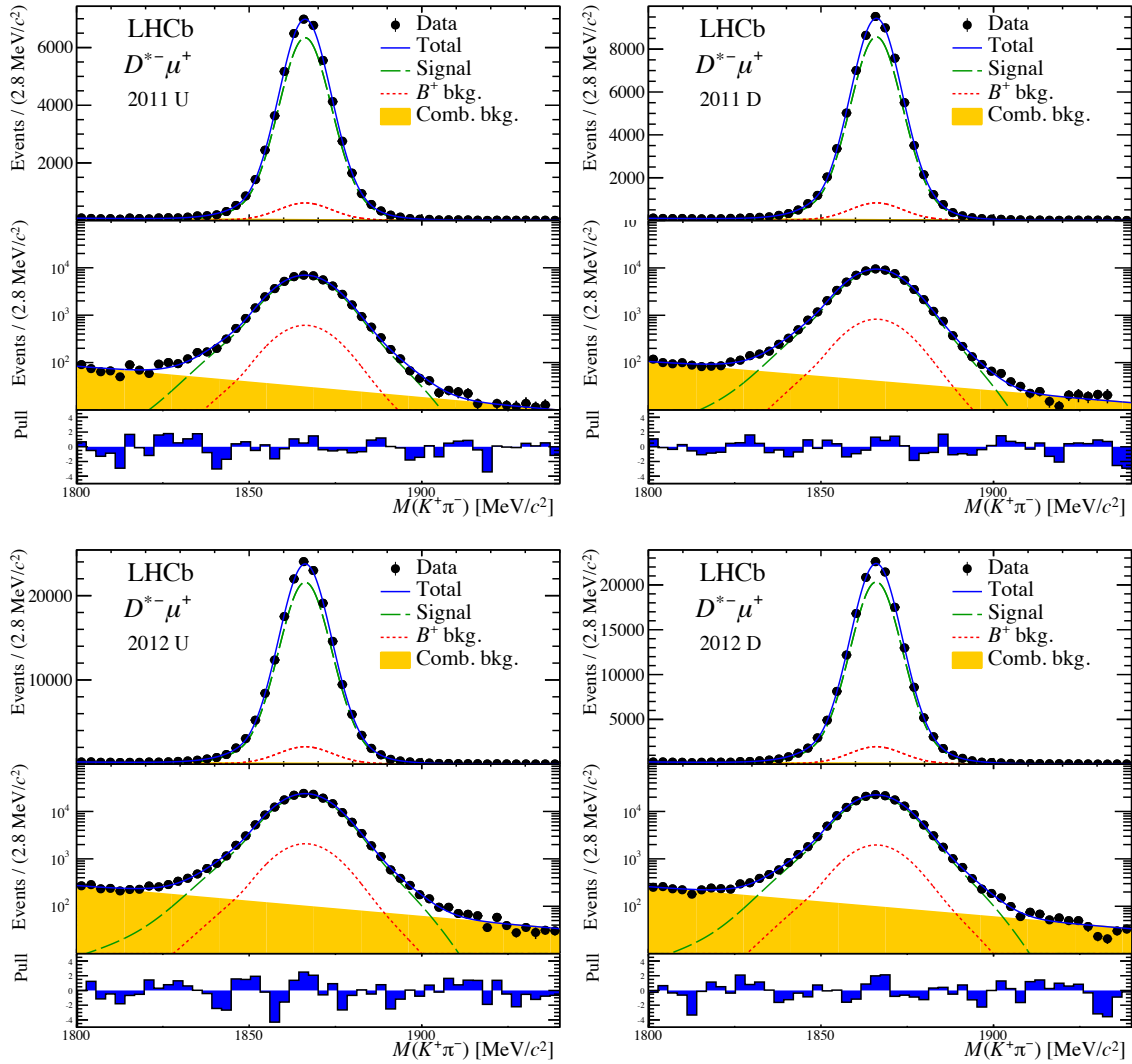


Figure B.6: Projection of the D^- invariant mass in the nominal fit to (top) 2011 and (bottom) 2012 data, with magnet polarity (left) up (U) and (right) down (D), in the $B^0 \rightarrow D^{*-}\mu^+\nu_\mu X$ sample. The distribution of the fit residual divided by the error (pull) is shown below.

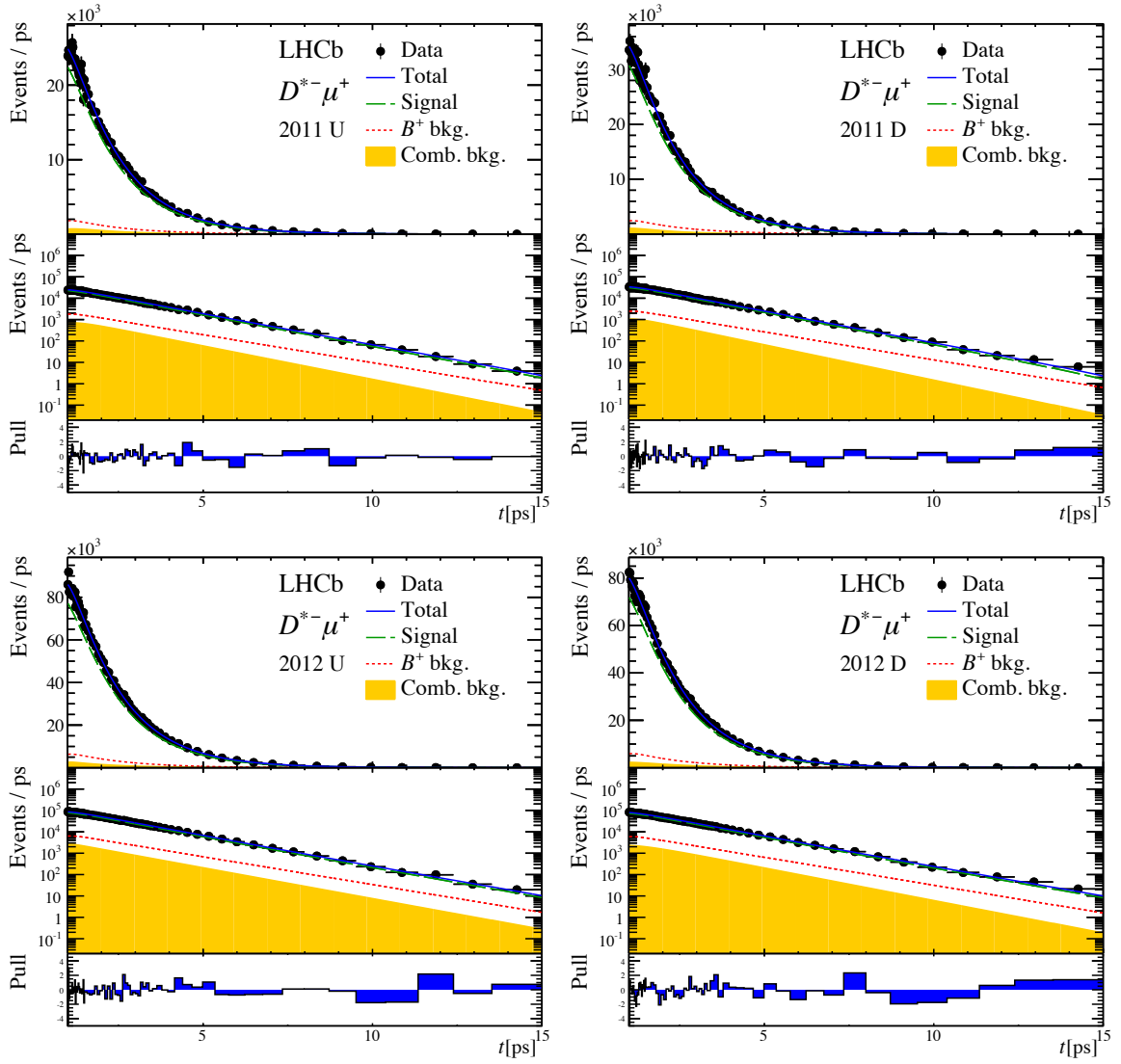


Figure B.7: Projection of the B^0 decay time in the nominal fit to (top) 2011 and (bottom) 2012 data, with magnet polarity (left) up (U) and (right) down (D), in the $B^0 \rightarrow D^{*-}\mu^+\nu_\mu X$ sample. The distribution of the fit residual divided by the error (pull) is shown below.

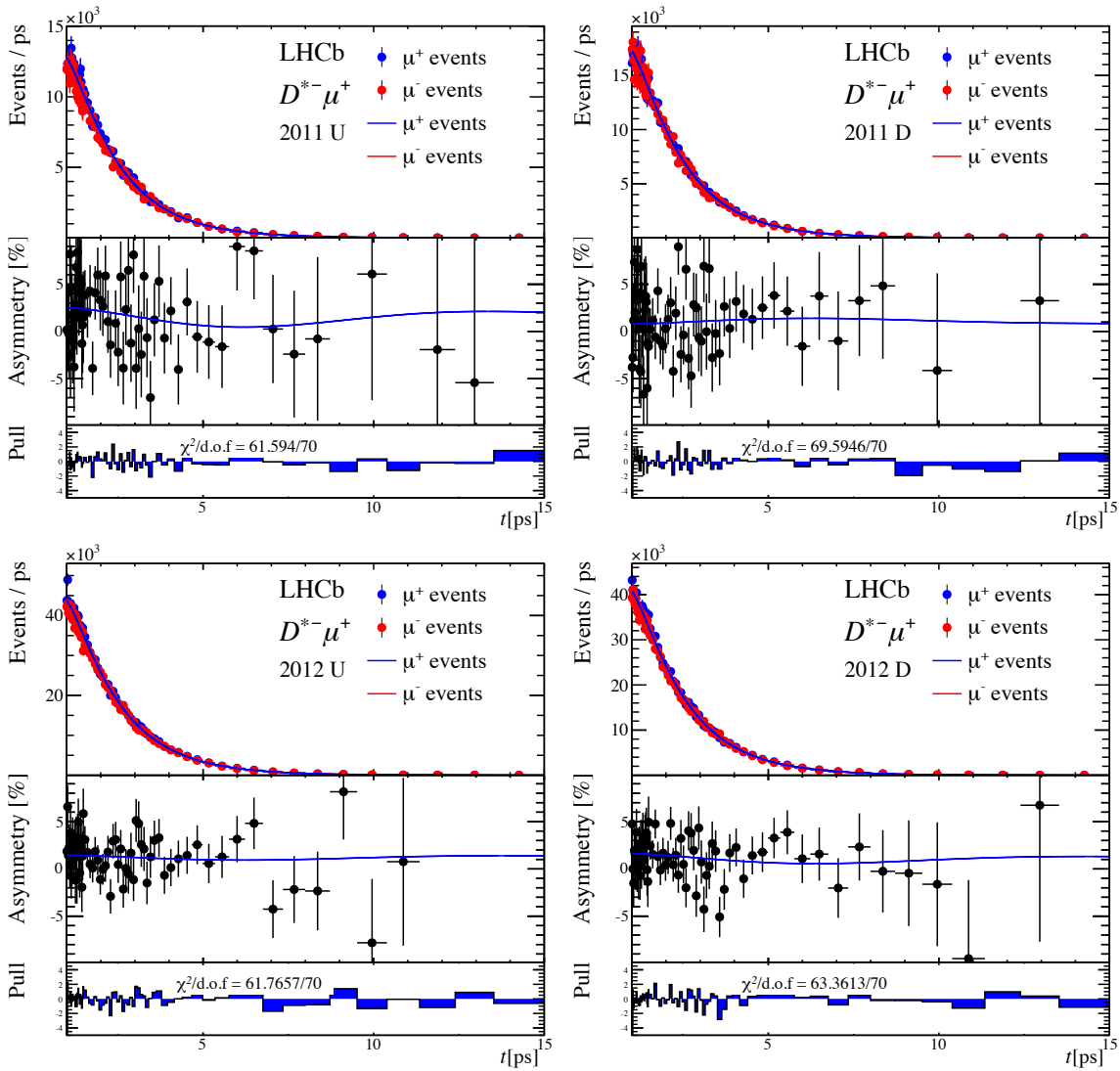


Figure B.8: Projection of the charge asymmetry in the nominal fit to (top) 2011 and (bottom) 2012 data, with magnet polarity (left) up (U) and (right) down (D), in the $B^0 \rightarrow D^{*-} \mu^+ \nu_{\mu} X$ sample. The distribution of the fit residual divided by the error (pull) is shown below.

C

Additional material in the a_{sl}^s analysis

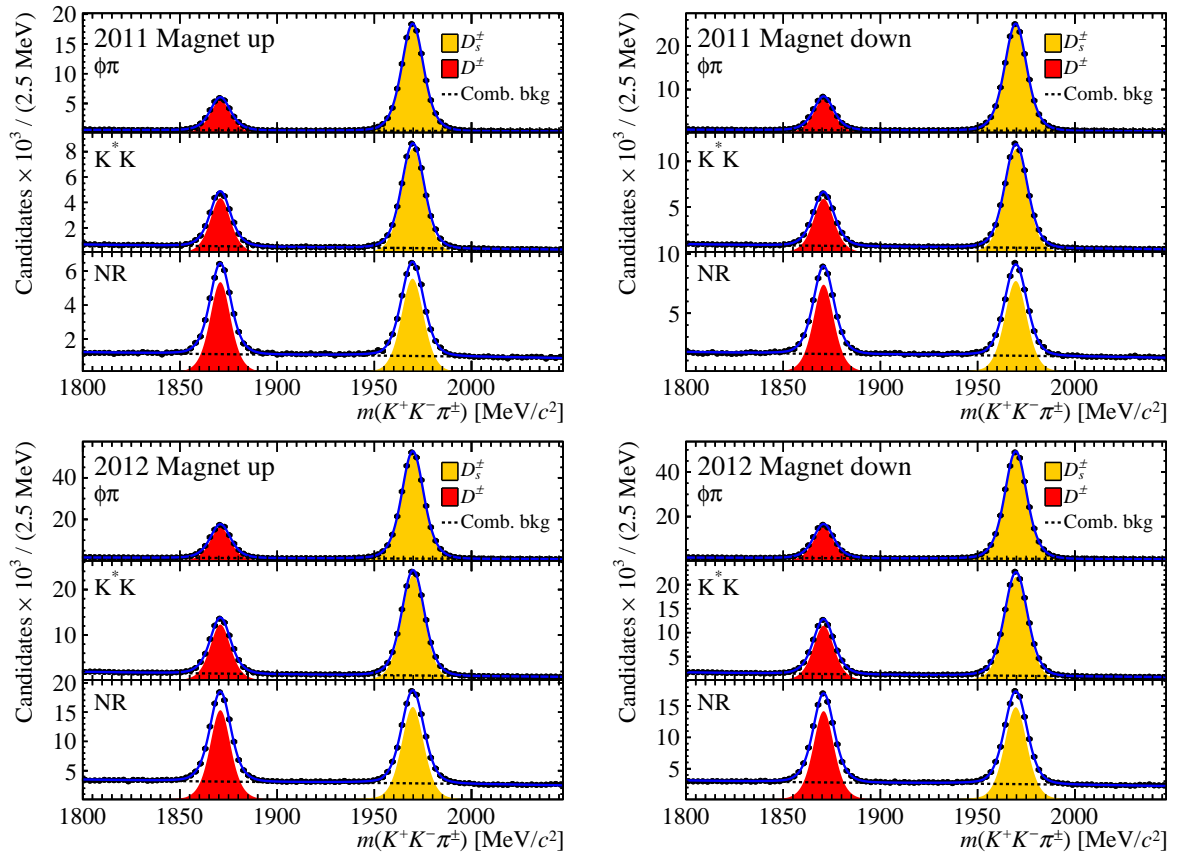


Figure C.1: Invariant mass distribution of the $K^+K^-\pi^\pm$ combinations in the a_{sl}^s signal sample, for each magnet polarity and data-taking year. The fit result is overlaid.

D

Using hadronic decays

This appendix considers using the Cabibbo-favoured hadronic decay mode $B^0 \rightarrow D^- \pi^+$ instead of the semileptonic mode $B^0 \rightarrow D^- \mu^+ \nu_\mu X$ to measure a_{sl}^d . Since $B^0 \rightarrow D^- \pi^+$ decays are not flavour-specific, one has to take into account contributions from CP violation in interference to A_{CP}^{meas} . After including the decay amplitudes to final states f and \bar{f} , additional terms appear in the transition probabilities of Eq. 1.2.22,

$$\begin{aligned}
 P(\bar{B}^0 \rightarrow f)(t) &= |A_f|^2 \left| \frac{p}{q} \right|^2 \left(|g_-(t)|^2 + |\lambda_f|^2 |g_+(t)|^2 + 2\Re[\lambda_f g_+(t) g_-^*(t)] \right), \\
 P(B^0 \rightarrow \bar{f})(t) &= |\bar{A}_{\bar{f}}|^2 \left| \frac{q}{p} \right|^2 \left(|g_-(t)|^2 + |\bar{\lambda}_{\bar{f}}|^2 |g_+(t)|^2 + 2\Re[\bar{\lambda}_{\bar{f}} g_+(t) g_-^*(t)] \right), \\
 P(B^0 \rightarrow f)(t) &= |A_f|^2 \left(|g_+(t)|^2 + |\lambda_f|^2 |g_-(t)|^2 + 2\Re[\lambda_f g_+^*(t) g_-(t)] \right), \\
 P(\bar{B}^0 \rightarrow \bar{f})(t) &= |\bar{A}_{\bar{f}}|^2 \left(|g_+(t)|^2 + |\bar{\lambda}_{\bar{f}}|^2 |g_-(t)|^2 + 2\Re[\bar{\lambda}_{\bar{f}} g_+^*(t) g_-(t)] \right), \quad (\text{D.0.1})
 \end{aligned}$$

where

$$\begin{aligned}
 \lambda_f &= \frac{q \bar{A}_f}{p A_f} \\
 \bar{\lambda}_{\bar{f}} &= 1/\lambda_{\bar{f}} = 1/\left(\frac{q \bar{A}_{\bar{f}}}{p A_{\bar{f}}} \right), \quad (\text{D.0.2})
 \end{aligned}$$

and $|A_f|^2$ is the amplitude of $B^0 \rightarrow f$, $|\bar{A}_{\bar{f}}|^2$ is the amplitude of $\bar{B}^0 \rightarrow \bar{f}$, etc. For flavour-specific final states, we have $\bar{A}_f = A_{\bar{f}} = 0$ and hence $\lambda_f = \bar{\lambda}_{\bar{f}} = 0$, so we get back to Eq. 1.2.22. To first order, there is no penguin diagram in this decay, such that we can assume that there is no direct CP violation,

$$\frac{|A_f|}{|\bar{A}_{\bar{f}}|} = \frac{|A_{\bar{f}}|}{|A_f|} = 1. \quad (\text{D.0.3})$$

Using the measured branching ratios [2]

$$\begin{aligned}
 \mathcal{B}(B^0 \rightarrow D^- \pi^+) &= (2.52 \pm 0.13) \times 10^{-3} \\
 \mathcal{B}(B^0 \rightarrow D^+ \pi^-) &= (7.4 \pm 1.3) \times 10^{-7}, \quad (\text{D.0.4})
 \end{aligned}$$

we obtain

$$\frac{|A_{\bar{f}}|^2}{|A_f|^2} = 2.9 \times 10^{-4} \equiv \alpha^2, \quad (\text{D.0.5})$$

and we can write

$$\begin{aligned} \lambda_f &= \left| \frac{q}{p} \right| \alpha e^{-i\phi}, \\ \bar{\lambda}_{\bar{f}} &= \left| \frac{p}{q} \right| \alpha e^{-i\phi}, \end{aligned} \quad (\text{D.0.6})$$

where ϕ is the phase associated with CP violation in interference. In the SM, this phase in $B^0 \rightarrow D^- \pi^+$ decays is equal to the CKM angle combination $\phi = (2\beta + \gamma)$, which has been measured to be about 118° [3]. Inserting

$$\begin{aligned} |g_{\pm}(t)|^2 &= \frac{e^{-\Gamma t}}{2} \left(\cosh\left(\frac{1}{2}\Delta\Gamma t\right) \pm \cos(\Delta m t) \right), \\ g_+(t)g_-^*(t) &= \frac{e^{-\Gamma t}}{2} \left(\sinh\left(\frac{1}{2}\Delta\Gamma t\right) - i \sin(\Delta m t) \right), \\ g_+(t)^*g_-(t) &= \frac{e^{-\Gamma t}}{2} \left(\sinh\left(\frac{1}{2}\Delta\Gamma t\right) + i \sin(\Delta m t) \right), \end{aligned} \quad (\text{D.0.7})$$

and using $\Delta\Gamma_d \approx 0$ and $\alpha^2 \approx 0$, we can write

$$\begin{aligned} P(\bar{B}^0 \rightarrow f)(t) &\propto \left| \frac{p}{q} \right|^2 \left(1 - \cos(\Delta m_d t) \right) + 2 \left| \frac{p}{q} \right| \alpha \sin(\phi) \sin(\Delta m_d t), \\ P(B^0 \rightarrow \bar{f})(t) &\propto \left| \frac{q}{p} \right|^2 \left(1 - \cos(\Delta m_d t) \right) + 2 \left| \frac{q}{p} \right| \alpha \sin(\phi) \sin(\Delta m_d t), \\ P(B^0 \rightarrow f)(t) &\propto \left(1 + \cos(\Delta m_d t) \right) - 2 \left| \frac{q}{p} \right| \alpha \sin(\phi) \sin(\Delta m_d t), \\ P(\bar{B}^0 \rightarrow \bar{f})(t) &\propto \left(1 + \cos(\Delta m_d t) \right) - 2 \left| \frac{p}{q} \right| \alpha \sin(\phi) \sin(\Delta m_d t). \end{aligned} \quad (\text{D.0.8})$$

Using these probabilities, the untagged mixing asymmetry (without detection effects, i.e. $A_{\text{det}} = A_P = 0$) is

$$\begin{aligned} A_{CP}^{\text{mix}}(t) &= \frac{P(\bar{B} \rightarrow f) + P(B \rightarrow f) - P(B \rightarrow \bar{f}) - P(\bar{B} \rightarrow \bar{f})}{P(\bar{B} \rightarrow f) + P(B \rightarrow f) + P(B \rightarrow \bar{f}) + P(\bar{B} \rightarrow \bar{f})} \\ &\approx \frac{a_{\text{sl}}^d \left(1 - \cos(\Delta m_d t) \right) + 2\alpha a_{\text{sl}}^d \sin(\phi) \sin(\Delta m_d t)}{2}, \end{aligned} \quad (\text{D.0.9})$$

where in the last step the approximations $|q/p| \approx (1 - a_{\text{sl}}/2)$ and $|p/q| \approx (1 + a_{\text{sl}}/2)$ are used (see Eq. 1.2.23). Equation D.0.9 is actually the same as the one used in Chapter 1 (Eq. 1.2.37), when ignoring the term proportional to αa_{sl}^d , which is small.

Bibliography

- [1] S. Tolk, *Rare B decays and lepton flavour universality tests at LHCb*, J. Phys. : Conf. Ser. **800** (2017) 012012.
- [2] Particle Data Group, C. Patrignani *et al.*, *Review of particle physics*, Chin. Phys. **C40** (2016) 100001.
- [3] HFLAV collaboration, Y. Amhis *et al.*, *Averages of b-hadron, c-hadron and τ -lepton properties as of summer 2016*, [arXiv:1612.07233](https://arxiv.org/abs/1612.07233), and online update at <http://www.slac.stanford.edu/xorg/hflav>.
- [4] M. Roos, *Dark Matter: The evidence from astronomy, astrophysics and cosmology*, [arXiv:1001.0316](https://arxiv.org/abs/1001.0316).
- [5] J. Conrad and O. Reimer, *Indirect dark matter searches in gamma and cosmic rays*, Nat. Phys. **13** (2017) 224.
- [6] AMS collaboration, M. Aguilar *et al.*, *Antiproton flux, antiproton-to-proton flux ratio, and properties of elementary particle fluxes in primary cosmic rays measured with the Alpha Magnetic Spectrometer on the International Space Station*, Phys. Rev. Lett. **117** (2016) 091103.
- [7] ALPHA collaboration and Charman, A.E., *Description and first application of a new technique to measure the gravitational mass of antihydrogen*, Nat. Commun. **4** (2013) 1785.
- [8] WMAP collaboration, C. L. Bennett *et al.*, *Nine-year Wilkinson Microwave Anisotropy Probe (WMAP) observations: final maps and results*, Astrophys. J. Suppl. Ser. **208** (2013) 19, [arXiv:1212.5225](https://arxiv.org/abs/1212.5225).
- [9] C. Jarlskog, *Commutator of the quark mass matrices in the Standard Electroweak Model and a measure of maximal CP nonconservation*, Phys. Rev. Lett. **58** (1987) 1698.
- [10] C. S. Wu *et al.*, *Experimental test of parity conservation in beta decay*, Phys. Rev. **105** (1957) 1413.
- [11] F. Englert and R. Brout, *Broken symmetry and the mass of gauge vector mesons*, Phys. Rev. Lett. **13** (1964) 321.

- [12] P. Higgs, *Broken symmetries and the masses of gauge bosons*, Phys. Rev. Lett. **13** (1964) 508.
- [13] S. L. Glashow, *Partial-symmetries of weak interactions*, Nucl. Phys. **22** (1961) 579.
- [14] S. Weinberg, *A model of leptons*, Phys. Rev. Lett. **19** (1967) 1264.
- [15] A. Salam, *Weak and electromagnetic interactions*, Conf. Proc. **C680519** (1968) 367.
- [16] ATLAS collaboration, G. Aad *et al.*, *Observation of a new particle in the search for the Standard Model Higgs boson with the ATLAS detector at the LHC*, Phys. Lett. **B716** (2012) 1, [arXiv:1207.7214](#).
- [17] CMS collaboration, G. Aad *et al.*, *Observation of a new boson at a mass of 125 GeV with the CMS experiment at the LHC*, Phys. Lett. B **716** (2012) 30, [arXiv:1207.7235](#).
- [18] C. A. Baker *et al.*, *An improved experimental limit on the electric dipole moment of the neutron*, Phys. Rev. Lett. **97** (2006) 131801, [arXiv:hep-ex/0602020](#).
- [19] S. F. King, *Neutrino mass models*, Rept. Prog. Phys. **67** (2004) 107, [arXiv:hep-ph/0310204](#).
- [20] A. D. Sakharov, *Violation of CP invariance, C asymmetry, and baryon asymmetry of the universe*, Pisma Zh. Eksp. Teor. Fiz. **5** (1967) 32.
- [21] J. M. Cline, *Baryogenesis*, [arXiv:hep-ph/0609145](#), (2006).
- [22] S. B. Treiman and F. Wilczek, *Thermalization of baryon asymmetry*, Phys. Lett. **B95** (1980) 222.
- [23] V. A. Kuzmin, V. A. Rubakov, and M. E. Shaposhnikov, *On anomalous electroweak baryon-number non-conservation in the early universe*, Phys. Lett. **B155** (1985) 36, [arXiv:hep-ph/9603208](#).
- [24] T. D. Lee, R. Oehme, and C. N. Yang, *Remarks on possible noninvariance under time reversal and charge conjugation*, Phys. Rev. **106** (1957) 340.
- [25] K. Anikeev *et al.*, *B physics at the Tevatron: run II and beyond*, [arXiv:hep-ph/0201071](#).
- [26] M. Artuso, G. Borissov, and A. Lenz, *CP violation in the B_s^0 system*, Rev. Mod. Phys. **88** (2016) 045002, [arXiv:1511.09466](#).
- [27] LHCb collaboration, R. Aaij *et al.*, *Measurement of CP violation in $B^0 \rightarrow J/\psi K_S^0$ decays*, Phys. Rev. Lett. **115** (2015) 031601, [arXiv:1503.07089](#).
- [28] LHCb collaboration, R. Aaij *et al.*, *Precision measurement of CP violation in $B_s^0 \rightarrow J/\psi K^+ K^-$ decays*, Phys. Rev. Lett. **114** (2015) 041801, [arXiv:1411.3104](#).

-
- [29] A. Lenz and U. Nierste, *Theoretical update of $B_s - \bar{B}_s$ mixing*, J. High Energy Phys. **06** (2007) 072, [arXiv:hep-ph/0612167](#).
- [30] C. Gay, *B mixing*, Ann. Rev. Nucl. Part. Sci. **50** (2000) 577, [arXiv:hep-ex/0103016](#).
- [31] A. J. Buras, M. Jamin, and P. H. Weisz, *Leading and next-to-leading QCD corrections to the ε -parameter and $B^0 - \bar{B}^0$ mixing in the presence of a heavy top quark*, Nucl. Phys. **B347** (1990) 491.
- [32] A. Lenz and U. Nierste, *Numerical updates of lifetimes and mixing parameters of B mesons*, [arXiv:1102.4274](#).
- [33] P. Langacker, *The physics of heavy Z' gauge bosons*, Rev. Mod. Phys. **81** (2009) 1199, [arXiv:0801.1345](#).
- [34] J. H. Christenson, J. W. Cronin, V. L. Fitch, and R. Turlay, *Evidence for the 2π decay of the K_2^0 Meson*, Rev. Rev. Lett. **13** (1964) 138.
- [35] BaBar collaboration, B. Aubert *et al.*, *Evidence for $D^0 - \bar{D}^0$ mixing*, Phys. Rev. Lett. **98** (2007) 211802, [arXiv:hep-ex/0703020](#).
- [36] Belle collaboration, M. Staric *et al.*, *Evidence for $D^0 - \bar{D}^0$ mixing*, Phys. Rev. Lett. **98** (2007) 211803, [arXiv:hep-ex/0703036](#).
- [37] CDF collaboration, T. Aaltonen *et al.*, *Evidence for $D^0 - \bar{D}^0$ mixing using the CDF II detector*, Phys. Rev. Lett. **100** (2008) 121802, [arXiv:0712.1567](#).
- [38] ARGUS collaboration, H. Albrecht *et al.*, *Observation of $B^0 - \bar{B}^0$ mixing*, Phys. Lett. **B192** (1987) 245.
- [39] M. Artuso *et al.*, *$B^0 - \bar{B}^0$ mixing at the $\Upsilon(4S)$* , Phys. Rev. Lett. **62** (1989) 2233.
- [40] CDF collaboration, A. Abulencia *et al.*, *Observation of $B_s^0 - \bar{B}_s^0$ oscillations*, Phys. Rev. Lett. **97** (2006) 242003, [arXiv:hep-ex/0609040](#).
- [41] Belle collaboration, E. Nakano *et al.*, *Charge asymmetry of same-sign dileptons in $B^0 - \bar{B}^0$ mixing*, Phys. Rev. **D73** (2006) 112002, [arXiv:hep-ex/0505017](#).
- [42] BaBar collaboration, J. P. Lees *et al.*, *Search for CP violation in $B^0 - \bar{B}^0$ mixing using partial reconstruction of $B^0 \rightarrow D^{*-} X \ell^+ \nu_\ell$ and a kaon tag*, Phys. Rev. Lett. **111** (2013) 101802, [arXiv:1305.1575](#).
- [43] D0 collaboration, V. M. Abazov *et al.*, *Measurement of the semileptonic charge asymmetry in B^0 meson mixing with the D0 detector*, Phys. Rev. **D86** (2012) 072009, [arXiv:1208.5813](#).
- [44] D0 collaboration, V. M. Abazov *et al.*, *Measurement of the semileptonic charge asymmetry using $B_s^0 \rightarrow D_s \mu X$ decays*, Phys. Rev. Lett. **110** (2013) 011801, [arXiv:1207.1769](#).

- [45] D0 collaboration, V. M. Abazov *et al.*, *Measurement of the anomalous like-sign dimuon charge asymmetry with 9 fb^{-1} of $p\bar{p}$ collisions*, Phys. Rev. **D84** (2011) 052007, [arXiv:1106.6308](#).
- [46] G. Borissov and B. Hoeneisen, *Understanding the like-sign dimuon charge asymmetry in $p\bar{p}$ collisions*, Phys. Rev. **D87** (2013) 074020, [arXiv:1303.0175](#).
- [47] D0 collaboration, V. M. Abazov *et al.*, *Study of CP-violating charge asymmetries of single muons and like-sign dimuons in $p\bar{p}$ collisions*, Phys. Rev. **D89** (2014) 012002, [arXiv:1310.0447](#).
- [48] LHCb collaboration, R. Aaij *et al.*, *Measurement of the flavour-specific CP-violating asymmetry a_{sl}^s in B_s^0 decays*, Phys. Lett. **B728** (2014) 607, [arXiv:1308.1048](#).
- [49] BaBar collaboration, J. P. Lees *et al.*, *Study of CP asymmetry in $B^0 - \bar{B}^0$ mixing with inclusive dilepton events*, Phys. Rev. Lett. **114** (2015) 081801, [arXiv:1411.1842](#).
- [50] A. Lenz *et al.*, *Constraints on new physics in $B - \bar{B}$ mixing in the light of recent LHCb data*, Phys. Rev. **D86** (2012) 033008, [arXiv:1203.0238](#).
- [51] LHCb collaboration, R. Aaij *et al.*, *Opposite-side flavour tagging of B mesons at the LHCb experiment*, Eur. Phys. J. **C72** (2012) 2022, [arXiv:1202.4979](#).
- [52] P. Nason *et al.*, *Bottom production*, [arXiv:hep-ph/0003142](#).
- [53] LHCb collaboration, A. A. Alves Jr. *et al.*, *The LHCb detector at the LHC*, JINST **3** (2008) S08005.
- [54] LHCb collaboration, R. Aaij *et al.*, *LHCb detector performance*, Int. J. Mod. Phys. **A30** (2015) 1530022, [arXiv:1412.6352](#).
- [55] *LHCb public webpage*, <http://lhcb-public.web.cern.ch>, 2017.
- [56] R. Alemany-Fernandez *et al.*, *Operation and configuration of the LHC in run 1*, 2014. CERN-ACC-NOTE-2013-0041.
- [57] C. Levèfre, *The CERN accelerator complex*, 2008. CERN-DI-0812015.
- [58] B. J. Holzer, R. Versteegen, and R. Alemany, *Vertical crossing angle in IR8*, 2013. CERN-ATS-Note-2013-024 PERF.
- [59] B. Andersson, G. Gustafson, G. Ingelman, T. Sjöstrand, *Parton fragmentation and string dynamics*, Phys. Rept. **97** (1983) 31.
- [60] LHCb collaboration, *LHCb magnet: Technical Design Report*, CERN-LHCC-2000-007. LHCb-TDR-001.
- [61] M. Losasso *et al.*, *Tests and field map of the LHCb dipole magnet*, IEEE Trans. Appl. Supercond. **16** (2006) 1700, and update in LHCb-INT-2012-012.

-
- [62] LHCb collaboration, *LHCb VELO (VERtex LOcator): Technical Design Report*, CERN-LHCC-2001-011. LHCb-TDR-005.
- [63] R. Aaij *et al.*, *Performance of the LHCb Vertex Locator*, J. Instrum. **9** (2014) P09007, [arXiv:1405.7808](#).
- [64] G. A. Cowan *et al.*, *Performance of the LHCb silicon tracker*, Nucl. Instrum. Meth. **A699** (2013) 156.
- [65] LHCb collaboration, *LHCb inner tracker: Technical Design Report*, CERN-LHCC-2002-029. LHCb-TDR-008.
- [66] J. M. Amoraal, *Alignment with Kalman filter fitted tracks and reconstruction of $B_s^0 \rightarrow J/\psi \phi$ decays*, CERN-THESIS-2011-011.
- [67] LHCb collaboration, *LHCb outer tracker: Technical Design Report*, CERN-LHCC-2001-024. LHCb-TDR-006.
- [68] R. Arink *et al.*, *Performance of the LHCb Outer Tracker*, J. Instrum. **9** (2014) P01002, [arXiv:1311.3893](#).
- [69] H. A. Bethe, *Molière's theory of multiple scattering*, Phys. Rev. **89** (1953) 1256.
- [70] LHCb collaboration, R. Aaij *et al.*, *Measurement of the track reconstruction efficiency at LHCb*, J. Instrum. **10** (2015) P02007, [arXiv:1408.1251](#).
- [71] J. A. N. van Tilburg, *Track simulation and reconstruction in LHCb*, CERN-THESIS-2005-040.
- [72] LHCb collaboration, *LHCb RICH: Technical Design Report*, CERN-LHCC-2000-037. LHCb-TDR-003.
- [73] M. Adinolfi *et al.*, *Performance of the LHCb RICH detector at the LHC*, Eur. Phys. J. **C73** (2013) 2431, [arXiv:1211.6759](#).
- [74] LHCb collaboration, *LHCb calorimeters: Technical Design Report*, CERN-LHCC-2000-036. LHCb-TDR-002.
- [75] LHCb collaboration, *Performance of the LHCb calorimeters*, LHCb-DP-2013-004, in preparation.
- [76] LHCb collaboration, *LHCb muon system: Technical Design Report*, CERN-LHCC-2001-010. LHCb-TDR-004.
- [77] A. A. Alves Jr. *et al.*, *Performance of the LHCb muon system*, J. Instrum. **8** (2013) P02022, [arXiv:1211.1346](#).
- [78] M. Anelli *et al.*, *Performance of the LHCb muon system with cosmic rays*, J. Instrum. **5** (2010) P10003, [arXiv:1009.1963](#).

- [79] LHCb collaboration, *LHCb trigger system: Technical Design Report*, CERN-LHCC-2003-031. LHCb-TDR-010.
- [80] R. Aaij *et al.*, *The LHCb trigger and its performance in 2011*, J. Instrum. **8** (2013) P04022, [arXiv:1211.3055](#).
- [81] J. Albrecht, V. V. Gligorov, G. Raven, and S. Tolk, *Performance of the LHCb High Level Trigger in 2012*, J. Phys. Conf. Ser. **513** (2014) 012001, [arXiv:1310.8544](#).
- [82] LHCb collaboration, *LHCb online system, data acquisition and experiment control: Technical Design Report*, CERN-LHCC-2001-040. LHCb-TDR-007.
- [83] LHCb collaboration, *LHCb computing: Technical Design Report*, CERN-LHCC-2005-019. LHCb-TDR-011.
- [84] M. Frank *et al.*, *Deferred high level trigger in LHCb: a boost to CPU resource utilization*, J. Phys. Conf. Ser. **513** (2014) 012006.
- [85] T. Sjöstrand, S. Mrenna, and P. Skands, *PYTHIA 6.4 physics and manual*, J. High Energy Phys. **05** (2006) 026, [arXiv:hep-ph/0603175](#); T. Sjöstrand, S. Mrenna, and P. Skands, *A brief introduction to PYTHIA 8.1*, Comput. Phys. Commun. **178** (2008) 852, [arXiv:0710.3820](#).
- [86] I. Belyaev *et al.*, *Handling of the generation of primary events in Gauss, the LHCb simulation framework*, J. Phys. Conf. Ser. **331** (2011) 032047.
- [87] LHCb collaboration, R. Aaij *et al.*, *Measurement of charged particle multiplicities and densities in pp collisions at $\sqrt{s} = 7$ TeV in the forward region*, Eur. Phys. J. **C74** (2014) 2888, [arXiv:1402.4430](#).
- [88] D. J. Lange, *The EvtGen particle decay simulation package*, Nucl. Instrum. Meth. **A462** (2001) 152.
- [89] P. Golonka and Z. Was, *PHOTOS Monte Carlo: A precision tool for QED corrections in Z and W decays*, Eur. Phys. J. **C45** (2006) 97, [arXiv:hep-ph/0506026](#).
- [90] Geant4 collaboration, J. Allison *et al.*, *Geant4 developments and applications*, IEEE Trans. Nucl. Sci. **53** (2006) 270; Geant4 collaboration, S. Agostinelli *et al.*, *Geant4: A simulation toolkit*, Nucl. Instrum. Meth. **A506** (2003) 250.
- [91] M. Clemencic *et al.*, *The LHCb simulation application, Gauss: Design, evolution and experience*, J. Phys. Conf. Ser. **331** (2011) 032023.
- [92] LHCb collaboration, R. Aaij *et al.*, *Measurement of the track reconstruction efficiency at LHCb*, J. Instrum. **10** (2015) P02007, [arXiv:1408.1251](#).
- [93] LHCb collaboration, R. Aaij *et al.*, *Measurement of the $D_s^+ - D_s^-$ production asymmetry in 7 TeV pp collisions*, Phys. Lett. **B713** (2012) 186, [arXiv:1205.0897](#).

-
- [94] Particle Data Group, K. A. Olive *et al.*, *Review of particle physics*, Chin. Phys. **C38** (2014) 090001.
- [95] A. S. Carroll *et al.*, *Total cross sections of π^\pm and K^\pm on protons and deuterons between 50 GeV/c and 200 GeV/c*, Phys. Rev. Lett. **33** (1974) 932.
- [96] A. S. Carroll *et al.*, *Total cross sections of π^\pm , K^\pm , p , and \bar{p} on protons and deuterons between 23 GeV/c and 280 GeV/c*, Phys. Lett. **B61** (1976) 303.
- [97] A. S. Carroll *et al.*, *Total cross-sections of π^\pm , K^\pm , p and \bar{p} on protons and deuterons between 200 GeV/c and 370 GeV/c*, Phys. Lett. **B80** (1979) 423.
- [98] LHCb collaboration, R. Aaij *et al.*, *Measurement of CP asymmetry in $D^0 \rightarrow K^- K^+$ and $D^0 \rightarrow \pi^- \pi^+$ decays*, J. High Energy Phys. **07** (2014) 041, arXiv:1405.2797.
- [99] S. Stahl, *Measurement of CP asymmetry in muon-tagged $D^0 \rightarrow K^- K^+$ and $D^0 \rightarrow \pi^- \pi^+$ decays at LHCb*, CERN-THESIS-2014-274.
- [100] M. Pivk and F. R. Le Diberder, *sPlot: A statistical tool to unfold data distributions*, Nucl. Instrum. Meth. **A555** (2005) 356, arXiv:physics/0402083.
- [101] LHCb collaboration, R. Aaij *et al.*, *Measurement of the semileptonic CP asymmetry in $B^0 - \bar{B}^0$ mixing*, Phys. Rev. Lett. **114** (2015) 041601, arXiv:1409.8586.
- [102] LHCb collaboration, R. Aaij *et al.*, *Measurement of CP asymmetries in the decays $B^0 \rightarrow K^{*0} \mu^+ \mu^-$ and $B^+ \rightarrow K^+ \mu^+ \mu^-$* , JHEP **09** (2014) 177, arXiv:1408.0978.
- [103] LHCb collaboration, R. Aaij *et al.*, *First evidence of direct CP violation in charmless two-body decays of B_s^0 mesons*, Phys. Rev. Lett. **108** (2012) 201601, arXiv:1202.6251.
- [104] LHCb collaboration, R. Aaij *et al.*, *Measurement of the B^\pm production asymmetry and the CP asymmetry in $B^\pm \rightarrow J/\psi K^\pm$ decays*, Phys. Rev. **D95** (2017) 052005, arXiv:1701.05501.
- [105] LHCb collaboration, R. Aaij *et al.*, *Measurement of b hadron production fractions in 7 TeV pp collisions*, Phys. Rev. **D85** (2012) 032008, arXiv:1111.2357.
- [106] LHCb collaboration, R. Aaij *et al.*, *Study of beauty baryon decays to $D^0 p h^-$ and $\Lambda_c^+ h^-$ final states*, Phys. Rev. **D89** (2014) 032001, arXiv:1311.4823.
- [107] LHCb collaboration, R. Aaij *et al.*, *Observation of the $\Lambda_b^0 \rightarrow J/\psi p \pi^-$ decay*, J. High Energy Phys. **07** (2014) 103, arXiv:1406.0755.
- [108] LHCb collaboration, R. Aaij *et al.*, *Measurement of the CP asymmetry in $B_s^0 - \bar{B}_s^0$ mixing*, Phys. Rev. Lett. **117** (2016) 061803, arXiv:1605.09768.

- [109] D. Martínez Santos and F. Dupertuis, *Mass distributions marginalized over per-event errors*, Nucl. Instrum. Meth. Phys. Res. **A 764** (2014) 150, [arXiv:1312.5000](#).
- [110] LHCb collaboration, R. Aaij *et al.*, *Measurement of the fragmentation fraction ratio f_s/f_d and its dependence on B meson kinematics*, JHEP **04** (2013) 001, [arXiv:1301.5286](#), f_s/f_d value updated in LHCb-CONF-2013-011.
- [111] LHCb collaboration, R. Aaij *et al.*, *Study of the productions of Λ_b^0 and \bar{B}^0 hadrons in pp collisions and first measurement of the $\Lambda_b^0 \rightarrow J/\psi p K^-$ branching fraction*, Chin. Phys. **C40** (2015) 011001, [arXiv:1509.00292](#).
- [112] K. De Bruyn and R. Fleischer, *A roadmap to control penguin effects in $B^0 \rightarrow J/\psi K_s^0$ and $B_s^0 \rightarrow J/\psi \phi$* , J. High Energy Phys. **03** (2015) 145, [arXiv:1412.6834](#).
- [113] LHCb collaboration, R. Aaij *et al.*, *Measurement of B^0 , B_s^0 , B^+ and Λ_b^0 production asymmetries in 7 and 8 TeV proton-proton collisions*, Phys. Lett. **B774** (2017) 139, [arXiv:1703.08464](#).
- [114] LHCb collaboration, R. Aaij *et al.*, *Measurement of the D_s^\pm production asymmetry with $D_s^\pm \rightarrow K^+ K^- \pi^\pm$ decays*, , in preparation.
- [115] C. Bobeth *et al.*, *On new physics in $\Delta\Gamma_d$* , J. High Energy Phys. **1406** (2014) 040, [arXiv:1404.2531](#).
- [116] S. Bar-Shalom, G. Eilam, M. Gronau, and J. L. Rosner, *Second-order direct CP asymmetry in $B_s^0 \rightarrow X l \nu$* , Phys. Lett. **B694** (2011) 374, [arXiv:1008.4354](#).
- [117] S. Descotes-Genon and J. F. Kamenik, *On the origin of the $D0$ like-sign dimuon charge asymmetry*, [arXiv:1207.4483](#).
- [118] R. Fleischer and K. K. Vos, *$B_s^0 - \bar{B}_s^0$ oscillations as a new tool to explore CP violation in D_s^\pm decays*, Phys. Lett. **B770** (2016) 319, [arXiv:1606.06042](#).
- [119] LHCb collaboration, R. Aaij *et al.*, *Measurement of CP violation parameters and polarisation fractions in $B_s^0 \rightarrow J/\psi \bar{K}^{*0}$ decays*, [arXiv:1509.00400](#), submitted to JHEP.
- [120] V. Syropoulos, *Controlling penguins: an estimate of penguin topologies contributing to the weak phase ϕ_s* , CERN-THESIS-2017-164.
- [121] A. Lenz, *A simple relation for B_s^0 -mixing*, Phys. Rev. **D84** (2011) 031501, [arXiv:1106.3200](#).
- [122] LHCb collaboration, R. Aaij *et al.*, *Measurement of the CP-violating phase ϕ_s in $\bar{B}_s^0 \rightarrow D_s^+ D_s^-$ decays*, Phys. Rev. Lett. **113** (2014) 211801, [arXiv:1409.4619](#).
- [123] LHCb collaboration, R. Aaij *et al.*, *Search for CP violation in $D^0 \rightarrow \pi^- \pi^+ \pi^0$ decays with the energy test*, Phys. Lett. **B740** (2015) 158, [arXiv:1410.4170](#).

-
- [124] O. Deschamps *et al.*, *Photon and neutral pion reconstruction*, LHCb-2003-091.
- [125] LHCb collaboration, R. Aaij *et al.*, *Measurement of the B^0 - \bar{B}^0 oscillation frequency Δm_d with the decays $B^0 \rightarrow D^- \pi^+$ and $B^0 \rightarrow J/\psi K^{*0}$* , Phys. Lett. **B719** (2013) 318, [arXiv:1210.6750](#).
- [126] LHCb collaboration, R. Aaij *et al.*, *Precision measurement of the B_s^0 - \bar{B}_s^0 oscillation frequency in the decay $B_s^0 \rightarrow D_s^- \pi^+$* , New J. Phys. **15** (2013) 053021, [arXiv:1304.4741](#).
- [127] M. A. Baak, *Measurement of CKM-angle γ with charmed B^0 meson decays*, CERN-THESIS-2007-165.
- [128] LHCb collaboration, R. Aaij *et al.*, *Measurement of the ratio of branching fractions $\mathcal{B}(\bar{B}' \rightarrow \mathcal{D}^{*+} \tau^- \bar{\nu}_\tau) / \mathcal{B}(\bar{B}' \rightarrow \mathcal{D}^{*+} \mu^- \bar{\nu}_\mu)$* , Phys. Rev. Lett. **115** (2015) 111803, [arXiv:1506.08614](#).
- [129] M. Cacciari, M. L. Mangano, and P. Nason, *Gluon PDF constraints from the ratio of forward heavy quark production at the LHC at $\sqrt{s} = 7$ and 13 TeV*, [arXiv:1507.06197](#).
- [130] G. Dujany and B. Storaci, *Real-time alignment and calibration of the LHCb detector in run II*, J. Phys. Conf. Ser. **664** (2015) 082010.
- [131] B. Sciascia, *LHCb run 2 trigger performance*, PoS **BEAUTY2016** (2016) 029, CERN-LHCb-PROC-2016-020.
- [132] LHCb collaboration, H. Schindler, *The LHCb detector upgrade*, Nucl. Instrum. Meth. Phys. Res. **A732** (2013) 44.
- [133] LHCb collaboration, *LHCb Tracker Upgrade Technical Design Report*, CERN-LHCC-2014-001. LHCb-TDR-015.
- [134] J. Albrecht, C. Fitzpatrick, V. Gligorov, and G. Raven, *The upgrade of the LHCb trigger system*, J. Instrum. **9** (2014) C10026, [arXiv:1410.5012](#).

Summary

The understanding of fundamental processes in nature has greatly improved over the last century. This has led to the ambition to explain large-scale cosmological observations starting from the very small scale of particle interactions. In doing so, the Standard Model (SM) of particle physics is incomplete in describing these observations. It does not describe gravity, and in particular, it is unable to explain the large matter-over-antimatter dominance that we observe in our universe. Physics beyond the SM, in the form of additional particles and forces, may help to explain this difference. In this thesis, the search for new physics is done by precisely measuring processes that are sensitive to the contribution of unknown particles through quantum loops. If a deviation from the SM prediction is observed, new physics can explain the difference. In this thesis, the sensitive process that is measured is CP violation in the mixing of B^0 and B_s^0 mesons. These neutral mesons change into their own antipartner — \bar{B}^0 or \bar{B}_s^0 — over time with a certain frequency, before they decay. This process is called mixing. After a certain time, these mesons decay to a lighter set of particles known as the final state. A final state is chosen such that it is specific for the state at the time of decay: $B_{(s)}^0 \rightarrow f$ and $\bar{B}_{(s)}^0 \rightarrow \bar{f}$.

A difference in the rate at which $B_{(s)}^0$ transforms to $\bar{B}_{(s)}^0$ and decays to \bar{f} , compared to the antimatter-equivalent process $\bar{B}_{(s)}^0 \rightarrow B_{(s)}^0 \rightarrow f$, is known as CP violation in the mixing. In the SM this difference is practically equal to zero. However, recent measurements by the D0 collaboration have hinted that these rates might be different at three standard deviations. This might indicate that new particles contribute to this process, and could help explain the matter-antimatter asymmetry in our universe.

In order to confirm or disprove these results, a new, more precise measurement is necessary. Exploiting the high energy and luminosity of the pp collisions at the Large Hadron Collider (LHC), the LHCb detector has collected data about millions of B^0 and B_s^0 meson decays. While this detector is specifically designed to perform such measurements, the level of precision allowed by this amount of data requires careful inspection of all possible sources of asymmetries in the detection; a higher detection efficiency for matter with respect to antimatter would artificially induce a non-zero measurement of the CP asymmetry. Possible sources of such asymmetries are due to interactions of particles with the detector material, misalignment, an asymmetry in the shape of the detector, particle identification and the online triggering of interesting events. These effects are calibrated to permille-level precision by using data from well-known decays of more abundant particles. In addition, there might be an asymmetry in the produced amount of $B_{(s)}^0$ and $\bar{B}_{(s)}^0$ mesons,

which could affect the measurement.

The asymmetry in the mixing of B^0 and \bar{B}^0 mesons is measured as a function of the decay time of the B^0 or \bar{B}^0 . This allows to disentangle the amount of CP violation in mixing, known as a_{sl}^d , from a possible production asymmetry: the latter only affects the offset of the observed mixing oscillation, while a_{sl}^d also affects the amplitude. The final state that is used to reconstruct the B^0 meson is the semileptonic decay $B^0 \rightarrow D^{(*)-} \mu^+ \nu_\mu$. These decays have a large branching fraction, although the energy of the B^0 meson is not fully reconstructed due to the neutrino escaping detection. This biases and smears the reconstructed decay time of the B^0 meson, which is obtained from the measured B^0 decay length and momentum. The bias in the decay time is corrected by using simulated B^0 decays. The broad B^0 invariant mass peak resulting from the missing neutrino includes contributions from various backgrounds with a similar final state, in particular from B^+ mesons. These can be separated by their different decay-time behaviour, and the production asymmetry of B^+ mesons is taken from other measurements. The final result is

$$a_{\text{sl}}^d = (-0.02 \pm 0.19 \pm 0.30)\%,$$

where the first uncertainty is statistical and the second systematic. This is the most precise measurement of a_{sl}^d to date.

In contrast, the asymmetry in the mixing of B_s^0 and \bar{B}_s^0 mesons, called a_{sl}^s , is measured integrated over their decay time. This is similar to a counting experiment, and is possible due to the high mixing frequency in this system, which washes out any production asymmetry to negligible level. The semileptonic decay mode $B_s^0 \rightarrow D_s^- \mu^+ \nu_\mu$ is used to reconstruct the B_s^0 meson. The contributing backgrounds are dominated by $B \rightarrow DD$ -like decays, where B can be B^+ , B^0 , B_s^0 or A_b^0 . The various contributions are determined from the known production- and branching fractions, and their efficiencies are studied using simulated events. These backgrounds dilute the measured asymmetry, and any production or CP asymmetry in these modes can bias the measurement. The size of these asymmetries is taken from earlier LHCb measurements. The final result is

$$a_{\text{sl}}^s = (0.39 \pm 0.26 \pm 0.20)\%,$$

which is the most precise measurement of a_{sl}^s to date.

These results of a_{sl}^d and a_{sl}^s are compatible with the SM prediction, and only marginally compatible with the D0 result. The latter uses a different measurement strategy which allows for contributions other than just a_{sl}^d and a_{sl}^s which might explain the observed deviation from the SM. Since the precision of the measurements of a_{sl}^d and a_{sl}^s is limited by the amount of data, significant improvements are expected as LHCb collects more data in the near future. The role of these analyses in future searches for new physics is complementary to that of other measurements of CP violation, with ample room for a 5-standard-deviation discovery after the upgrade of the LHCb detector.

Onbalans in het universum

Alles om ons heen bestaat uit kleine deeltjes. Deze deeltjes vormen de atomen en moleculen waar alles in het universum uit is opgebouwd. Deeltjesfysica draait om het bestuderen van deze deeltjes en hun wisselwerkingen. De deeltjes die we om ons heen vinden, zijn opgebouwd uit de lichte u en d quarks, en begrijpen we inmiddels redelijk goed. Er zijn echter ook nog andere deeltjes, die vooral een rol speelden in het vroege universum. Een voorbeeld zijn de zware beauty quarks (b), die tijdens de afkoeling van het universum na de oerknal vervallen zijn in lichtere deeltjes. Al deze bekende deeltjes en hun wisselwerkingen worden beschreven met het succesvolle standaardmodel (SM) van de deeltjesfysica. Sinds het begin van de 20ste eeuw weten we dat van alle deeltjes in het SM ook een soort spiegelbeeldversies bestaan, die antideeltjes worden genoemd. Deze werden aanvankelijk als zeer zeldzaam ervaren, maar uit onderzoek blijkt dat bij processen die materie voortbrengen uit energie — zoals bij de oerknal — de hoeveelheden deeltjes en antideeltjes altijd in balans zijn. Vandaag de dag is antimaterie niet zo bijzonder meer, en heeft bijvoorbeeld toepassingen in het ziekenhuis. De vraag is dan ook waarom alles in het universum opgebouwd lijkt te zijn uit materie, en waarom antimaterie zo zelden gezien wordt. Het begrijpen waar deze onbalans vandaan komt zal inzicht bieden in de natuurwetten die een rol spelen bij de geboorte van het universum.

***CP* schending**

In de zwakke interactie van het SM is een klein verschil tussen materie en antimaterie. Dit effect heet *CP* schending, maar is te klein om het geobserveerde verschil tussen de hoeveelheden materie en antimaterie in het universum te verklaren. De bijdrage van nieuwe deeltjes en/of krachten, die nog niet beschreven worden door het SM, kan de hoeveelheid *CP* schending vergroten en biedt een mogelijke verklaring. Het feit dat deze deeltjes nog niet gezien zijn, betekent waarschijnlijk dat ze erg zwaar zijn, en dat het veel energie vergt om deze te produceren. De zoektocht naar directe productie van nieuwe deeltjes in hoog-energetische botsingen is een manier om nieuwe fysica te vinden. Ook wordt verwacht dat nieuwe deeltjes een invloed uitoefenen op reeds bekende processen in het SM, via interferentie van zogeheten “kwantumlussen”. Bijdragen van nieuwe deeltjes aan deze processen kunnen worden gevonden door precies gemeten waarden te vergelijken met de voorspellingen. Het voordeel van kwantumlussen is dat de nieuwe deeltjes niet direct geproduceerd hoeven te worden, en zodanig een gevoeligheid voor nieuwe deeltjes

met zeer hoge massa's — tot ordes van grootte hoger dan de beschikbare energie in de botsingen — bereikt wordt.

In deze dissertatie is gekeken naar het proces waarin zware deeltjes, neutrale B mesonen, via kwantumlussen veranderen in anti- B mesonen, $B \rightarrow \bar{B}$. Dit proces heet mixing. Volgens het SM gaat mixing de ene kant op bijna even snel als andersom, $\bar{B} \rightarrow B$, en dus is de asymmetrie in dit proces,

$$a_{\text{sl}} = \frac{P(\bar{B} \rightarrow B) - P(B \rightarrow \bar{B})}{P(\bar{B} \rightarrow B) + P(B \rightarrow \bar{B})},$$

bij de huidige experimentele gevoeligheid bij goede benadering gelijk aan nul. Er zijn twee soorten B mesonen, de B^0 (bevat een \bar{b} en d quark) en B_s^0 (bevat een \bar{b} en een s quark). Indien de bijbehorende asymmetry, genaamd a_{sl}^d resp. a_{sl}^s , niet nul is spreekt men van CP schending in mixing in dat systeem.

In 2011 kwam het D0 experiment met een gecombineerde meting van a_{sl}^d en a_{sl}^s , die afweek van nul met een significantie van bijna 4 standaard deviaties. Dit is een serieuze hint dat er nieuwe deeltjes zijn die een rol spelen in dit proces. De manier waarop deze meting gedaan is, staat echter toe dat andere bijdragen naast die van a_{sl}^d en a_{sl}^s kunnen zorgen voor deze afwijking. Er is een individuele meting van a_{sl}^d en a_{sl}^s nodig met hoge precisie — met een onzekerheid van een paar promille — om duidelijkheid te scheppen waar deze afwijking vandaan komt.

Het LHCb experiment

De Large Hadron Collider (LHC) is een deeltjesversneller die in staat is om zowel de energie als de intensiteit te leveren die nodig is om deze metingen te doen. Protonen worden versneld in een 27 kilometer lange ring tot een paar gigaelectronvolt (GeV) aan energie, voordat ze op elkaar botsen. Hierbij ontstaan onder andere B^0 en B_s^0 mesonen. Na een korte levensduur van $1.5 \times 10^{-12} s$ vervallen deze B mesonen. Dit verval gaat hoofdzakelijk naar een D meson, muon en een neutrino: $D_{(s)}^- \mu^+ \nu_\mu$. De anti- B mesonen vervallen naar $D_{(s)}^+ \mu^- \bar{\nu}_\mu$. Het neutrino ontsnapt in beide vervallen aan de waarneming, maar het D meson en het muon worden gedetecteerd door de LHCb detector, die gespecialiseerd is in het reconstrueren van de vervallen van B mesonen. In totaal zijn er een paar miljoen B^0 en B_s^0 mesonen gemeten tijdens de jaren 2011 en 2012, welke zijn gebruikt in deze analyses.

Het meten van asymmetrieën

Er zijn verschillende achtergronden die een bijdrage geven tijdens de reconstructie van de B^0 en B_s^0 deeltjes. De meest belangrijke hiervan vinden hun oorsprong niet in misreconstructies, maar in daadwerkelijke fysische vervallen van andere deeltjes. Deze verminderen de gevoeligheid van de analyses voor a_{sl}^d en a_{sl}^s , en kunnen bovendien de waarde van de gemeten asymmetrie verschuiven, in het geval dat er een inherente asymmetrie in de achtergrondvervallen aanwezig is. Dit kan bijvoorbeeld komen door CP schending in deze achtergrondvervallen, of door een asymmetrie in de productie van deze deeltjes en

hun antideeltjes in de proton-proton botsingen. De grootte van deze bijdragen en hun asymmetrieën zijn reeds gemeten in andere analyses, en de efficiëntie van de reconstructie van deze vervallen in de huidige analyses is bestudeerd met simulaties.

Daarnaast is het bij het meten van de asymmetrie tussen B en \bar{B} vervallen van belang dat de efficiëntie om beide vervallen waar te nemen, hetzelfde is. Dit is niet direct het geval, vanwege onder meer een verschil in de interactie van deeltjes en antideeltjes met het materiaal van de LHCb detector. Mogelijke oorzaken van zogeheten detectieasymmetrieën zijn geïdentificeerd, en vervolgens nauwkeurig gekwantificeerd met kalibratiekanalen.

Resultaten

De gemeten CP asymmetrieën, na inachtneming van het bovenstaande, zijn

$$a_{\text{sl}}^d = (-0.02 \pm 0.19 \pm 0.30)\%,$$
$$a_{\text{sl}}^s = (0.39 \pm 0.26 \pm 0.20)\%,$$

waarbij de eerste fout statistisch is, en de tweede komt door systematische onzekerheden in de meting. Dit zijn tot nu toe de meest nauwkeurig gemeten waarden van a_{sl}^d en a_{sl}^s ter wereld. Deze getallen zijn compatibel met de waarden van het SM, en slecht te vergelijken met de afwijkende waarde van D0, zoals te zien is in Figuur D.1. Dit betekent dat CP schending in mixing alleen deze afwijking niet kan verklaren. Mogelijk zijn andere bronnen van asymmetrieën die een bijdrage leveren hier over het hoofd gezien, zowel binnen het SM als mogelijke nieuwe fysica.

De verwachting is dat het LHCb experiment in de komende jaren zeker een factor tien meer data gaat verzamelen dan gebruikt is in deze analyses. De upgrade van de LHCb detector speelt hierin een belangrijke rol. Dit zal de fout op a_{sl}^d en a_{sl}^s dusdanig verkleinen, dat een ontdekking van nieuwe deeltjes nog steeds tot de mogelijkheden behoort. Hierbij is het van belang om ook andere, complementaire metingen van CP schending in B systemen te bestuderen.

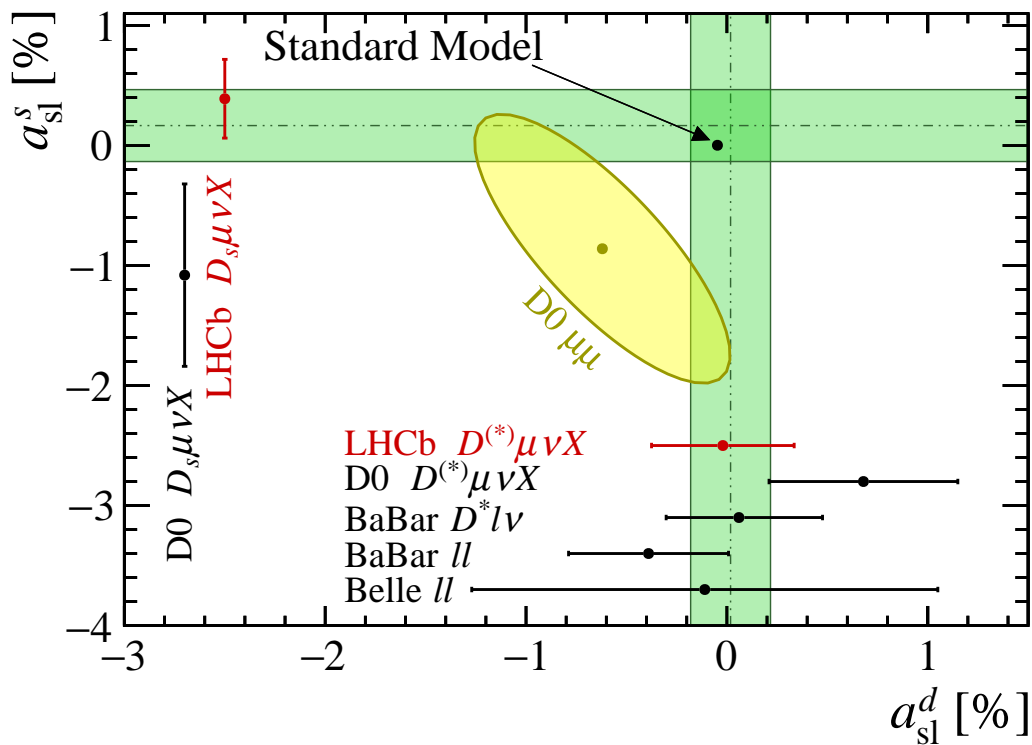


Figure D.1: Overzicht van de a_{sl}^d en a_{sl}^s metingen na de LHCb resultaten die gepresenteerd zijn in dit proefschrift, die aangegeven zijn met rode punten. De zwarte punten representeren de metingen van a_{sl}^d of a_{sl}^s van andere experimenten. De groene banden geven de gemiddelden van deze metingen van a_{sl}^d of a_{sl}^s aan. De SM voorspelling is aangegeven met een stip en een pijl. De afwijkende meting van D0, geïnterpreteerd in termen van a_{sl}^d en a_{sl}^s , is aangegeven met de gele ellips.

Acknowledgements

Although there is only one name on the cover, these four years would have been impossible without the help of many close colleagues, friends, and many enthusiastic experts. This section is dedicated to all of you who helped in establishing this work, in one way or another.

Most importantly, I want to deeply thank my supervisor, Jeroen van Tilburg. Jeroen, working with you has been a delight, and your honest, down-to-earth “Dutch” communication style has helped my scientific reasoning a lot. I’m glad you were always open for discussion on any subject, ranging from the SciFi simulation to personal matters. Usually you turned out to be right in the end, although I cherish my small victories. Without your effort, this thesis would be far from its current state. Thank you.

Marcel, “de grote roerganger” and promotor, it still amazes me how you always manage to stay on top of things. One of which is the beer keg. Although I have heard most of your jokes a few times by now, another consistency is your willingness to help out in any situation, and your success at doing so. I believe that combination makes for an excellent group leader, and I am glad I could always rely on your advice.

Niels, as your master student we have already had a lot of interaction, and as part of the outer tracker group this continued. Your openness always feels like there exist no dumb questions or ideas, and your fascination for physics — especially after a few beers — is an endless inspiration. I’m also very grateful to the members of staff that I was less directly involved with. Wouter, Gerhard, Antonio and Patrick, thank you for your informal attitude, and all your time for discussions. The same holds for all-rounder and sportsman Mika, during my time at CERN.

Many thanks goes to the LHCb semileptonic working group, as well as the referees of the analyses, Olaf, Thomas, Ulrik and Angelo, for improving the quality of the research. In addition I would like thank my direct analysis proponents. It was a pleasure working with, and learning from you, time-tracking Lucia, tracking-efficiency experts Matt and Marian, charming Suzanne and s(t)imulating Laurent. Not only did we have a great time professionally, but without you, the CERN experience would not have been the same. To that last category I should add running Michael, triggering Sasha, space buddy Elena Villhauer, isolating Basem and aligning Giulio. Also Szöke Zsolt and my other housemates

in Pregnin played a significant role in the latter. Laurent, too long — or arguably too little — time have we spent in one office together. Your down-to-earth directness has forced me to stay critical at myself. Besides that, you've made most time in the office a pleasure (and outside that as well). Arigatō.

As every beginning is hard, I am especially grateful to the senior PhD students and postdocs that helped me get started in the group with physics and computing. Consulting Jeroen van Leerdam, compiling Roel, violating Greg and hidden Pieter, thank you for answering my torrent of questions all the time. I consider myself lucky that I could always rely on your expertise to help me out. And ratio Rose, thank you for being my supervisor during my master thesis in the group — modelling hadronic backgrounds is a pain, but you've managed to motivate me enough to do a PhD.

The fruitful working environment at Nikhef has been stimulating and fun. The discussions over coffee breaks or beer create an excellent academic atmosphere, and I have many to thank for that, besides the people already mentioned above. In particular, Veerle, Vasilis, Suvayu and Panos from the 'old generation', our strong interaction has been incredibly pleasant. In the 'new generation', my close colleagues, rocking Maarten, fantasy Lennaert, magic Mick, strongman Sean, chocolate Elena, scoring Katya, higgys Lydia, daq-ing Mauricio, crypto Lex and very rare Flavio, you have made sure to keep my orientation when falling down the rabbit hole of subatomic physics. Your unique and diverse personalities keep life interesting. Dankjewel.

While doing high-level analyses it is sometimes easy to forget the complex low-level effort that goes into producing the data. A big thanks goes to the outer tracker group, with which I have had a wonderful hands-on experience in the pit. You have given me the chance to show responsibility in a relatively small collaborative effort. A big thank you also goes to the fibre tracker (SciFi) simulation group. It has been a delight working in such close collaboration with hardware and electronics measurements on one side, and the large LHCb reconstruction framework on the other.

Obvious or not, there exists a world outside of particle physics. A lot of people have reminded me of this important fact, and have meant a lot to me in the past four years. Jeroen Hofman and Thijs Krijger, both of you know what it is like to do a PhD in physics. Where applicable, we talked, and where not, we leisured. I am lucky to have you as friends. To my high school friends in Wageningen, I'm glad we stayed connected over the years. There are few people whom I have experienced such a large part of my 28 years with, which can lead to surprising insights after some drinks. Bart, Rob, Sjors, Erwin, Sandra, Floris, Henk, Rens and Arne, I am fond of our holidays and semi-regular visits, in whatever country that may be. In addition, Timo and Laury, thanks for the adventures in Amsterdam. Finally, a special mention goes to Arvid, whose fantastic futuristic art adorns the cover of this thesis. May your own dissertation be written in a flash.

I want to mention my housemates in Utrecht, during the first 1.5 years of my PhD. Merel, Iris, Doortje, Hidde, Joeri, Frank, Lieke, Han-Thijs, Ineke, Yvonne and Chris, thank you for all the pancakes and always family-like atmosphere at home. Besides pancakes, the same holds for my housemates in Amsterdam, during the last 1.5 years of my PhD. Tess, Jeroen, Eva, Claire, Joanne, Sjoerd and Bart, thanks for always knowing where the party is at.

Lara, I sometimes forget how similar we think. Not expecting relevant advice from my little sister was an obvious mistake. Dad, tige tank for all the statistical discussions over Sunday morning breakfast, and the genetic interest in science. Paula and Michel, thank you for your warm home, and treating me like one of your own. And Linde, thank you for your support. The journey was not always simple, but your everlasting faith has made a difference at crucial times. Merci, chérie.

